Preparation and characterization of iron oxide electrode materials for lithium-ion batteries by electrochemical and spectroscopic (XPS, ToF-SIMS) methods

Bingbing Tian

THÈSE

L'UNIVERSITÉ PIERRE ET MARIE CURIE

ÉCOLE DOCTORALE:
ED388: Chimie physique et chimie analytique de Paris Centre

Présentée par **M. Bingbing Tian**

POUR OBTENIR LE GRADE DE

DOCTEUR de l'Université Pierre et Marie Curie

SPÉCIALITÉ: Chimie physique et chimie analytique

Sujet de la thèse

Preparation and characterization of iron oxide electrode materials for lithium-ion batteries by electrochemical and spectroscopic (XPS, ToF-SIMS) methods

Soutenue le: 10 juillet 2014
Devant le jury composé de:

M. Michel Rosso	Directeur de recherche au CNRS École Polytechnique	Rapporteur
M. Rémi Dedryvère	Professeur Université de Pau et des Pays de l'Adour	Rapporteur
M. Didier Devilliers	Professeur Université Pierre et Marie Curie	Examinateur
M. Stéphane Laruelle	Professeur Université de Picardie Jules Verne	Examinateur
M. Jean-Pierre Pereira-Ramos	Directeur de recherche au CNRS Université Paris-Est	Examinateur
M. Philippe Marcus	Directeur de recherche au CNRS Chimie ParisTech	Directeur de thèse
M. Vincent Maurice	Directeur de recherche au CNRS Chimie ParisTech	Codirecteur de thèse
Mme. Jolanta Światowska	Chargé de recherche au CNRS Chimie ParisTech	Encadrante

Résumé de la thèse

1. Etat de l'art

Les batteries lithium-ion sont largement utilisées comme source d'énergie pour les appareils électroniques portables. Récemment, beaucoup d'efforts ont été faits pour promouvoir leur application dans les véhicules électriques hybrides et les systèmes dispersés de stockage d'énergie, qui requièrent faible poids, petit volume, densité d'énergie élevée et sécurité d'usage (**Figure 1**). [1,2,3]

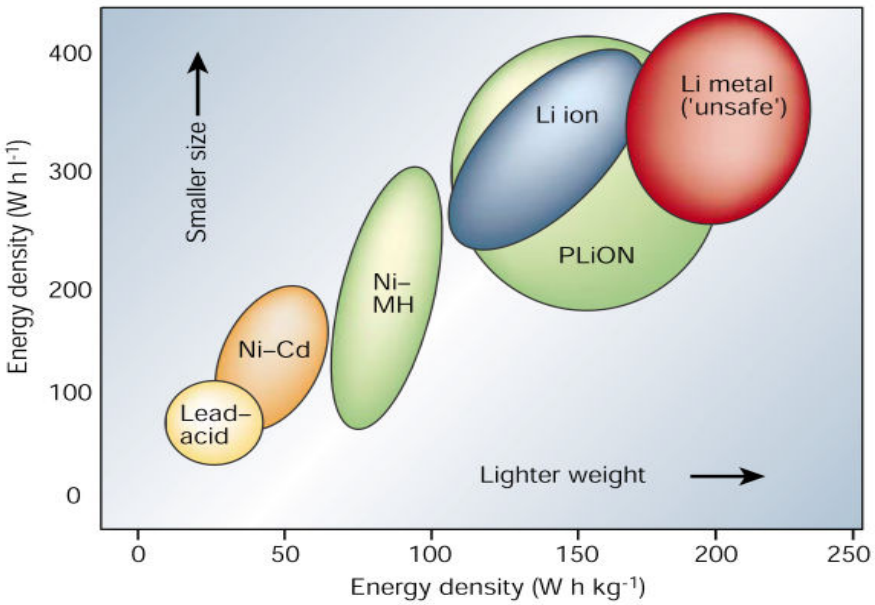

Figure 1 Comparaison de différents systèmes en fonction de leur densité d'énergie volumique et massique.

En tant que matériau d'anode prometteur pour les batteries lithium-ion, les oxydes de métaux de transition présentent de nombreux avantages par rapport au graphite actuellement utilisé, tels que très grande capacité, large disponibilité, bonne stabilité, et respect de

[1] Tarascon, J.-M., Armand, M., Issues and challenges facing rechargeable lithium batteries, *Nature*, **2001**, 414, 359-367.

[2] Bruce P.G., Scrosati B., Tarascon J.-M., Nanomaterials for Rechargeable Lithium Batteries, *Angew. Chem. Int. Ed.*, **2008**, 47, 2930-2946.

[3] Bruce P.G., Freunberger S.A., Hardwick L.J., Tarascon J.-M., Li-O_2 and Li-S batteries with high energy storage, *Nat. Mater.*, **2012**, 11, 19-29.

l'environnement. Cependant, certains obstacles empêchent l'utilisation de ces matériaux, à savoir une faible conductivité électronique/ionique, de grandes variations de volume, de faibles performance en cyclage et un rendement faradique faible dans le premier cycle. [4,5] L'oxyde de fer (principalement α-Fe_2O_3), l'un des oxydes de métal de transition les plus important, a suscité l'intérêt scientifique depuis qu'il a été reporté comme matériau d'anode pour les batteries lithium-ion en raison de sa capacité théorique élevée (1007 mAh g^{-1}), de son respect de l'environnement, de son abondance et de son faible coût. [6,7]

Dans cette thèse, une électrode modèle en couche mince d'oxyde de fer a été préparée par simple oxydation thermique à 300 °C dans l'air d'un substrat de fer métallique pur, utilisé aussi comme collecteur de courant. Une variété de techniques d'analyse, électrochimiques (CV, EIS et cyclage galvanostatique), spectroscopiques (XPS, ToF-SIMS) et microscopiques (MEB et AFM), ont été mises en oueuvre pour comprendre les mécanismes réactionnels de l'oxyde de fer en tant que matériaux d'anode dans les batteries lithium-ion.

2. Expériences

a) Polissage mécanique

Les échantillons sont polis sur des draps imprégnés de pâtes diamantées de granulométrie décroissante. Des pâtes diamantées de 6µm, 3µm, 1µm, et 1/4µm sont utilisées, en fonction de la rugosité initiale. La granulométrie des pâtes diamantées est diminuée lorsque toutes les rayures sur l'échantillon sont homogènes. A la fin du polissage mécanique, les échantillons sont nettoyés, aux ultra-sons, dans l'éthanol et dans l'eau ultra pure, puis séchés à l'air comprimé filtré. La **Figure 2** présente le dispositif de polissage mécanique.

---

[4] Larcher D., Masquelier C., Bonnin D., Chabre Y., Mason V., Leriche J.B., Tarascon J.-M., Effect of Particle Size on Lithium Intercalation into α-Fe_2O_3, *J. Electrochem. Soc.*, **2003**, 150, A133-A139.

[5] Larcher D., Bonnin D., Cortes R., Rivals I., Personnaz L., Tarascon J.-M., Combined XRD, EXAFS, and Mössbauer Studies of the Reduction by Lithium of α-Fe_2O_3 with Various Particle Sizes, *J. Electrochem. Soc.*, **2003**, 150, A1643-A1650.

[6] H. Li, P. Balaya, J. Maier, Li-Storage via Heterogeneous Reaction in Selected Binary Metal Fluorides and Oxides, *J. Electrochem. Soc.*, **2004**, *151*, A1878-A1885.

[7] Zu C.-X., Li H., Thermodynamic analysis on energy densities of batteries, *Energy Environ. Sci.*, **2011**, 4, 2614-2624.

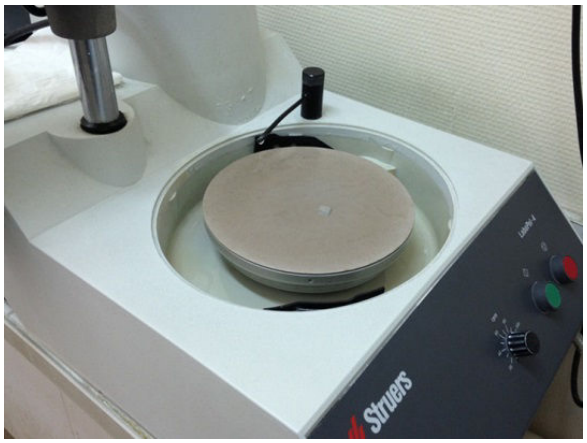

Figure 2 Photo de l'installation utilisée pour le polissage mécanique.

b) Caractérisations électrochimiques (CV, EIS et cyclage galvanostatique)

La voltammétrie cyclique (CV) a été réalisée à température ambiante en utilisant un potentiostat-galvanostat Autolab (AUT30). Une cellule en verre à trois électrodes a été utilisée avec le film mince d'oxyde (préparé comme décrit ci-dessus) comme électrode de travail et deux feuilles de Li utilisées comme électrodes de référence et contre-électrode. Les voltammogrammes ont été réalisés à partir du potentiel de circuit ouvert, dans le sens cathodique puis dans la direction anodique. Plus de détails sur les tests (vitesse de balayage, nombre de cycles) sont donnés dans chaque chapitre.

La spectroscopie d'impédance électrochimique (EIS) a été largement appliquée succès à l'étude des matériaux pour batteries lithium-ion et s'avère une méthode puissante et précise pour étudier la diffusion du lithium. Dans ce travail, l'EIS a également été réalisée à température ambiante en utilisant un Autolab (AUT30), sur une gamme de fréquences de 10 MHz à 1 MHz sous une perturbation potentielle de 5 mV.

Le cyclage galvanostatique (décharge-charge galvanostatique) a été réalisé dans deux types de cellules, cellule en verre à trois électrodes et cellule Swagelok à deux électrodes respectivement contrôlées par un Autolab (AUT30) et un poste de travail CE-Lab (Bio-Logic Instruments sciences), en appliquant une densité de courant constante dans le domaine de potentiel de 3,0 à 0,01 V et avec le film mince d'oxyde comme électrode de travail et des feuilles Li comme électrodes de référence et contre-électrode.

c) Spectroscopie de photoélectrons induits par rayons X (XPS)

La spectroscopie de photoélectrons induits par rayons X (XPS ou ESCA) est basée sur la détermination à haute résolution de l'énergie de liaison des photoélectrons issus des niveaux de coeur des éléments. Elle permet de détecter tous les éléments chimiques présents à la surface d'un matériau (à l'exception de l'hydrogène et de l'hélium), de renseigner sur l'environnement chimique des éléments en présence et de quantifier les espèces en termes de proportions atomiques (si le matériau est homogène en profondeur) et en termes d'épaisseur de couches si ces couches n'excèdent pas quelques nanomètres d'épaisseur. [8,9]

La photoemission est basé sur le principe de l'effet phoélectrique (voir **Figure 3**).

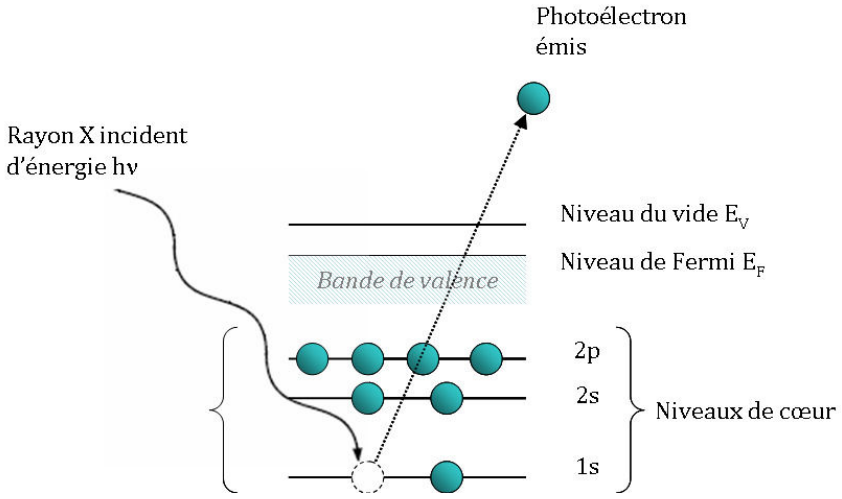

Figure 3 Schéma de principe de la photoémission.

Pour les analyses XPS, un spectromètre ESCALAB 250 de Thermo Electron Corporation a été utilisé. L'échantillon est irradié dans la chambre d'analyse sous ultravide (de l'ordre de 10^{-6} Pa). Ce vide très poussé est nécessaire pour obtenir une bonne collecte des photoélectrons qui doivent parcourir jusqu'à plusieurs dizaines de centimètres pour atteindre le détecteur en subissant un minimum de collisions inélastiques avec des molécules de gaz, mais également pour limiter la contamination des échantillons. Pour nos manipulations, une source de rayons X monochromatique (AlKα: hν = 1486. 6 eV) a été utilisée. Les rayons X

[8] Ray S., Shard A.G., Quantitative Analysis of Adsorbed Proteins by X-ray Photoelectron Spectroscopy, *Analytical Chemistry*, **2011**, 83, 8659-8666.

[9] Watts J.F., Wolstenholme J., An Introduction to Surface Analysis by XPS and AES, *Wiley Interscience*, **2003**.

sont produits par bombardement d'électrons de haute énergie sur un matériau qui joue le rôle d'anode. L'énergie hν du rayon produit est dépendante de la nature de l'anode. La raie AlKα de la source est monochromatisée afin de réduire la largeur des raies de rayon X et d'obtenir une meilleure résolution spectrale. Le monochromateur permet également de supprimer les pics dus à la non monochomatisation de la source et de focaliser, dans une certaine mesure, les rayons X. Cette focalisation autorise l'analyse de régions de l'échantillon de 100 μm à 500 μm de large.

Un analyseur hémisphérique permet de collecter et de focaliser les électrons émis par l'échantillon grâce à une série de lentilles électrostatiques. Les électrons sont séparés en fonction de leur énergie cinétique. L'analyseur est constitué de deux hémisphères aux bornes desquelles une différence de potentiel est appliquée. Il existe une relation de proportionnalité entre l'énergie cinétique des électrons, que l'on veut déterminer, et cette différence de potentiel. En mode «constant analyser energy» (CAE), le potentiel de l'analyseur est maintenu constant et l'utilisateur peut définir un potentiel appelé retardateur, à l'entrée de l'analyseur. L'utilisateur choisit ainsi l'énergie à laquelle les électrons sont accélérés ou retardés, soit l'énergie que les électrons possèdent quand ils entrent dans l'analyseur (ou énergie de passage). Cette énergie de passage influence la résolution des spectres et la transmission de l'analyseur. Le choix d'une énergie de passage plus faible (par exemple 20 eV) conduit à une meilleure résolution (en énergie) et est donc plus appropriée pour obtenir un spectre en haute résolution d'un élément. Une énergie de passage plus élevée (par exemple 100 eV) fournira une transmission plus élevée (meilleur taux de comptage) ce qui permettra d'obtenir un spectre général de la surface avec tous les éléments présents, cependant la résolution sera plus faible. Lors de nos analyses, l'angle entre l'analyseur et la surface des échantillons (ou angle d'émergence) a été fixé à θ=90°.

d) Spectrométrie de masse d'ions secondaires (ToF-SIMS)

La spectrometrie de masse d'ions secondaires avec detection a temps de vol (ToF-SIMS) permet de l'analyse élémentaire et moleculaire surfacique avec une très haute sensibilité. Cette technique d'extrême surface est utilisable pour tous les matériaux à l'état solide

compatibles avec l'ultravide (métaux, alliages, semi-conducteurs, dépôts de couches minces, échantillons biologiques, bois, verres, céramiques, textiles, etc…) et ne nécessite pas de préparation particulière des échantillons. [10,11]

Une source pulsée émet des ions primaires (Ga^+, Bi^+ en général) avec une énergie de quelques keV qui bombardent la surface (voir schéma de principe en **Figure 4**). Ces ions primaires produisent des ions secondaires issus des premières couches atomiques de l'échantillon. Il est possible, grâce a un balayage d'ions primaires sur la surface, d'effectuer une cartographie en fonction des éléments chimiques avec une résolution submicronique ou encore d'établir des profils de composition en profondeur par l'alternance de phases d'acquisition et d'abrasion avec une résolution nanométrique. [12,13]

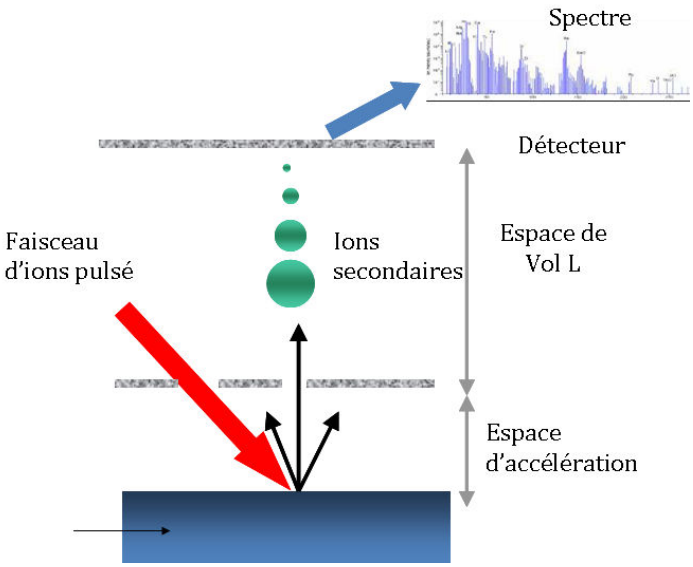

Figure 4 Schéma de principe du ToF-SIMS.

Un spectromètre ToF-SIMS 5 (IONTOF) a été utilisé avec, comme source d'ions

[10] Benninghoven, A., Chemical Analysis of INorganic and Organic Surfaces and Thin Films by Static Time-of-Flight Secondary Ion Mass Spectrometry (ToF-SIMS), *Angewandte Chemie International in English*, **1994**, 33, 1023-1043.

[11] Mogk D.W., Time-of-Flight Secondary Ion Mass Spectrometry (ToF-SIMS), *Montana State University*, http://serc.carleton.edu/research_education/geochemsheets/techniques/ToFSIMS.html

[12] VanVaeck, L., Adriaens, A., Gijbels, R., Static Secondary Ion Mass Spectrometry: (S-SIMS) Part 1. Methodology and Structural Interpretation, *Mass Spectrometry Reviews*, **1999**, 18, 1-47.

[13] Adriaens, A., VanVaeck, L., Adams, F., Static Secondary Ion Mass Spectrometry (S-SIMS) Part 2: Material Science Applications, *Mass Spectrometry Reviews*, **1999**, 18, 48-81.

primaires, un faisceau d'ions pulsés Bi^+ d'énergie 25 keV délivrant 1 pA sur une surface de 100×100 μm^2. La pression au cours de l'analyse est fixée à 10^{-9} mbar. Pour les profils en profondeur, les phases d'acquisition sont alternées avec des phases d'abrasion par un second faisceau d'ions. Les profils ont été principalement effectués en mode négatif car la sensibilité était meilleure pour les fragments les plus caractéristiques. L'acquisition des données a été faite grâce au logiciel Ion-Spec. Le canon d'abrasion utilisé pour les profils en profondeur utilise un faisceau d'ions Cs^+.

Les échantillons sont introduits dans une chambre d'introduction et mis sous vide : le temps de pompage varie en fonction de la nature des échantillons. Un temps de pompage de 1 à 2 heures est nécessaire pour atteindre un vide inférieur à 10^{-8} mbar. Les échantillons dégazés sont ensuite introduits dans la chambre d'analyse. Pour les profils en profondeur, es éléments ou molécules d'intérêt sont sélectionnés à partir des spectres de masses et une calibration peut parfois être faite.

e) Microscopie électronique à balayage (MEB)

La microscopie électronique à balayage (MEB ou SEM : Scanning Electron Microscopy) est considérée comme une technique standard en science des matériaux, c'est pourquoi nous ne présenterons pas son principe de base. Dans ce travail, l'imagerie MEB des électrodes à film mince a été réalisée avec un appareil ZEISS Ultra-55 Field Emission (FE-SEM, Allemagne) au Laboratoire Interfaces et Systèmes Electrochimiques, Université Pierre et Marie Curie.

f) Microscopie à force atomique (AFM)

La microscopie à force atomique (ou atomic force microscopy, AFM) appartient à une famille plus large de techniques d'analyse de surface par balayage d'une sonde (scanning probe techniques, SPM). Il est admis que la plupart de ces techniques sont issues de l'invention de la STM en 1982. Quatre ans plus tard, Binnig, Quate et Gerber accèdaient, grâce à l'adaptation de l'un de ces microscopes, au premier microscope à force atomique.

[14,15]

Dans cette thèse, l'imagerie AFM a été réalisée avec un microscope à force atomique Agilent 5500 fonctionnant en mode contact intermittent (mode Tapping) dans l'air. Les images AFM ont été acquises à l'aide d'une pointe en silicium montée sur un bras de levier ayant une constante de force de 25 - 75 N m^{-1} et une fréquence de résonance de 282,6 kHz. Visualisation et analyse des données (valeur moyenne, RMS) ont été réalisées avec le logiciel Gwyddion 2.31.

3. Résultats et conclusion

Afin d'avoir une meilleure compréhension des mécanisme réactionnels de l'oxyde de fer comme matériau d'anode, une approche en couches minces a été utilisée et des méthodes électrochimiques ont été combinées avec des techniques de surface et d'interface. XPS et ToF-SIMS ont été utilisés pour étudier des couches minces d'oxyde de fer à différents stades de lithiation/délithiation. En outre, l'analyse XPS combinée avec un décapage avec des ions Ar^+ de faible énergie a été utilisée pour l'analyse chimique en profondeur de l'électrode lithiée (jusqu'à 0,01 V *vs.* Li/Li^+). Sur la base des résultats obtenus, la formation d'un film passif appelé « Solid Electrolyte Interphase » (SEI), la composition chimique de l'électrode en couche mince et les mécanismes de conversion/déconversion de l'oxyde de fer comme matériau d'anode pour les batteries lithium-ion ont été examinés et discutés.

La **Figure 5** présente le premier cycle (voltammogramme) de l'électrode d'oxyde de fer en couche mince dans 1 M $LiClO_4$-PC. Elle montre un très petit pic cathodique à environ 1,7 V suivi d'une faible augmentation du courant cathodique jusqu'à 1 V, correspondant au processus d'insertion de Li dans la matrice de l'oxyde de fer pour former l'intermédiaire $Li_xFe_2O_3$ ($0<x\leq2$). Un pic cathodique étroit et intense suit à environ 0,75 V et correspond à la

[14] Lang K.M., Hite D.A., Simmonds R.W., McDermott R., Pappas D.P., Martinis J.M., Conducting atomic force microscopy for nanoscale tunnel barrier characterization, *Review of Scientific Instruments*, **2004**, 75, 2726-2731.

[15] Leite F.L., Mattoso L.H.C., Oliveira Jr O.N., Herrmann Jr P.S.P., The Atomic Force Spectroscopy as a Tool to Investigate Surface Forces: Basic Principles and Applications, *Modern Research and Educational Topics in Microscopy*, **©FORMATEX 2007**, 747-757.

réduction électrochimique du lithium avec l'oxyde de fer et à la réduction électrochimique concomitante de l'électrolyte conduisant à la formation de la couche de SEI. Dans le processus de polarisation anodique, un large pic anodique à environ 1,55 V est lié au processus de conversion de Li_2O avec du fer métallique selon la réaction:

$$3Li_2O + 2Fe \leftrightarrow Fe_2O_3 + 6Li^+ + 6e^-$$

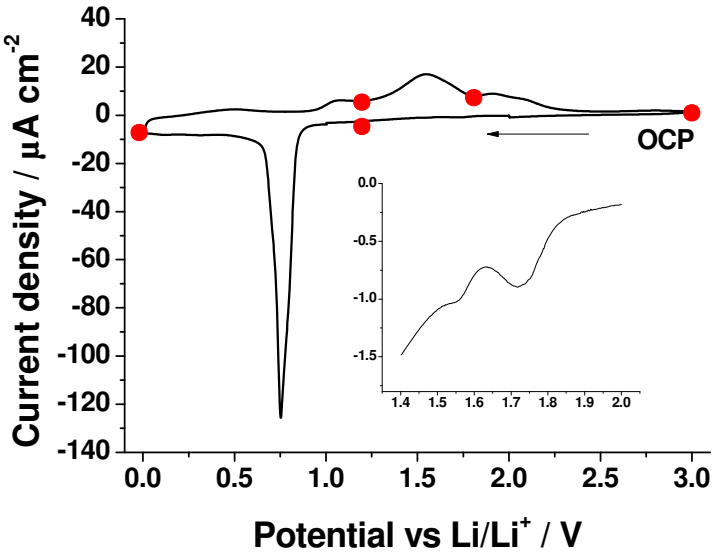

Figure 5 Premier cycle (voltammogramme) de l'électrode d'oxyde de fer en couche mince dans 1 M $LiClO_4$-PC dans la fenêtre de potentiel 0,01 à 3,0 V (vitesse de balayage de 0,2 mV s^{-1}). L'encart montre l'agrandissement du pic cathodique à 1,7 V. Les points sur les courbes indiquent les potentiels sélectionnés pour les analyse XPS, ToF-SIMS et EIS.

Les spectres XP des niveaux de cœur C1s et Fe2p des échantillons non traités et des échantillons lithiés/delithiés dans 1 M de $LiClO_4$-PC aux potentiels sélectionnés sont présentés **Figure 6**. Le spectre C1s révèle une contamination organique de la surface de l'échantillon vierge et la formation d'une couche SEI sur les surfaces d'électrodes traitées électrochimiquement. La couche de SEI est formée par décomposition réductrice de l'électrolyte (carbonate de propylène) dès le potentiel de 1,2 V. La décomposition du spectre XPS du $Fe2p_{3/2}$ montre que la surface vierge est composée principalement de α-Fe_2O_3 avec des quantités mineures de Fe^{2+} oxyde et FeOOH. Un spectre de Fe, ré-émergent après délithiation à 3,0 V, montre une décomposition partielle de la couche SEI pendant le

processus de délithiation.

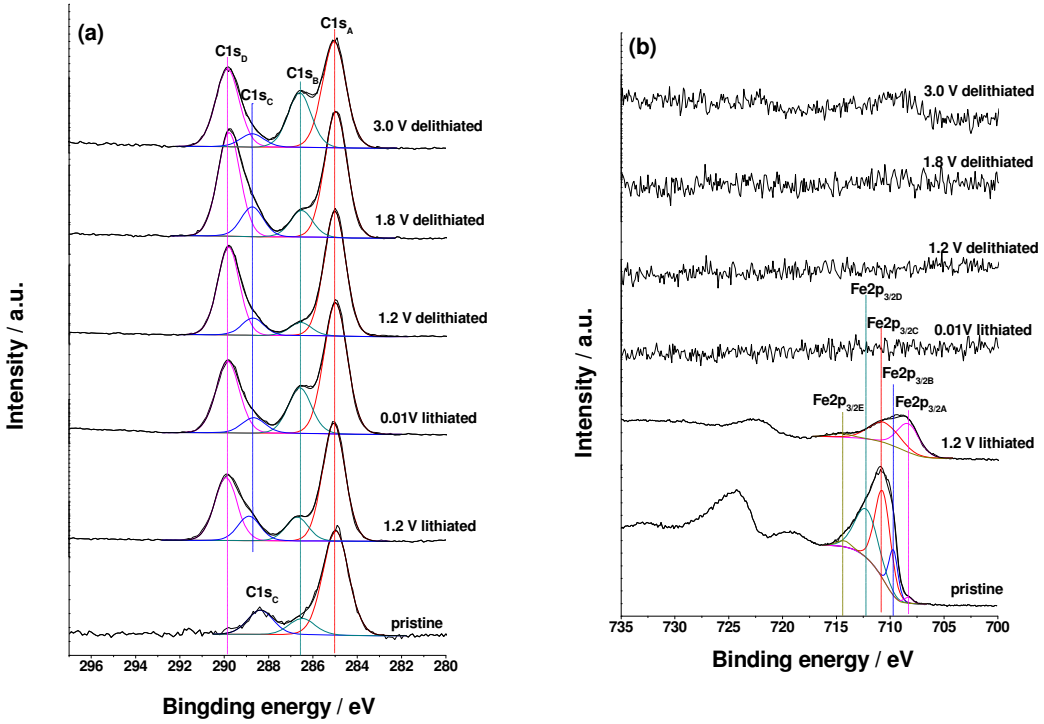

Figure 6 Spectres XPS (a) C1s et (b) Fe2p pour les films minces d'oxyde de fer vierge et les échantillons traités dans 1 M de $LiClO_4$-PC à des potentiels choisis dans le premier cycle de lithiation/délithiation.

La variation du spectre XPS Fe2p de l'échantillon lithié à 0,01 V avec le temps de pulvérisation par des ions Ar^+ (cf.**Figure 7**) révèle que la majeure partie de l'électrode d'oxyde de fer a été réduit en Fe métallique et Li_2O. Toutefois, l'oxyde de fer n'a pas été complètement converti en LiO_2 et Fe métallique, comme l'indique la présence d'un pic d'oxyde Fe^{3+} après 24 min de pulvérisation Ar^+.

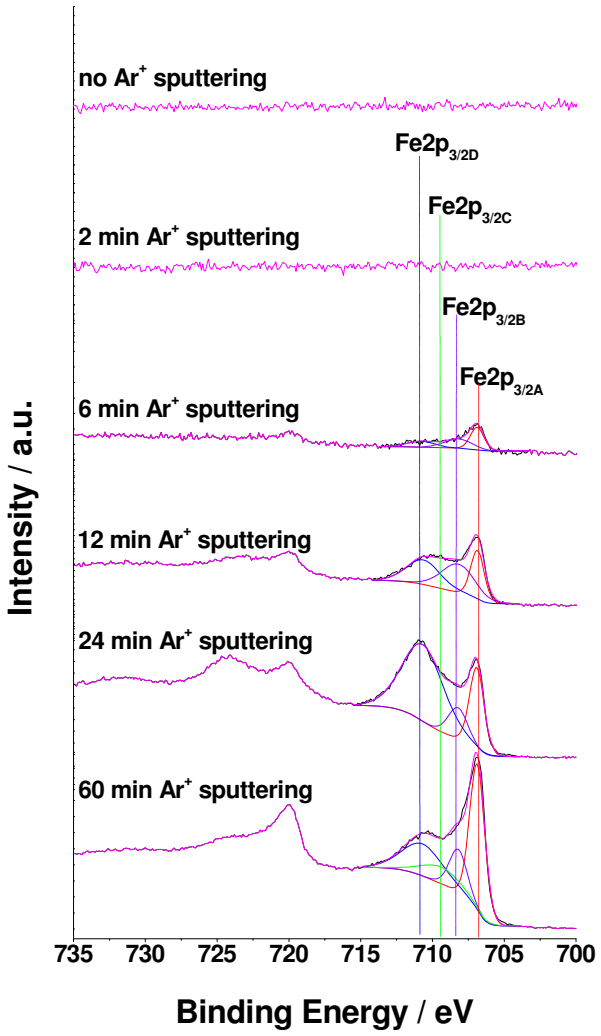

Figure 7 Spectres XPS Fe2p pour l'échantillon lithié à 0,01 V pour des temps croissants de décapage par les ions Ar^+.

La **Figure 8** montre les profils en profondeur ToF-SIMS de des ions contenant du Li (Li^-, LiO^-) et du Fe (FeO^-, FeO_2^-, Fe_2^-, Fe_2O_3, $Fe_3O_4^-$) pour le film vierge et des échantillons lithiès à 0,01 V et delithiés à 3,0 V. Le temps plus long (×3) de pulvérisation du film mince à l'état lithié par rapport à électrode vierge indique l'expansion de volume au cours du processus de lithiation. De même, le temps de pulvérisation plus court à l'état délithié indique que le volume diminue pendant le processus de délithiation. En outre, l'accumulation importante et le piégeage de lithium dans l'oxyde après délithiation indique que le processus lithiation/délithiation n'est pas complètement réversible et limité par le transport de matière.

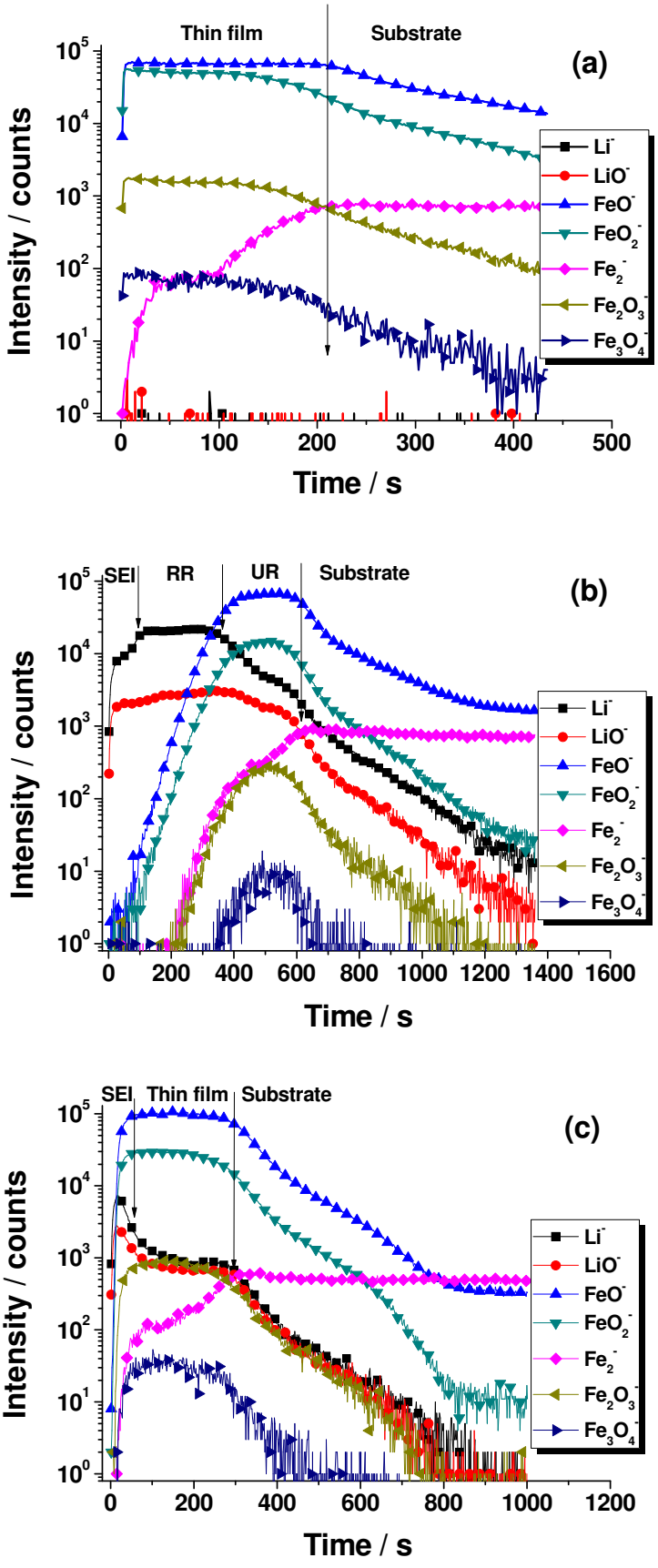

Figure 8 Profils ToF-SIMS en profondeur d'ions négatifs de l'électrode(a) vierge, (b) lithiée à 0,01 V et (c) delithiée à 3,0 V.

Les mécanismes de vieillissement par cyclage de l'oxyde de fer ont également été étudiés de façon approfondie en combinant les techniques d'analyse spectroscopiques (XPS, ToF-SIMS) et microscopiques (MEB, AFM). Les résultats montrent que la couche SEI a une composition stable (Li_2CO_3 avec quantité mineur de $ROCO_2Li$) mais augmente en épaisseur au cours du cyclage. Les profils ToF-SIMS en profondeur mettent en évidence le piégeage du lithium dans la couche mince d'oxyde de fer, ce qui est une des raisons de chute de la capacité. L'analyse morphologique de l'électrode, réalisée par MEB et AFM (voir **Figure 9 et 10**), révéle la pulvérisation de la couche d'oxyde de fer et l'agglomération des particules au cours des cycles répétés de lithiation/délithiation. Après pulvérisation initiale de la microstructure du film mince, la croissance des grains et leur l'agrégation sont promus par le cyclage répété. Au cours des cinq premiers cycles, ceci favorise l'augmentation de la capacité, mais l' expansion du volume et l'accumulation de matière non déconvertie conduit conduit à la détérioration des performances de l'électrode. Ces modifications peuvent aussi conduire à l'exfoliation du matériau d'oxyde actif, qui est une autre explication raisonnable de la chute de capacité de l'oxyde de fer pendant les cycles suivants. La pénétration de la SEI dans la couche mince de l'électrode accompagne la pulvérisation de l'électrode au cours du cyclage.

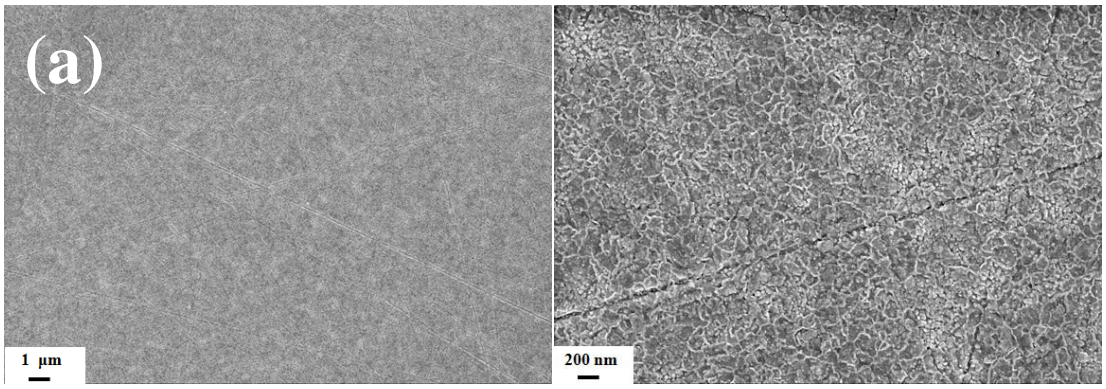

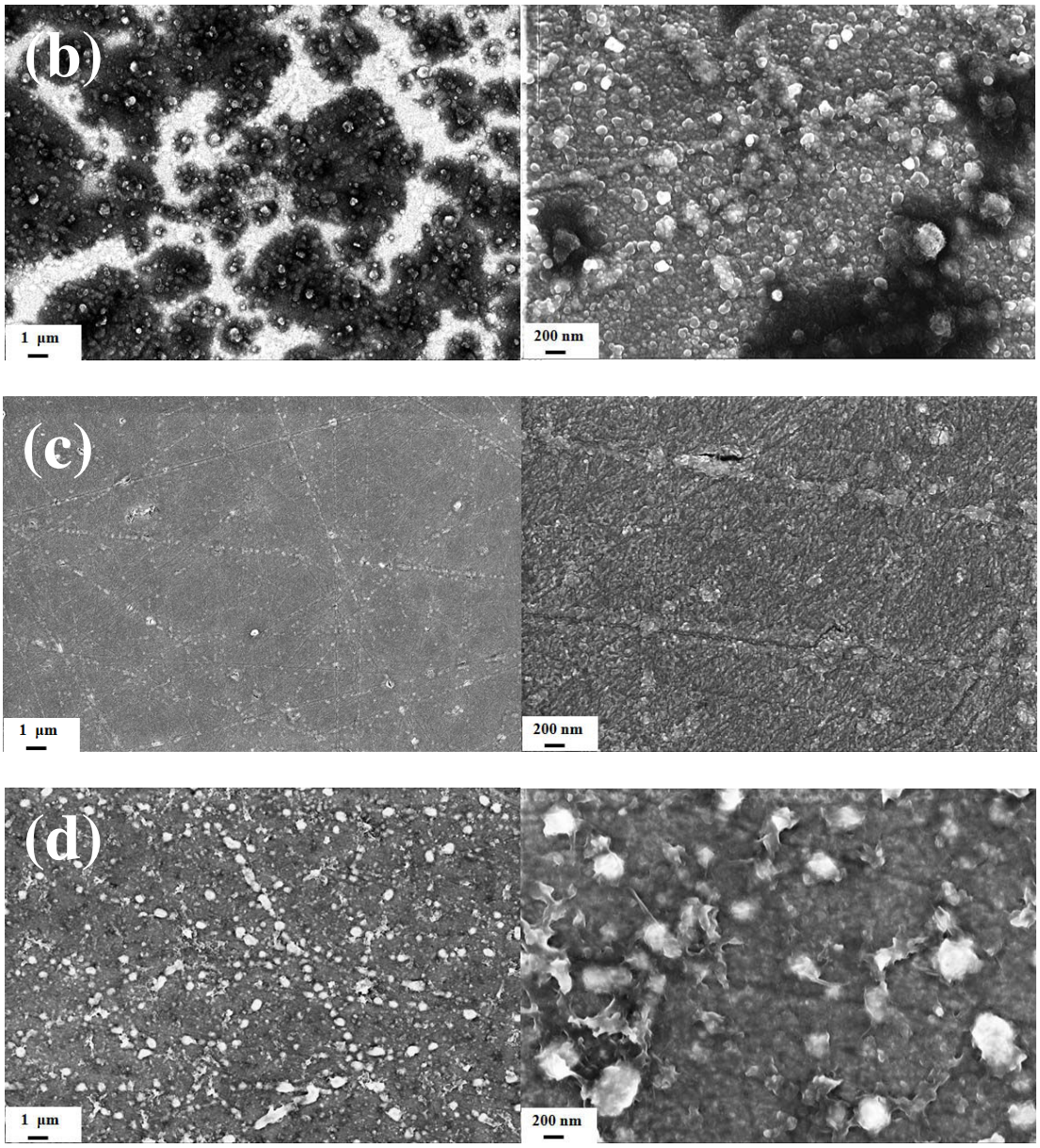

Figure 9 Images MEB de (a) l'échantillon vierge et après (b) 1/2 CV (arrêté à 0,01 V), (c) 1 CV et (d) 15 CVs.

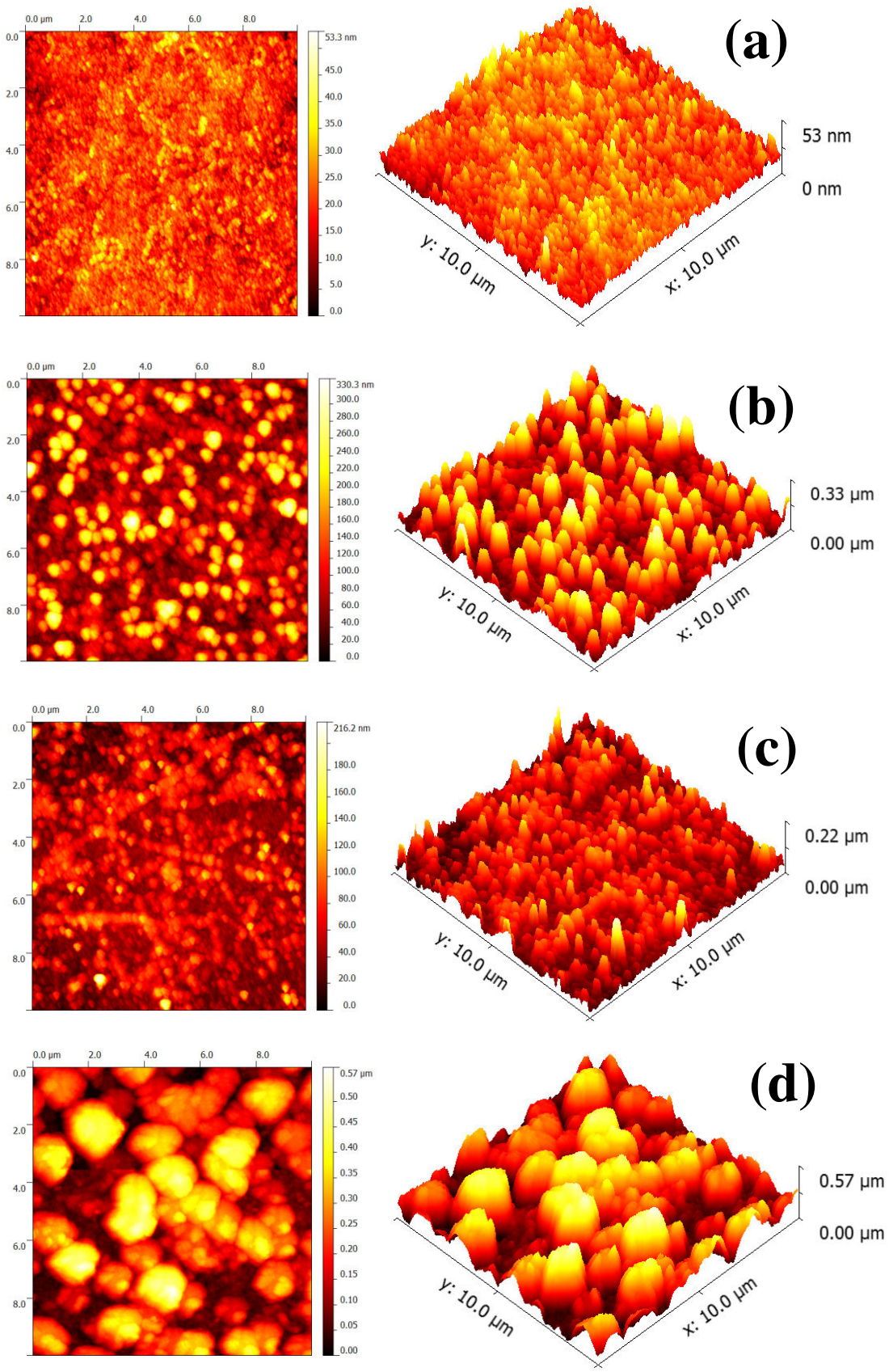

Figure 10 Images topographique AFM (10 um × 10 um) (a) de l'échantillon vierge et après (b) 1/2 CV (arrêté à 0,01 V), (c) 1 CV et (d) et 15 CVs.

L'oxyde de fer comme matériau d'électrode négative pâtit d'une faible conductivité électronique/ionique, ce qui est un des principaux obstacles à l'amélioration de ses propriétés électrochimiques. Ainsi, l'application d'un tel matériau dans les batteries lithium-ion requiert la maîtrise de la cinétique des réactions conversion/déconversion. Cela nécessite une bonne compréhension du transport (diffusion) des ions Li dans la matrice de l'électrode lors de l'insertion de lithium. Le coefficient de diffusion des ions Li dans un matériau hôte peut être obtenue à partir de la distribution de la concentration dans le matériau d' électrode. Toutefois, dans le pratique, la répartition des ions Li dans le matériau hôte est difficile à mesurer du fait de l'absence de techniques sensibles et précises. De façon courante, la variation de la concentration en ions lithium dans le matériau hôte est déduit de la distribution du potentiel à l'aide de l'équation de Nernst et de techniques de caractérisation électrochimiques tels que EIS, CV, PITT (titrage intermittent potentiostatique), GITT (titrage intermittent galvanostatique) et PRT (relaxation du potentiel). Cependant, il est nécessaire de développer de nouvelles méthodes directes de mesure de diffusion du Li dans les matériaux d'électrodes basées sur la mesure des ions en profondeur par profilometrie. Dans ce travail, le ToF-SIMS a été appliqué pour la première fois à la mesure du coefficient de diffusion apparent du lithium dans un matériau d'électrode de conversion (α-Fe_2O_3) par une approche de film mince. L'analyse a été basée sur la variation de la concentration en profondeur en Li obtenue pour un échantillon partiellement lithié (voir **Figure 11**). Le coefficient de diffusion apparent calculé à partir de l'intégration de la deuxième loi de Fick pour la diffusion à une dimension est de l'ordre de 10^{-15} cm^2 s^{-1}. Ce résultat est en accord avec les valeurs obtenues à partir de données de voltamétrie et d'impédance électrochimiques. Le coefficient de diffusion obtenu montre que la vitesse de lithiation de ce matériau de conversion est nettement plus lente que pour les matériaux d'intercalation ou d'alliage. L'utilisation de la méthode directe ToF-SIMS pour la détermination du coefficient de diffusion peut être appliquée aux différents types de matériaux d'électrode. Cette nouvelle approche élargie l'horizon pour l'étude de cinétique de diffusion de Li dans les matériaux d'électrode pour les batteries lithium-ion.

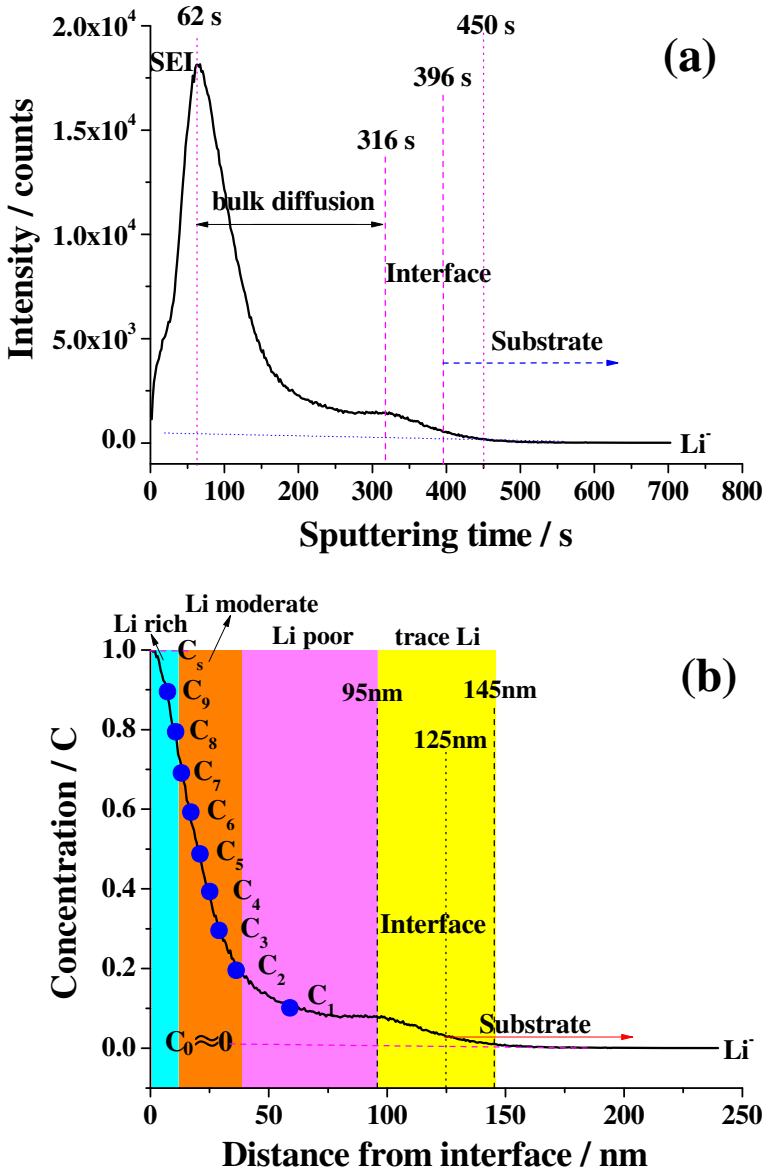

Figure 11 (a) Profil ToF-SIMS en profondeur des ions Li, (b) variation normalisée de la concentration en ions Li dans la profondeur de l'électrode après 5591 s de lithiation à 0,84 V.

L'un des autres principaux obstacles de l'application de l'oxyde de fer comme matériau d'anode pour les LIBs est son potentiel de conversion élevé (tension de travail). Afin de réduire la potentiel de lithiation, un film mince d'oxyde binaire (Fe, Cr) a été préparé sur sur un substrat d'acier inoxydable (AISI410, $FeCr_{12.5}$) également utlisée comme collecteur de courant. Les courbes de décharge/charge galvanostatique réalisées sur 20 cycles montrent que la substitution de l'oxyde de fer par le chrome n'améliore pas les performances électrochimiques, tels que la capacité spécifique et la stabilité en cyclage. La position du pic

cathodique sur les voltammogrammes montre que le remplacement de l'oxyde de fer par le chrome ne réduit pas la tension de travail de cet oxyde binaire. Le rendement faradique de l'électrode d'oxyde binaire dans le premier cycle de décharge/charge est un peu moins bon que celui de l'oxyde de fer, mais supérieur à celui de l'oxyde de chrome (**Figure 12**).

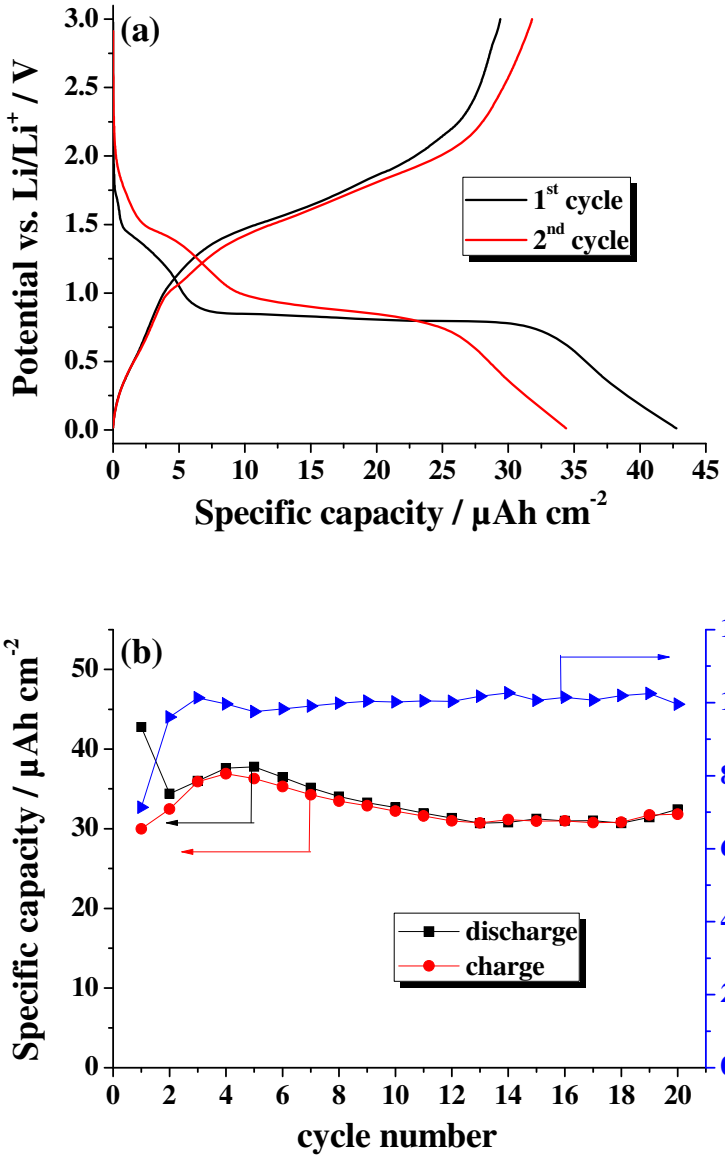

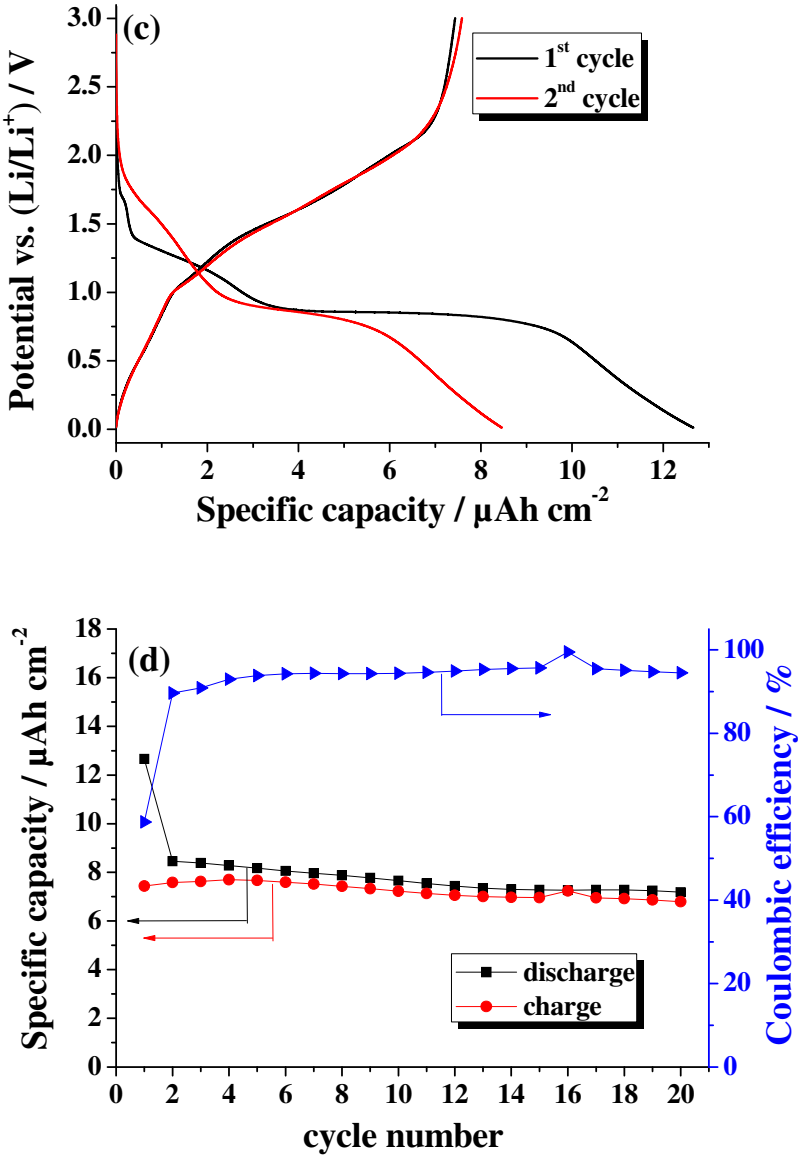

Figure 12 Première et deuxième courbes de décharge-charge; performances en cyclage et rendement coulombien de l'électrode (a), (b) d'oxyde de fer pur et (c), (d) d'oxyde binaire (Fe, Cr).

La **Figure 13** montre les profils en profondeur ToF-SIMS des ions négatifs Fe_2^-, FeO_2^-, CrO_2^- et Li^- ions pour des échantillons vierges et traités électrochimiquement. Ces résultats montrent que le processus de conversion de l'oxyde binaire est cinétiquement contrôlé, et que l'oxyde de chrome ne réagit pas avec suffisamment de lithium en raison de son activité de conversion électrochimique médiocre.

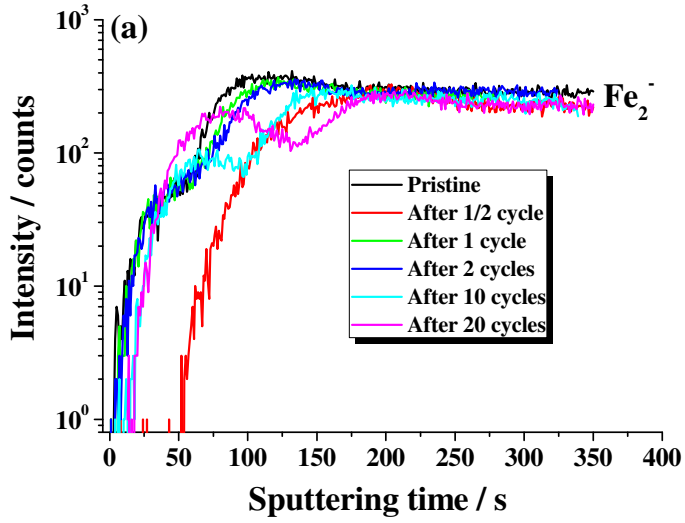
(a)
Intensity / counts
Sputtering time / s
Fe2-
Pristine
After 1/2 cycle
After 1 cycle
After 2 cycles
After 10 cycles
After 20 cycles

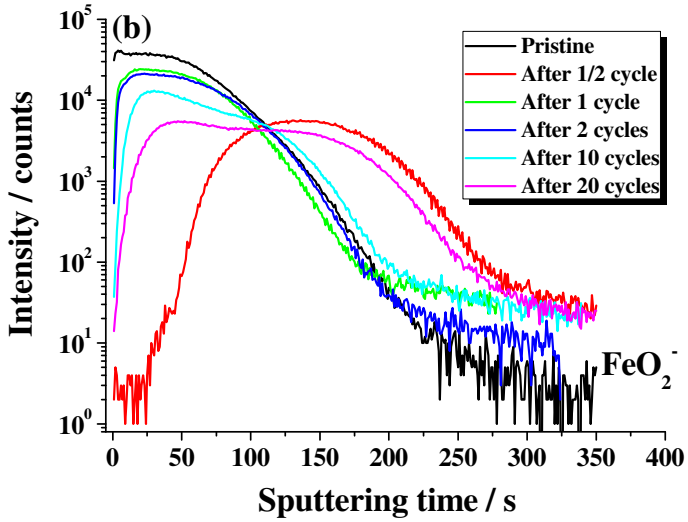
(b)
Intensity / counts
Sputtering time / s
FeO2-
Pristine
After 1/2 cycle
After 1 cycle
After 2 cycles
After 10 cycles
After 20 cycles

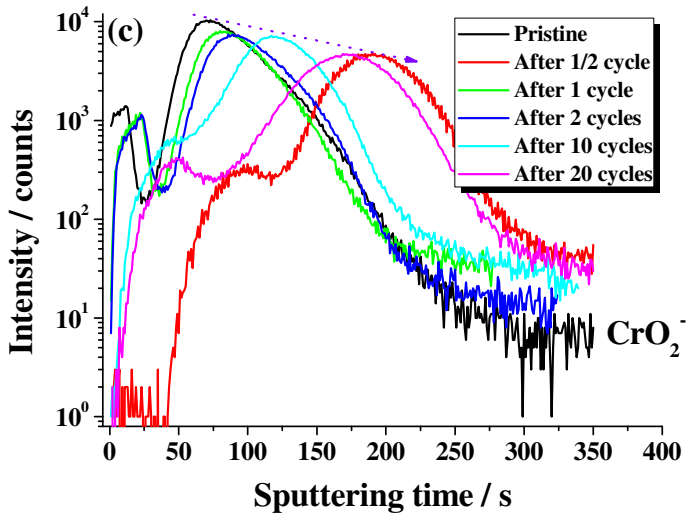
(c)
Intensity / counts
Sputtering time / s
CrO2-
Pristine
After 1/2 cycle
After 1 cycle
After 2 cycles
After 10 cycles
After 20 cycles

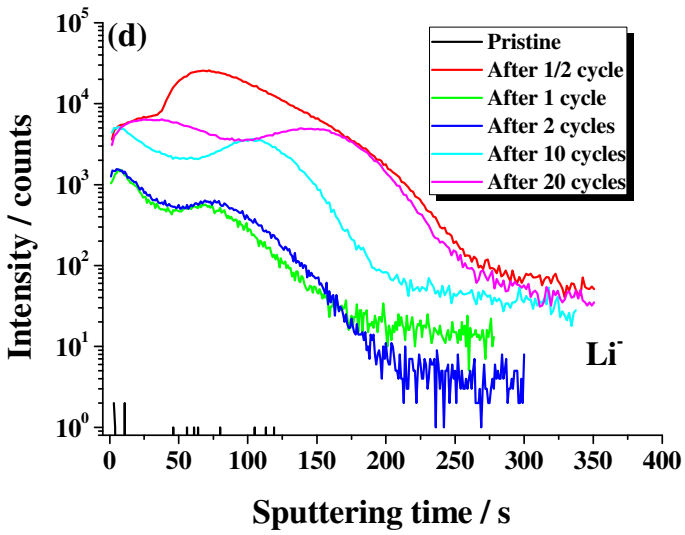

Figure 13 Profils TOF-SIMS en profondeur d'ions négatifs (a) Fe_2^-, (b) FeO_2^-, (c) CrO_2^- et (d) Li-ions pour l'électrode d'oxyde binaire vierge et après 1/2, 1, 2, 10 et 20 cycles.

Les données MEB et AFM montrent que les modifications morphologiques de l'électrode sont indistinctes dans les deux premiers cycles mais augmenté de façon significative au cours de cyclage après 10 et 20 cycles (cf. **Figure 14 et 15**).

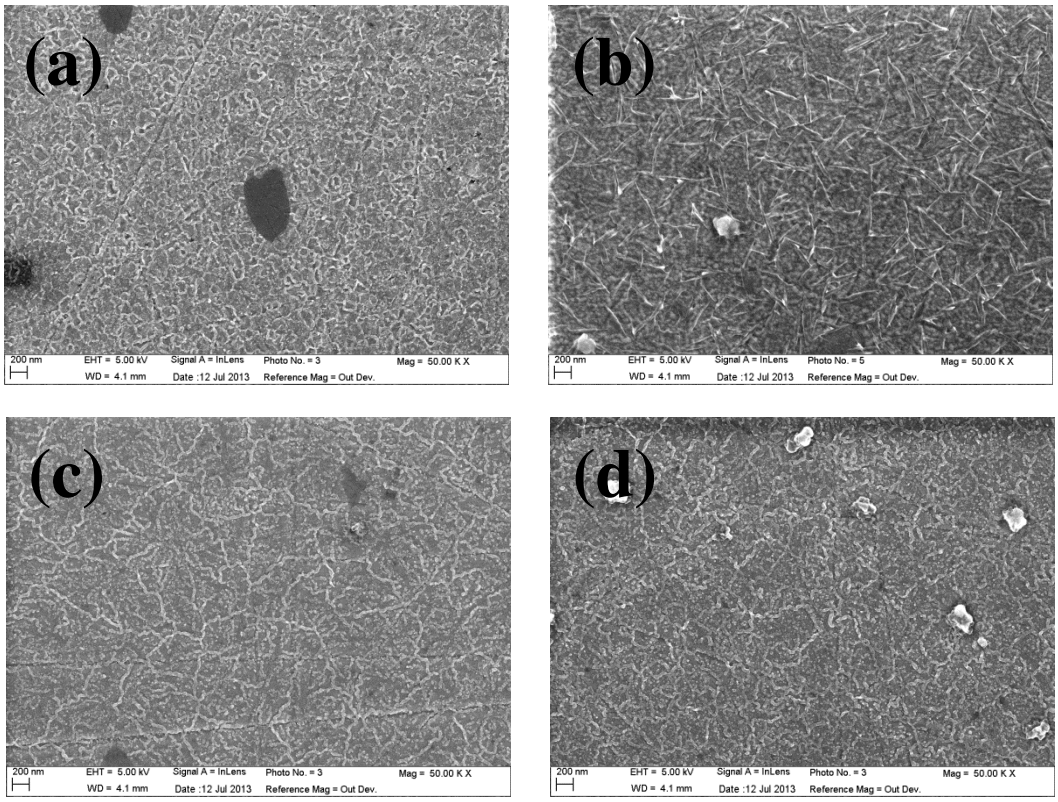

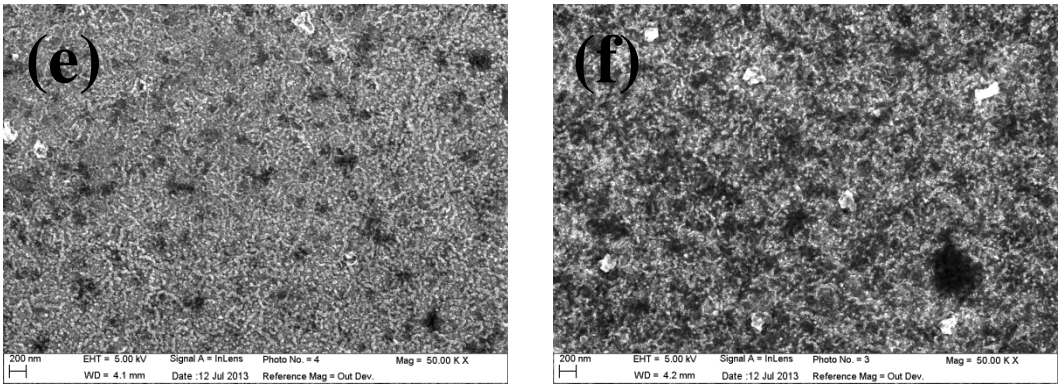

Figure 14 Images MEB des (a) électrodes vierges et après (b) 1/2, (c) 1, (d) 2, (e) et 10 (f) 20 cycles.

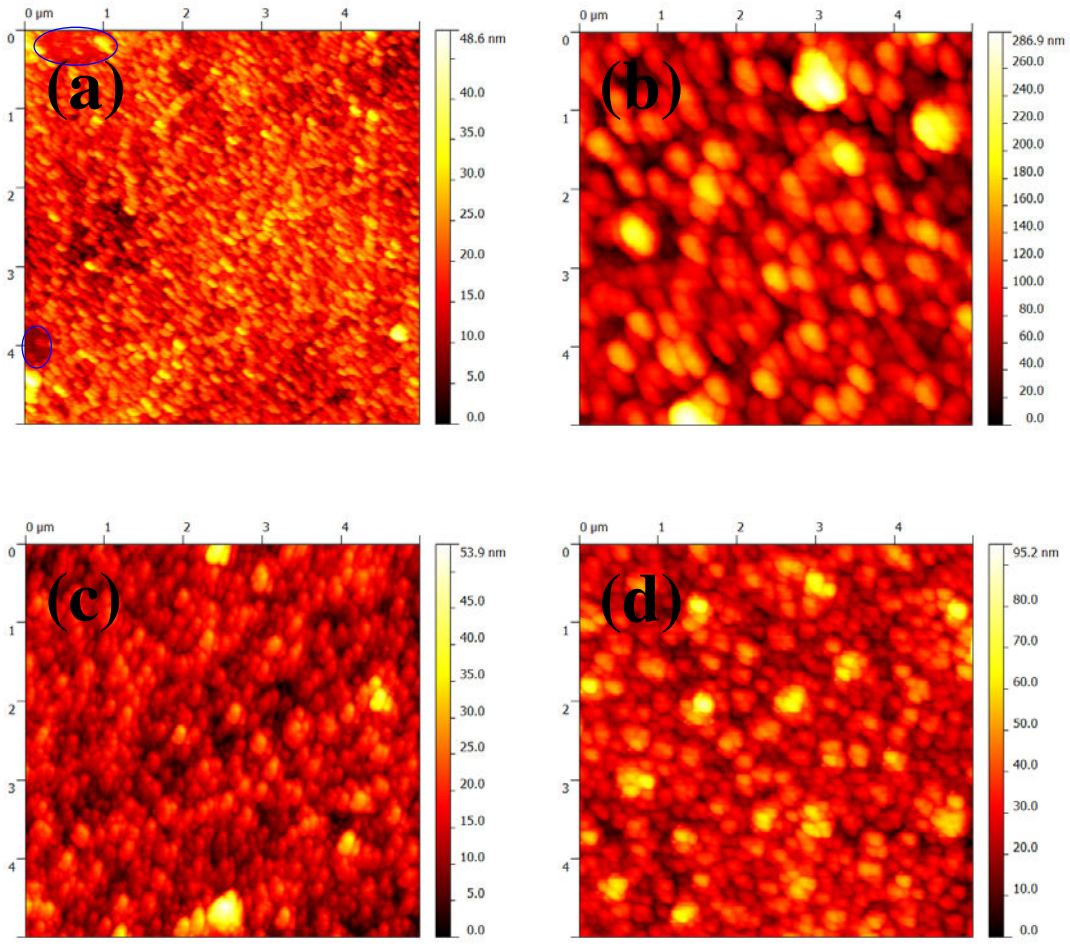

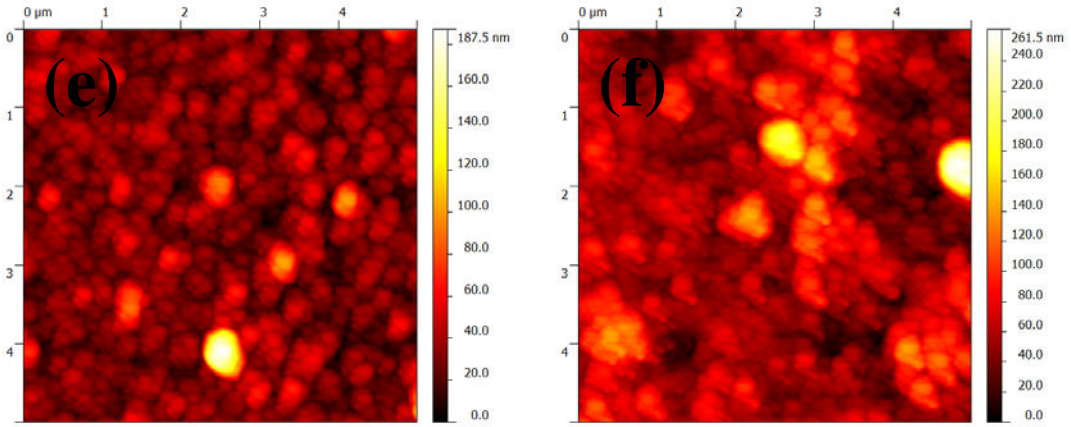

Figure 15 Images topographique AFM des (a) électrodes vierges et après (b) 1/2, (c) 1, (d) 2, (e) et 10 (f) 20 cycles.

4. Perspectives

Deux possibiltées sont proposées pour la poursuite des travaux sur le fer et l'oxyde de fer comme matériaux d'électrodes:

- Synthèse d' électrodes d'oxyde de fer nanostructurée réalisées par dépôt de couches atomiques (ALD) pour application en micro-batteries au lithium-ion en utilisant l'oxyde anodique d'aluminium (AAO) comme gabarit de croissance;

- Comportement électrochimique du fer et de l'oxyde de fer pour les batteries Fe-air en mettant l'accent sur le rôle des additifs d'électrolyte (ex. Na_2S) comme inhibiteur de le réaction d'évolution de l'hydrogène.

Table of Contents

Abstract

Lithium-ion batteries (LIBs) are widely used as power sources for portable electronic devices. Recently, much effort has been made to promote their application in hybrid electric vehicles and dispersed energy storage systems, which demands light weight, small volume, high energy density and safety. As a promising anode material for lithium-ion batteries, transition metal oxides exhibit many advantages compared to the currently used graphite, such as very high capacity, widespread availability, good stability, and environmental benignity. However, there are also obstacles that hinder the practical application of these materials, i.e., poor electronic/ionic conductivity, large volume changes and poor cycling performance, low coulombic efficiency in the first cycle.

Iron oxide (mainly α-Fe_2O_3), as one of the most important transition metal oxide, has attracted attention due to its high theoretical capacity (1007 mAh g^{-1}), environmental friendliness, abundance and low cost since reported as anode material for LIBs. In this thesis, an iron oxide thin film model electrode was prepared by simple thermal oxidation of pure metallic iron substrate at 300 ^{o}C in air for 5 min, also used as a current collector.

In order to have a better understanding of the reaction mechanisms of iron oxide as anode material, a thin film approach was used and electrochemical methods (CV, EIS and galvanostatic cycling) were combined with surface analytical techniques (XPS, ToF-SIMS), to investigate the iron oxide thin film at different stages of lithiation/delithiation. XPS analysis was also combined with low energy Ar^+ sputtering for depth profiling the lithiated electrode (up to 0.01 V vs Li/Li^+). Based on the results, the formation of the passive film called Solid Electrolyte Interphase (SEI) layer, the chemical composition of the thin film electrode and the conversion reaction mechanism of iron oxide are discussed as anode materials for lithium-ion batteries.

The first cyclic voltammogram performed on the iron oxide thin film electrode in 1 M $LiClO_4$-PC shows a very small cathodic peak at about 1.7 V followed by small cathodic current increase until 1 V, corresponding to the process of Li insertion into the iron oxide matrix to form intermediate $Li_xFe_2O_3$ ($0 < x \leq 2$). A sharp and intense cathodic peak follows at about 0.75 V, corresponding to the electrochemical reduction of lithium with iron oxide and

to the concomitant reductive decomposition of the electrolyte and resulting formation of the SEI layer. In the anodic polarization process, the broad anodic peak at around 1.55 V is related to the reverse de-conversion process of Li_2O with metallic iron according to reaction:

$$3Li_2O + 2Fe \leftrightarrow Fe_2O_3 + 6Li^+ + 6e^-$$

The XP C1s spectra reveal organic contamination of the surface for the pristine sample and SEI layer formation on the electrochemical treated electrode surfaces. The SEI layer is formed by reductive decomposition of the electrolyte (propylene carbonate) already at the lithiation potential of 1.2 V. The XP $Fe2p_{3/2}$ core level peak fitting shows that the pristine surface is composed predominantly of α-Fe_2O_3 with minor amounts of Fe^{2+} oxide and FeOOH. A re-emerging Fe spectrum after delithiation to 3.0 V shows partial decomposition of the SEI layer during the delithiation process. The variation of the XP Fe2p spectra of the sample lithiated to 0.01 V with Ar^+ sputtering reveals that the bulk of the iron oxide electrode was reduced to metallic Fe and Li_2O when lithiated to 0.01 V. However, iron oxide was not completely converted to LiO_2 and metallic Fe as shown by the presence a Fe^{3+} oxide peak after 24 min Ar^+ sputtering.

ToF-SIMS depth profiles of Li-containing ions (Li^-, LiO^-) and Fe-containing ions (FeO^-, FeO_2^-, Fe_2^-, $Fe_2O_3^-$, $Fe_3O_4^-$) shows dynamic variation of the sputtering time to the substrate for the samples lithiated to 0.01 V and delithiated to 3.0 V. A x3 longer sputtering time for the sample in lithiated state in comparison to pristine thin film electrode indicates volume expansion during the lithiation process. Accordingly, the shorter sputtering time in the delithiation state indicates volume shrinking during delithiation. Moreover, significant accumulation and trapping of lithium in the oxide after delithiation indicates that the lithiation/delithiation process is not completely reversible due to mass transport limitation.

The multi-cycling induced aging mechanisms of iron oxide thin film anode were also investigated thoroughly by combining spectroscopic (XPS, ToF-SIMS) and microscopic (SEM, AFM) analytical techniques. The results show that the SEI layer has a stable composition (Li_2CO_3 with minor $ROCO_2Li$) but dynamically increases in thickness during cycling. ToF-SIMS ion depth profiles evidenced lithium trapping in the bulk of iron oxide thin film electrode upon cycling, which is one reason of capacity fading. The analysis of the

electrode morphology, performed by SEM and AFM, revealed that the iron oxide layer undegoes pulverization resulting in particle agglomeration during repeated lithiation/delithiation. After initial pulverization of the thin film microstructure, grain growth and aggregation are promoted by multi-cycling. In the first five cycles, this promotes capacity increase but upon further cycling volume expansion and accumulation of non deconverted material lead to deterioration of the electrode performances. These modifications may also lead to exfoliation of iron oxide active electrode material, which is another reasonable explanation of the capacity fading of iron oxide during further multi-cycling. Penetration of the SEI layer along with pulverization of the electrode due to irreversible conversion/deconversion also occurs in the bulk electrode material upon cycling.

Iron oxide as negative electrode material suffers from poor electronic/ionic conductivity, which is one main obstacle for improving the rate capability of this material in a battery. So the future of such a conversion-type material in LIB applications relies on mastering the kinetics of the electrode lithiation reaction. This requires a good understanding of transport (diffusion) mechanisms of Li ions into the bulk electrode matrix during lithium insertion. The diffusion coefficient of Li ions in a host material can be obtained from the Li-ion concentration distribution in the bulk electrode material. In practical application, the distribution of Li ions in the host material is difficult to measure due to the lack of sensitive and precise techniques. In common practice, the variation of the Li-ion concentration in the host material is deduced from the potential distribution using the Nernst equation and electrochemical characterization techniques such as EIS, CV, PITT (potentiostatic intermittent titration), GITT (galvanostatic intermittent titration) and PRT (potential relax techniques). However, it is necessary to develop new and more direct methods for precise measurement of Li diffusion in bulk electrode materials based on precise Li-ion depth profiling. In this work, ToF-SIMS has been applied for the first time to measure the apparent diffusion coefficient of lithium into a conversion-type electrode material (α-Fe_2O_3) by a thin film approach. The analysis was based on the in-depth variation of the Li-ion concentration obtained by depth profiling a partially lithiated sample. The apparent diffusion coefficient obtained from the infinite integration of Fick's second law for one-dimensional diffusion is of the order of 10^{-15} cm^2 s^{-1} in the converted region, in agreement with values obtained from CV

and EIS data. This value evidences that the rate of lithiation in this conversion-type material is markedly slower than in intercalation or alloying-type materials. The direct methodology using ToF-SIMS for determining the diffusion coefficient can be applied to any type of electrode material. It enlarges the horizon for the study of Li diffusion kinetics into electrode for LIBs.

One of the other main obstacles of iron oxide for LIB material is its high conversion potential (working voltage). In order to reduce the working voltage, a (Fe, Cr)-binary oxide thin film was prepared on a stainless steel (AISI410, $FeCr_{12.5}$) current collector to tune energy density and working voltage. Galvanostatic discharge/charge during 20 cycles show that the substitution of iron oxide by chromium did not improve the electrochemical performance, such as specific capacity, cycling performance and capacity retention ratio. The cathodic peak position in the CV curves shows the substituting iron by chromium did not reduce the working voltage. However, the coulombic efficiency of the thin film binary oxide electrode in the first discharge/charge cycle is slightly poorer than that for iron oxide but better than that for chromium oxide. ToF-SIMS results demonstrate a kinetically controlled conversion process in the binary oxide electrode, and the substituting chromium oxide does not react sufficiently with lithium due to its poor electrochemical activity. SEM and AFM show that morphological modifications of the electrode are indistinctive in the first two cycles but significantly increase during further cycling.

Finally, two perspectives are proposed for further work:

- Synthesis of nanostructured iron oxide by means of atomic layer deposition (ALD) using anodic aluminum oxide (AAO) membrane template for application in lithium ion microbatteries;
- Electrochemical behaviour of iron and iron oxide in Fe-air batteries with emphasis of the role of electrolyte additives (i.e. Na_2S) on the inhibition of hydrogen evolution in Fe-air batteries.

Chapter 1. State of the art and objectives

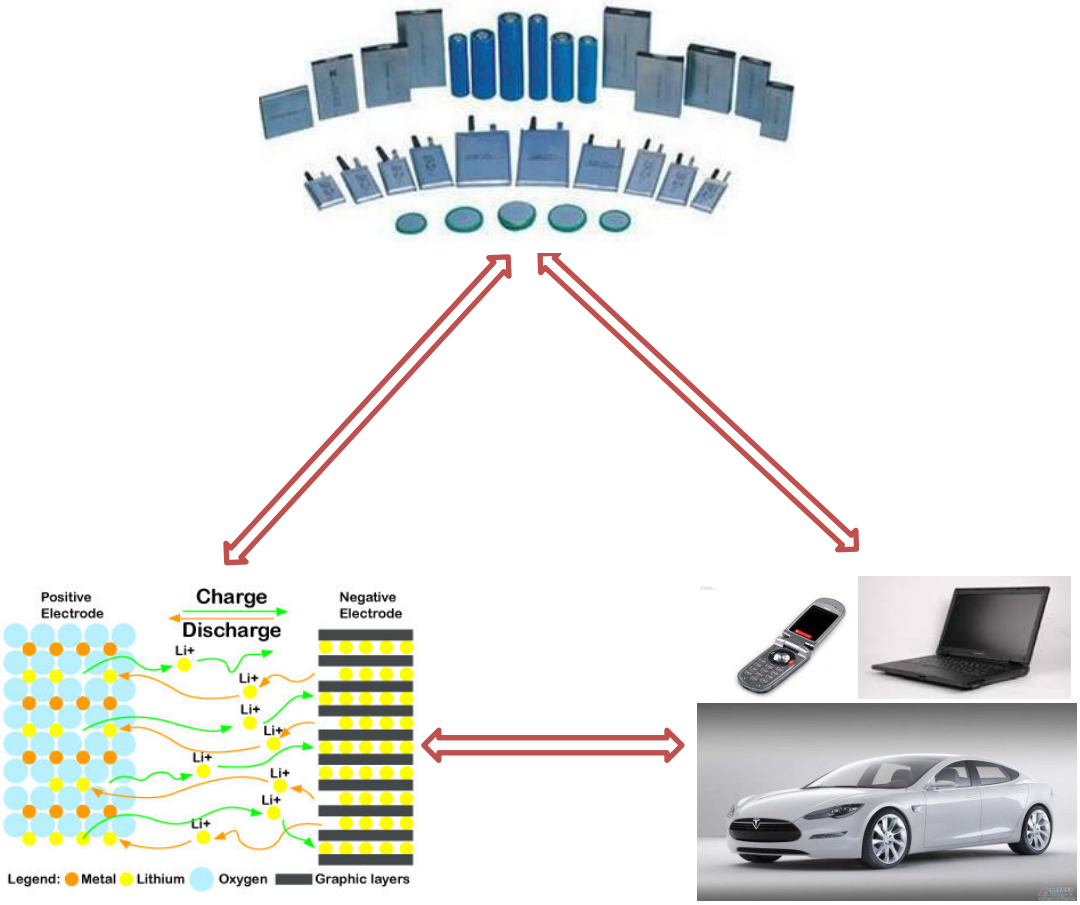

Abstract: In this chapter, the history and principle of LIBs are briefly introduced. The LIB contains four primary components: cathode, electrolyte, separator and anode. In order to improve the energy density of LIB, negative electrode materials need to be developed. According to the lithiation/delithiation process, the negative electrode materials can be classified into intercalation-type, alloy-type and conversion-type materials. The electrochemical performance of LIBs also depends on surface reactions occurring at the surface of the electrodes. A solid electrolyte interphase layer (SEI) can be formed at the surface of negative electrodes due to reductive electrolyte decomposition. The details concerning the formation of the SEI layer as well as the influence of the SEI layer on the electrochemical performance of the LIBs will be presented. As this study focused on iron oxide, the properties of iron oxide electrode (nanostructured and thin film) are also specified in this chapter.

Keywords: Lithium-ion batteries; Anode; Reaction mechanism; Conversion; Iron oxide; Thin-film

1. Lithium-ion batteries (LIBs)

Among the myriad of energy storage technologies, lithium batteries are playing an increasingly important role because of their high specific energy (energy per unit weight) and energy density (energy per unit volume) compared to other batteries available on the market (Figure 1-1), such as lead-acid (Pb-acid), and nickel-metal hydride (Ni-MH) batteries. The use of Pb-acid batteries is restricted mainly to SLI (starting, lighting, ignition) in automobiles or standby applications, whereas Ni-Cd batteries remain the most suitable technologies for high-power applications (for example, power tools). Since their introduction in 1991, lithium-ion battery (Li-ion battery or LIB) has transformed portable electronic devices, such as laptops, cell phones, digital cameras and other consumer electronics.[1-3]

The first commercialized LIBs were developed by Sony Corporation in 1991 with a graphite anode, a $LiCoO_2$ cathode and the electrolyte, and have been dominant in the Li-ion battery market for 20 years due to their high energy density and long cycle life. However, this combination is not suitable for large scale batteries for vehicle and grid use. Firstly, the high cost of $LiCoO_2$ is due to scarcity and not environmental friendliness of cobalt resources. Secondly, there are potential safety hazards in such a system which will greatly enlarge in large-scale batteries. The safety hazards arise from the strongly oxidizing delithiated $Li_{1-x}CoO_2$ cathode in the charged state, which can release O_2, and the reducing lithiated graphite anode, coupled with a flammable electrolyte, that commonly co-exist in a LIBs system. To circumvent these issues, high-safety, low-cost cathode material $LiFePO_4$ was proposed for large-scale LIBs.[4] High voltage and zero-strain $Li_5Ti_4O_{12}$ anode was also proposed to couple with high voltage cathodes (i.e., $LiMn_2O_4$, $LiCo_{1/3}Ni_{1/3}Mn_{1/3}O_2$ and $LiMn_{0.8}Fe_{0.2}PO_4$) for potential usage.[5-7] However, these systems have lower working voltages than that of $LiCoO_2$/graphite, which compromise their energy density.

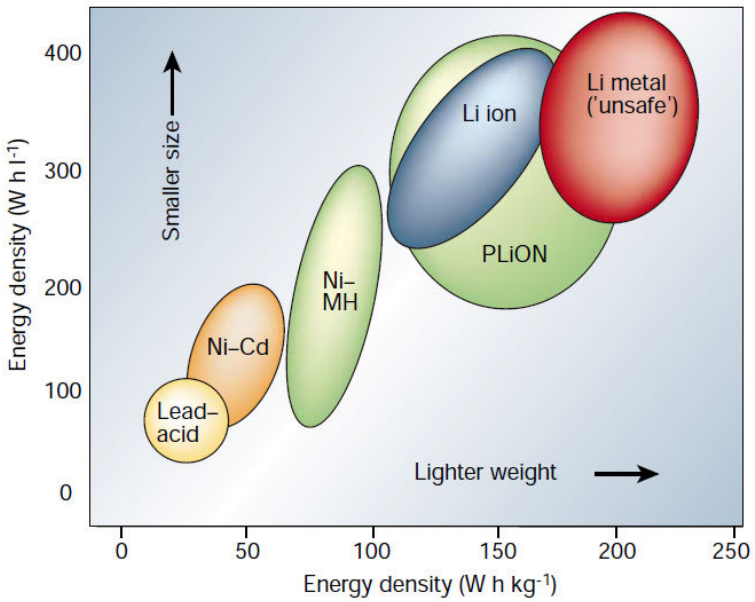

Figure 1-1 Comparison of the different battery technologies in terms of volumetric and gravimetric energy density.[1]

1.1 Principle of LIBs

A lithium-ion battery is a Li ion concentration cell essentially, which is composed of two different embedded lithium ion compounds as the positive and negative electrodes. As a member of the family of rechargeable battery types, lithium ions move from the negative electrode (anode) to the positive electrode (cathode) during discharge and back when charging. To keep balance of charge, there are equal amounts of electrons transmitted through the external circuit together with Li ions move back and forth between positive and negative electrodes, to maintain a certain potential corresponding to redox reaction in the process of charging and discharging. Working potential is influenced by properties of lithium compounds that compose the positive and negative electrodes, Li ion concentration etc. A schematic drawing of working-mechanism of LIBs is shown in Figure 1-2. The negative electrode is a graphitic carbon that holds Li in its layers, whereas the positive electrode is a Li-intercalation compound - usually an oxide because of its higher potential - that often is characterized by a layered structure. Both electrodes are able to reversibly insert and remove Li ions from their respective structures. On charging, Li ions are removed or de-intercalated from the layered oxide compound and intercalated into the graphite layers. The process is reversed on discharge. The electrodes are separated by a non-aqueous electrolyte that

transports Li ions between the electrodes.

A commercialized lithium-ion battery use a $LiCoO_2$ as cathode and an intercalated lithium compound (such as graphite) as the anode material compared to the metallic lithium used in non-rechargeable lithium battery. The charge and discharge reaction could be described by equation[8] (1-1):

$$LiCoO_2 + C \Leftrightarrow Li_xC + Li_{1-x}CoO_2 \qquad (1\text{-}1)$$

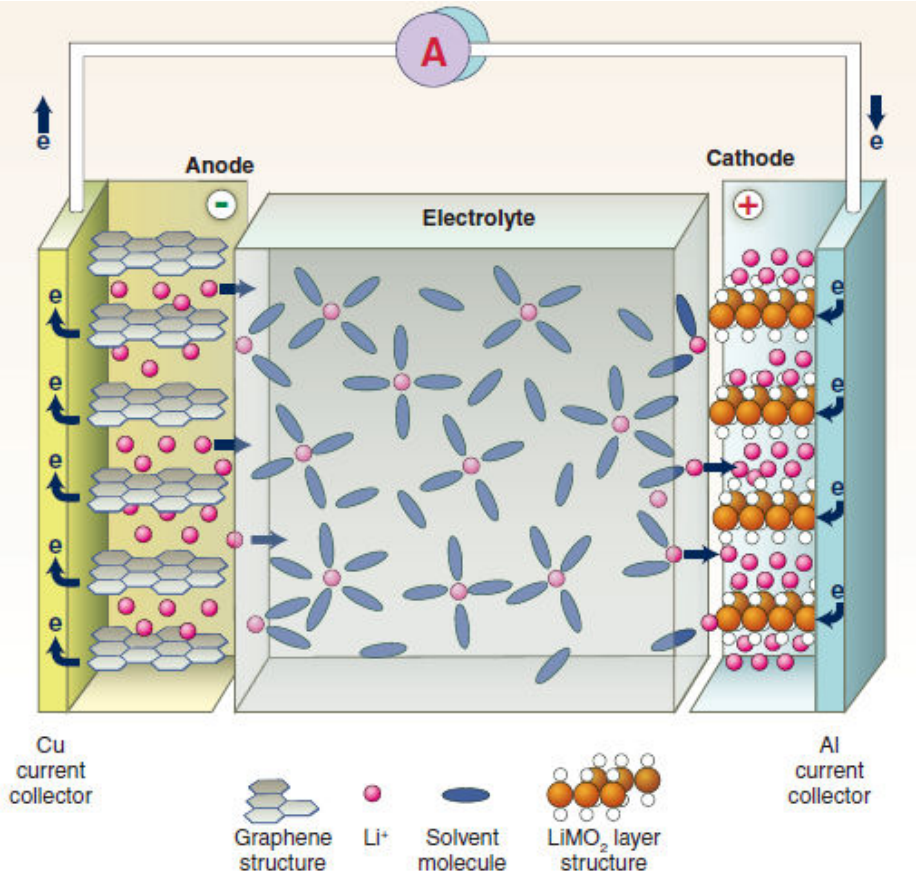

Figure 1-2 Schematic of a LIB, discharge process. [9]

1.2 Structure of LIBs

The current commercialized LIBs can be divided into liquid and polymer LIBs. A general LIB is composed of four primary functional components: cathode, electrolyte, separator and anode. At present, Li-ion cells are available in configurations of different shapes and components, which can generally be divided into four groups, as shown in Figure 1-3. The basic requirement of LIBs for primary functional materials is specified below in each section.

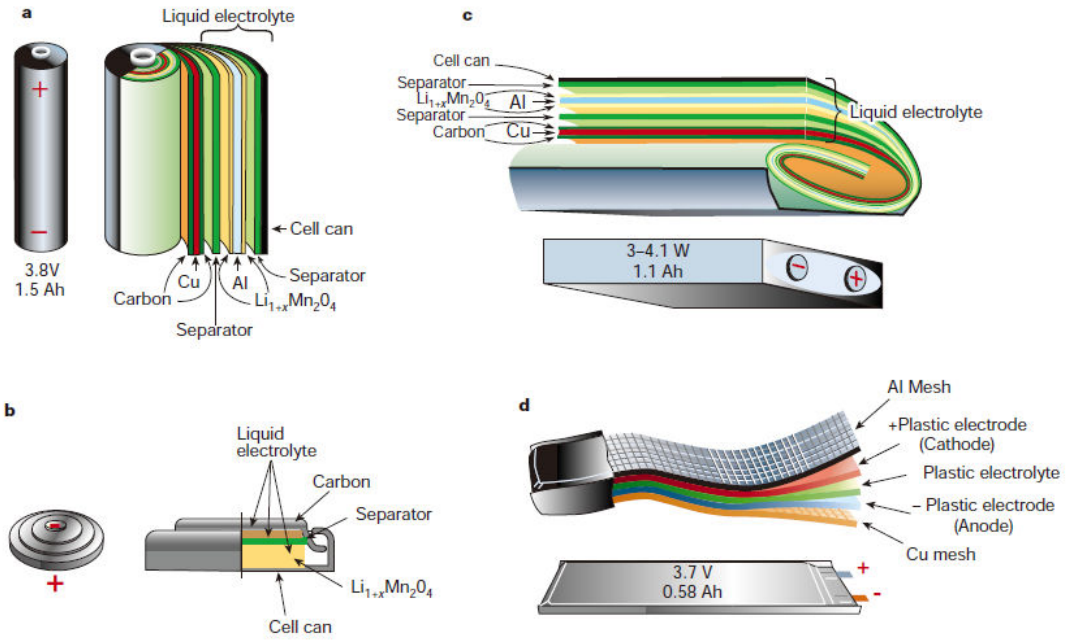

Figure 1-3 Schematic drawing showing the shapes and components of various lithium-ion batteries. a: cylindrical; b: coin; c: prismatic, d: thin and flat (plastic Li ion (PLiON)). [1]

1.2.1 Cathode

The cathode material is one of the key materials of manufacturing lithium-ion batteries. The performance and price of the cathode material is crucial to the LIBs. The performance of cathode material in LIBs can be evaluated from the following aspects: the cathode material should have high open circuit voltage, large specific capacity, good cycling performance, high safety, rapid charge and discharge ability, and also be cheap in price, environmentally friendly in synthesis and industrialization, etc. At present, high potential inserted lithium transition metal oxides are the most popular cathode materials under investigation, which contain layered $LiCoO_2$ and $LiNiO_2$, spinel $LiMn_2O_4$, olivine $LiFePO_4$, and their derivatives and doping compounds.

1.2.2 Electrolyte

The electrolyte, as the media for lithium ion transport, is in contact with the active material directly in a LIB, thus affecting the performance of a cell. The ideal electrolyte should meet the requirements of various performances of the lithium-ion battery: (1) a wide electrochemical window, namely stable in a wide range of potential (0 ~ 5 V); (2) low viscosity, high dielectric constant and ionic conductivity; (3) good thermal stability and

chemical stability; (4) high safety, low toxicity and low cost, etc. Normally, the electrolyte in lithium-ion battery mainly consists of non-aqueous solvents and inorganic lithium salts. The most common used electrolyte categories are organic liquid electrolyte, polymer electrolyte and molten salt electrolyte. The most commercialized electrolytes are organic liquid electrolytes and polymer electrolytes.

1.2.3 Separator

A separator is used to separate the positive and negative electrodes and to prevent short circuit of the two electrodes. The separator itself is not conductive, but lithium ion can get through it. Therefore, an ideal separator should possess the following properties: low electrical conductivity, good permeability to electrolyte ions (high ionic conductivity), low resistance during charge/discharge, good chemical and electrochemical stability in electrolyte at working temperature, good wettability to the electrolyte, high mechanical strength and small in thickness. The commonly used separators in cells are cellulose paper, non-woven or synthetic resin microporous membrane. The commercialized separators in LIBs are single-layer polyethylene (PE), single-layer polypropylene (PP), 3-layer PP/PE/PP composite membrane.

1.2.4 Anode

The requirements for anode materials are roughly the same as for cathode materials, mainly reflected in low electrode potential, high specific energy, long cycling life, safety, excellent rate capability, environmental pollution-free, easy to synthesize and prepare, low cost, etc. In the commercialized LIBs, carbonaceous anode materials (typically specified into three groups, namely, graphite and graphitized materials, ungraphitized soft carbon, and hard carbon) are the most widely used. Recently, alloying-type Si, Sn, lithium titanium oxide and transition metal oxides were widely studied as anode materials for LIBs.

1.3 Reversible energy storage mechanisms in LIBs

Energy storage, an intermediate step to the versatile, clean, and efficient use of energy, has received worldwide attention and increasing research interest. In a typical energy storage

process, one type of energy is converted into another form of energy that can be stored and converted for use when needed. Therefore, various energy storage systems are being developed aimed at proper utilization of different energy sources.[10] However, among all the efforts to develop new reversible energy storage systems, studying and understanding the corresponding reversible energy storage mechanisms is crucial and important.

In order to have a good understanding of the energy storage in LIBs, it is necessary to clarify the reaction mechanisms for lithium storage. The most commonly reported lithium storage mechanisms (Figure 1-4) are summarized below.[11]

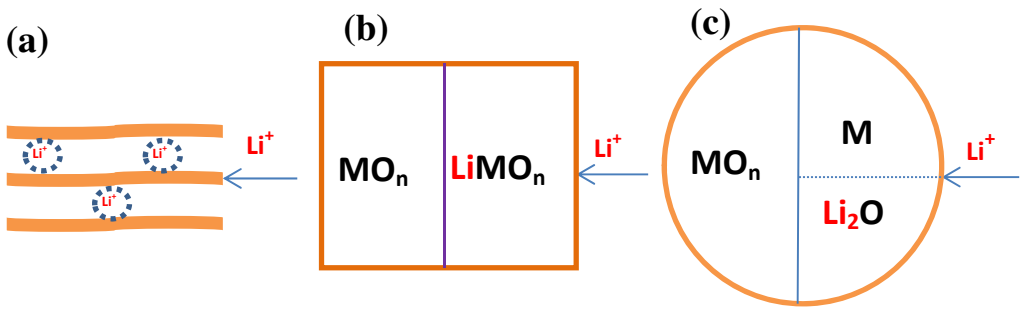

Figure 1-4 Schematic of reversible lithium storage mechanisms: (a) Intercalation reaction; (b) Phase transition; (c) Conversion reaction.

1.3.1 Intercalation reaction mechanism

An intercalation reaction is based on charge transfer in the structure of the host compounds (H) where the guest atoms (Li) are accommodated:[12-14]

$$xLi^+ + xe^- + H \Leftrightarrow Li_xH \qquad (1\text{-}2)$$

A layered structure is preferred for the host compounds, but not limited to this. The "rocking-chair concept" for rechargeable lithium batteries, in which the intercalation compounds were suggested for use in both the positive and negative electrodes, were firstly suggested by M. Armand [15] and commercialized by SONY. In current LIBs for portable electronic devices, the most common structure are layered graphite (*R-3m* space group) and $LiCoO_2$ (*R-3m* space group) used as negative and positive electrode material, respectively. Thus, the guest atoms occupy the host lattice continuously and the chemical potential of the host is modified gradually. The voltage profile of charging and discharging within a single-phase intercalation regime normally shows a slope behavior and can be explained by a

lattice gas model.[16,17] The reversible lithium storage capacity is determined by the available vacancy sites for guest atoms, a transferrable charge number above 0 V vs. Li/Li^+ and the structure stability of the host materials. Typically, the reversible lithium storage capacity for the graphite negative electrode is 300-350 mAh g^{-1} (theoretical capacity is 372 mAh g^{-1} for forming LiC_6) and is around 135-145 mAh g^{-1} for the $LiCoO_2$ positive electrode (the theoretical capacity is 274 mAh g^{-1} for extracting one mole of Li).

1.3.2 Phase transition mechanism

In a phase transition reaction, the reactant transforms directly and continuously from the initial phase into another phase during charging or discharging. For example, $LiFePO_4$ converts into $FePO_4$ during charging (delithiation, theoretical capacity is 170 mAh g^{-1}) and $Li_4Ti_5O_{12}$ anode converts into $Li_7Ti_5O_{12}$ during discharging (lithiation, theoretical capacity is 175 mAh g^{-1}).[4,5] In addition, it is also common that the electrode material undergoes a series of phase transitions during continuous lithium insertion or extraction. Taking the alloying-type reaction as an example, Si can form a series of Li-Si alloys during electrochemical lithiation (the theoretical capacity is 4200 mAh g^{-1} for forming $Li_{22}Si_5$) at high temperatures and show several voltage plateaus in the voltage profile.[18]

The open circuit potential profile of each phase transition reaction will show one plateau when the Gibbs formation energy of the reactants and products do not vary upon lithium insertion and extraction within the phase transition regime. For example, $LiFePO_4$ shows a ~3.5 V plateau and $Li_4Ti_5O_{12}$ displays a ~1.55 V plateau but Si as anode shows no obvious potential plateau.[4,5,18]

1.3.3 Conversion reaction mechanism

The "conversion reaction" is a kind of phase transition mechanism. The term is used here to define specifically the decomposition reaction from one parent compound into two or more products after lithium insertion. Reversible heterogeneous conversion reactions of transition metal oxides (MO) with lithium were reported for the first time by Poizot et al.:[19]

$$2Li + MO \Leftrightarrow Li_2O + M(M = Co, Ni, Cu, Fe) \qquad (1\text{-}3)$$

Later, reversible lithium storage has been observed in transition metal fluorides, sulfides, nitrides, phosphides and hydrides.[20-24] Recently, the reversible conversion reaction is also extended to other polyanion compounds, such as the reaction (1-4):[25]

$$xLi + Cu_{2.33}V_4O_{11} \Leftrightarrow Li_xV_4O_{11} + 2.33Cu \qquad (1\text{-}4)$$

The lithium storage capacity through the conversion reaction can be as high as 1480 mAh g^{-1} in the case of MgH_2 anode for Li batteries (the theoretical capacity is 2062 mAh g^{-1} for forming Mg and 2LiH). [24] Many materials undergoing the conversion reaction have been considered as positive or negative electrode materials.

In spite of their high capacity, most conversion reaction type electrode materials suffer from high voltage polarization between the charging and discharging, and the low initial Coulombic efficiency due to the inherent thermodynamic properties and poor kinetics of these type materials.[26,27]

Moreover, some mechanisms, i.e., reversible chemical bonding, surface charging, organic free radical, under potential deposition, interfacial charging, are also possible in lithium storage, but not dominated in the existing system of LIBs.[11]

Lithium-ion batteries are currently rapidly expanding into very large-scale applications, such as hybrid (electrical) cars. As certain applications have dramatically expanded, a better understanding of the Li storage mechanisms is much-needed in developing next generation battery materials.

2. Surface and interface science in LIBs - SEI layer

Surface chemistry of the electroactive material and complex electrode/electrolyte interfacial properties is crucial for electrochemical performance (i.e. cycling performance and rate capability) of a LIB.[28-30] In the early 1970s, a passivation film was found to cover the lithium metal electrode used as anode in a secondary battery. This passivation film plays a very important role in the battery system during charge and discharge cycling. With the in-depth study of this phenomenon, the researchers have proposed approximate formation mechanisms of this passivation layer and several models have also been proposed according to these mechanisms. Among all these models, one model is commonly considered as the

most convincing and widely applied, which is known as the solid electrolyte interphase (SEI) layer model.[31,32]

2.1 Formation of SEI layer - mechanism and features

2.1.1 Formation mechanism of SEI

The SEI layer is normally formed on the negative electrode surface due to electrolyte decomposition at potential below 1 V *vs.* Li/Li^+ (typically 0.7 V *vs.* Li/Li^+ for most organic electrolytes). In the case of carbonaceous electrodes, the formation of the SEI layer proceeds from the deposition of organic and inorganic compounds during the first five charge/discharge cycles.[33] However, the formation mechanism of the SEI is a subject under debate. The initial models have treated the surface reduction like a simple 2D surface process, while Besenhard et al. proposed a mechanism that involved the unique structure of graphite anodes.[34] Based on their earlier studies of intercalation phenomenon on graphite, they proposed that the electrolyte solvents, especially PC, tend to co-intercalate and form the so-called ternary graphite intercalation compounds (GIC).[35] Thus it is reasonable to speculate that the formation of SEI must also experience a similar step, i.e., before the potential of graphite anode becomes reductive enough to induce decomposition of electrolyte solvent molecules, these molecules would co-intercalate in the graphene interlayers. In other words, the interphase thus formed, as schematically shown in Figure 1-5, would concentrate near the edge sites of the graphite particles and partially penetrate the graphite lattice. This formation mechanism is thus known as “3D model of SEI”.[35,36]

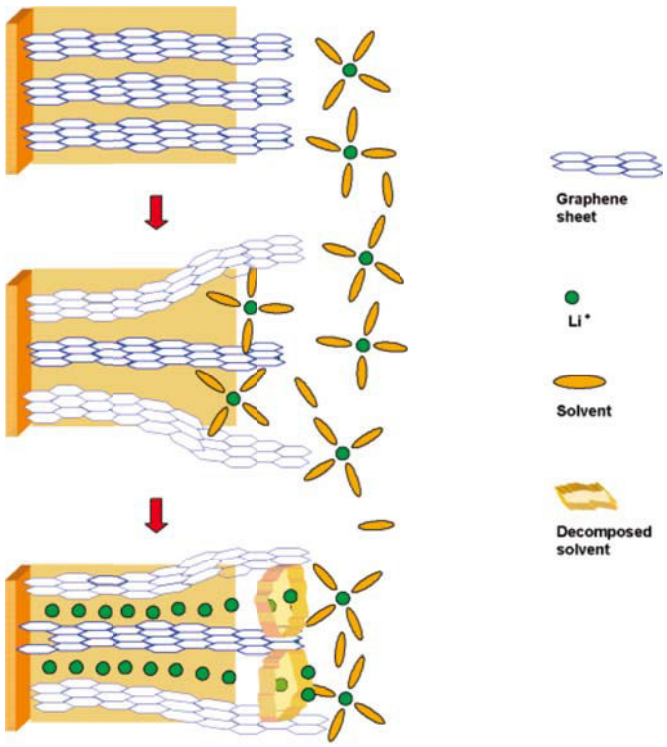

Figure 1-5 Schematic illustration of the SEI formation mechanism *via* the decomposition of $Li(solv)_xC_y$.[37]

2.1.2 Components of SEI

The composition of the SEI is also a highly debated subject. Generally speaking, the SEI is a very complicated layer consisting of inorganic components which are normally salt degradation products and organic components originating from a partial or a complete reduction of the electrolyte. Some most common components used in electrolyte are solvent (i.e., Propylene carbonate (PC), Ethylene carbonate (EC), Ethyl methyl carbonate (EMC), Diethyl carbonate (DEC), Dimethyl carbonate (DMC), 1,2-dimethoxyethane (DME)…) and salt (i.e., $LiClO_4$, $LiPF_6$, $LiAsF_6$, $LiBF_4$, $LiCF_3SO_3$, $LiN(CF_3SO_2)_2$…). The reported SEI composition varies from one research group to another, as operating conditions in different laboratories can be different (see Table 1-1). It is highly dependent on numerous factors, such as chemical factors (lithium salt and solvent), electrochemical conditions and temperature of cycling. [38]

Table 1-1 Composition of the SEI layer reported in the literature.[38]

Component	Notes	References
Li_2CO_3	Normally present in the SEI formed in PC or EC based electrolytes. It may also appear as a reaction product of semicarbonates with HF or water or CO_2.	39-42
$(CH_2OCO_2Li)_2$	Found mostly in the SEI of the EC based electrolytes. Being a two electron reduction product of EC.	39,43-46
$ROCO_2Li$	Occurs in most PC containing electrolytes, especially when the concentration of PC in the electrolyte is high. They are present in outer part of SEI layer and are absent near Li.	39,40,41,43,44,47
ROLi	Most commonly found in the SEI formed in ether electrolytes like tetrahydrofuran (THF), but may also appear as DMC or EMC reduction product. It is soluble and may thus undergo further reactions.	43,48-55
LiF	Mostly found in electrolytes comprising of fluorinated salts like $LiAsF_6$, $LiPF_6$ and $LiBF_4$. It is a major salt of decomposition products. HF contaminant also reacts with semi carbonates to give LiF byproduct. Amount of LiF increases during storage.	42,56-58
LiOH	Mainly formed due to water contamination. It may also result from reaction of Li_2O with water or with ageing.	46,49,59-62
Li_2O	It may be a degradation product of Li_2CO_3 during Ar^+ sputtering in the XPS experiment. In a conversion-type electrode material, Li_2O could be the reduction product.	1,57,63-65
$Li_2C_2O_4$	Found to be present in Li-ion 18650 rechargeable cells assembled in Argonne National Labs containing 1.2 M $LiPF_6$ in EC:EMC (3:7) electrolyte. Li carboxylate and Li methoxide were also found in their SEI.	49,53
HCOLi	Present when methyl formate is used as co-solvent or additive.	47

Polycarbonates	Present in the outermost layer of the SEI, close to the electrolyte phase. This part imparts flexibility to the SEI.	[56,66]
……	……	……

2.1.3 Features of ideal SEI

The formation of the SEI layer on the electrode surface will prevent further decomposition of the electrolyte in the successive cycles. Therefore, an ideal SEI layer should be a compact layer and well adhered onto the electrode material, be stable and insoluble in the electrolyte even at high temperatures, and have minimum electronic and maximum Li^+ conductivity. Moreover, an ideal SEI should also have uniform morphology and composition. It should be elastic and flexible to accommodate volume variations during lithiation/delithiation process.[38,43,54,67]

2.1.4 Influence of SEI on the electrochemical performances of LIBs

The SEI layer plays a very important role in the electrochemical performances of LIBs. The battery performance parameters affected by the SEI are irreversible charge loss (ICL), self-discharge, cyclability, rate capability, and safety. Every parameter and property of the SEI significantly affects battery performance. The composition, thickness, morphology, and compactness are a few to name.[38]

In commercial LIBs, graphite cannot be cycled in PC based electrolyte ($LiPF_6$/PC or $LiClO_4$/PC) because the undesirable SEI layer is not able to prevent the co-intercalation of solvent molecules in the graphite leading to the formation of gas responsible for an increase of the pressure in graphene layers and then electrode destruction by exfoliation.[33] The exfoliation phenomenon is governed by low quality SEI layer which depends on its composition and morphology. The use of EC as co-solvent with PC increases significantly the cycling ability. Indeed, the composition of the SEI influences the electronic insulating properties of the SEI layer and its chemical stability. The morphology of the SEI layer, its porosity and thickness, will govern the conduction of lithium ions through the SEI layer. Therefore, the charge capacity and the irreversible capacity will depend strongly on the

quality of the SEI layer.[68]

For the conversion-type and alloying-type electrode materials, which have a large volume expansion during lithiation process, the SEI layer also affects the electrochemical performances of the electrodes in LIBs. As evidenced from XPS and ToF-SIMS studies performed on the iron oxide and iron sulfide thin-film electrodes, the SEI layer formed by reductive decomposition of the electrolyte penetrated into the bulk of the oxide thin film upon repeated conversion/deconversion, which leads to deterioration of the electrode performances upon further multi-cycling.[69,70] XPS analysis performed on silicon thin films-α-Si:H model electrodes shows a thicker SEI layer formed after cycling in PC-based electrolyte as compared to EC:DMC electrolyte. [71] Investigation on Si nanowires (SiNWs) shows the SEI modifications caused by the lithiation/delithiation rate and the modifications of the Si electrode upon cycling. Low lithiation/delithiation rate improves electrochemical performance due to a better penetration depth of lithium into the SiNW electrode and the formation of a homogeneous solid electrolyte interphase (SEI) layer on the SiNWs after the first cycle. However, after repeated cycling, SiNWs suffered strong mechanical stress leading to a rough or porous SiNW structure covered by a porous SEI layer.[72]

2.2 Variation of SEI layer - influential factors

The SEI layer, as the reaction product of the electrode material and electrolyte, is formed on the electrode surface during charging and discharging of a LIB. Its composition, structure, density and stability is mainly determined by the nature of electrodes and electrolyte, but also influenced by the temperature, cycle number and current density of charging and discharging.

2.2.1 Anode materials

Various properties of anode materials, including types of material, composition, structures and morphology, especially surface morphology, of the electrodes have a critical influence on the formation of SEI layers. In a commercial LIB, the SEI layer is mainly formed on the surface of carbonaceous negative active materials, thus the type of carbon significantly affects the SEI. In-depth studies of various types of carbon anode materials (i.e. pyrolytic carbon, carbon fiber, petroleum coke, artificial graphite and natural graphite)

showed that the degree of graphitization and orderliness seriously affect properties of the SEI layer. Even for the same carbon material, the SEI formation can be different in composition and morphology depending on the electrode surface (i.e., basal plane, cross section and edges), and particle size.[57,73-76]

2.2.2 Lithium salt

The composition and contents of the SEI layer are partially determined by the types of lithium salt in the electrolyte. Generally, the lithium salt is considered more reductive than the solvent and its reduction product becomes part of the SEI layer. The commonly used lithium salt, $LiClO_4$, is less secure due to its strong oxidizing property. $LiAsF_6$ is highly toxic although it has better electrochemical properties for carbon anode. $LiPF_6$ has poor thermal stability and will decompose into LiF at 60~80 ^oC. Therefore, looking for new lithium salt is still in progress.

The main difference of various lithium salts is the type of anionic species, which results in different formation potential and chemical composition of the SEI layer. Reduction products of the lithium salts are present in the SEI layer when Cl and F are contained in inorganic lithium salts. Experimental results show that high contents of LiF and LiCl are found in the SEI layer due to the Cl and F elements contained in the electrolyte (lithium salt), which may be caused by the following reactions:[56]

$$LiPF_6\ (solv) + H_2O(l) \rightarrow LiF(s) + 2HF(solv) + POF_3(g) \qquad (1\text{-}5)$$

$$LiBF_4\ (solv) + H_2O(l) \rightarrow LiF(s) + 2HF(solv) + BOF(s) \qquad (1\text{-}6)$$

Furthermore, the decomposition of the inorganic lithium salt could also generate direct formation of the following compounds:

$$LiPF_6(solv) \rightarrow LiF(s) + PF_5(s) \qquad (1\text{-}7)$$

According to thermodynamic calculations, the inorganic lithium compounds are more likely to be generated than the organic compounds as products of electrolyte decomposition. A SEI layer containing more inorganic lithium salts will be much more stable according to thermodynamics, and less SEI dissolution will occur during electrochemical cycling. For instance, EIS analysis showed a significant increase of the resistance when $TBAPF_6$ (TBA^+

denotes tetrabutylammonium ions) is used in place of $LiPF_6$ as an electrolyte lithium salt. This is mainly because the volume of TBA^+ ions is larger, causing serious damage to graphite electrode when co-intercalating in graphite layers.[77]

2.2.3 Electrolyte solvent

The components of the SEI layer are mainly the decomposition products of electrolyte solution under negative potential. Different kinds of electrolyte solvents play an important role in the formation of SEI layer.

Organic electrolyte solvents require high electrical conductivity, low viscosity, high flash point and good stability. It is difficult to satisfy all the properties for a single solvent. Commonly, carbonate mixtures of several solvents, i.e., ternary solvent of EC/DEC/DMC, are widely used. Recent studies show that additives of aliphatic esters, such as ethyl acetate, methyl acetate, in the ternary solvent could effectively improve the conductivity and stability of the SEI layer. This is because the CO_2, produced by decomposition of the esters, can promote the formation of a stable SEI layer.[78]

In a PC solution, SEI layers cannot cover the electrode surface completely, and the electrolyte decomposed on the graphite surface which produced irreversible capacity in battery cycling. In a pure EC solvent, the main component of SEI films is $(CH_2OCOOLi)_2$. However, C_2H_5COOLi and Li_2CO_3 will dominate the SEI composition when DEC and DMC, respectively, are added in the EC-based solution. Obviously, the SEI layer contains C_2H_5COOLi and Li_2CO_3 is much more stable than that with more $(CH_2OCOOLi)_2$ component. In the EC-based solution (EC/DEC and EC/DMC), only EC decomposed to form SEI layer. DEC and DMC, that improve conductivity and solubility of the solution, are not involved in the formation of the SEI layer.[79]

2.2.4 Temperature

Generally, high temperature will decrease the stability of the SEI layer and then deteriorate the cycling performance of the electrode. That is because dissolution of the SEI and co-intercalation of the solvent molecules both increase with increasing temperature.

When a dense SEI layer with good stability and low resistance is formed, the electrodes

present the best cycling performance at low temperature (-20 ^{o}C) in $LiPF_6$-PC/DMC electrolyte. [80] Andersson's study on the relationship between temperature and performances of Li/graphite half-cells shows that the original SEI layer reformed at a high temperature (80 ^{o}C) under continued cycling. A porous SEI layer is formed after dissolution and re-deposition of the SEI, so that the electrolyte can be in contact with the electrode and continues to generate further reduction.[56]

Currently, the insulation aging at 30-60 ^{o}C, commonly used in the industry operation for improving cycling performance and optimizing battery storage, is based on the SEI reforming mechanism at high temperature.[56]

2.2.5 Current density

The reaction on the electrode surface is a competitive reaction of passivation film formation and charge transfer. The electrochemical reaction properties and the SEI layer composition will vary at different current densities due to the different diffusion rates of various ions and the different ion transport numbers.

Dollé et al.[81] reported that the current density affects composition more than thickness during formation of the SEI layer. For a low current density, they showed the different steps in the passivating layer formation with apparition of Li_2CO_3 from the beginning and apparition of lithium alkyl-carbonates at the end of discharge. At higher current density, the SEI layer is solely composed of Li_2CO_3 and there is no lithium alkyl-carbonates at the end of discharge. This explains why the resistance of the SEI levels off rather than increases as observed previously but with an increased capacitance value.

Ota and coworkers [82] disclosed that the structure of SEI on the graphite anode significantly depends upon current density as investigated by combination of temperature programmed desorption or decomposition-gas chromatography/mass spectrometry (TPD-GC/MS), X-ray photoelectron spectroscopy (XPS), scanning electron microscopy (SEM), and chemical analysis. In the case of high current density, the inorganic SEI was first formed at high potential and, around the potential where the intercalation of lithium occurs, the organic SEI was formed later. On the other hand, at a low current density, the SEI composed of only an organic component was immediately formed from the starting potential

(1.5 V *vs.* Li/Li^+). However, there is no inorganic component in the SEI layer. This is different from Dollé's results, which may be due to the use of different electrolytes.

2.3 Characterization of SEI layers - research methods and techniques

The characterization of SEI layers is focused on morphology, structure, composition and electrochemical performance. Electrochemical, microscopic and spectroscopic (including electron spectroscopy, chromatography and mass spectrometry) techniques are the main research methods and approaches. In recent years, a variety of *in situ* study techniques have been widely used.

2.3.1 Electrochemical methods

Electrochemical methods (i.e., electrochemical impedance spectroscopy (EIS), cyclic voltammetry (CV) and electrode charge/discharge test) have been widely used for studying the SEI layer. The characteristics of the SEI layer could be speculated from some electrochemical parameters of the electrodes.

EIS technique is a powerful tool to understand the electrode processes in LIBs. EIS studies can clearly expose deposition and dissolution process of the SEI layer which corresponds to the impedance increases and decreases. At the same time, from the fit and simulation of the Nyquist plots, a suitable equivalent circuit can be obtained to further describe the structural characteristics and electrochemical behaviors of SEI layer.[83-86]

Cyclic voltammetry is also a powerful tool. The potential window of SEI formation could be clearly shown by using cyclic voltammetry. A strong cathodic peak is observed at around 0.65 V in the first cyclic voltammograms but disappeared in the second scan for the fresh graphite electrode. Apparently, this reduction peak is the current peak of SEI formation.[85,86]

In addition, other electrochemical methods i.e., galvanostatic method, potentiostatic method, pulse voltammetry and steady state polarization method are useful to analyze SEI kinetics.

2.3.2 Microscopic methods

With the development of electron microscopy, the properties, structure and morphology of the SEI layer can not only be indirectly speculated from electrochemical and optical data, but also be observed directly by microscopic methods on the surface of the electrode. Microscopic techniques i.e., scanning electron microscope (SEM), [87] transmission electron microscope (TEM),[88] atomic force microscope (AFM)[89-91] and scanning probe microscope (SPM)[92,93] have been gradually applied in the study of SEI layer. These microscopic techniques can directly display the SEI within a nanoscale of around 10 nm, which provides the most direct methodology of characterizing SEI layer.

2.3.3 Spectroscopic methods

Modern technology offers a variety of spectroscopic and chromatographic techniques as useful tools for the study of SEI composition. The spectroscopic and chromatographic analysis of the SEI provides not only qualitative but also quantitative information on the components. Amongst the various spectroscopic techniques used to analyze the SEI, Fourier transform infrared spectroscopy (FTIR),[47,94] Raman spectroscopy, [73] X-ray photoelectron spectroscopy (XPS),[64] and time-of-flight secondary ion mass spectrometry (ToF-SIMS) [57] have proved to be very useful.

Moreover, chromatography and mass spectrometry are often used for analyzing the composition of SEI. Especially, combining these two techniques, Ogumi et al. [95] analyzed the chemical constituents of the SEI layer formed on graphite negative electrode in EC-based electrolyte solutions by pyrolysis/gas chromatography/mass spectroscopy (Pyro/GC/MS), to obtain direct evidence for decomposed products of relatively high-molecular weights. The results showed that oligomers with oxyethylene units, such as ethylene glycol, di(ethylene glycol), and tri(ethylene glycol) methyl ester, were detected, and their presence suggested that the SEI layer contained polymer-like substances that have repeated oxyethylene units. Similar studies on the SEI layer were also implemented by Ota et al.[82]

2.3.4 *In situ* techniques

Existing state-of-the-art characterization techniques have reached a high level of maturity. Rapid progress in microscopic, spectroscopic, and scattering methods has already

led to new and fascinating insights into the nature of chemical and interfacial processes in LIBs research. *In situ*, non-invasive characterization techniques are considered a great challenge, yet a vital approach, to achieve better understanding of the mechanisms of the underlying processes relevant to energy storage in the operating environments and conditions.[96]

In situ studies do not refer to a specific type of research method or technique. It is a transformation in the way of research. Generally, *in situ* study instrument is connected to a model cell which is currently charging/discharging or ongoing potential polarization. The electrode can be easily analyzed in a certain potential range or a charge/discharge state. *In situ* study can monitor changes of the electrode at any time. It also eliminates the steps of removing the electrode and then exposing to atmosphere (H_2O and O_2) in the process of transfer or analysis. Recently, more and more researchers began to study the application of the *in situ* characterization techniques. These include X-ray absorption near-edge structure,[97,98] nuclear magnetic resonance (NMR),[99] Mössbauer spectroscopies,[100] Raman spectroscopy, [73] AFM, [89,101] TEM,[81] and even SEM.[102]

Surface and interface science on negative electrode in LIBs, mainly SEI layer, is an important requirement for good performance of a Li-ion battery. Studying, analyzing and understanding the SEI have underlined the significance of the many aspects related to it.

3. Iron oxide for LiBs - state of the art

Iron oxide (mainly α-Fe_2O_3) is one of the most interesting and important transition metal oxides for application in LIBs due to its high theoretical capacity (1007 mAh g^{-1}), abundance and environmental friendliness, and it has been studied as candidate anode material since first reported as conversion-type material.[21,103,104]

3.1 Structure and electrochemical performance of hematite (α-Fe_2O_3)

Hematite (α-Fe_2O_3) is a thermodynamically stable form in the iron oxide family. The α-Fe_2O_3 crystallizes in the hexagonal corundum (Al_2O_3) structure (rhombohedral system) and naturally occurs as the mineral hematite (Figure 1-6). Due to high theoretical capacity and

being a cheap material, its anodic properties have been studied, with micrometer and nanometer size particles and with carbon as conducting additives.[105]

Li cycling of Fe_2O_3 was first reported by Larcher et al.,[103, 104] who showed that 0.5 mol of Li per formula unit can be reversibly intercalated into nano-α-Fe_2O_3 (20 nm) in the potential range 1.5-4.0 V. Under deep discharge conditions (0.005-3.0 V *vs.* Li), 8.5 mol of Li per mole of Fe_2O_3 react resulting in crystal structure destruction and formation of nano-metal particles (Fe^0) and Li_2O by conversion reaction and a polymeric layer on Fe^0 as a result of the decomposition of the solvents in the electrolyte. The reaction of n-Fe_2O_3 (for nanometric) with lithium proceeds successively as follows,[103,104]

$$n - Fe_2O_3 \xrightarrow{\text{monophasic}} \alpha - LiFe_2O_3 \xrightarrow{\text{biphasic}} \text{cubic } Li_2Fe_2O_3 \xrightarrow{\text{biphasic}} Fe^0 + Li_2O \quad (1\text{-}8)$$

The reaction of M-Fe_2O_3 (for Micrometric) with lithium can be schemed as follows, with evident large overlapping of the different processes,

$$M - Fe_2O_3 \xrightarrow{\text{monophasic}} \alpha - Li_{0.03}Fe_2O_3 \xrightarrow{\text{biphasic}} \text{cubic } Li_2Fe_2O_3 \xrightarrow{\text{biphasic}} Fe^0 + Li_2O \quad (1\text{-}9)$$

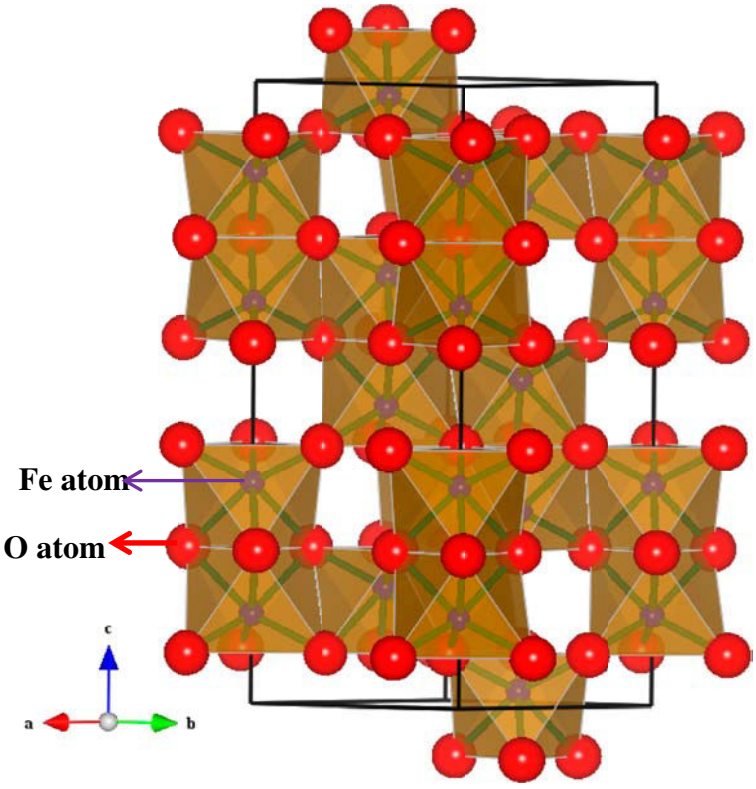

Figure 1-6 General crystallographic presentation of hematite, Fe_2O_3. FeO_6 octahedra are shown. Outline of the unit cell is also shown.[105]

3.2 Nanostructured iron oxide

Nanostructure engineering has been demonstrated as an effective approach to improve the electrochemical performance of electrode materials. Constructing nanostructured materials has been considered as a promising avenue towards the development of high-performance LIBs with high energy density, high power density, long cycle life, and improved safety. [1,2,106-109] In general, nanostructures can provide reduced distance for ion and electron transport, larger electrode/electrolyte contact area, and good accommodation ability of the volume changes. Thus the electrochemical processes in nanostructured material-based electrodes are significantly boosted. Faster charge/discharge capability (i.e., higher rate capability/power density) and higher specific capacity (i.e., higher energy density) can be expected for LIBs based on advanced nanostructured electrode materials.[107, 110 - 114] Additionally, some of the structural features, such as low-dimensional morphologies and hollow spaces, are able to better withstand the huge volume change during the charge/discharge process, thus leading to enhanced cycling performance.[115,116]

To maximize the advantages of nanostructured materials, the morphology, composition, porosity, and surface characteristics need to be optimized. Therefore, a wide variety of nanostructured iron oxides with diverse geometric shapes and morphologies has been extensively explored, such as porous particles,[117,118] 0D nanoparticles,[119] 1D nanowires and nanotubes,[120, 121] 2D nanosheets and nanoflakes,[122 - 126] and 3D hollow structures.[127 - 130] Nanostructured Fe_2O_3, prepared as submicro-flowers, nanorods, nanowires, nanoparticles, hollow spheres, and composites with carbon, have been studied as anodes with good capacity and improved cyclability.

3.3 Thin-film iron oxide

Thin films, especially porous films, can effectively buffer the volume expansion while lithium is inserted into the electrode. Thin films of Fe_2O_3 of various morphologies and on various substrates have been prepared, characterized, and found to perform well as anodes in LIBs.[125,131-135]

Sputter-deposited iron oxide thin films were investigated as a possible negative electrode for LIBs. [132] The conductivities of the amorphous thin films were found to be very

high compared with those of the respective crystalline forms. The amorphous state presents an interesting characteristic regarding the intercalation/de-intercalation process. The open structure gives rise to a large number of available intercalation sites and, therefore, the volume variation of the electrode is limited during the intercalation/de-intercalation process. Regarding the electrochemical behavior, Fe_2O_3-based thin films electrodes are able to store and reversibly exchange lithium ions. At a C/2 charge/discharge rate with 100% depth-of-discharge (DOD), the specific capacity of these amorphous thin film electrodes remains almost constant and close to 330 Ah/kg after more than 120 charge/discharge cycles.

The reversible Li-cycling properties of the α-Fe_2O_3 nanoflakes grown on Cu foil substrate have been evaluated by cyclic voltammery, galvanostatic discharge-charge cycling, and impedance spectral measurements. [125] The galvanostatic discharge-charge results show that the first-discharge profile (Li insertion) is different from the subsequent profiles and indicates Li intercalation into Fe_2O_3 to give $Li_2(Fe_2O_3)$ at ~1.2 V vs. Li, and this is followed by amorphization and crystal structure destruction at ~0.75 V by an additional consumption of 4 mol of Li to yield nanophase Fe^0 and Li_2O *via* the two-phase reactions. This is followed by a sloping voltage profile upon further discharge process up to 0.005 V, indicating the formation of SEI and a polymeric layer on the Fe metal particles. The first-charge profile (Li extraction) up to 3 V indicates the conversion reaction to give FeO or Fe_2O_3, as shown by the voltage plateau at ~2.1 V. The differential capacity vs. voltage plots clearly delineate the voltages at which the reactions occur during the 1st and 50th cycle. The capacity vs. cycle number plot shows that, after 10-15 cycles, the Coulombic efficiency improves to ~98%, and a stable and reversible capacity of (680±20) mAh g^{-1} is observed up to 80 cycles when cycled at 65 mA g^{-1} (0.1 C rate) in the voltage range 0.005-3 V. Cyclic voltammetry and impedance studies were reported to support the conversion reaction mechanism in α-Fe_2O_3.

Porous carbon-free α-Fe_2O_3 films with two types of pore size distribution were prepared by electrostatic spray deposition, and they were characterized by X-ray diffraction, scanning electron microscopy and X-ray absorption near-edge spectroscopy. [134] The 200 ^oC-deposited thin film exhibits a high reversible capacity of up to 1080 mAh g^{-1}, while the initial capacity loss is at a remarkable low level (19.8%). Besides, the energy efficiency and energy specific average potential (E_{av}) of the Fe_2O_3 films during charge/discharge process were investigated.

The results indicate that the porous α-Fe_2O_3 films have significantly higher energy density than $Li_4Ti_5O_{12}$ while it has a similar E_{av} of about 1.5 V. Due to the porous structure that can buffer the volume changes during lithium intercalation/de-intercalation, the films exhibit stable cycling performance. As a potential anode material for high performance LIBs that can be applied on electric vehicle and energy storage, rate capability and electrochemical performance under high-low temperatures were also investigated in this work.

3.4 Scientific issues of iron oxide in LIBs

Iron oxide (mainly α-Fe_2O_3), as a transition-metal oxide, is based on a conversion reaction. In spite of a high specific capacity, iron oxide usually suffers from large voltage hysteresis between charge and discharge, which severely retards the round-trip efficiency of the electrode, and shows poor electronic/ionic conductivity, which is the main obstacle for improving the charge/discharge rate capability of the battery. Recent advancements of nanostructured materials open new opportunities to improve both the rate capability and cyclicality of this Li-ion anode.[136] Hereafter, surface and interface chemistry, thermodynamics and kinetics properties of this kind of conversion-type material, are emphasized to highlight the scientific issues on iron oxide in LIBs.

3.4.1 Surface and interface chemistry

It is believed that the surface and interface chemistry have important effects on the physico-chemical properties of the electrode materials. Surface and interface chemistry in LIBs on carbonaceous electrodes have been widely studied in literature.

For the conversion-type iron oxide which undergoes a large volume expansion during lithiation, surface and interface chemistry of the electrodes in LIBs is also crucial in determining the electrochemical performance of this material. The theoretical expansion for the conversion reaction (1-10) is 193% as deduced from molar volume calculation (30.5 cm^3/mol for Fe_2O_3, 7.1 cm^3/mol for Fe and 14.84 cm^3/mol for Li_2O).[65]

$$Fe_2O_3 + 6Li^+ + 6e^- \rightarrow 3Li_2O + 2Fe \qquad (1\text{-}10)$$

Such a volume expansion is expected to not only fracture the iron oxide electrode, but also

modify the SEI layer on the electrode surface.[65,69] So, a systematic study of the surface and interface chemistry of the iron oxide in LIBs is one of the most important tasks of this work.

3.4.2 Thermodynamics and kinetics

Chemical thermodynamics is the study of the interrelation of heat and work with chemical reactions or with physical changes of state within the confines of the laws of thermodynamics. Chemical thermodynamics involves not only laboratory measurements of various thermodynamic properties, but also the application of mathematical methods to the study of chemical questions and the spontaneity of processes. From the first and second laws of thermodynamics, four equations called the "fundamental equations of Gibbs" can be derived.[137] For a deeper understanding of the Li storage phenomenon in iron oxide, systematic work on thermodynamic calculation with speculated chemical reactions is necessary. These thermodynamics aspects could be useful in order to understand the reaction mechanisms of the iron oxide and then to apply it as an anode for better LIBs.

The development of electrode materials with high rate capabilities, which will contribute mainly to the superior electrochemical kinetic, is a critical issue to commercialize rechargeable LIBs as a power source for EV/HEV. [138] The iron oxide (α-Fe_2O_3) electrode suffers from poor electronic/ionic conductivity, which is the main obstacle for improving rate capability. So the future applications of such conversion electrode material lies in understanding and improving their kinetics, including lithium diffusion kinetics in bulk electrode and SEI layer.

4. Objectives of this work

As iron oxide (α-Fe_2O_3) is an interesting candidate material for application as anode in LIBs, the electrochemical performance, surface and interface chemistry, thermodynamics and kinetics properties were investigated by a thin film approach in this work. These thin film oxide electrodes were prepared *via* simple thermal oxidation of iron metal substrate, without conductive carbon additives and binder (PVDF), so as to investigate thoroughly the conversion mechanism, aging mechanism and the SEI-induced surface passivation

mechanism in 1 M $LiClO_4$-PC electrolyte. The main topics of the work include:

- Conversion/deconversion mechanisms. An investigation of the conversion/deconversion mechanisms (process reversibility) of iron oxide electrode in the first lithiation/delithiation cycle is important to understand the conversion-type electrode materials in LIBs.
- Aging mechanisms. Capacity degradation is one of the most common issues of the electrode materials during battery cycling. For thin film iron oxide electrodes, the cycling performance evaluated both by CV and galvanostatic cycling is necessary in LIBs. The influence of multi-cycling on both the compositional and morphological modifications of the iron oxide electrode surface was analyzed to understand the aging mechanisms of iron oxide as anode material in LIBs.
- Surface passivation mechanisms – SEI layer. The SEI is critical for the reversibility of the cycling performance. However, for transition metal oxides, it is rarely studied especially during cycling. Here, the formation and stability of the SEI layer on conversion-type iron oxide electrode during lithiation/delithiation (accompanied by volume expansion/shrinkage) is presented. The compositional and morphological modifications of the SEI layer were also studied during multi-cycling.
- Kinetics. Iron oxide electrode suffers from poor electronic/ionic conductivity, which is the main obstacle for improving the charge/discharge rate capability of the battery. This requires a good understanding of transport (diffusion) mechanisms of Li ions into the bulk electrode matrix during lithium insertion. Measurements of an apparent diffusion coefficient of lithium (D_{Li}) into α-Fe_2O_3 electrodes using appropriate techniques were performed.
- Performance improving. One of the other main obstacles of iron oxide for LIB material is its high conversion potential (working voltage). In order to reduce the working voltage, binary metal oxide ((Fe, Cr)-oxide) was prepared to tune energy density and working voltage.

In order to investigate the conversion/deconversion mechanisms, aging mechanisms and surface passivation mechanisms of iron oxide for LIB anode, CV and EIS were performed in a half cell. For chemical characterization, surface and depth profile analysis of the lithiated

and delithiated thin film electrodes was performed by means of XPS and ToF-SIMS, and for morphological characterization SEM and AFM were applied. The apparent diffusion coefficient of lithium (D_{Li}) into iron oxide thin film electrode was evaluated by combining CV, EIS and ToF-SIMS. (Fe, Cr)-binary oxide thin film electrodes were investigated by electrochemical (CV, galvanostatic cycling), spectroscopic (XPS, ToF-SIMS) and microscopic (SEM, AFM) analyses to uncover the influence of Cr ions in a mixed Fe-Cr binary oxide electrode.

5. Contents of the thesis

This thesis is based on a collection of chapters comprising results that have been presented either in international conferences, or published and/or submitted for publication in international journals. The papers have been arranged in the order described below.

Following the state of the art and objectives presented in the present introduction chapter (Chapter 1), Chapter 2 presents the study of the formation and stability of the SEI layer and conversion/deconversion mechanisms in the first cycle of lithiation/delithiation of iron oxide used as anode material for LiBs. Surface (XPS and ToF-SIMS) and electrochemical (CV and EIS) analytical techniques were combined.

Chapter 3 discusses the cycling-induced modifications of the electrode and its passivation film as well as the aging mechanisms. The morphological modifications of the thin-film iron oxide electrode were studied by microscopy techniques (SEM, AFM).

Chapter 4 describes the solid-state diffusion of lithium into the α-Fe_2O_3 thin film electrode during electrochemical lithiation and delithiation process. The diffusion coefficient of lithium (D_{Li}) was estimated by CV, EIS as well as ToF-SIMS depth profiling.

Chapter 5 explores the mechanisms of lithiation/delithiation of a binary oxide in LiBs. The influence of substituting of iron oxide by chromium oxide was evaluated. The kinetically controlled conversion process of the binary oxide shows that lithium transport in the binary oxide also depends on oxide species.

Finally, Chapter 6 presents the main conclusions of this study as well as the perspectives.

The Appendix gives an overview of electrochemical, spectroscopic and microscopic analysis techniques used for studying the thin film electrode. Principles and instruments, advantages and drawbacks of these techniques are discussed.

References

[1] Tarascon, J.-M., Armand, M., Issues and challenges facing rechargeable lithium batteries, *Nature*, **2001**, 414, 359-367.

[2] Bruce P.G., Scrosati B., Tarascon J.-M., Nanomaterials for Rechargeable Lithium Batteries, *Angew. Chem. Int. Ed.*, **2008**, 47, 2930-2946.

[3] Bruce P.G., Freunberger S.A., Hardwick L.J., Tarascon J.-M., Li-O_2 and Li-S batteries with high energy storage, *Nat. Mater.*, **2012**, 11, 19-29.

[4] Padhi A.K., Nanjundaswamy K.S., Goodenough J.B., Phospho-olivines as Positive-Electrode Materials for Rechargeable Lithium Batteries, *J. Electrochem. Soc.*, **1997**, 144, 1188-1194.

[5] Ohzuku T., Ueda A., Yamamoto N., Zero-Strain Insertion Material of $Li[Li_{1/3}Ti_{5/3}]O_4$ for Rechargeable Lithium Cells, *J. Electrochem. Soc.*, **1995**, 142, 1431-1435.

[6] Ohzuku T., Y. Makimura, Layered Lithium Insertion Material of $LiCo_{1/3}Ni_{1/3}Mn_{1/3}O_2$ for Lithium-Ion Batteries, *Chem. Lett.*, **2001**, 642-643.

[7] Borgel V., Gershinsky G., Hu T., Theivanayagam M.G., Aurbach D., $LiMn_{0.8}Fe_{0.2}PO_4/Li_4Ti_5O_{12}$, a Possible Li-Ion Battery System for Load-Leveling Application, *J. Electrochem. Soc.*, **2013**, 160, A650-A657.

[8] Nishi Y., Lithium ion secondary batteries: past 10 years and the future, *J. Power Sources*, **2001**, 100, 101-106.

[9] Dunn B., Kamath H., Tarascon J.-M., Electrical Energy Storage for the Grid: A Battery of Choices, *Science*, **2011**, 334, 928-935.

[10] Liu C., Li F., Ma L.-P., Cheng H.-M., Advanced Materials for Energy Storage, *Adv. Mater.*, **2010**, 22, E28-E62.

[11] Zu C.-X., Li H., Thermodynamic analysis on energy densities of batteries, *Energy Environ. Sci.*, **2011**, 4, 2614-2624.

[12] Whittingham M.S., Chemistry of intercalation compounds: metal guests in chalcogenide hosts, Prog. *Solid State Chem.*, **1978**, 12, 41-99.

[13] Julien C.M., Lithium intercalated compounds charge transfer and related properties, *Mater. Sci. Eng. R: Report*, **2003**, 40, 47-102.

[14] Winter M., Besenhard J.O., Spahr M. E., Novák P., Insertion Electrode Materials for Rechargeable Lithium Batteries, *Adv. Mater.*, **1998**, 10, 725-763.

[15] Armand M.B., in Fast Ion Transport in Solids, (ed. Van Gool, W.), New York, *North-Holland Amsterdam*, **1973**, 665-673.

[16] Coleman S.T., McKinnon W.R., Dahn J.R., Lithium intercalation in $Li_xMo_6Se_8$: A model mean-field lattice gas, *Phys. Rev. B*, **1984**, 29, 4147-4149.

[17] Kalikmanov V.I., Koudriachova M.V., Leeuw de S.W., Lattice-gas model for intercalation

compounds, *Solid State Ionics*, **2000**, 136-137, 1373-1378.

[18] Boukamp B.A., Lesh G.C., Huggins R.A., All-Solid Lithium Electrodes with Mixed-Conductor Matrix, *J. Electrochem. Soc.*, **1981**, 128, 725-729.

[19] Poizot P., Laruelle S., Grugeon S., Dupont L., Tarascon J.-M., Nano-sized transition-metal oxides as negative-electrode materials for lithium-ion batteries, *Nature*, **2000**, 407, 496-499.

[20] Li H., Richter G., Maier J., Reversible formation and decomposition of LiF clusters using transition metal fluorides as precursors and their application in rechargeable Li batteries, *Adv. Mater.*, **2003**, 15, 736-739.

[21] Poizot P., Laruelle S., Grugeon S., Tarascon J.-M., Rationalization of the Low-Potential Reactivity of 3d-Metal-Based Inorganic Compounds toward Li, *J. Electrochem. Soc.*, **2002**, 149, A1212-A1217.

[22] Pereira N., Klein L.C., Amatucci G.G., The Electrochemistry of Zn_3N_2 and LiZnN: A Lithium Reaction Mechanism for Metal Nitride Electrodes, *J. Electrochem. Soc.*, **2002**, 149, A262-A271.

[23] Silva D.C.C., Crosnier O., Ouvrard G., Greedan J., Safa-Sefat A., Nazar L.F., Reversible Lithium Uptake by FeP_2, *Electrochem. Solid-State Lett.*, **2003**, 6, A162-A165.

[24] Oumellal Y., Rougier A., Nazri G.A., Tarascon J.-M., Aymard L., Metal hydrides for lithium-ion batteries, *Nat. Mater.*, **2008**, 7, 916-921.

[25] Poizot P., Chevallier F., Laffont L., Morcrette M., Rozier P., Tarascon J.-M., Evidence of an Electrochemically Assisted Ion Exchange Reaction in $Cu_{2.33}V_4O_{11}$ Electrode Material vs. Li, *Electrochem. Solid-State Lett.*, **2005**, 8, A184-A187.

[26] Sun J., Tang K., Yu X., Hu J., Li H., Huang X., Overpotential and electrochemical impedance analysis on Cr_2O_3 thin film and powder electrode in rechargeable lithium batteries, *Solid State Ionics*, **2008**, 179, 2390-2395.

[27] Zhong K.F., Xia X., Zhang B., Li H., Wang Z.X., Chen L.Q., MnO powder as anode active materials for lithium ion batteries, *J. Power Sources*, **2010**, 195, 3300-3308.

[28] Aurbach D., Review of Selected Electrode-solution Interactions Which Determine the Performance of Li and Li Ion Batteries. *J. Power Sources* **2000**, 89, 206-218.

[29] Ensling D., Thissen A., Jaegermann W., On the Formation of Lithium Oxides and Carbonates on Li Metal Electrodes in Comparison to $LiCoO_2$ Surface Phases Investigated by Photoelectron Spectroscopy, *Appl. Surf. Sci.*, **2008**, 255, 2517-2523.

[30] Aurbach D., Markovsky B., Salitra G., Markevich E., Talyossef Y., Koltypin M., Nazar L., Ellis B., Kovacheva D., Review on Electrode-electrolyte Solution Interactions, Related to Cathode Materials for Li-ion Batteries. *J. Power Sources* **2007**, 165, 491-499.

[31] Peled E., The electrochemical behavior of alkali and alkaline earth metals in nonaqueous battery systems-The solid electrolyte interphase model, *J. Electrochem. Soc.*, **1979**, 126,

2047-2051.

[32] Munichandraiah N., Scanlon L.G., Marsh R.A., Surface films of lithium: an overview of electrochemical studies, *J. Power Sources*, **1998**, 72, 203-210.

[33] Chagnes A., Swiatowska J., Lithium Ion Batteries-New Developments, in: I. Belharouak (Ed.), Electrolyte and Solid-Electrolyte Interphase Layer in Lithium-Ion Batteries, *INTECH*, **2012**, 145-172.

[34] Besenhard J.O., Winter M., Yang J., Biberacher W., Filming mechanism of lithium-carbon anodes in organic and inorganic electrolytes, *J. Power Sources*, **1993**, 54, 228-231.

[35] Xu K., Cresce von A., Interfacing electrolytes with electrodes in Li ion batteries, *J. Mater. Chem.*, **2011**, 21, 9849-9864.

[36] Wagner M.R., Albering J.H., Moeller K.C., Besenhard J.O., Winter M., XRD evidence for the electrochemical formation of View the MathML source in PC-based electrolytes, *Electrochem. Commun.*, **2005**, 7, 947-952.

[37] Xu K., Nonaqueous Liquid Electrolytes for Lithium-Based Rechargeable Batteries, *Chem. Rev.*, **2004**, 104, 4303-4417.

[38] Verma P., Maire P., Novák P., A review of the features and analyses of the solid electrolyte interphase in Li-ion batteries, *Electrochim. Acta*, **2010**, 55, 6332-6341.

[39] Aurbach D., Markovsky B., Shechter A., Ein-Eli Y., Cohen H., A Comparative Study of Synthetic Graphite and Li Electrodes in Electrolyte Solutions Based on Ethylene Carbonate‐Dimethyl Carbonate Mixtures, *J. Electrochem. Soc.*, **1996**, 143, 3809-3820.

[40] Aurbach D., Zaban A., Impedance spectroscopy of lithium electrodes: Part 1. General behavior in propylene carbonate solutions and the correlation to surface chemistry and cycling efficiency, *J. Electroanal. Chem.*, **1993**, 348, 155-179.

[41] Aurbach D., Eineli Y., Chusid O., Carmeli Y., Babai M., Yamin H., The Correlation Between the Surface Chemistry and the Performance of Li-Carbon Intercalation Anodes for Rechargeable 'Rocking-Chair' Type Batteries, *J. Electrochem. Soc.*, **1994**, 141, 603-611.

[42] Peled E., Golodnitsky D., Menachem C., Bar-Tow D., An Advanced Tool for the Selection of Electrolyte Components for Rechargeable Lithium Batteries, *J. Electrochem. Soc.*, **1998**, 145, 3482-3486.

[43] Aurbach D., Levi M.D., Levi E., Schechter A., Failure and Stabilization Mechanisms of Graphite Electrodes, *J. Phys. Chem. B*, **1997**, 101, 2195-2206.

[44] Aurbach D., Gofer Y., Benzion M., Aped P., The behaviour of lithium electrodes in propylene and ethylene carbonate: the major factors that influence Li cycling efficiency, *J. Electroanal. Chem.*, **1992**, 339, 451-471.

[45] Aurbach D., Eineli Y., Markovsky B., Zaban A., Luski S., Carmeli Y., Yamin H., The Study of

Electrolyte Solutions Based on Ethylene and Diethyl Carbonates for Rechargeable Li Batteries II. Graphite Electrodes, *J. Electrochem. Soc.*, **1995**, 142, 2882-2890.

[46] Kominato A., Yasukawa E., Sato N., Ijuuin T., Asahina H., Mori S., Analysis of surface films on lithium in various organic electrolytes, *J. Power Sources*, **1997**, 68, 471-475.

[47] Ein-Eli Y., Markovsky B., Aurbach D., Carmeli Y., Yamin H., Luski S., The dependence of the performance of Li-C intercalation anodes for Li-ion secondary batteries on the electrolyte solution composition, *Electrochim. Acta*, **1994**, 39, 2559-2569.

[48] Kang S.-H., Abraham D.P., Xiao A., Lucht B.L., Investigating the solid electrolyte interphase using binder-free graphite electrodes, *J. Power Sources*, **2008**, 175, 526-532.

[49] Zhuang G.R.V., Ross P.N., Analysis of the chemical composition of the passive film on Li-ion battery anodes using attentuated total reflection infrared Spectroscopy, *Electrochem. Solid State Lett.*, **2003**, 6, A136-A139.

[50] Mori S., Asahina H., Suzuki H., Yonei A., Yokoto K., Chemical properties of various organic electrolytes for lithium rechargeable batteries: 1. Characterization of passivating layer formed on graphite in alkyl carbonate solutions, *J. Power Sources*, **1997**, 68, 59-64.

[51] Zhang H.L., Li F., Liu C., Tan J., Cheng H.M., New insight into the solid electrolyte interphase with use of a focused ion beam, *J. Phys. Chem. B*, **2005**, 109, 22205-22211.

[52] Aurbach D., Moshkovich M., A Study of Lithium Deposition-Dissolution Processes in a Few Selected Electrolyte Solutions by Electrochemical Quartz Crystal Microbalance, *J. Electrochem. Soc.*, **1998**, 145, 2629-2639.

[53] Augustsson A., Herstedt M., Guo J.H., Edstrom K., Zhuang G.V., Ross P.N., Rubensson J.E., Nordgren J., Solid electrolyte interphase on graphite Li-ion battery anodes studied by soft X-ray spectroscopy, *Phys. Chem. Chem. Phys.*, **2004**, 6, 4185-4189.

[54] Aurbach D., Electrode-solution interactions in Li-ion batteries: a short summary and new insights, *J. Power Sources*, **2003**, 119-121, 497-503.

[55] Aurbach D., Markovsky B., Weissman I., Levi E., Ein-Eli Y., On the correlation between surface chemistry and performance of graphite negative electrodes for Li ion batteries, *Electrochim. Acta*, **1999**, 45, 67-86.

[56] Andersson A.M., Edstrom K., Chemical Composition and Morphology of the Elevated Temperature SEI on Graphite, *J. Electrochem. Soc.*, **2001**, 148, A1100-A1109.

[57] Peled E., Bar-Tow D., Merson A., Gladkich A., Burstein L., Golodnitsky D., Composition, depth profiles and lateral distribution of materials in the SEI built on HOPG-TOF SIMS and XPS studies, *J. Power Sources*, **2001**, 97-98, 52-57.

[58] Aurbach D., Einely Y., Zaban A., The Surface Chemistry of Lithium Electrodes in Alkyl Carbonate Solutions, *J. Electrochem. Soc.*, **1994**, 141, L1-L3.

[59] Kanamura K., Tamura H., Takehara Z., XPS analysis of a lithium surface immersed in propylene carbonate solution containing various salts, *J. Electroanal. Chem.*, **1992**, 333, 127-142.

[60] Odziemkowski M., Irish D.E., An Electrochemical Study of the Reactivity at the Lithium Electrolyte/Bare Lithium Metal Interface II. Unpurified Solvents, *J. Electrochem. Soc.*, **1993**, 140, 1546-1555.

[61] Aurbach D., Cohen Y., The Application of Atomic Force Microscopy for the Study of Li Deposition Processes, *J. Electrochem. Soc.*, **1996**, 143, 3525-3532.

[62] Aurbach D., Daroux M.L., Faguy P.W., Yeager E., Identification of Surface Films Formed on Lithium in Propylene Carbonate Solutions, *J. Electrochem. Soc.*, **1987**, 134, 1611-1620.

[63] Morigaki K.-I., Ohta A., Analysis of the surface of lithium in organic electrolyte by atomic force microscopy, Fourier transform infrared spectroscopy and scanning auger electron microscopy, *J. Power Sources*, **1998**, 76, 159-166.

[64] Bar-Tow D., Peled E., Burstein L., A Study of Highly Oriented Pyrolytic Graphite as a Model for the Graphite Anode in Li-Ion Batteries, *J. Electrochem. Soc.*, **1999**, 146, 824-832.

[65] Tian B., Światowska J., Maurice V., Zanna S., Seyeux A., Klein L.H., Marcus P., Combined Surface and Electrochemical Study of the Lithiation/Delithiation Mechanism of Iron Oxide Thin Film Anode for Lithium-Ion Batteries, *J. Phys. Chem. C*, **2013**, 117, 21651-21661.

[66] Genies S., L'Institut National Polytechnique de Grenoble, *PhD thesis*, France, **1998**, p. 226.

[67] Aurbach D., Zinigrad E., Cohen Y., Teller H., A short review of failure mechanisms of lithium metal and lithiated graphite anodes in liquid electrolyte solutions, *Solid State Ionics*, **2002**, 148, 405-416.

[68] Chagnes A., Carre B., Willmann P., Dedryvere R., Gonbeau D., Lemordant D., Cycling Ability of γ-Butyrolactone-Ethylene Carbonate Based Electrolytes, *J. Electrochem. Soc.*, **2003**, 150, A1255-A1261.

[69] Tian B., Światowska J., Maurice V., Zanna S., Seyeux A., Klein L.H., Marcus P., Aging-induced chemical and morphological modifications of thin film iron oxide electrodes for lithium-ion batteries, *Langmuir*, **2014**, 30, 3538-3547.

[70] Liao F., Światowska J., Maurice V., Seyeux A., Klein L.H., Zanna S., Marcus P., Ageing mechanisms of conversion-type electrode material studied oniron sulfide thin films, *Electrochimica Acta*, **2014**, 120, 359-368.

[71] Pereira-Nabais C., Światowska J., Chagnes A., Ozanam F., Gohier A., Tran-Van P., Cojocaru C. S., Cassir M., Marcus P., Interphase Chemistry of Si Electrodes Used as Anodes in Li-Ion Batteries. *App. Surf. Sci.*, **2013**, 266, 5-16.

[72] Pereira-Nabais C., Światowska J., Chagnes A., Gohier A., Zanna S., Seyeux A., Tran-Van P., Cojocaru C. S., Cassir M., Marcus P., Insight into the Solid Electrolyte Interphase on Si

Nanowires in Lithium-Ion Battery: Chemical and Morphological Modifications upon Cycling, *J. Phys. Chem. C*, **2014**, 118, 2919-2928.

[73] Kong F., Kostecki R., Nadeau G., Song X., Zaghib K., Kinoshita K., McLarnon F., In situ studies of SEI formation, *J. Power Sources*, **2001**, 97-98: 58-66.

[74] Edström K., Andersson A.M., Bishop A., Fransson L., Lindgren J., Hussénius A., Carbon electrode morphology and thermal stability of the passivation layer, *J. Power Sources*, **2001**, 97-98, 87-91.

[75] Laik B., Chausse A., Messina R., Barthes-Labrousse M.G., Nedelec J.Y., Paven-Thivet Le C., Grillon F., Analysis of the surface layer on a petroleum coke electrode in tetraglyme solutions of lithium salts, *Electrochim. Acta*, **2000**, 46, 691-700.

[76] Kim J.-S., Park Y.-T., Characteristics of surface films formed at a mesocarbon microbead electrode in a Li-ion battery, *J. Power Sources*, **2000**, 91, 172-176.

[77] Chung G.-C., Kim H.-J., Yu S.-I., Jun S.-H., Choi J.-W., Kim M.-H., Origin of Graphite Exfoliation An Investigation of the Important Role of Solvent Cointercalation, *J. Electrochem. Soc.*, **2000**, 147, 4391-4398.

[78] Ratnakumar B.V., Smart M.C., Surampudi S., Effects of SEI on the kinetics of lithium intercalation, *J. Power Sources*, **2001**, 97-98, 137-139.

[79] Yang C.R., Wang Y.Y., Wan C.C., Composition analysis of the passive film on the carbon electrode of a lithium-ion battery with an EC-based electrolyte, *J. Power Sources*, **1998**, 72, 66-70.

[80] Ishikawa M., Tasaka Y., Yoshimoto N., Morita M., Optimization of physicochemical characteristics of a lithium anode interface for high-efficiency cycling: an effect of electrolyte temperature, *J. Power Sources*, **2001**, 97-98, 262-264.

[81] Dollé M., Grugeon S., Beaudoin B., Dupont L., Tarascon J.-M., In situ TEM study of the interface carbon/electrolyte, *J. Power Sources*, **2001**, 97-98, 104-106.

[82] Ota H., Sato T., Suzuki H., Usami T., TPD-GC/MS analysis of the solid electrolyte interface (SEI) on a graphite anode in the propylene carbonate/ethylene sulfite electrolyte system for lithium batteries, *J. Power Sources*, **2001**, 97-98, 107-113.

[83] Yang C.R., Song J.Y., Wang Y.Y., Wan C.C., Impedance spectroscopic study for the initiation of passive film on carbon electrodes in lithium ion batteries, *J. Appl. Electrochem.*, **2000**, 30, 29-34.

[84] Ong T.S., Yang H., Symmetrical cell for electrochemical AC impedance studies of lithium intercalation into graphite, *Electrochem. Solid State Lett.*, **2001**, 4, A89-A92.

[85] Fransson L., Eriksson T., Edstrom K., Gustafsson T., Thomas J.O., Influence of carbon black and binder on Li-ion batteries, *J. Power Sources*, **2001**, 101, 1-9.

[86] Winter M., Wrodnigg G.H., Besenhard J.O., Biberacher W., Novak P., Dilatometric

investigations of graphite electrodes in nonaqueous lithium battery electrolytes, *J. Electrochem. Soc.*, **2000**, 147, 2427-2431.

[87] Zane D., Antonini A., Pasquali M., A morphological study of SEI film on graphite electrodes, *J. Power Sources*, **2001**, 97-98, 146-150.

[88] Naji A., Ghanbaja J., Willmann P., Billaud D., TEM characterization of the passivating layer formed during the reduction of graphite electrodes in selected electrolytes, *J. Power Sources*, **1999**, 81-82, 207-211.

[89] Jeong S.K., Inaba M., Abe T., Ogumi Z., Surface Film Formation on Graphite Negative Electrode in Lithium-Ion Batteries: AFM Study in an Ethylene Carbonate-Based Solution, *J. Electrochem. Soc.*, **2001**, 148, A989-A993.

[90] Hirasawa K.A., Nishioka K., Sato T., Yamaguchi S., Mori S., Investigation of graphite composite anode surfaces by atomic force microscopy and related techniques, *J. Power Sources*, **1997**, 69, 97-102.

[91] Jeong S.K., Inaba M., Iriyama Y., Abe T., Ogumi Z., Surface film formation on a graphite negative electrode in lithium-ion batteries: AFM study on the effects of co-solvents in ethylene carbonate-based solutions, *Electrochim. Acta*, **2002**, 47, 1975-1982.

[92] Inaba M., Kawatate Y., Funabiki A., Jeong S.-K., Abe T., Ogumi Z., STM study on graphite/electrolyte interface in lithium-ion batteries: solid electrolyte interface formation in trifluoropropylene carbonate solution, *Electrochim. Acta*, **1999**, 45, 99-105.

[93] Alliata D., Kötz R., Novák P., Siegenthaler H., Electrochemical SPM investigation of the solid electrolyte interphase film formed on HOPG electrodes, *Electrochem. Commun.*, **2000**, 2, 436-440.

[94] Gachot G., Grugeon S., Armand M., Pilard S., Guenot P., Tarascon J.-M., Laruelle S., Deciphering the multi-step degradation mechanisms of carbonate-based electrolyte in Li batteries, *J. Power Sources*, **2008**, 178, 409-421.

[95] Ogumi Z., Sano A., Inaba M., Abe T., Pyrolysis/gas chromatography/mass spectroscopy analysis of the surface film formed on graphite negative electrode, *J. Power Sources*, **2001**, 97-98, 156-158.

[96] Liaw B.Y., Kostecki R., In Situ Characterization of Lithium Ion Battery Materials, Electrodes, and Cells, *The Electrochemical Society Interface*, **Fall 2011**, 41-42.

[97] Delmas C., Peres J.P., Rougier A., Demourgues A., Weill F., Chadwick A., Broussely M., Perton F., Biensan P., Willmann P., On the behavior of the $LixNiO_2$ system: an electrochemical and structural overview, *J. Power Sources*, **1997**, 68, 120-125.

[98] Yoon W.-S., Lee K.-K., Kim K.-B., Structural and electrochemical properties of $LiAl_yCo_{1-y}O_2$ cathode for Li rechargeable batteries, *J. Electrochem. Soc.*, **2000**, 147, 2023-2028.

[99] Grey C.P., Dupre N., NMR studies of cathode materials for lithium-ion rechargeable batteries, *Chem. Rev.,* **2004**, 104, 4493-4512.

[100] Aldon L., Ionica C.M., Lippens P.E., Larcher D., Tarascon J.-M., Olivier-Fourcade J., Jumas J.-C., In situ ^{119}Sn Mössbauer spectroscopy used to study lithium insertion in c-Mg_2Sn, *Hyperfine Interact.*, **2006**, 167, 729-732.

[101] Jeong S.K., Inaba M., Mogi R., Iriyama Y., Abe T., Ogumi Z., Surface film formation on a graphite negative electrode in lithium-ion batteries: Atomic force microscopy study on the effects of film-forming additives in propylene carbonate solutions, *Langmuir*, **2001**, 17, 8281-8286.

[102] Orsinia F., Pasquier A., Beaudouin B., Tarascon J.-M., Trentin M., Langenhuizen N., Beer E., Notten P., In situ SEM study of the interfaces in plastic lithium cells, *J. Power Sources*, **1999**, 81-82, 918-921.

[103] Larcher D., Masquelier C., Bonnin D., Chabre Y., Mason V., Leriche J.B., Tarascon J.-M., Effect of Particle Size on Lithium Intercalation into α-Fe_2O_3, *J. Electrochem. Soc.*, **2003**, 150, A133-A139.

[104] Larcher D., Bonnin D., Cortes R., Rivals I., Personnaz L., Tarascon J.-M., Combined XRD, EXAFS, and Mössbauer Studies of the Reduction by Lithium of α-Fe_2O_3 with Various Particle Sizes, *J. Electrochem. Soc.*, **2003**, 150, A1643-A1650.

[105] Reddy M.V., Subba Rao G.V., Chowdari B.V.R., Metal Oxides and Oxysalts as Anode Materials for Li Ion Batteries, *Chem. Rev.*, **2013**, 113, 5364-5457.

[106] Wakihara M., Yamamoto O., (Eds.) Lithium Ion Batteries: Fundamentals and Performance, *Wiley VCH: Weinheim*, **2008**, p. 261.

[107] Aricò A.S., Bruce, P., Scrosati, B., Tarascon, J.-M., Schalkwijk Van W., Nanostructured materials for advanced energy conversion and storage devices, *Nat. Mater.*, **2005**, 4, 366-377.

[108] Armand M., Tarascon J.-M., Building better batteries, *Nature*, **2008**, 451, 652-657.

[109] Goodenough J.B., Park K.S., The Li-ion rechargeable battery: a perspective, *J. Am. Chem. Soc.*, **2013**, 135, 1167-1176.

[110] Guo Y.-G., Hu J.S., Wan L.J., Nanostructured Materials for Electrochemical Energy Conversion and Storage Devices, *Adv. Mater.*, **2008**, 20, 2878-2887.

[111] Li H., Wang Z.X., Chen L.Q., Huang X.J., Research on Advanced Materials for Li-ion Batteries, *Adv. Mater.*, **2009**, 21, 4593-4607.

[112] Cheng F.Y., Liang J., Tao Z.L., Chen J., Functional Materials for Rechargeable Batteries, *Adv. Mater.*, **2011**, 23, 1695-1715.

[113] Ji L.W., Lin Z., Alcoutlabi M., Zhang X.W., Recent developments in nanostructured anode materials for rechargeable lithium-ion batteries, *Energy Environ. Sci.*, **2011**, 4, 2682-2699.

[114] Jiang J., Li Y.Y., Liu J.P., Huang X.T., Yuan C.Z., Lou X.W., Recent Advances in Metal

Oxide-based Electrode Architecture Design for Electrochemical Energy Storage, *Adv. Mater.*, **2012**, 24, 5166-5180.

[115] Wang Z.Y., Zhou L., Lou X.W., Metal Oxide Hollow Nanostructures for Lithium-ion Batteries, *Adv. Mater.*, **2012**, 24, 1903-1911.

[116] Chen J.S., Archer L.A., Lou X.W., SnO_2 hollow structures and TiO_2 nanosheets for lithium-ion batteries, *J. Mater. Chem.*, **2011**, 21, 9912-9924.

[117] Chen J.S., Zhu T., Yang X.H., Yang H.G., Lou X.W., Top-down fabrication of α-Fe_2O_3 single-crystal nanodiscs and microparticles with tunable porosity for largely improved lithium storage properties, *J. Am. Chem. Soc.*, **2010**, 132, 13162-13164.

[118] Xu X., Cao R., Jeong S., Cho J., Spindle-like Mesoporous alpha-Fe_2O_3 Anode Material Prepared from MOF Template for High-Rate Lithium Batteries, *Nano Lett.*, **2012**, 12, 4988-4991.

[119] Hu X.L., Yu J.C., Continuous Aspect-Ratio Tuning and Fine Shape Control of Monodisperse α-Fe_2O_3 Nanocrystals by a Programmed Microwave-Hydrothermal Method, *Adv. Funct. Mater.*, **2008**, 18, 880-887.

[120] Liu H., Wexler D., Wang G.X., One-pot facile synthesis of iron oxide nanowires as high capacity anode materials for lithium ion batteries, *J. Alloys Compd.*, **2009**, 487, L24-L27.

[121] Chen J., Xu L.N., Li W.Y., Gou X.L., α-Fe_2O_3 Nanotubes in Gas Sensor and Lithium-Ion Battery Applications, *Adv. Mater.*, **2005**, 17, 582-586.

[122] Han Y., Wang Y.J., Li L., Wang Y.P., Jiao L.F., Yuan H.T., Liu S.X., Preparation and electrochemical performance of flower-like hematite for lithium-ion batteries, *Electrochim. Acta*, **2011**, 56, 3175-3181.

[123] Zhong L.S., Hu J.S., Liang H.P., Cao A.M., SongW.G., Wan L.J., Self-Assembled 3D Flowerlike Iron Oxide Nanostructures and Their Application in Water Treatment, *Adv. Mater.*, **2006**, 18, 2426-2431.

[124] Lei D.N., Zhang M., Qu B.H., Chen L.B., Wang Y.G., Zhang E.D., Xu Z., Li Q.H., Wang T.H., α-Fe_2O_3 nanowall arrays: hydrothermal preparation, growth mechanism and excellent rate performances for lithium ion batteries, *Nanoscale*, **2012**, 4, 3422-3426.

[125] Reddy M.V., Yu T., Sow C.H., Shen Z.X., Lim C.T., Rao G.V.S., Chowdari B.V.R., α-Fe_2O_3 Nanoflakes as an Anode Material for Li-Ion Batteries, *Adv. Funct. Mater.*, **2007**, 17, 2792-2799.

[126] Yu T., Zhu Y.W., Xu X.J., Yeong K.S., Shen Z.X., Chen P., Lim C.T., Thong J.T.L., Sow C.H., Substrate-Friendly Synthesis of Metal Oxide Nanostructures Using a Hotplate, *Small*, **2006**, 2, 80-84.

[127] Wang B., Chen J.S., Wu H.B., Wang Z.Y., Lou X.W., Quasiemulsion-Templated Formation of α-Fe_2O_3 Hollow Spheres with Enhanced Lithium Storage Properties, *J. Am. Chem. Soc.*, **2011**, 133, 17146-17148.

[128] Wang Z.Y., Luan D., Li C.M., Su F.B., Madhavi S., Boey F., Lou X.W., Engineering non-spherical hollow structures with complex interiors, *J. Am. Chem. Soc.*, **2010**, 132, 16271-16277.

[129] Zhang L., Wu H.B., Lou X.W., Metal-Organic-Frameworks-Derived General Formation of Hollow Structures with High Complexity, *J. Am. Chem. Soc.*, **2013**, 135, 10664-10672.

[130] Jeong J.-M., Choi B.G., Lee S.C., Lee K.G., Chang S.-J., Han Y.-K., Lee Y.B., Lee H.U., Kwon S., Lee G., Lee C.-S., Huh Y.S., Hierarchical Hollow Spheres of Fe_2O_3@Polyaniline for Lithium Ion Battery Anodes, *Adv. Mater.*, **2013**, 25, 6250-6255.

[131] Wu M.S., Ou Y.H., Lin Y.P., Electrodeposition of iron oxide nanorods on carbon nanofiber scaffolds as an anode material for lithium-ion batteries, *Electrochim. Acta*, **2010**, 55, 3240-3244.

[132] Sarradin J., Guessous A., Ribes M., Synthesis and characterization of lithium intercalation electrodes based on iron oxide thin films, *J. Power Sources*, **1996**, 62, 149-154.

[133] Hosono E., Fujihara S., Honma I., Ichihara M., Zhou H.S., Fabrication of Nano/Micro Hierarchical Fe_2O_3/Ni Micrometer-Wire Structure and Characteristics for High Rate Li Rechargeable Battery, *J. Electrochem. Soc.*, **2006**, 153, A1273-A1278.

[134] Wang L., Xu H.W., Chen P.C., Zhang D.W., Ding C.X., Chen C.H., Electrostatic spray deposition of porous Fe_2O_3 thin films as anode material with improved electrochemical performance for lithium-ion batteries, *J. Power Sources*, **2009**, 193, 846-850.

[135] Ortiz G.F., Hanzu I., Lavela P., Tirado J.L., Knauth P., Djenizian T., A novel architectured negative electrode based on titania nanotube and iron oxide nanowire composites for Li-ion microbatteries, *J. Mater. Chem.*, **2010**, 20, 4041-4046.

[136] Chen J., Recent Progress in Advanced Materials for Lithium Ion Batteries, *Materials*, **2013**, 6, 156-183.

[137] Ott B.J., Boerio-Gates J., Chemical Thermodynamics: Principles and Applications (1st Edition), *Academic Press*, **2000**, p.260.

[138] Ma J., Wang C., Wroblewski S., Kinetic characteristics of mixed conductive electrodes for lithium ion batteries, *J. Power Sources*, **2007**, 164, 849-856.

Chapter 2. Combined surface and electrochemical study of the lithiation/delithiation mechanism of iron oxide thin film anode for lithium-ion batteries

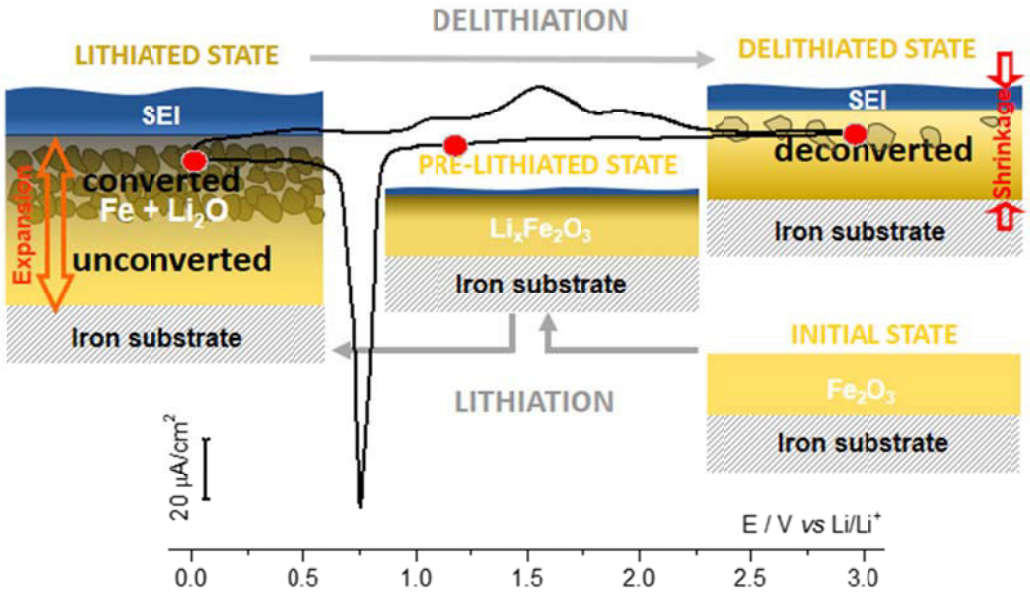

A version of this chapter has been published in *The Journal of Physical Chemistry C* (ACS Publications), 2013, 117, 21651-21661.

Some results of this chapter also contributed to *LiBD 2013*, June 16-21, 2013, Arcachon, France.

Abstract: Iron oxide (mostly α-Fe_2O_3) model thin film electrodes were prepared by thermal oxidation of pure metal iron substrates at $300 \pm 5\ ^{o}C$ in air, and used for comprehensive investigation of the lithiation/delithiation mechanisms of anode material undergoing electrochemical conversion reaction with lithium ions. Surface (X-ray Photoelectron Spectroscopy (XPS) and Time-of-Flight Secondary Ion Mass Spectrometry (ToF-SIMS)) and electrochemical (Cyclic Voltammetry (CV) and Electrochemical Impedance Spectroscopy (EIS)) analytical techniques were combined. The results show that intercalation of Li in the Fe_2O_3 matrix and Solid Electrolyte Interphase (SEI) layer formation both precede conversion to metallic iron and Li_2O upon lithiation. Depth profile analysis evidences stratification of the converted thin film electrode into fully and partially lithiated outer and inner parts, respectively, due to mass transport limitation. The SEI layer has a stable composition (Li_2CO_3 with minor $ROCO_2Li$) but dynamically increases/decreases in thickness upon lithiation/delithiation. Conversion, proceeding mostly in the outer part of the electrode, causes material swelling accompanied by SEI layer thickening. Upon delithiation, lithium is trapped in the deconverted electrode subjected to shrinking and the SEI layer mostly decomposes and reduces in thickness after deconversion. The non-reversibility of both conversion and surface passivation mechanisms is demonstrated.

Keywords: Fe_2O_3 anode material; conversion mechanism; SEI layer; XPS; ToF-SIMS

1. Introduction

Lithium-ion batteries (LiBs) are widely used for portable electronic devices and have become the most competitive candidate for electric vehicles due to numerous advantages, such as light weight and high energy and power density. Graphite, the currently used commercial anode material, has a limited theoretical specific capacity (372 mAh g^{-1}) and presents safety issues. Much effort is made to develop new types of anode materials such as transition metal oxides (e.g. CoO, Co_3O_4, NiO, CuO, Cu_2O, FeO, Fe_2O_3, Fe_3O_4, Cr_2O_3),[1-4] lithium-based alloys (e.g. Li-Si, Li-Sn)[6-13] or other metal binary alloys (e.g. Si-based and Sn-based intermetallics)[14-18] that present high interest due to high theoretical capacities and improved safety.

Iron oxides (including FeO, Fe_2O_3, Fe_3O_4) have attracted much interest.[1,4,19-21] Among them, α-Fe_2O_3 (hematite) and spinel Fe_3O_4 (magnetite) are much promising as anode materials owing to their high capacity, environment friendliness, abundance and low cost.[4,22] However, they are not used in commercial LiBs due to capacity fading upon cycling, high operating potentials and poor lithiation/delithiation kinetics. These limitations are all related to the unique lithium storage mechanism, the so-called "conversion reaction", by which formation of amorphous lithium oxide (Li_2O) and iron metal occurs.[1]

In recent years, efforts have been made to improve the electrochemical properties of iron oxides as anode material. However, in these studies, iron oxides were widely investigated as powder and/or nanostructured materials for the purpose of improving electrochemical performance.[4,22, 23] Only few studies focused on the preparation and electrochemical performance of thin film electrode without any conducting additives and binder[23,24] and, to our knowledge, no study used the thin film approach to address the conversion mechanism and the formation of the Solid Electrolyte Interphase (SEI) layer in details. Thin film electrodes without conducting additives and binder are more suitable for fundamental studies of energy storage mechanisms and interfacial modifications than powder electrodes since better suited for the application of surface and interface analytical methods.

Here we report on iron oxide thin film electrodes prepared *via* simple thermal oxidation of iron metal substrate used as current collector with the objective to investigate thoroughly the conversion mechanism and the SEI-induced surface passivation. Surface and depth profile

analysis of the lithiated and delithiated thin film electrodes was performed with X-Ray Photoelectron Spectroscopy (XPS) and Time-of-Flight Secondary Ion Mass Spectrometry (ToF-SIMS). Cyclic Voltammetry (CV) in a half cell with 1 M $LiClO_4$-PC as electrolyte was used to control the electrochemical lithiation/delithiation process and Electrochemical Impedance Spectroscopy (EIS) was applied to characterize the charge transfer process. Formation and stability of the SEI layer and conversion/deconversion mechanism are discussed for the first cycle of lithiation/delithiation of iron oxide used as anode material for LiBs, with some preliminary electrochemical studies of the cycling performance of the iron oxide thin film electrode. More detailed analyses on the cycling-induced modifications of the electrode and its passivation film as well as the aging mechanisms will be discussed in Chapter 3.

2. Experimental section

2.1 Preparation of iron oxide thin films

Pure (99.99 wt%) iron plates (1 mm thick) were purchased from Goodfellow and then cut into square (8×8 mm^2) substrate samples. The surfaces were prepared by mechanical polishing with diamond spray down to 1/4 μm and then rinsed in ultrasonic baths of acetone, ethanol and Millipore© water (resistivity > 18 MΩ cm) for 2 min and dried in a flow of compressed air.

Iron oxide thin films were prepared by thermal oxidation in air. The samples were placed in a quartz tube that could be inserted in a cylindrical oven set in temperature at 300°C ± 5 °C. The samples were placed in the pre-thermalized oven for 5 min and then the quartz tube was quenched with 0°C water for cooling. The average thickness of the pristine oxide thin films was 85 - 95 nm as estimated from XPS depth profile analysis. Raman spectroscopy (Horiba Xplora system, Ar^+ laser, λ = 532 nm) was employed for phase identification of the thermal oxide.

2.2 Electrochemical measurements

All electrochemical measurements (CV and EIS) were performed in an Ar-filled glovebox (Jacomex) with H_2O and O_2 contents lower than 1 ppm. A home-made

three-electrode glass cell (see Appendix 1) similar to typical commercial cells was used with the iron oxide thin film (prepared as described above) as working electrode and two Li foils (Sigma-Aldrich) used as reference and counter electrodes (~2 cm^2). The surface of the counter or reference electrode was around 2 cm^2. All potentials hereafter are given versus Li/Li^+. The cell was operated at room temperature using an Autolab (AUT30) electrochemical workstation. The geometrical working electrode area was delimited to 0.28 cm^2 by a O-ring. The electrolyte was 1 M $LiClO_4$ in propylene carbonate (1 M $LiClO_4$-PC, Sigma-Aldrich). Cyclic voltammograms were recorded in the potential range 0.01 - 3.0 V at a scanning rate of 0.2 mV s^{-1}, starting form OCP (~3.0 V) into the cathodic direction. For EIS measurements, the frequency range was 10 mHz to 1 MHz and the potential perturbation was 5 mV. The cell was kept at selected potential value for more than 30 min before performing EIS and the equilibrium of the cells was deemed to be reached when the change of voltage was less than 0.01 V in 10 min.

For surface and depth profile analysis the thin films were electrochemically treated at various stages of the first cycle. After scanning the potential to the selected value, the cell was disassembled and the samples were rinsed with acetonitrile (99.8%, Sigma-Aldrich) and dried with Ar flow. The samples were then transferred directly from the glovebox to the ultra-high vacuum XPS analysis chamber.[25] Thereafter, they were transferred in an air-tight vessel under argon atmosphere from the XPS to the ToF-SIMS system.

2.3 X-ray photoelectron spectroscopy (XPS)

XPS analysis was carried out on a VG ESCALAB 250 spectrometer with a UHV preparation chamber directly connected to the glovebox. Base pressure during analysis was 10^{-9} mbar. An Al Kα monochromatized radiation (hv = 1486.6 eV) was employed as X-ray source. Take-off angle of the photoelectrons was 90^o. Survey spectra were recorded with a pass energy of 100 eV at a step size of 1 eV and high resolution spectra of the Fe2p, O1s, C1s core level and valence band (VB) regions were recorded with a pass energy of 20 eV at a step size of 0.1 eV. The data processing (curve fitting) was performed using the Avantage software provided by Thermo Electron Corporation. An iterative Shirley-type background and Lorentzian/Gaussian peak shape at a fixed ratio of 30/70 were used. Binding energies

were calibrated by setting the C1s hydrocarbon (-CH_2-CH_2-) component peak at 285.0 eV. XPS depth profiling was performed by combining analysis with Ar^+ sputtering performed in the preparation chamber. A 2 keV Ar^+ sputter beam giving 0.2 μA mm^{-2} of sample current yielded a calibrated etching rate of about 2.5 nm min^{-1}. The depth profiles were stopped after etching about 150 nm.

2.4 Time-of-flight secondary ion mass spectrometry (ToF-SIMS)

Depth profiling was also performed using a ToF-SIMS 5 spectrometer (Ion Tof - Munster, Germany). The operating pressure of the spectrometer was about 10^{-9} mbar. A pulsed 25 keV Bi^+ primary ion source was employed for analysis, delivering 1.2 pA current over a 100 × 100 μm^2 area. Depth profiling was carried out using a 1 keV Cs^+ sputter beam giving a 70 nA target current over a 300 × 300 μm^2 area. Ion-Spec software was used for acquiring and processing the data. Negative ion depth profiles were recorded for better sensitivity to fragments originating from oxide matrices.

3. Results and discussion

3.1 Raman phase identification

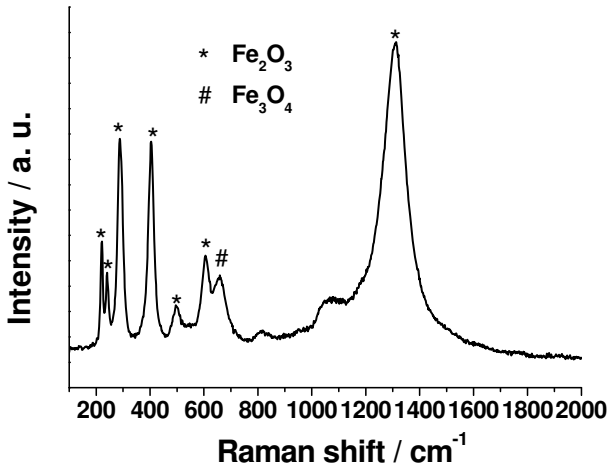

Figure 1 Raman spectra of iron oxide thin film grown by thermal oxidation of pure iron metal at 300 ± 5 °C in air.

Figure 1 displays the Raman spectrum of the as prepared thermal iron oxide thin film. There are several peaks in the range of 100 - 2000 cm^{-1}. Based on reference

compounds,[23,26-28] the spectrum is indicative of a crystalline thin film consisting mostly of the thermodynamically stable α-Fe_2O_3 (hematite) phase together with Fe_3O_4 (magnetite) in small amount. The peaks located at 222, 241, 287, 404, 495, 606 and 1313 cm^{-1} all correspond to the α-Fe_2O_3 phase. They are assigned to two A_{1g} modes (at 222 and 495 cm^{-1}) and five E_g modes (at 241, 287, shoulder near 287, 404 and 606 cm^{-1}). The intense peak at 1313 cm^{-1} is assigned to two-magnon scattering which arises from the interaction of antiparallel close spin sites.[28] The peak at 659 cm^{-1} can be assigned to an A_{1g} mode of Fe_3O_4 (magnetite). The relative intensities of the peaks at 241, 404 and 1313 cm^{-1} are much higher than reported in the literature for reference compounds,[23,28,29] which is indicative of the presence of α-FeOOH (goethite) also supported by the XPS data presented below.

3.2 Electrochemical properties of iron oxide by cyclic voltammetry and electrochemical Impedance spectroscopy

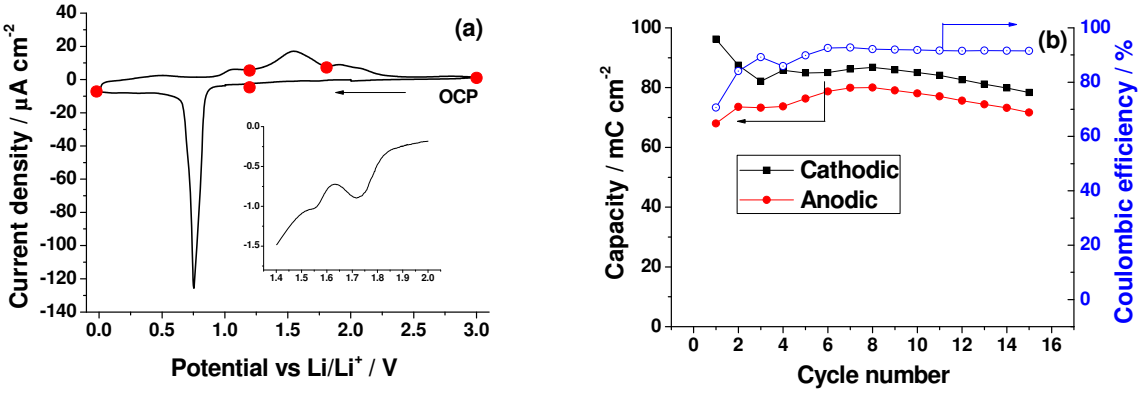

Figure 2 (a) Cyclic voltammogram (CV) of 1st lithiation/delithiation of iron oxide thin film electrode in 1 M $LiClO_4$-PC in 0.01-3.0 V potential range (scan rate of 0.2 mV s^{-1}). The inset shows the magnified cathodic peak at 1.7 V. Points on the curves indicate the selected potentials for XPS, ToF-SIMS and EIS analysis. (b) Anodic and cathodic charge and columbic efficiency calculated from the 15 cycles performed by cycling voltammetry.

Figure 2 (a) shows the CV corresponding to the 1st lithiation/delithiation cycle of the iron oxide thin film electrode. Only visible in the inset, the CV shows a small cathodic peak at about 1.7 V followed by moderate cathodic current increase until 1 V. This small cathodic peak followed by increased cathodic current has been assigned to the process of Li intercalation into the Fe_2O_3 matrix to form $Li_xFe_2O_3$ ($0<x\leq2$), as shown by *in situ* X-Ray Diffraction.[21] The sharp and intense cathodic peak located at 0.75 V corresponds to the

process of electrochemical reduction of lithium with iron oxide (mainly α-Fe_2O_3), as described by Equation (1):[19-21,30-33]

$$Fe_2O_3 + 6Li^+ + 6e^- \rightarrow 3Li_2O + 2Fe \quad (1)$$

This cathodic peak has also been assigned to the electrochemical formation of the SEI layer by reductive decomposition of the electrolyte on the surface of other conversion-type electrode material such as Cr_2O_3, on which the reaction is expected to be similar to that on Fe_2O_3. The reaction is described by Equation (2):[5]

$$C_4H_6O_3(PC) + 2Li^+ + 2e^- \rightarrow Li_2CO_3 + CH_3CH=CH_2 \quad (2)$$

In the anodic scan, there is a broad peak centered at 1.55 V, which is related to the deconversion process of Li_2O with metallic iron (Fe^0) and can be described by Equation (3):

$$3Li_2O + 2Fe \rightarrow Fe_2O_3 + 6Li^+ + 6e^- \quad (3)$$

The coulombic efficiency calculated from the ratio of integral of anodic to cathodic is only 71 %, which can be assigned to incomplete reversible deconversion and some charge irreversibly consumed to form the SEI layer.

The potential values at different stages of lithiation (cathodic) and delithiation (anodic) process for EIS, XPS and ToF-SIMS analyses are marked on the CV: 1.2 V (before cathodic peak), 0.01 V (at cathodic vertex potential), and 1.2 V (before anodic peak), 1.8 V (after anodic peak), and 3.0 V (at anodic vertex potential).

Figure 2 (b) shows the cycling performance of the iron oxide thin film electrode calculated from integral of the cathodic and anodic processes of CV results during 15 cycles. The cathodic capacity (96.2 mC cm^{-2}) is much higher than anodic capacity (68.0 mC cm^{-2}) in the first CV cycle, which presents a high initial irreversible capacity related to electrolyte decomposition and formation of the SEI layer as discussed before. The reversible capacity for the cathodic process is slightly decreasing with the cycle number to reach ~82 % of the first cycle at 15th cycle. A low columbic efficiency (~70%) observed in the beginning of cycling, stabilize at higher cycling number and attains 92% in the end of cycling. More detailed studies concerning the cycling performance of thin film iron oxide electrode and its morphological and chemical modifications induced by electrochemical lithiation/delithiation process will be discussed in Chapter 3.

As widely discussed in EIS studies of intercalation/deintercalation-type materials,[34-37] a semi-circle in the high frequency spectral region relates to charge transfer resistance and a straight line at 45° against real axis in the low frequency range corresponds to a Warburg impedance, which is valid in the semi-infinite diffusion conditions.[38] However, for conversion-type Fe_2O_3, a phase change characterizes the lithiation/delithiation process.[21,23] So it seems that some impedance parameters (such as Warburg impedance describing solid-state diffusion of Li^+ in α-Fe_2O_3) may not be as meaningful as for intercalation/deintercalation-type materials because of this phase change.

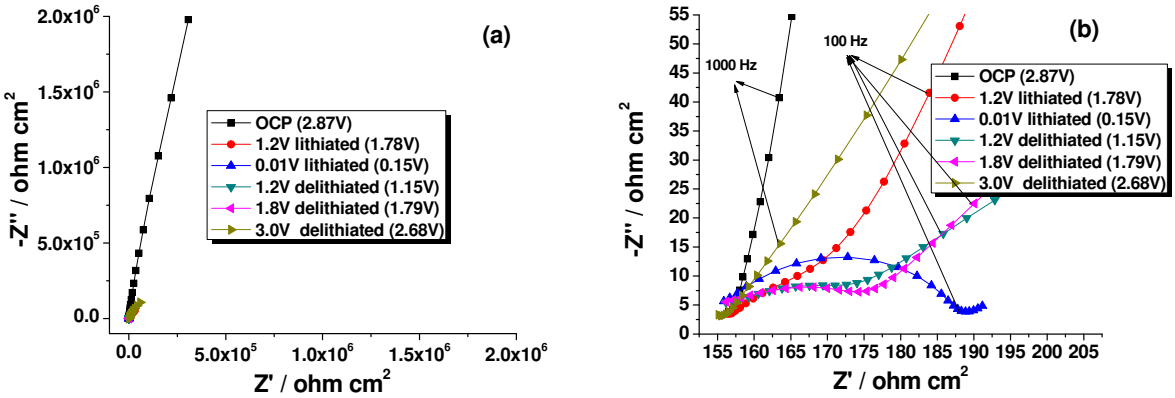

Figure 3 (a) EIS (Nyquist plots) spectra of iron oxide thin film electrode at selected potentials in 1st lithiation/delithiation cycle in 1 M $LiClO_4$-PC; (b) Magnified high frequency region of spectra in (a). Potentials given in brackets are equilibrium values reached at each stage.

Figure 3 shows the electrochemical impedance spectra (Nyquist plots) of the electrode at the various selected stages of the first lithiation/delithiation cycle. The potential values in parenthesis are the equilibrium values reached before the EIS measurement for relaxed cells. The high electrolyte resistance (~156 Ω cm^2) observed for all analysed samples is due to the geometrical configuration of the 3-electrode cell (i.e. large distance between working, reference and counter electrodes) and not a poor electrolyte conductivity which is a classical known electrolyte used in LiB. For the pristine sample (at OCP) the EIS shows an almost straight line without any obvious semi-circle in the high frequency region, implying that the system represents only a bulk solution resistance before any lithiation occurs.[39] Moreover, the slope of the line is the highest at this stage, which is probably due to finite diffusion in the limited thickness of the unmodified thin film electrode.

With lithiation, a depressed semi-circle appears at high frequency. The presence of one-semicircle was also observed in several previous studies performed on the iron oxide electrode. [23,32,40-42] The varying diameter of the depressed semi-circle indicates a gradual increase of a charge transfer resistance from ~14 $\Omega\,cm^2$ in the lithiated state at 1.2 V to ~32 $\Omega\,cm^2$ in the completely lithiated state at 0.01 V. It is conjectured that this increase is related to the growth of the SEI layer on the thin film electrode, as previously reported.[43] If so, the present data indicates that growth of the SEI layer would be initiated already at 1.2 V before conversion of the electrode, which is confirmed by the XPS data presented below. In the lithiated state at 1.2 V, the straight line with 45^o angle at low frequency indicates semi-infinite diffusion in the not yet converted thin film electrode. At 0.01 V, the depressed semi-circle in the whole frequency range corresponds to the SEI layer dominating the impedance response.

With delithiation, the impedance spectra markedly change. The decreasing depressed semi-circles at high frequency are attributed to decomposition of the SEI layer and the straight lines at low frequency are indicative of diffusion in the deconverting thin film electrode. At 1.2 V (delithiation state), the charge transfer resistance is about ~250 $\Omega\,cm^{-2}$, close to the maximum value, indicating some partial decomposition of the SEI layer already before deconversion of the thin film electrode. No further decomposition is observed at 1.8 V after deconversion, suggesting stability of the SEI layer during the main deconversion reaction. It is only at 3.0 V that the semi-circle nearly vanishes, indicating further but not complete decomposition of the SEI layer at this stage. At low frequency, only a slightly higher slope is observed at 1.8 V after deconversion, suggesting that the reaction may not be fully reversible at this stage. At 3.0 V, the slope markedly increases but remains lower than for the pristine sample indicating that the electrochemically-induced modifications of the electrode are not fully reversible.

3.3 Modification of iron oxide thin film upon the first lithiation/delithiation shown by XPS

The XP C1s, O1s, Fe2p, Fe3p-Li1s core levels and VB region spectra for the pristine iron oxide thin film and samples treated at the selected potentials are shown in Figure 4.

Binding energies (E_B), full widths at half-maximum (fwhm) and relative intensity of the component peaks obtained by peak fitting are given in Table 1.

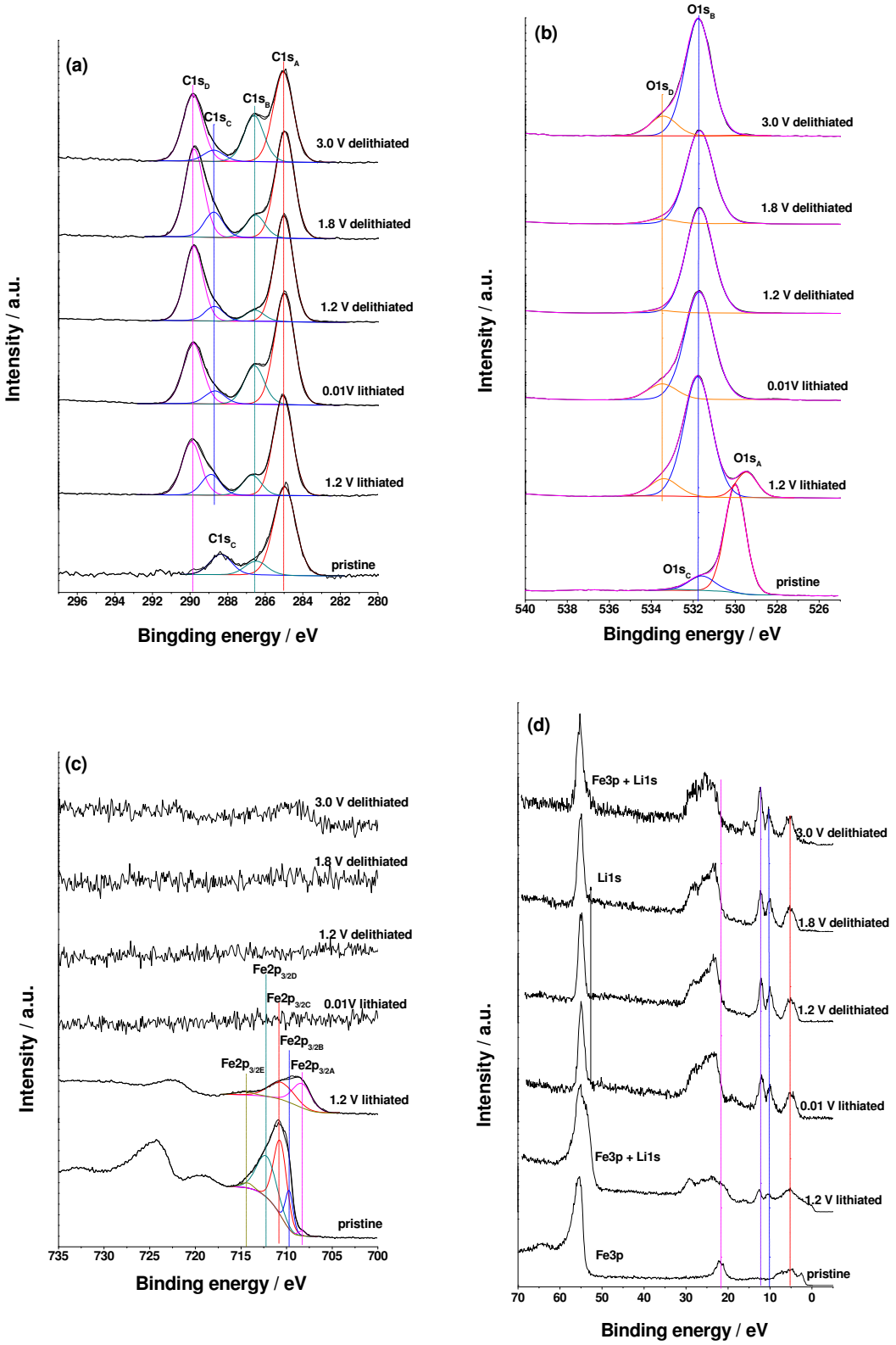

Figure 4 XP (a) C1s, (b) O1s, (c) Fe2p core levels and (d) Fe3p-Li1s core levels and VB region spectra for the pristine iron oxide thin film and samples treated at selected potentials in the 1st lithiation/delithiation cycle in 1 M $LiClO_4$-PC.

Table 1 Binding energies (E_B), full widths at half-maximum (fwhm) and relative intensity of the XPS component peaks obtained by peak fitting for the samples lithiated/delithiated to different potentials.

	pristine			1.2 V lithiated			0.01 V lithiated			1.2 V delithiated			1.8 V delithiated			3.0 V delithiated		
	E_B (eV)	fwhm (eV)	Area Ratio	E_B (eV)	fwhm (eV)	Area Ratio	E_B (eV)	fwhm (eV)	Area Ratio	E_B (eV)	fwhm (eV)	Area Ratio	E_B (eV)	fwhm (eV)	Area Ratio	E_B (eV)	fwhm (eV)	Area Ratio
$C1s_A$	285.0	1.41	1.00	285.0	1.24	1.00	285.0	1.29	1.00	285.0	1.20	1.00	285.0	1.23	1.00	285.0	1.29	1.00
$C1s_B$	286.5	1.41	0.15	286.7	1.24	0.20	286.6	1.29	0.35	286.6	1.20	0.11	286.5	1.23	0.21	286.6	1.29	0.51
$C1s_C$	288.4	1.41	0.23	288.9	1.24	0.21	288.7	1.29	0.12	288.7	1.20	0.14	288.7	1.23	0.24	288.7	1.29	0.12
$C1s_D$				289.9	1.24	0.53	289.9	1.29	0.55	289.8	1.20	0.71	289.8	1.23	0.82	289.8	1.29	0.74
$O1s_A$	530.0	1.21	1.00	529.5	1.23	0.16										529.5	1.54	0.01
$O1s_B$	531.6	1.51	0.17	531.8	1.63	1.00	531.7	1.70	1.00	531.7	1.61	1.00	531.7	1.61	1.00	531.8	1.54	1.00
$O1s_C$	532.8	1.51	0.01															
$O1s_D$				533.4	1.63	0.14	533.5	1.70	0.15	533.6	1.61	0.02	533.6	1.61	0.05	533.4	1.54	0.17
$Fe2p_{3/2A}$	708.3	0.96	0.04	708.3	2.51	1.00												
$Fe2p_{3/2B}$	709.7	1.02	0.30															
$Fe2p_{3/2C}$	710.7	1.77	1.00	710.6	3.36	0.95												
$Fe2p_{3/2D}$	712.2	2.63	0.82															
$Fe2p_{3/2E}$	714.3	1.56	0.06	714.5	2.50	0.12												

For the pristine sample, the C1s signal is indicative of the carbonaceous contamination routinely observed on oxide surfaces. It is decomposed into one major component at 285.0 eV ($C1s_A$) assigned to -CH_2-CH_2- bonds and two minor components at 286.5 eV ($C1s_B$) and 288.4 eV ($C1s_C$) assigned to C-O bonds and O=C (carbonyl) and/or O=C-O (carboxyl) bonds, respectively.[5,44,45]

The major oxygen component peak at E_B ($O1s_A$) = 530.0 eV is attributed to Fe-O bonds in the iron oxide matrix. The minor component at E_B ($O1s_B$) = 531.6 eV can be ascribed to surface contamination (C=O bonds and/or O=C-O bonds).[44,45] This component can also correspond to hydroxyl groups.[46] These species would originate from iron oxyhydroxide (FeOOH) which presence is also confirmed by the Fe2p core level. A third component at E_B ($O1s_C$) = 532.8 eV, corresponding to water molecules,[5] is barely observed on the pristine film.

The Fe2p spectrum shows the 3/2-1/2 spin orbit doublet. Only the $Fe2p_{3/2}$ core level peak was fitted for simplicity. It displays five components. The two adjacent peaks ($Fe2p_{3/2B}$ and $Fe2p_{3/2C}$) with a binding energy separation of 1 eV observed at 709.7 and 710.7 eV are assigned to Fe(III) in an oxide matrix (Fe_2O_3 and/or Fe_3O_4).[46-48] The peak at 708.3 eV ($Fe2p_{3/2A}$) is assigned to Fe(II) in an oxide matrix (in agreement with the Raman spectrum showing the minor presence of Fe_3O_4) and that at 712.2 eV ($Fe2p_{3/2D}$) is assigned to Fe(III) in an oxyhydroxide matrix (FeOOH). The minor component at 714.3 eV ($Fe2p_{3/2E}$) is attributed to a Fe(II)$2p_{3/2}$ satellite.[48] Thus, the $Fe2p_{3/2}$ core level is consistent with the predominance of α-Fe_2O_3 in the thermally grown oxide film and some presence of Fe(II) oxide (Fe_3O_4) and Fe(III) oxyhydroxide (FeOOH) as concluded from the Raman data. The low intensity of the Fe(II) oxide component can result from the preferential formation of Fe_3O_4 in the inner part of the film, as supported by ToF-SIMS depth profile analysis. The larger intensity of the Fe(III) oxyhydroxide component is consistent with this species concentrated at the oxide thin film surface and resulting from reaction with water vapor.

After lithiation to 1.2 V, one new $C1s_D$ component is observed at 289.9 eV and assigned to Li_2CO_3 and/or $ROCO_2Li$.[5,44,45] It indicates, in agreement with the EIS data,

that the formation of the SEI layer occurs already at this potential although it is mainly expected to be formed at about 0.75 V. The $O1s_A$ component is shifted to 529.5 eV indicating modification of the oxide matrix, possibly by intercalation of lithium as previously concluded from XRD data.[20,21] Its attenuation is consistent with growth of the SEI layer. The $O1s_B$ peak, assigned to carbonates, markedly increases in relative intensity showing SEI layer growth. Its intensity is about 7 times that of the $O1s_D$ peak at 533.4 eV assigned to Li-alkyl carbonates. This indicates that Li_2CO_3 and $ROCO_2Li$ are the major and minor components of the SEI layer, respectively, already at this initial stage of lithiation.

In the $Fe2p_{3/2}$ spectrum, the Fe(III)OOH component ($Fe2p_{3/2D}$) has vanished and the Fe(III) oxide component ($Fe2p_{3/2C}$) and Fe(II) oxide component ($Fe2p_{3/2A}$) have respectively decreased and increased in intensity. This is consistent with the formation of $Li_xFe_2O_3$ ($0<x\leq2$) previously observed at this potential.[21,22] The formation of Fe(II) is confirmed by the enlargement at lower binding energy of the Fe3p-Li1s peak between 50 to 60 eV. Thus, both the CV data and the XP O1s, Fe2p and Fe3p-Li1s spectra are consistent with the intercalation of lithium in the iron oxide matrix at 1.2 V. According to Larcher's work on Fe_2O_3 nanoparticles, there is less than 2 mol Li per Fe_2O_3 intercalated into the electrode at this stage.[19] Here, $Li_{1.03}Fe_2O_3$ is deduced from the relative intensity of the two iron components (Fe(II)/Fe(III) = 1.00/0.95), a value consistent with Li intercalation in the Fe_2O_3 thin film matrix.

After lithiation to 0.01 V, the Fe2p intensity is completely attenuated by the growth of the SEI layer, like observed for other anode materials in the lithiated state.[5,17,49] Consistently, full attenuation of the $O1s_A$ component and Fe3p peak is also observed (only a sharp Li1s peak is observed at about 55 eV). The SEI layer can be estimated to be at least 10 nm thick. The XP C1s and O1s core levels show no major change of the SEI layer composition, still dominated by the presence of Li_2CO_3 and with $ROCO_2Li$ as minor constituent. In the VB region, different features can be distinguished. The composite peak between 20-30 eV can be assign to O2s band. For the pristine sample, a much narrow peak at ~21-22 eV can be attributed to O2s from

the iron oxide. Similarly the composite peak between 3-8 eV observed on the pristine sample corresponds to O2p band from iron oxide. For the sample lithiated at 1.2 V, these peaks are overlapped with peaks that can be assigned to carbonate anion molecular orbitals (MO). After lithiation to 0.01 V, the composite peaks at 20-30 eV and 3-8 eV correspond entirely to MOs of carbonate. New peaks at ~10.0 and ~13.0 eV are representative of C-O bond in Li_2CO_3.[50,51] The presence of Li_2CO_3 is thus confirmed to be the major component of the SEI layer like observed on other anode materials in the lithiated state.[5,11,17,18]

After delithiation at 1.2 and 1.8 V, the XP Fe2p and Fe3p core levels are still fully attenuated by the SEI layer, which precludes any discussion of the deconversion mechanism. Only after delithiation at 3.0 V, some signal arise in the Fe2p region, confirming further decomposition of the SEI layer in this later stage of the delithiation process. Consistently, the Fe3p-Li1s peak is lightly enlarged at higher binding energy. This phenomenon has also been reported for carbon materials[52] and rutile TiO_2.[49] The C1s and O1s spectra show that no additional species appears in the SEI layer during the delithiation process. Only the relative intensities of the component peaks slightly vary, indicating small variations in the proportions of the constituents. The VB region remains quite similar to that observed in the lithiated state at 0.01 V. Thus, XPS is consistent with the EIS data showing that only partial decomposition of the SEI layer occurs upon delithiation until 3.0 V. In addition, it shows that the SEI layer composition remains dominated by Li_2CO_3 during the whole lithiation/delithiation process. The dominant components of the SEI layer can vary as a function of salt (i.e. $LiPF_6$) and solvent (mixture of carbonates) used in electrolytes.[53]

3.4 XPS depth profile analysis of sample lithiated at 0.01 V

Figure 5 presents the XP C1s, O1s, Fe2p and Fe3p-Li1s core levels and VB region spectra of the sample lithiated to 0.01 V for increasing Ar^+ sputtering time. The E_B and fwhm values and relative intensities of the component peaks are compiled in Table 2.

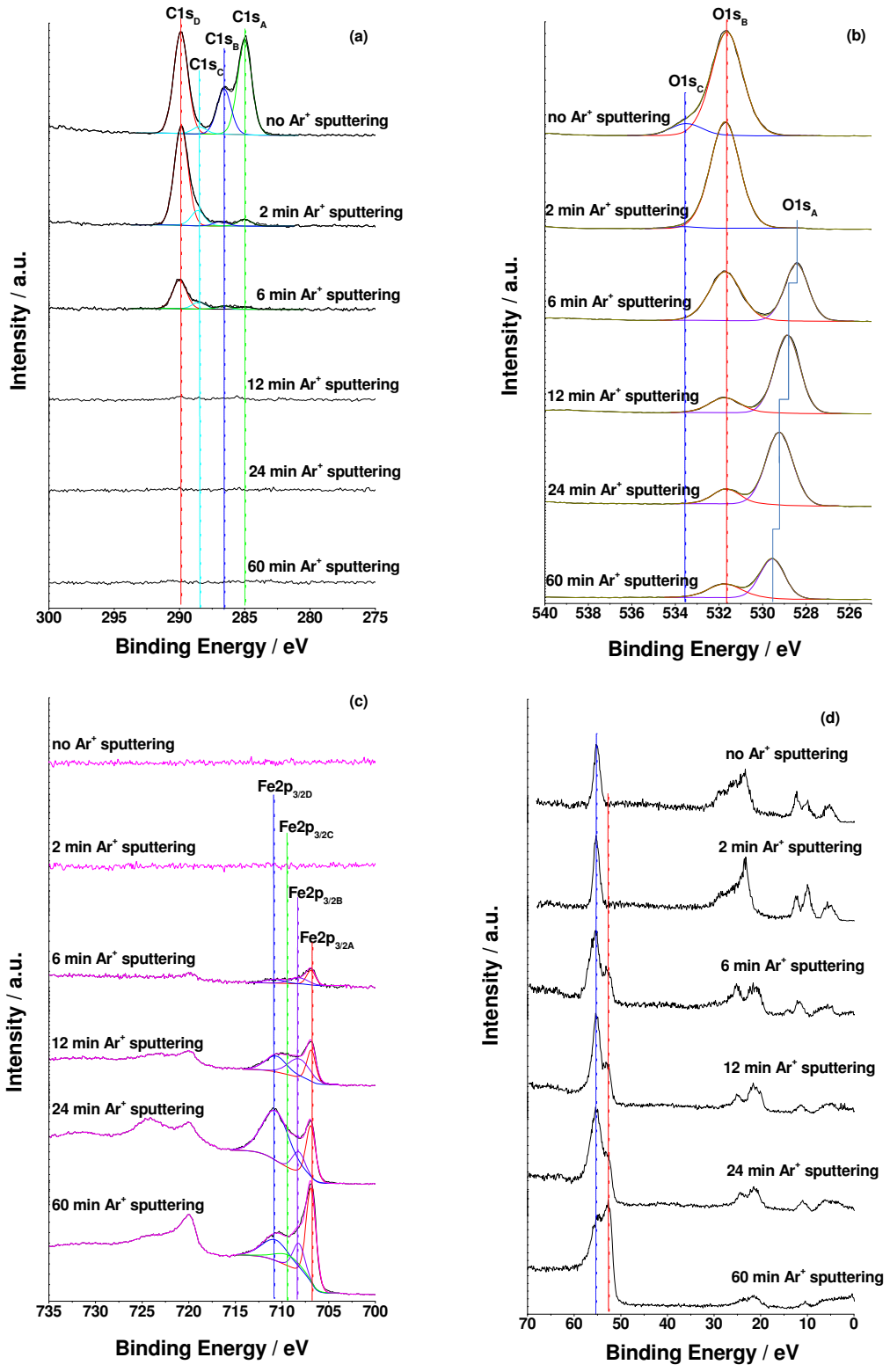

Figure 5 XP (a) C1s, (b) O1s, (c) Fe2p core levels and (d) Fe3p-Li1s core levels and VB region spectra of the sample lithiated to 0.01 V for increasing Ar^+ sputtering time.

Table 2 Binding energies (E_B), full widths at half-maximum (fwhm) and relative intensity of the XPS component peaks obtained by peak fitting for the sample lithiated to 0.01 V as function of depth sputtering time.

	0.01 V lithiated			2 min V sputtering			6 min V sputtering			12 min V sputtering			24 min V sputtering			60 min V sputtering		
	E_B (eV)	fwhm (eV)	Area Ratio	E_B (eV)	fwhm (eV)	Area Ratio	E_B (eV)	fwhm (eV)	Area Ratio	E_B (eV)	fwhm (eV)	Area Ratio	E_B (eV)	fwhm (eV)	Area Ratio	E_B (eV)	fwhm (eV)	Area Ratio
C $1s_A$	285.0	1.31	0.94	285.0	1.28	0.07	285.0	1.27	0.09									
C $1s_B$	286.6	1.31	0.44	286.8	1.28	0.05	286.6	1.27	0.11									
C $1s_C$	288.5	1.31	0.07	288.6	1.28	0.16	288.5	1.27	0.24									
C $1s_D$	289.9	1.31	1.00	290.0	1.28	1.00	290.0	1.27	1.00									
O $1s_A$							528.4	1.33	0.87	528.9	1.40	1.00	529.2	1.51	1.00	529.6	1.38	1.00
O $1s_B$	531.6	1.76	1.00	531.7	1.65	1.00	531.7	1.79	1.00	531.7	1.74	0.24	531.7	1.53	0.21	531.7	1.88	0.47
O $1s_C$	533.5	1.76	0.12	533.7	1.65	0.02												
Fe $2p_A$							706.9	1.16	1.00	706.9	1.19	0.73	706.9	1.23	0.38	706.9	1.28	1.00
Fe $2p_B$							708.2	2.35	0.85	708.3	2.93	1.00	708.2	1.65	0.19	708.2	1.53	0.35
Fe $2p_C$																709.4	3.35	0.30
Fe $2p_D$							710.8	2.35	0.54	710.7	2.93	0.87	710.7	3.50	1.00	710.7	3.47	0.59

As discussed above, C1s and O1s spectra before sputtering are indicative of the composition (Li_2CO_3 and $ROCO_2Li$) of the SEI layer formed at the surface of the electrode. The photoelectrons emitted by the converted electrode are fully attenuated by the SEI surface layer and, as a consequence, the Fe3p-Li1s core level and VB (3-30 eV) spectra are characteristic of the SEI layer (no Fe3p component).

After 2 min Ar^+ sputtering (about 5 nm etched), the $C1s_A$ component markedly decreases in intensity, indicating removal of the outer part of the surface carbonaceous layer mostly consisting of hydrocarbons. The decrease of the relative intensity of the $O1s_C$ component indicates that $ROCO_2Li$ species are also preferentially removed. Complete attenuation of the Fe2p intensity is still observed indicating that profiling is still in the bulk SEI layer region. Consistently, the Fe3p-Li1s core level and VB (3-30 eV) spectra are still those of the SEI layer with slight changes in the relative intensities of the VB caused by removal of the outermost hydrocarbons.

After 6 min Ar^+ sputtering, a metallic iron Fe(0) component at 706.9 eV along with lower intensity Fe(II) and Fe(III) oxide components at 708.2 eV and 710.8 eV, respectively, and an oxide $O1s_A$ component at 528.4 eV are detected. Consistently, a Fe3p contribution is observed at lower binding energy in the Fe3p-Li1s core level spectrum and the VB spectrum region is changed. The principal modifications of VB spectrum are the appearance of a new component at ~21 eV attributed to O2s from the iron oxide as discussed above, and the disappearance of a component at ~10 eV attributed to carbonate anion MO. At the same time, the intensity of the $C1s_D$ component at 290.0 eV has markedly decreased and that of the $C1s_A$ component at 285.0 eV almost disappeared. This means that most of the SEI layer and almost all surface hydrocarbons were removed. According to the Ar^+ sputtering rate, about 15 nm of material were sputtered, which gives an approximation of the thickness of the SEI layer formed on the electrode surface lithiated at 0.01 V in $LiClO_4$-PC. Small nitrogen peaks (NO_2 and/or NO components, not shown) were detected, indicating surface contamination brought by Ar^+ sputtering. The fact that both metallic and iron oxide components are measured points to partial conversion of the thin film material.

After 12 min Ar^+ sputtering, the C1s core level shows nearly no intensity anymore, indicating full removal of the surface SEI layer. For binding energy calibration and for consistent comparison, the binding energy of the $O1s_B$ peak (C=O and/or N=O bonds) was set at 531.7 eV. It is then clearly seen that the lower binding energy $O1s_A$ peak of metal oxides shifts from 528.4 eV to 528.9 eV, which is consistent with a component change of metal oxides from lithium oxides to iron oxides. Consistently with the removal of the SEI layer, the intensity of the Fe2p core level increases as well as that of the Fe3p-Li1s core level with displacement of this composite peak to lower binding energies. The relative intensity of the Fe(0) component remains high, indicating that profiling is still in the converted region of the iron oxide film. However, the increasing relative intensity of the Fe(III) components indicates that profiling approaches the unconverted inner part of the thin film.

After 24 min Ar^+ sputtering, the Fe(III) peak at 710.7 eV becomes the dominant component of the $Fe2p_{3/2}$ core level spectrum, showing the characteristics of the pristine iron oxide film ($O1s_A$ peak further shifted to 529.2 eV). This means that profiling has further approached an unconverted (or partly converted) region in the inner part of the thin film as confirmed by the ToF-SIMS results presented below. After 60 min Ar^+ sputtering (corresponding to about 150 nm of thickness), the markedly enhanced metallic Fe(0) peak at 706.9 eV and decreased intensity of the $O1s_A$ peak indicate that the substrate region has been reached with only traces of the original iron oxide film remaining. This is confirmed by the change of the shape of the Fe3p-Li1s peak. The marker peaks characteristic of the MOs of carbonate anion are no longer observed. The low intensity peak at ~21 eV and large peak between 3-8 eV correspond to O2s and O2p bands, respectively, from the remaining iron oxide traces.

3.5 *ToF-SIMS depth profiles analysis of pristine, lithiated and delithiated samples*

Figure 6 shows the negative ion depth profiles of the Li-containing ions (Li^-, LiO^-) and Fe-containing ions (FeO^-, FeO_2^-, Fe_2^-, $Fe_2O_3^-$, $Fe_3O_4^-$) of the pristine,

lithiated (to 0.01 V) and delithiated (to 3.0 V) samples. All profiles were recorded in the same conditions to allow direct comparison between samples. The intensity is presented using a logarithmic scale in order to magnify the low intensity signals. The ion intensity modifications with sputtering time reflect the in-depth variations of concentration but are also dependent on the matrix from which the ions are emitted.

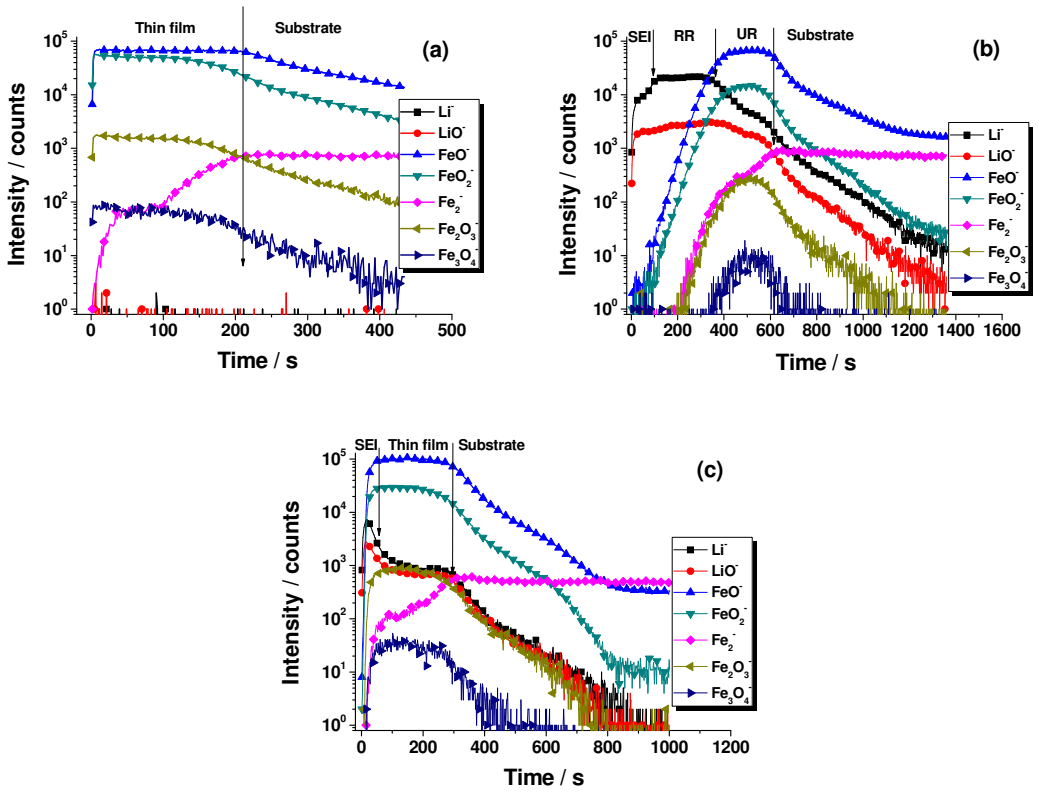

Figure 6 ToF-SIMS negative ion depth profiles of (a) the pristine, (b) lithiated to 0.01 V and (c) delithiated to 3.0 V samples.

For the pristine sample (Figure 6 (a)), extremely low intensity Li-containing ion profiles are shown for comparison with the electrochemically treated samples discussed below. Several regions can be distinguished from the depth profiles of the Fe-containing ions. At beginning of sputtering, all ions intensities increase for a few seconds to reach stationary conditions. After about 5 s, a plateau characterizes the variation of the FeO^-, FeO_2^-, $Fe_2O_3^-$ and $Fe_3O_4^-$ ions profiles. It corresponds to the bulk region of the iron oxide film. The Fe_2^- ion curve shows a gradual increase from ~100 to ~210 s, corresponding to the transition from the mixed higher valent (Fe^{3+}/Fe^{2+}, as shown by XPS and Raman) iron oxide region to the metallic substrate region and thus

marking the interfacial region between oxide film and substrate. After about 120 s, the intensities of the FeO_2^-, $Fe_2O_3^-$ and $Fe_3O_4^-$ ions start to decrease slowly whereas that of the FeO^- ions remains stable. This is consistent with the predominance of lower valent (Fe^{2+}) iron ions in the inner part of the oxide film at the interface with the substrate. After about 210 s sputtering, the Fe_2^- ions are stable in intensity, confirming that the iron substrate region is reached.

For the sample lithiated to 0.01 V (Figure 6 (b)), the sputtering time to reach the substrate region has increased to about 610 s, which is almost 3 times that of the pristine sample. Undoubtedly, the prolonged sputtering time reflects swelling of the iron oxide thin film caused by volume expansion during the lithiation process. However, it does not mean that the thickness of the lithiated oxides layer has tripled, because matrix effect can affect the sputtering yield. Actually, the theoretical expansion for the conversion reaction (1) is 193% as deduced from molar volume calculation (30.5 cm^3/mol for Fe_2O_3, 7.1 cm^3/mol for Fe and 14.84 cm^3/mol for Li_2O). Such a volume expansion is expected to fracture the oxide thin film, which may be one reason for the inferior cycling performance of this kind of material. Indeed, large volume changes induced by cycling have been reported to fracture large hematite particle in contrast to nano-rods which undergo only pulverisation but no electrode damage.[54]

According to the XPS data presented above, the thickness expansion for the sample lithiated to 0.01 V can be estimated to about 170% (150 nm/(85-95 nm)), which is slightly lower than the theoretical value of volume expansion and consistent with an incomplete conversion of the thin film electrode, also shown by the XPS.

The SEI layer region has a width of ~80 s in sputtering time (from ~20 s to ~100 s). The interface between the SEI layer and the converted oxides is well marked by the Li-containing ions (Li^-, LiO^-). Under the SEI layer, a plateau with a stable intensity of the Li-containing ions is observed, which can be assigned to the main converted region of the oxide film (reacted region, RR in Figure 6 (b)). The intensities of the Fe-containing ions (FeO^-, FeO_2^-, $Fe_2O_3^-$, $Fe_3O_4^-$) are quite low compared to those for the pristine sample, indicating a high conversion ratio in this main reacted

region. After ~360 s, the intensities of the Fe-containing ions (FeO^-, FeO_2^-, $Fe_2O_3^-$, $Fe_3O_4^-$) reach their maximum. The intensity of FeO^- ions in this region is similar to that for the pristine oxide sample, but the intensities of FeO_2^-, $Fe_2O_3^-$ and $Fe_3O_4^-$ ions are one order of magnitude smaller than for the pristine sample. In this inner unreacted region (UR in Figure 6 (b)) at the interface with the current collector (substrate), the iron oxide film is partially lithiated, possibly to lower valence Fe(II) oxides, which is further supported by the slowly declining intensities of the Li-containing ions. This stratification of the iron oxide film into a fully lithiated outer part and a partially lithiated inner part most likely results from the limitation of the lithiation reaction by mass transport, like previously observed for Cr_2O_3, and Sn-Co and Sn-Ni alloys.[5,17,18]

For the sample delithiated to 3.0 V (Figure 6 (c)), the sputtering time to reach the substrate has decreased to about 300 s, reflecting volume shrinking upon delithiation. However, this value is higher than for the pristine film, which is a first indication of a non-fully reversible lithiation process. The Fe-containing ions (FeO^-, FeO_2^-, $Fe_2O_3^-$, $Fe_3O_4^-$) display a plateau from ~55 to ~300 s of sputtering, which is assigned to deconversion of Fe with Li_2O to form Fe_2O_3 (reaction (3)). It seems that the main reaction region (RR) in the 0.01 V lithiated sample has disappeared, indicating reaction and diffusion of Li^+ ions in and out of the film. Compared to the 0.01 V lithiated sample, the profiles of Li-containing ions (Li^-, LiO^-) display higher intensities for a shorter sputtering time before decreasing to a lower plateau level, indicating a delithiation process of Li^+ ions through the SEI layer. The narrower region of high intensities of the Li-containing ions (~55 s vs. ~80 s in the lithiated state) is attributed to the SEI layer, which is partially decomposed after deconversion, in agreement with the EIS and XPS data. In contrast to the pristine sample, Li-containing ions are markedly present in the delithiated sample. This evidences that there is some lithium trapped in the deconverted oxide, indicating that the process is not totally reversible. This points to a delithiation process being mainly limited by mass transport to the electrolyte/oxides interface as observed above for the lithiation process. This was also observed previously for Cr_2O_3.[5]

4. Conclusions

Surface and depth profile analysis (XPS and ToF-SIMS) was combined with electrochemical techniques (CV and EIS) to study the lithiation/delithiation mechanism of iron oxide as anode material for LiBs. A thin film model electrode was prepared by a simple thermal oxidation process at 300°C in air of pure iron substrate, used as current collector. Raman, XPS and ToF-SIMS showed that the oxide film consists of Fe(III) ions forming a α-Fe_2O_3 phase in majority with lower valent Fe(II) ions forming a Fe_3O_4 phase in the inner part of the film at the interface with the current collector.

The SEI layer formed by reductive decomposition of the $LiClO_4$-PC electrolyte on the iron oxide thin film electrode is mainly constituted of Li_2CO_3 with $ROCO_2Li$ as minor constituent, independently of the lithiation/delithiation of the electrode. It was shown here for the first time that the thickness of the SEI layer formed on the surface of conversion-type metallic oxide electrode material evolves upon lithiation/delithiation process. After lithiation to 1.2 V (i.e. before conversion occurring at 0.75 V), Li intercalates in the α-Fe_2O_3 matrix to form $Li_{1.03}Fe_2O_3$ as measured by XPS. The SEI layer is already formed at this stage. After lithiation to 0.01 V, the SEI layer grows in thickness to at least 15 nm. The thin film electrode approach allowed us to show that the conversion reaction leading to formation of metallic Fe and Li_2O is accompanied by material swelling, except in its inner part where an unconverted and/or partially converted material subsists due to limitation of the conversion reaction by mass transport. Deconversion, occuring at ~1.55 V, is not totally reversible and also limited by mass transport. It causes shrinking of the electrode material with lithium trapped in the deconverted part. The SEI layer mostly decomposes and reduces in thickness above 1.8 V, i.e. after the main deconversion reaction.

References

[1] Poizot, P.; Laruelle, S.; Grugeon, S.; Dupont, L.; Tarascon, J.-M. Nano-sized Transition-Metal Oxides as Negative-Electrode Materials for Lithium-Ion Batteries. *Nature* **2000**, *407*, 496-499.

[2] Wang, G. X.; Chen, Y.; Konstantinov, K.; Lindsay, M.; Liu H. K.; Dou, S. X. Investigation of Cobalt Oxides as Anode Materials for Li-ion Batteries. *J. Power Sources* 2002, *109*, 142-147.

[3] Aricò, A. S.; Bruce, P.; Scrosati, B.; Tarascon, J.-M.; Schalkwijk, W. V. Nanostructured Materials for Advanced Energy Conversion and Storage Devices. *Nat. Mater.* **2005**, *4*, 366-377.

[4] Taberna, P. L.; Mitra, S.; Poizot, P.; Simon, P.; Tarascon, J.-M. High Rate Capabilities Fe_3O_4-based Cu Nano-architectured Electrodes for Lithium-ion Battery Applications. *Nat. Mater.* **2006**, *5*, 567-573.

[5] Li, J. T.; Maurice, V.; Światowska-Mrowiecka, J.; Seyeux, A.; Zanna, S.; Klein, L.; Sun, S. G.; Marcus, P. XPS, Time-of-Flight-SIMS and Polarization Modulation IRRAS Study of Cr_2O_3 Thin Film Materials as Anode for Lithium Ion Battery. *Electrochim. Acta* **2009**, *54*, 3700-3707.

[6] Wen, C. J.; Huggins, R. A. Thermodynamic Study of the Lithium - Tin System. *J. Electrochem. Soc.* **1981**, *128*, 1181-1187.

[7] Winter, M.; Besenhard, J. O. Electrochemical Lithiation of Tin and Tin-Based Intermetallics and Composites. *Electrochim. Acta* 1999, *45*, 31-50.

[8] Nobili, F.; Mancini, M.; Dsoke, S.; Tossici, R.; Marassi, R. Low-Temperature Behavior of Graphite–Tin Composite Anodes for Li-ion Batteries. *J. Power Sources* **2010**, *195*, 7090-7097.

[9] Lai, S. C. Solid Lithium - Silicon Electrode. *J. Electrochem. Soc.* **1976**, *123*, 1196-1197.

[10] Sharma, R. A.; Seefurth, R. N. Thermodynamic Properties of the Lithium - Silicon System. *J. Electrochem. Soc.* **1976**, *123*, 1763-1768.

[11] Pereira-Nabais, C.; Światowska, J.; Chagnes, A.; Ozanam, F.; Gohier, A.; Tran-Van, P.; Cojocaru, C.-S.; Cassir, M.; Marcus, P. Interphase Chemistry of Si Electrodes Used as Anodes in Li-ion Batteries. *App. Surf. Sci.* **2013**, *266*, 5-16.

[12] Philippe, B.; Dedryvère, R.; Allouche, J.; Lindgren, F.; Gorgoi, M.; Rensmo, H.; Gonbeau, D.; Edström, K. Nanosilicon Electrodes for Lithium-ion Batteries: Interfacial Mechanisms Studied Hard and Soft X-Ray Photoelectron Spectroscopy. *Chem. Mater.* **2012**, *24*, 1107-1115.

[13] Cui, Z.; Gao, F.; Cui, Z.; Qu, J. A Second Nearest-Neighbor Embedded Atom Method Interatomic Potential for Li–Si Alloys. *J. Power Sources* **2012**, *207*, 150-159.

[14] Weydanz, W. J.; Wohlfahrt-Mehrens, M.; Huggins, R. A. A Room Temperature Study of the Binary Lithium–Silicon and the Ternary Lithium–Chromium–Silicon System for Use in Rechargeable Lithium Batteries. *J. Power Sources* **1999**, *81-82*, 237-242.

[15] Jayaprakash, N.; Kalaiselvi, N.; Doh, C. H. A New Class of Tailor-Made $Fe_{0.92}Mn_{0.08}Si_2$ Lithium Battery Anodes: Effect of Composite and Carbon Coated $Fe_{0.92}Mn_{0.08}Si_2$ Anodes.

Intermetallics **2007**, *15*, 442-450.

[16] Kamali, A. R.; Fray, D. J. Tin-Based Materials as Advanced Anode Materials for Lithium Ion Batteries: a Review. *Rev. Adv. Mater. Sci.* **2011**, *27*, 14-24.

[17] Li, J. T.; Świątowska, J.; Seyeux, A.; Huang, L.; Maurice, V.; Sun, S. G.; Marcus, P. XPS and ToF-SIMS Study of Sn–Co Alloy Thin Films as Anode for Lithium Ion Battery. *J. Power Sources* **2010**, *195*, 8251-8257.

[18] Li, J. T.; Świątowska J.; Maurice, V.; Seyeux, A.; Huang, L.; Sun, S. G.; Marcus, P. XPS and ToF-SIMS Study of Electrode Processes on Sn–Ni Alloy Anodes for Li-Ion Batteries. *J. Phys. Chem. C* **2011**, *115*, 7012-7018.

[19] Thackeray, M. M.; David, W. I. F.; Goodenough, J. B. High-Temperature Lithiation of α-Fe_2O_3: A Mechanistic Study. *J. Solid State Chem.* **1984**, *55*, 280-286.

[20] Larcher, D.; Masquelier, C.; Bonnin D.; Chabre, Y.; Mason, V.; Leriche, J. B.; Tarascon, J.-M. Effect of Particle Size on Lithium Intercalation into α-Fe_2O_3. *J. Electrochem. Soc.* **2003**, *150*, A133-A139.

[21] Larcher, D.; Bonnin, D.; Cortes, R.; Rivals, I.; Personnaz, L.; Tarascon, J.-M. Combined XRD, EXAFS, and Mössbauer Studies of the Reduction by Lithium of α-Fe_2O_3 with Various Particle Sizes. *J. Electrochem. Soc.* **2003**, *150*, A1643-A1650.

[22] Cherian, C. T.; Sundaramurthy, J.; Kalaivani, M.; Ragupathy, P.; Suresh Kumar, P.; Thavasi, V.; Reddy, M. V.; Sow, C. H.; Mhaisalkar, S. G.; Ramakrishna, S.; Chowdari, B. V. R. Electrospun α-Fe_2O_3 Nanorods as A Stable, High Capacity Anode Material for Li-ion Batteries. *J. Mater. Chem.* **2012**, *22*, 12198-12204.

[23] Reddy, M. V.; Yu, T.; Sow, C. H.; Shen, Z. X.; Lim, C. T.; Subba Rao, G. V.; Chowdari, B. V. R. α-Fe_2O_3 Nanoflakes as an Anode Material for Li-Ion Batteries. *Adv. Funct. Mater.* **2007**, *17*, 2792-2799.

[24] Mitra, S.; Poizot, P.; Finke, A.; Tarascon, J.-M. Growth and Electrochemical Characterization versus Lithium of Fe_3O_4 Electrodes Made by Electrodeposition. *Adv. Funct. Mater.* **2006**, *16*, 2281-2287.

[25] Świątowska-Mrowiecka, J.; Maurice, V.; Zanna, S.; Klein, L.; Marcus, P. XPS Study of Li Ion Intercalation in V_2O_5 Thin Films Prepared by Thermal Oxidation of Vanadium Metal. *Electrochim. Acta* **2007**, *52*, 5644-5653.

[26] Beattie, I. R.; Gilson, T. R. The Single-Crystal Raman Spectra of Nearly Opaque Materials. Iron(III) Oxide and Chromium(III) Oxide. *J. Chem. Soc. A* **1970**, *5*, 980-986.

[27] Zheng, Z.; Chen, Y.; Shen, Z. X.; Ma, J.; Sow, C. H.; Huang, W.; Yu, T. Ultra-Sharp Alpha-Fe_2O_3 Nanoflakes: Growth Mechanism and Field-Emission. *Appl. Phys. A* **2007**, *89*, 115-119.

[28] Faria, D. L. A.; Venâncio Silva, S.; Oliveira M. T. Raman Microspectroscopy of Some Iron Oxides and Oxyhydroxides. *J. Raman Spectrosc*. **1997**, *28*, 873-878.

[29] Bellot-Gurlet, L.; Neff, D.; Réguer, S.; Monnier, J.; Saheb, M.; Dillmann, P. Raman Studies of Corrosion Layers Formed on Archaeological Irons in Various Media. *J. Nano Research* **2009**, *8*, 147-156.

[30] Laruelle, S.; Grugeon, S.; Poizot, P.; Dolle, M.; Dupont, L.; Tarascon, J.-M. On the Origin of the Extra Electrochemical Capacity Displayed by MO/Li Cells at Low Potential. *J. Electrochem. Soc.* **2002**, *149*, A627-A634.

[31] Hosono, E.; Fujihara, S.; Honma, I.; Ichihara, M.; Zhou, H. Fabrication of Nano/Micro Hierarchical Fe_2O_3/Ni Micrometer-Wire Structure and Characteristics for High Rate Li Rechargeable Battery. *J. Electrochem. Soc.* **2006**, *153*, A1273-A1278.

[32] Nuli, Y. N.; Zeng, R.; Zhang, P.; Guo, Z. P.; Liu, H. K. Controlled Synthesis of a-Fe_2O_3 Nanostructures and Their Size-Dependent Electrochemical Properties for Lithium-Ion Batteries. *J. Power Sources* **2008**, *184*, 456-461.

[33] Chaudhari, S.; Srinivasan, M. 1D Hollow -Fe_2O_3 Electrospun Nanofibers as High Performance Anode Material for Lithium Ion Batteries. *J. Mater. Chem.* **2012**, *22*, 23049-23056

[34] Thevenin, J. Passivating Films on Lithium Electrodes. An Approach by Means of Electrode Impedance Spectroscopy. *J. Power Sources* **1985**, *14*, 45-52.

[35] Levi, M. D.; Aurbach, D. Diffusion Coefficients of Lithium Ions during Intercalation into Graphite Derived from the Simultaneous Measurements and Modeling of Electrochemical Impedance and Potentiostatic Intermittent Titration Characteristics of Thin Graphite Electrodes. *J. Phys. Chem. B* **1997**, *101*, 4641-4647.

[36] Shin, H. C.; Cho, W. II.; Jang, H. Electrochemical Properties of the Carbon-Coated $LiFePO_4$ as a Cathode Material for Lithium-ion Secondary Batteries. *J. Power Sources* **2006**, *159*, 1383-1388.

[37] Yang, Y.; Wang, C.; Yue, B.; Gambhir, S.; Too, C. O.; Wallace, G. G. Electrochemically Synthesized Polypyrrole/Graphene Composite Film for Lithium Batteries. *Adv. Energy Mater.* **2012**, *2*, 266-272.

[38] Lindström, R.; Maurice V.; Groult, H.; Perrigaud, L.; Zanna, S.; Cohen, C.; Marcus, P. Li-Intercalation Behaviour of Vanadium Oxide Thin Film Prepared by Thermal Oxidation of Vanadium Metal. *Electrochim. Acta* **2006**, *51*, 5001-5011.

[39] Yang, C. R.; Song, J. Y.; Wang, Y. Y.; Wan, C. C. Impedance Spectroscopic Study for the Initiation of Passive Film on Carbon Electrodes in Lithium Ion Batteries. *J. Appl. Electrochem.* **2000**, *30*, 29-34.

[40] Zhou, W.; Zhu, J.; Cheng, C.; Liu, J.; Yang, H; Cong, C.; Guan, C.; Jia, X.; Jin Fan, H. ; Yan, Q.; Ming Li, C.; Yu, T. A General Srategy Toward Graphene@Metal Oxide Core–Shell

Nanostructures for High-Performance Lithium Storage. *Energy Environ. Sci*. **2011**, *4*, 4954-4961.

[41] Zhao, X.; Xia, D.; Zheng, K. Fe_3O_4/Fe/Carbon Composite and Its Application as Anode Material for Lithium-Ion Batteries. *ACS Appl. Mater. Interfaces* **2012**, *4*, 1350-1356.

[42] Li, X.; Huang, X.; Liu, D.; Wang, X.; Song, S.; Zhou, L.; Zhang, H. Synthesis of 3D Hierarchical Fe_3O_4/Graphene Composites with High Lithium Storage Capacity and for Controlled Drug Delivery. J. Phys. Chem. C **2011**, *115*, 21567–21573.

[43] Lee, Y. M.; Lee, J. Y.; Shim, H. T.; Lee, J. K.; Park, J. K. SEI Layer Formation on Amorphous Si Thin Electrode during Precycling Batteries and Energy Storage. *J. Electrochem. Soc.* **2007**, *154*, A515-A519.

[44] Światowska-Mrowiecka, J.; Maurice, V.; Zanna S.; Klein, L.; Marcus, P. Ageing of V_2O_5 thin films induced by Li intercalation multi-cycling. *J. Power Sources,* **2007**, *170*, 160-172.

[45] Światowska-Mrowiecka, J.; Diesbach, S.; Maurice, V.; Zanna, S.; Klein, L.; Briand, E.; Vickridge, I.; Marcus, P. Li-Ion Intercalation in Thermal Oxide Thin Films of MoO_3 as Studied by XPS, RBS, and NRA. *J. Phys. Chem. C* **2008**, *112*, 11050-11058.

[46] McIntyre, N. S.; Zetaruk, D. G. X-Ray Photoelectron Spectroscopic Studies of Iron Oxides. *Anal. Chem.* **1977**, *49*, 1521-1529.

[47] Stambouli, V.; Palacio, C.; Mathieu, H. J.; Landolt, D. Comparison of In-Situ Low-Pressure Oxidation of Pure Iron at Room Temperature in O_2 and in O_2/H_2O Mixtures Using XPS. *Appl. Surf. Sci.* **1993**, *70-71*, 240-244.

[48] Bhargava, G.; Gouzman, I.; Chun, C. M.; Ramanarayanan, T. A.; Bernasek, S. L. Characterization of The "Native" Surface Thin Film on Pure Polycrystalline Iron: A High Resolution XPS and TEM Study. *Appl. Surf. Sci.* **2007**, *253*, 4322-4329.

[49] Bryngelsson, H.; Stjerndahl, M.; Gustafsson, T.; Edström, K. How Dynamic Is the SEI? *J. Power Sources* **2007**, *174*, 970-975.

[50] Dedryvère, R.; Gireaud, L.; Grugeon S.; Laruelle, S.; Tarascon, J.-M.; Gonbeau, D. Characterization of Lithium Alkyl Carbonates by X-Ray Photoelectron Spectroscopy : Experimental and Theoretical Study. *J. Phys. Chem. B* **2005**, *109*, 15868-15875.

[51] Coluzza, C.; Cimino, N; Decker, F.; Di Santo, G.; Liberatore, M.; Zanoni, R.; Bertolo, M.; La Rosa, S. Surface Analyses of In–V Oxide Films Aged Electrochemically by Li Insertion Reactions. *Phys. Chem. Chem. Phys.* **2003**, *5*, 5489-5498.

[52] Pfanzelt, M.; Kubiak, P.; Jacke, S.; Dimesso, L.; Jaegermann, W.; Wohlfahrt-Mehrens, M. SEI Formation on TiO_2 Rutile. *J. Electrochem. Soc.* **2012**, *159*, A809-A814.

[53] Verma, P.; Maire, P.; Novák, P. A Review of the Features and Analyses of the Solid Electrolyte Interphase in Li-Ion Batteries. *Electrochim. Acta* **2010,** *55*, 6332-6341.

[54] Lin, Y.-M.; Abel, P. R.; Heller, A.; Mullins, C. B. α-Fe_2O_3 Nanorods as Anode Material for

Lithium Ion Batteries. *J. Phys. Chem. Lett.* **2011**, *2*, 2885-2891.

Chapter 3. Aging-induced chemical and morphological modifications of thin film iron oxide electrodes for lithium-ion batteries

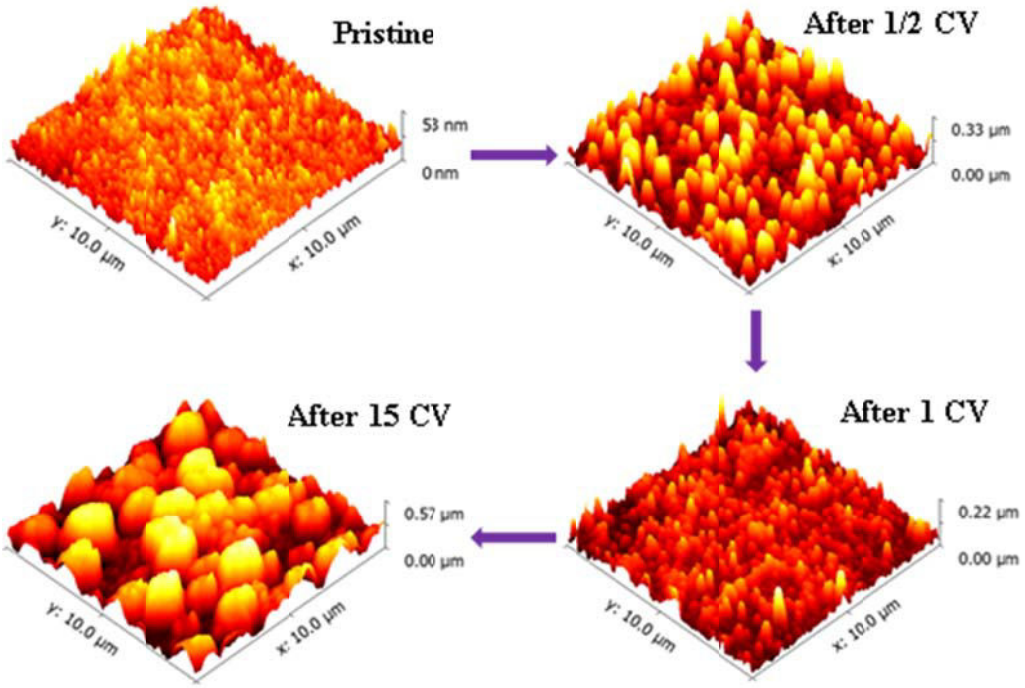

A version of this chapter has been published in *Langmuir* (ACS Publications), 2014, 30, 3538-3547.

Some results of this chapter also contributed to *4ème journée «Batterie Lithium Ile de France»*, September 10, 2013, Thiais, France.

Abstract: Spectroscopic (XPS, ToF-SIMS) and microscopic (SEM, AFM) analytical methods have been applied to iron oxide (~Fe_2O_3) using a thin film approach to bring new insight into the aging mechanisms of conversion-type anode materials for lithium-ion batteries. The results show that repeated lithiation/delithiation causes both chemical and morphological modifications affecting the electrochemical performance. The SEI layer formed by reductive decomposition of the electrolyte remains stable in composition (mostly Li_2CO_3) but irreversibly thickens upon multi cycling. Irreversible swelling of the material accompanied by penetration of the SEI layer and accumulation of non deconverted material in the bulk of the oxide thin film occurs upon repeated conversion/deconversion. After initial pulverization of the thin film microstructure, grain growth and aggregation are promoted by multi-cycling. In the first five cycles, this promotes capacity increase but upon further cycling volume expansion and accumulation of non deconverted material lead to deterioration of the electrode performances.

Keywords: iron oxide; thin-film electrode; electrochemical aging; SEI layer; chemical and morphological modifications

1. Introduction

Compared with commercially used graphite, iron oxide (Fe_2O_3), since reported as negative electrode material for lithium-ion batteries (LiBs), has attracted attention due to its high capacity (six Li react per formula unit yielding a theoretical capacity of 1007 mAh g^{-1}), environmental friendliness, abundance and low cost.[1-7] However, despite such advantages, rapid capacity loss upon cycling, drastic volume changes and inferior rate capability are drawbacks for commercial development. [6,7] One issue, affecting cycling performance and rate capability of the battery, is the control of the complex electrode/electrolyte interfacial properties that requires better understanding of the surface of the electroactive material in interaction with the electrolyte.[8-10]

The main electrode/electrolyte interfacial reactions for metallic oxide anodes in LiBs are formation of Solid Electrolyte Interphase (SEI) layer and displacement, or so-called conversion, of metal oxides by Li ions to form lithium oxide and metal. The SEI, critical for the reversibility of the cycling performance,[11] has been widely studied on negative electrodes such as graphite.[8,12-19] However, for transition metal oxides, it is rarely studied especially during cycling.

Recently, SEI layer formation and conversion/deconversion mechanism of iron oxide (Fe_2O_3) thin film without conducting additives and binder were thoroughly studied during the first lithiation/delithiation cycle using a thin film approach enabling the application of surface science analytical techniques like X-ray Photoelectron Spectroscopy (XPS) and Time-of-Flight Secondary Ions Mass Spectrometry (ToF-SIMS) for chemical characterization.[20] It was found that intercalation of Li in the Fe_2O_3 matrix and SEI layer formation both precede conversion to metallic iron and Li_2O upon lithiation. The SEI layer had a stable composition (Li_2CO_3 with minor $ROCO_2Li$) but dynamically increases/decreases in thickness upon lithiation/delithiation. Conversion, proceeding mostly in the outer part of the electrode due to mass transport limitation, caused material swelling accompanied by SEI layer thickening. Upon delithiation, lithium was trapped in the deconverted electrode subjected to shrinking and the SEI layer mostly decomposes and reduces in thickness after deconversion

Here, we report on the influence of multi-cycling on both the compositional and morphological modifications of the SEI layer and iron oxide electrode. The application of

XPS and ToF-SIMS for chemical characterization has been complemented by that of Scanning Electron Microscopy (SEM) and Atomic Force Microscopy (AFM) for morphological analysis. Their combination brings significant new insight into electrochemical aging of the iron oxide thin film anode in LiBs.

2. Experimental methods

The iron oxide thin films were prepared by thermal oxidation of iron foil (99.99 wt%, Goodfellow) at 300 ± 5 ^{o}C in air at ambient pressure during 5 min, as previously described in more details in Chapter 2.[20] The thermally grown thin films were crystallized to thermodynamically stable α-Fe_2O_3 (hematite) with a small amount of Fe_3O_4 (magnetite) and FeOOH with the average thickness of 90 nm as estimated from XPS depth profile analysis performed with a calibrated Ar^+ sputtering rate of ~2.5 nm min^{-1}.[20] A consistent thickness value of ~95 nm was obtained by profilometry after ToF-SIMS depth profiling.

Cyclic voltammetry (CV) and electrochemical impedance spectroscopy (EIS) were performed in a three-electrode glass cell with iron oxide as working electrode (0.28 cm^2 area delimited by a Viton O-ring) and Li foil (Sigma-Aldrich) as reference and counter electrodes. The electrochemical experiments were performed in an Ar-filled glovebox (Jacomex) with H_2O and O_2 contents lower than 1 ppm at room temperature. The CVs were recorded using an Autolab (AUT30) potentiostat/galvanostat over the potential range of 3.0 - 0.01 V at a scanning rate of 0.2 mV s^{-1}. After completion, the cells were disassembled and subsequently the samples were rinsed with acetonitrile (99.8%, Sigma-Aldrich) and dried with Ar flow before transfer for surface analysis. EIS was performed at open circuit potential (OCP) over a frequency range of 10 mHz to 1 MHz under a potential perturbation of 5 mV. Galvanostatic discharge-charge (discharge-charge refers to lithiation-delithiation of the anode in a LiB full cell configuration) was performed in a 2-electrode Teflon Swagelok-type cell (with a working electrode and Li as counter electrode) at a current density of 20 μA cm^{-2} in the potential range of 3.0 - 0.01 V using an EC-Lab electrochemical workstation. The electrolyte was 1 M $LiClO_4$ in propylene carbonate (1 mol L^{-1} $LiClO_4$/PC, Sigma-Aldrich). All potentials given in this chapter are referred to Li/Li^+ reference electrode.

A XPS VG ESCA-LAB 250 spectrometer operating at 2 × 10^{-9} mbar with an Al Kα

monochromatized radiation (hv = 1486.6 eV) was used for surface chemical analysis. After electrochemical preparation, samples were transferred directly from the glovebox to the ultra-high vacuum XPS analysis chamber. Survey spectra and high resolution core level spectra were recorded with a pass energy of 100 eV and 20 eV, respectively. Peak fitting was performed with the Avantage software v. 3.13 (Thermo Electron Corporation), using a Shirley type background and Lorentzian/Gaussian (30/70) peak shapes. The binding energies were corrected by setting the C1s hydrocarbon component peak (-CH_2-CH_2-) at 285.0 eV. A ToF-SIMS 5 spectrometer (IonTof) operating at 10^{-9} mbar was used for depth profile chemical analysis. Samples were transferred in an air-tight vessel under argon atmosphere from the glove box to the ToF-SIMS system. Negative ion depth profiles were recorded by interlacing analysis using a pulsed 25 keV Bi^+ primary ion source delivering 1.2 pA of target current over a 100 × 100 μm^2 area with sputtering using a 1 keV Cs^+ source beam delivering 70 nA of target current over a 300 × 300 μm^2 area. Ion-Spec software from ION-TOF GmbH was used for acquiring and processing the data.

SEM imaging of the thin film electrodes before and after electrochemical treatment was performed with a ZEISS Ultra-55 Field Emission Scanning Electron Microscope (FE-SEM, Germany). AFM imaging was performed with an Agilent 5500 Atomic Force Microscope operated in intermittent contact mode (tapping) in air. The AFM images were acquired in topographic and differential modes using a silicon tip with a force constant of 25 - 75 N m^{-1} and a resonance frequency of 282.6 kHz. AFM data visualization and analyses (average value, RMS) were performed with the Gwyddion 2.31 software.

3. Results and discussion

3.1. Galvanostatic cycling

The initial, second, tenth, and fiftieth galvanostatic discharge-charge curves and the cycling performance and evolution of the coulombic efficiency of the thin-film electrode in the potential range of 3.0 - 0.01 V are presented in Figure 1.

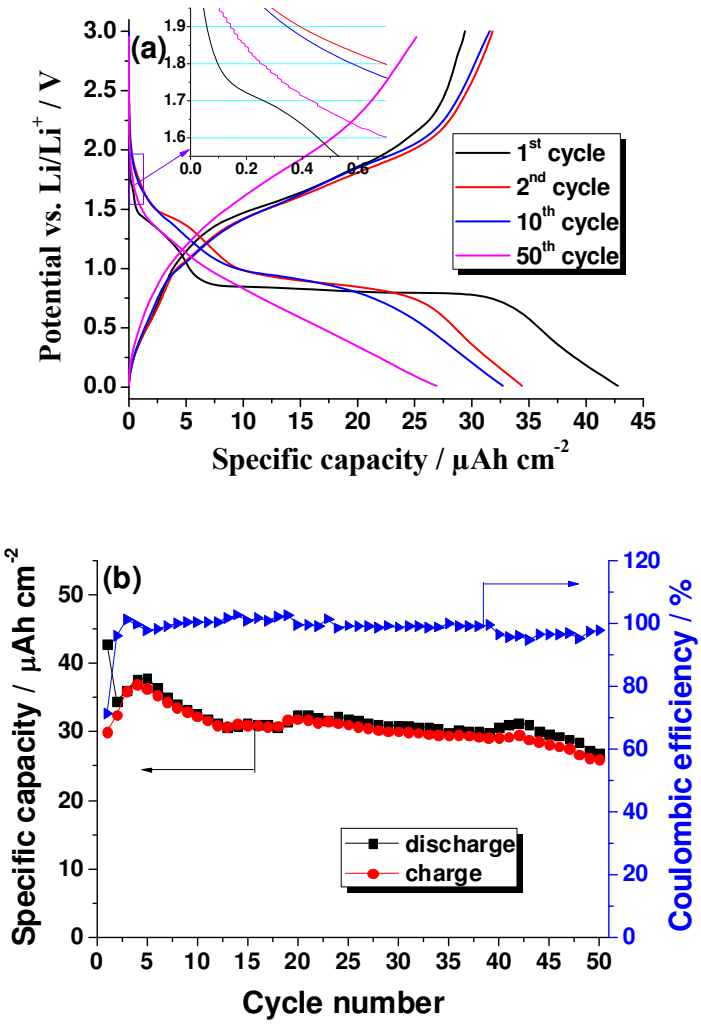

Figure 1 (a) Initial, second, tenth, and fiftieth discharge/charge curves and (b) cycling performance and evolution of coulombic efficiency of the iron oxide thin film electrode at a current density of 20 µA cm^{-1} in the potential range of 3.0-0.01 V.

In the initial discharge curve (Figure 1 (a)), the potential drops rapidly to a very short plateau at about 1.7 V, followed by continuous decrease until a long plateau at approximately 0.84 V. The short plateau around 1.7 V corresponds to the lithiation process of thin-film anode to form $Li_{0.03}Fe_2O_3$, as confirmed by *in situ* X-ray diffraction on micrometric α-Fe_2O_3 particles [21,22] and by XPS in Chapter 2. [20] The plateau at about 0.84 V corresponds to the main lithiation process of iron oxide together with formation of the SEI layer due to solvent (propylene carbonate) reductive decomposition, as discussed previously. [20] Upon subsequent charge, the voltage increases continuously with no noticeable potential plateau around 1.7 V, which has been assigned to biphasic coexistence of nanometer-sized metallic Fe (Fe^0) and amorphous Li_2O during the delithiation reaction. [2,23] Moreover, the initial discharge-charge

curves indicate a marked hysteresis in voltage between charge at 1.2-2.1 V and discharge at 0.8 V. This is one drawback which currently limits both the energy efficiency and the power capabilities of batteries using materials undergoing conversion reactions in practical cells.[4]

In the second discharge curve, one plateau develops at about 1.5 V and another at about 0.88 V, which is indicative of a two-step lithiation process typical of nanometric Fe_2O_3 materials. [21,22] The presence of nanometric Fe_2O_3 material in our case can be entailed to pulverization during the first lithiation/delithiation process. The initial compact iron oxide thin film, would form a defective, porous-like layer with presence of smaller nano-particles, as supported by the SEM data presented further on. These results also show that the morphological modifications of the thin-film electrode induced by discharge-charge play a significant role in determining the characteristics of the discharge curves.

In the tenth cycle, the plateau at about 1.5 V has evolved into a slope, which may be caused by Li^+ trapping in the electrode during cycling. In the fiftieth cycle, even the main plateau (at ~0.85 V) indicating conversion vanished in the discharge curve, showing a non-fully reversible conversion/deconversion process.

The cycling performance and evolution of the coulombic efficiency up to 50 cycles are shown in Figure 1 (b). The initial discharge capacity (42.8 μAh cm^{-2}) is much higher than the charge capacity (30.0 μAh cm^{-2}), with a high irreversible capacity (coulombic efficiency of 70.1%) related to the formation of SEI layer and a non-fully reversible conversion/deconversion process in the first lithiation/delithiation cycle. In subsequent cycles, the discharge and charge capacities are almost equal with a coulombic efficiency of ~100% until 39th cycle, which indicates excellent electrochemical reversibility. From the 40th to 50th cycle, the coulombic efficiency is slightly inferior but still higher than 95%. It is interesting to note that the charge capacity in the first 4 cycles increases with cycle number, which was also observed in earlier works.[4,23] The capacity increase is most likely caused by pulverization of the thin-film electrode with formation of nanometric Fe_2O_3 material, leading to increase of specific surface area (large electrolyte-electrode contact area) and enabling smaller diffusion lengths and improving reaction kinetics. Smaller nano-particle will also better accommodate strains induced by lithium insertion. [24, 25] One can notice that these morphological modifications could alter the electrolyte decomposition and contribute in the capacity

increase. However, it should be emphasized that the most significant electrolyte decomposition occurs principally in the first discharge process, as proved by CV, EIS, XPS and ToF-SIMS. This anode material does not show a good capacity retention ratio with only about 63% of the initial discharge capacity retained after 50 cycles. However, a better capacity retention ratio (78.3%) is calculated with respect to the second cycle.

From the Fe_2O_3 film thickness of about 90 nm (~13.2 µg) estimated by XPS and confirmed by ToF-SIMS, the specific capacity in the first discharge process is 907.5 mAh g^{-1}, which is smaller than the theoretical value of 1007 mAh g^{-1} for Fe_2O_3. Moreover, the charge contribution related to the SEI layer formation is also included. Thus, it can be concluded that the whole thin-film iron oxide electrode is not totally converted to metallic Fe and Li_2O during the first discharge process, in agreement with work in Chapter 2 that showed limited ingress of the conversion reaction.[20] The second discharge capacity is about 729.2 mAh g^{-1}, which is 80.3% of the initial discharge capacity. This capacity is mainly related to the conversion reaction of Fe_2O_3 to metallic Fe and Li_2O. [20-22] After 50 cycles, the discharge capacity is ~571.3 mAh g^{-1}, which is much lower than the theoretical capacity but still much higher than the capacity of the commercial graphite electrode (372 mAh g^{-1}).

3.2. First 15 cyclic voltammograms of the iron oxide thin-film electrode

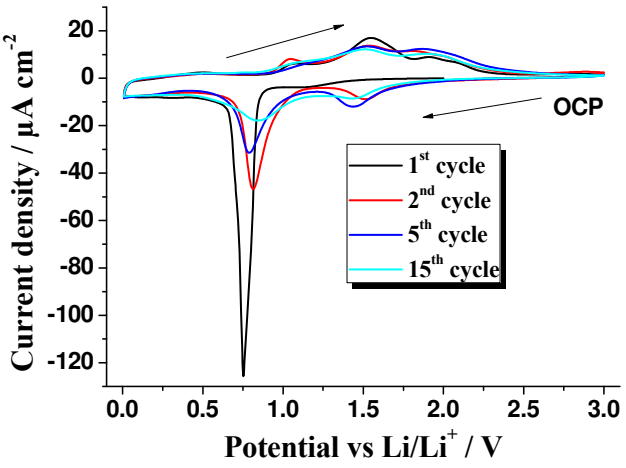

Figure 2 First 15 cyclic voltammograms of the iron oxide thin-film electrode in the potential range of 3.0 - 0.01V at a scanning rate of 0.2 mV s^{-1}.

Figure 2 shows the first 15 cyclic voltammograms of the iron oxide thin-film electrode.

In the first CV, a sharp cathodic peak located at about 0.75 V is observed upon electrochemical reduction. It corresponds to the conversion reaction of iron oxide with lithium and to the formation of the SEI layer. The coulombic efficiency calculated from the ratio of the anodic charge to cathodic discharge is 70.7%, in excellent agreement with the galvanostatic discharge-charge data. A broad shoulder is also observed from 1.6 V to 1.0 V in the reduction process. It corresponds to the intercalation of Li^+ into Fe_2O_3 to form the Li-poor intermediate product $Li_xFe_2O_3$ ($0 \leq x < 1$).[5, 20-22] One main anodic peak around 1.55 V with two shoulder peaks at about 1.2 V and 1.8 V are observed upon electrochemical oxidation. They correspond to the delithiation process of different valence state of iron, as discussed in Chapter 2. [20]

In the second CV cycle, a well-defined peak at about 1.5 V emerges in the reduction process and remains nearly stable in the subsequent cycles. According to literature, [20-22,26] this peak would correspond to the intercalation of Li^+ into Fe_2O_3 nanoparticles to form the intermediate product $Li_xFe_2O_3$ ($0 \leq x < 2$). The intensity of this peak is much larger than that of the broad shoulder in the first CV, thus displaying features of Li^+ intercalation into nano-Fe_2O_3. This supports a pulverization process of the thin-film electrode also inferred from the galvanostatic discharge-charge data and revealed by the SEM results discussed below. Thus, according to previous studies [20-26] and the present data, the electrochemical (de)conversion mechanism of the iron oxide (mainly Fe_2O_3) thin film with lithium proceeds in two steps described by the following equations:

$$Fe_2O_3 + xLi^+ + xe^- \Leftrightarrow Li_xFe_2O_3 \quad (0 \leq x < 2) \qquad (1)$$

$$Li_xFe_2O_3 + (6 - x)Li^+ + (6 - x)e^- \Leftrightarrow 3Li_2O + 2Fe \quad (0 \leq x < 2) \qquad (2)$$

And the net global reaction is:

$$Fe_2O_3 + 6Li^+ + 6e^- \Leftrightarrow 3Li_2O + 2Fe \qquad (3)$$

The significant intensity decrease of the cathodic peak at 0.75 V in the second CV indicates that the SEI layer is mostly formed in the first CV, which is also supported by the EIS data presented as Supporting Information at the end of this chapter and proved by the XPS and ToF-SIMS results presented below. Upon subsequent cycling, the peak at 0.75 V first stabilizes in position and then decreases in intensity in good agreement with the evolution of

the discharge capacity observed in the galvanostatic cycling. The cathodic peak intensity at 1.5 V is not significantly modified during the subsequent cycling. A stable current intensity of this peak indicates that the process of intercalation corresponding to this peak (as discussed above) is more stable in comparison to the conversion process where the significant changes of intensity of peak located at 0.75 V were observed.

3.3. Surface chemistry upon cycling studied by XPS

The XP C1s, O1s and Fe2p core level spectra of pristine and cycled samples are shown in Figure 3. Table 1 compiles the values of the binding energy (E_B) and full width at half maximum (FWHM) of the fitted C1s and O1s component peaks.

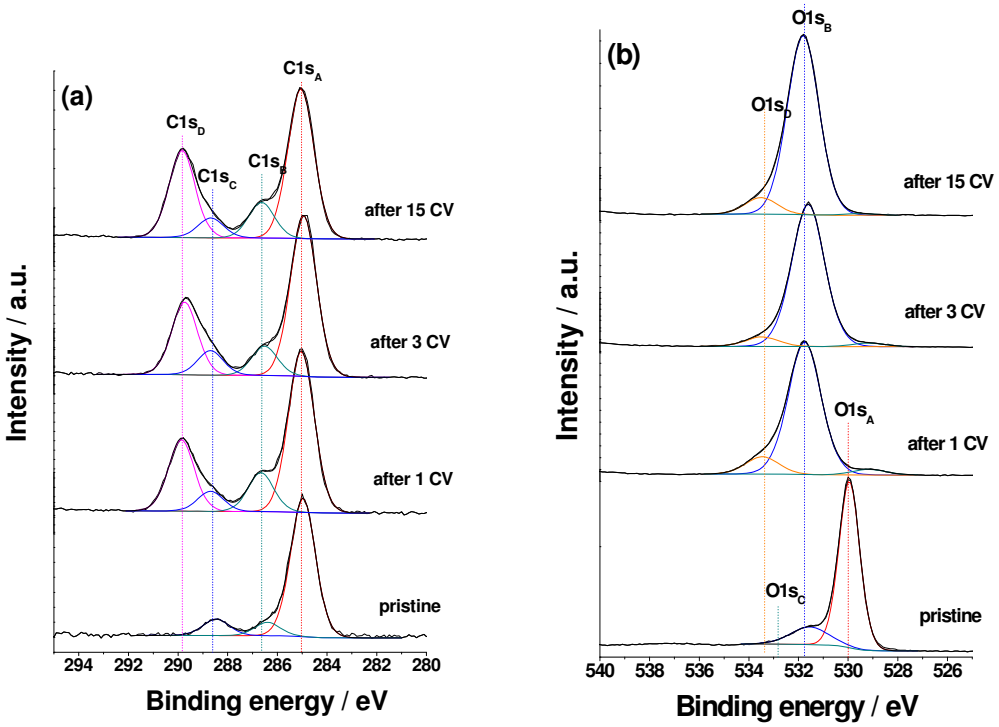

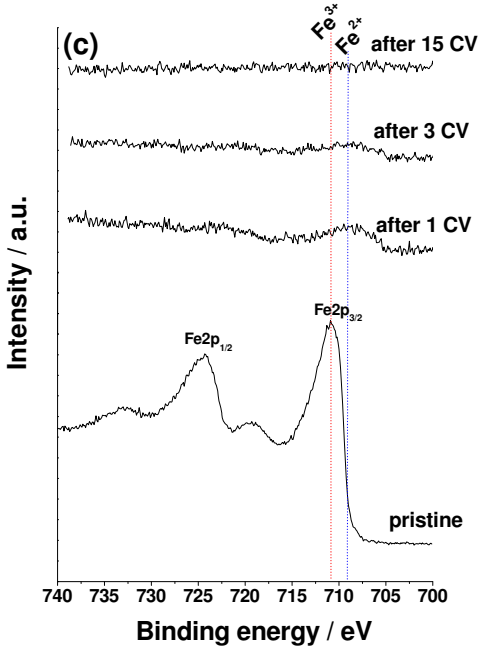

Figure 3 XP (a) C1s, (b) O1s and (c) Fe2p core level of pristine and cycled samples.

Table 1 Binding energies (E_B) and full widths at half-maximum (FWHM) of the component peaks of the C1s and O1s core levels obtained by peak fitting for pristine sample and after 1, 3 and 15 CV cycles.

	pristine	after 1CV	after 3CV	after 15CV
	E_B/FWHM (eV)	E_B/FWHM (eV)	E_B/FWHM (eV)	E_B/FWHM (eV)
$C1s_A$	285.0/1.4	285.0/1.3	285.0/1.3	285.0/1.3
$C1s_B$	286.4/1.4	286.7/1.3	286.5/1.3	286.6/1.3
$C1s_C$	288.4/1.4	288.7/1.3	288.7/1.3	288.7/1.3
$C1s_D$		289.9/1.3	289.7/1.3	289.8/1.3
$O1s_A$	530.0/1.2	529.2/1.5	529.3/1.5	529.6/1.5
$O1s_B$	531.6/1.5	531.8/1.6	531.6/1.6	531.8/1.6
$O1s_C$	532.8/1.5			
$O1s_D$		533.5/1.6	533.4/1.6	533.5/1.6

The C1s signal of the pristine sample (Figure 3(a)) originates from the organic contaminants

present on the surface. Three-component peak at E_B ($C1s_A$) = 285.0 eV, E_B ($C1s_B$) = 286.4 eV and E_B ($C1s_C$) = 288.4 eV are assigned to -CH_2-CH_2- bonds, C-O bonds and O=C-O or O=C-N bonds, respectively.[27] The O1s signal is also decomposed into three component peaks at 530.0, 531.6 and 532.8 eV (Figure 3(b)). The major component at E_B ($O1s_A$) = 530.0 eV is attributed to oxygen anions in the iron oxide matrix. The minor component at E_B ($O1s_B$) = 531.6 eV can be ascribed to organic contamination (O=C-O bonds and C-O bonds)[28-30] on the surface and/or hydroxyl groups[31] originating from iron oxyhydroxide (FeOOH) species. The component at E_B ($O1s_C$) = 532.8 eV, barely detected since its relative intensity is ~0.01, suggests the presence of traces of water molecules adsorbed on the electrode surface based on previous assignments of this component.[32,33]

After 1 CV cycle, the three C1s component peaks present on the pristine sample are still observed, and a new one at E_B ($C1s_D$) = 289.9 eV emerges, indicating the presence of Li_2CO_3 and/or $ROCO_2Li$ as main component of the SEI layer.[28,34,35] Compared with the pristine sample, the oxygen component at E_B ($O1s_A$) = 529.2 eV, corresponding to oxide anions, is strongly attenuated due to the growth of the SEI layer. The intensity of the component at E_B ($O1s_B$) = 531.8 eV increases along with formation of the SEI layer. This component is assigned to carbonate species (mainly Li_2CO_3) and/or O=C-O bonds, C-O bonds in contaminants. A new component peak at around 533.5 eV ($O1s_D$) is also observed on the cycled sample. It corresponds to the presence of Li-alkyl carbonates ($ROCO_2Li$) and/or Li-alkoxides (RCH_2OLi).[16,36] After 3 CV and 15 CV cycles, the C1s and O1s core level components almost do not change, indicating that the same species are present. This shows that the SEI layer composition remains stable after multi cycling.

On the pristine sample, the $Fe2p_{3/2}$ core level (Figure 3(c)) indicates the presence of Fe(III) oxide (α-Fe_2O_3) predominantly and Fe(II) oxide (Fe_3O_4 and FeOOH) in smaller amount, as discussed in Chapter 2. [20] After 1 CV cycle, the intensity of the Fe2p core level decreases strongly, in parallel with the attenuation of the $O1s_A$ component peak, due to formation of the SEI layer. Moreover, the Fe2p peak is also shifted to lower binding energy, which suggests formation of Fe(II) oxide and thus a non-fully reversible electrochemical process, as discussed previously.[20-24] However, precise peak identification and assignment is difficult due to the weak intensity signal. Further intensity attenuation is observed after 3 CV

cycles up to complete attenuation after 15 CV cycles. The same phenomena can be observed for the Fe3p core level (as shown in Supporting Information section of this chapter). This is due to the SEI layer growing in thickness with increasing cycle number. Thus these data show that although the SEI remains stable in composition it thickens upon multi cycling.

3.4. Surface and bulk modification analyzed by (ToF-SIMS)

The ToF-SIMS negative ion depth profiles of the pristine and cycled (1 and 15 CVs) samples are shown in Figure 4. The intensity variation (presented in logarithmic scale) with sputtering time reflects the modification of the in-depth concentration but is also dependent on the matrix from which the ions are emitted.[37] Fe_2^- ions were selected to characterize the iron substrate and the FeO^-, FeO_2^-, $Fe_2O_3^-$, $Fe_3O_4^-$, Li^- and LiO^- ions to reflect changes of the in-depth composition in the thin-film electrode. It has been thoroughly checked that the monitored ions and their profiles are characteristics of the cycled electrodes.

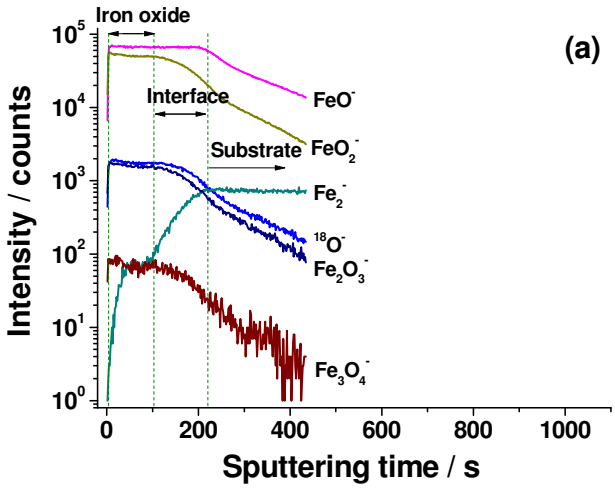

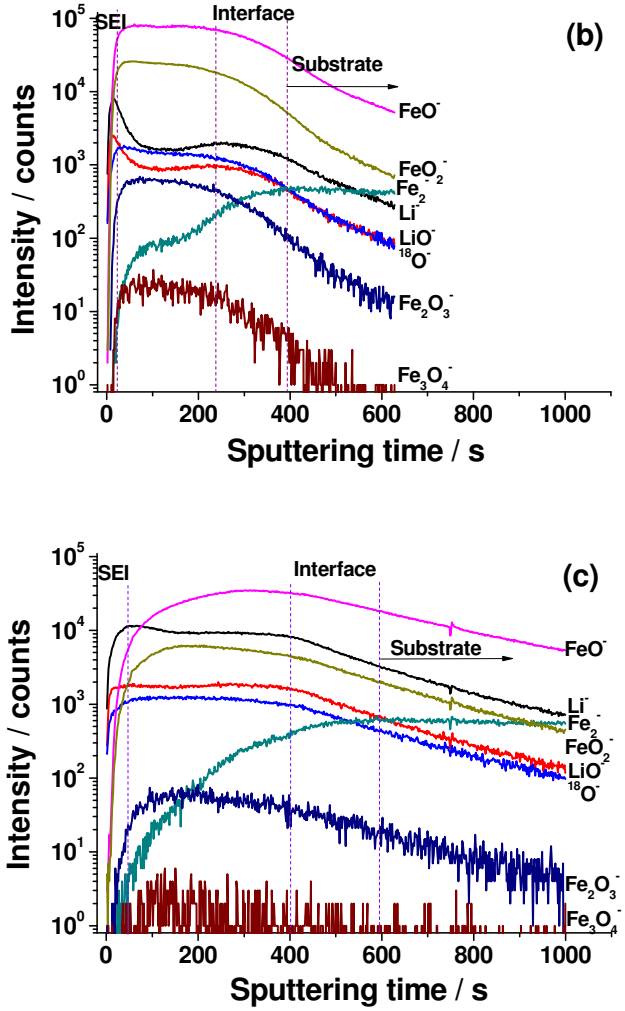

Figure 4 ToF-SIMS negative ion depth profiles of (a) pristine sample and after (b) 1 CV and (c) 15 CV cycles.

For the pristine sample (Figure 4 (a)) three distinct regions are observed. First plateau with a constant signals of FeO^-, FeO_2^-, $Fe_2O_3^-$, $Fe_3O_4^-$ ions defines the bulk region of the iron oxide thin film. After about 105 s sputtering, the Fe_2^- ions increase in intensity, marking the beginning of the interfacial region between the oxide thin film and the metal substrate, until about 215 s where the intensity stabilizes, indicating the end of this interfacial region.

After 1 CV cycle (Figure 4 (b)), a significantly longer sputtering time (390 s) of the bulk region of the iron oxide thin film is measured due to the presence of the SEI layer formed on the electrode surface and to irreversible volume expansion of the thin film caused by lithium insertion. It cannot be excluded that modifications of roughness and matrix (i.e. chemical composition) of the thin-film electrode also influence the sputtering time. After 15 CV cycles

(Figure 4 (c)), this sputtering time increases even more, to about 600 s, clearly indicating further irreversible volume expansion/material swelling induced by repeated lithiation/delithiation. Material swelling upon repeated cycling also causes morphological changes revealed by the SEM and AFM data presented below.

Li trapping in the electrode material is confirmed by the high intensity of Li^- ions in the thin film region, increasing from ~2000 to 10000 counts for 1 and 15 CVs, respectively. This intensity increase coincides with an intensity decrease of the FeO_2^- and $Fe_2O_3^-$ ion profiles plateaus in the thin-film region (i.e. from 50000 to 20000 and 5000 for the FeO_2^- ions after 0, 1 and 15 CV cycles, respectively). This is indicative of a non-fully reversible conversion reaction as previously discussed,[20] leading to accumulation of non deconverted material in the thin-film electrode with repeated cycling. This aging mechanism may contribute to the decrease of the capacity revealed by the galvanostatic discharge-charge data.

The Li^- and LiO^- ion profiles are also markers of the SEI layer formation and evolution. After 1 CV, both profiles exhibit maxima during the first seconds of sputtering before stabilizing in the bulk thin-film region. These peaks clearly stand for the presence of the SEI layer enriched with Li. However, the higher Li concentration in SEI layer than in the electrode bulk can be related to increase sputtering yield of the SEI matrix in comparison to bulk electrode material. After 15 CV cycles, these peaks become less well-defined. This is due to the intensities of the Li^- and LiO^- ion profiles increasing more in the thin-film region than in the SEI layer region. Thus not only non deconverted lithium species would accumulate in the bulk of the oxide thin film upon repeated lithiation/delithiation of the electrode material but the pulverization-induced morphological changes of the material would also induce penetration of the SEI layer into the oxide thin film. One also notices steady intensities of the Li^- and LiO^- ion profiles until the substrate region after 15 CV cycles, indicating that penetration of the SEI layer would reach the oxide film/metal substrate interface.

3.5. Morphology modifications studied by SEM and AFM

Figure 5 presents the FE-SEM data for the iron oxide thin film electrodes before and after electrochemical lithiation (1/2 CV) and delithiation (1 and 15 CV cycles). The

morphology of the pristine iron oxide thin film appears flat and homogeneous (Figure 5 (a) left). Scratches left by the substrate polishing are observed due to the nanometric thickness of the iron-oxide film. At higher magnification (Figure 5 (a) right), a granular morphology is revealed. The grains, having a lateral size of ~20-50 nm, are agglomerated and well delimited by grain boundaries.

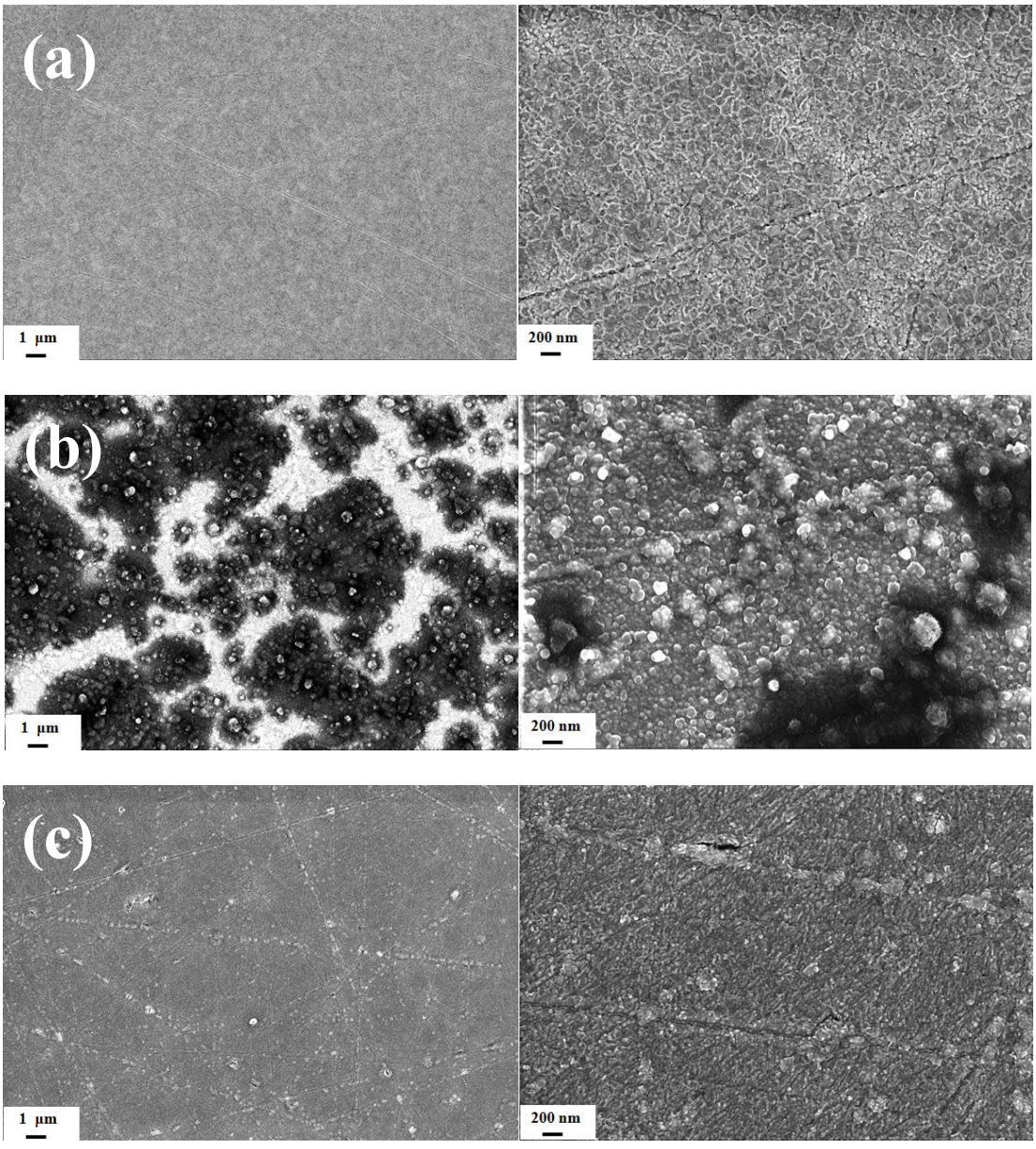

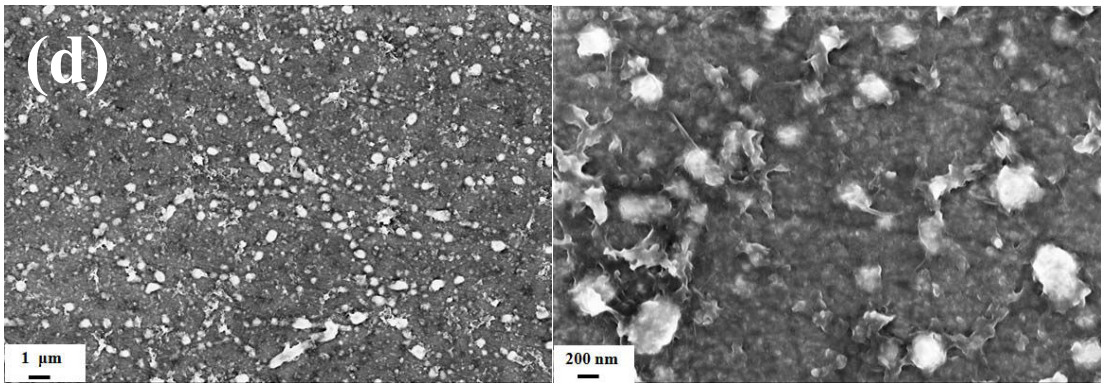

Figure 5 SEM images of (a) pristine sample and after (b) 1/2 CV (stopped at 0.01 V), (c) 1 CV and (d) after 15 CV cycles.

In the lithiated state (Figure 5 (b) left), the thin-film morphology appears less uniform. This may be caused by uneven growth of the SEI [38] and/or be related to uneven modification caused by short exposition to ambient air during sample transfer, which would confirm a lithiated state of the electrode very sensitive to oxidation. Higher magnification (Figure 6 (b) right) reveals grain growth (up to 150 nm in lateral size), which is consistent with volume expansion (i.e. swelling) of the thin-film material due to formation of the conversion reaction products (Li_2O and Fe). As a result the thin-film electrode is much rougher.

After one complete cycle (1 CV) (Figure 5 (c) left), a flatter and more homogeneous morphology is recovered, which is consistent with volume shrinkage of the material and partial decomposition of the SEI layer. At higher magnification (Figure 5 (c) right), the granular structure displays grains (~50 nm in lateral size) smaller than in the lithiated state and slightly bigger than on the pristine sample. This is indicative of the pulverization process inferred from the electrochemical data.

After 15 CV cycles, the morphology of the thin-film electrode is markedly modified. At lower magnification (Figure 5 (d) left), it is obvious that new larger grains, only nascent after 1 CV cycle, are developed and preferentially formed along the surface defects (i.e. scratches) of the substrate. The repeated process of volume expansion-shrinkage of the electrode material leads to 3D growth of grain aggregates exceeding 200 nm in lateral size. As a result the thin-film surface becomes much rougher than after 1 CV cycle due to non-uniform thickening of the electrode material. In between the grain aggregates, the thin-film matrix still consists of smaller grains. However the grains appear less well resolved than after 1 CV cycle.

Grain growth by aggregation may also occur here but thickening and penetration of the SEI layer, as shown by XPS and ToF-SIMS, can play a significant role in blurring the thin-film morphology. These modifications can have a significant influence on capacity fading. No pinholes are observed suggesting no loss of active material in these aging conditions.

Topographic AFM images of the iron oxide thin film electrodes before and after electrochemical lithiation (1/2 CV) and delithiation (1 and 15 CV cycles) are shown in Figure 6.

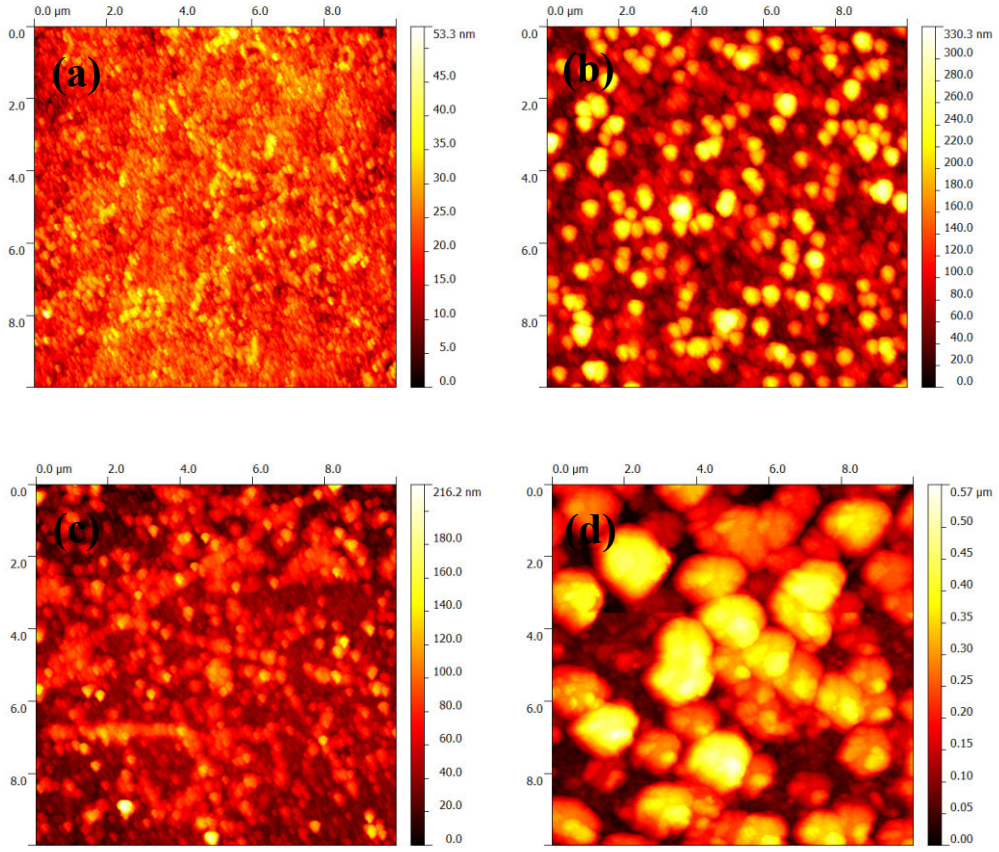

Figure 6 Topographic AFM images (10 µm × 10 µm) of (a) pristine sample and after (b) 1/2 CV (stopped at 0.01 V), (c) 1 CV and (d) after 15 CV cycles.

On the pristine sample (Figure 6 (a)), the observed surface morphology is consistent with a granular structure of the thin-film electrode. A dense arrangement of grains (forming stalagmite-like features) of nanometric dimensions is revealed, indicating a polycrystalline structure of the oxide film as observed by AFM for other thin films grown by thermal oxidation of metal substrates [39] and in agreement with the present SEM data. The average lateral dimension of the grains is ~22 nm, in good agreement with the SEM data. The RMS

roughness is 5.0 nm.

In the lithiated state (Figure 6 (b)), the surface topography shows the formation of much larger grains. The lateral mean dimension of the grains increases to around 112 nm, also in good agreement with the SEM data, and the RMS roughness increases to 56 nm. This confirms 3D growth of the oxide grains induced by the conversion reaction, and thus swelling of the thin-film material caused by volume expansion. These morphological modifications are not uniformly spread over the thin film electrode surface, as also observed by SEM.

After 1 CV cycle (Figure 6 (c)), an obvious phenomena of volume shrinkage is observed. The lateral mean dimension of the grains decreases to ~57 nm and the RMS roughness to 23.8 nm. These values remain higher than for the pristine surface, showing irreversible swelling of the electrode material in agreement with the ToF-SIMS data. One can see that the largest grains, indicative of the most advanced morphological modifications of the electrode material, are preferentially located along the substrate defects (i.e. scratches), as also shown by the SEM data. Smaller grains indicative of the pulverization of the electrode material are not observed.

After 15 CV cycles (Figure 6 (d)), the surface is covered with grain aggregates of even larger mean dimensions (average lateral dimension of 216 nm), showing amplification of the irreversible morphological modifications of the electrode material. The surface coverage by these grain aggregates is non-uniform at the nanometer scale, also confirming the SEM observation, and leading to further increase of the surface roughness (RMS value of 116 nm). Obviously, repeated volume expansion/contraction of the conversion-type electrode material combined with SEI layer penetration in the bulk of the thin film, as inferred from the ToF-SIMS data, leads to irreversible swelling of the electrode material. This phenomenon, generalized at the microscopic scale, is inhomogeneous at the nanoscopic scale and promoted at defect sites of the metal surface substrate, at least in the initial stages of aging.

4. Conclusions

These electrochemical (CV, EIS), spectroscopic (XPS, ToF-SIMS) and microscopic (SEM, AFM) data obtained on iron oxide (mostly Fe_2O_3) using a thin film approach combine consistently to demonstrate that both the SEI layer and iron oxide thin film anode evolve

during multi-cycling which influences the performance of iron oxide as anode in LIBs.

The following conclusions are drawn:

- The SEI layer formed by reductive decomposition of the electrolyte is principally composed of Li_2CO_3 and $ROCO_2Li$ and/or Li-alkoxides (RCH_2OLi). Multi-cycling induces no marked changes of the SEI composition but increases the thickness in the delithiated state.
- Penetration of the SEI layer and cumulative trapping of Li^+ ions due to irreversible conversion/deconversion occur in the bulk electrode material upon repeated lithiation/delithiation. Both contribute to irreversible swelling and compositional changes of the electrode material with accumulation of non deconverted material in the thin film electrode.
- Morphological changes include pulverization of the thin film electrode material and agglomeration of oxide nanograins upon cycling. In the first five cycles, this promotes capacity increase but upon further cycling volume expansion and accumulation of non deconverted material lead to deterioration of the electrode performances with capacity fading to about 78 % of the maximum capacity after 50 cycles.

References

[1] Thackeray M.M.; David W.I.F.; Goodenough J.B. High-temperature Lithiation of α-Fe_2O_3: A Mechanistic Study. *J. Solid State Chem.* **1984**, *55*, 280-286.

[2] Poizot P.; Laruelle S.; Grugeon S.; Dupont L.; Tarascon J.-M. Nano-sized Transition-metal Oxides as Negative-electrode Materials for Lithium-ion Batteries. *Nature* **2000**, *407*, 496-499.

[3] Aricò A.S.; Bruce P.; Scrosati B.; Tarascon J.-M.; Schalkwijk W.V. Nanostructured Materials for Advanced Energy Conversion and Storage Devices. *Nat. Mater.* **2005**, *4*, 366-377.

[4] Taberna P.L.; Mitra S.; Poizot P.; Simon P.; Tarascon J.-M. High Rate Capabilities Fe_3O_4-based Cu Nano-architectured Electrodes for Lithium-ion Battery Applications. *Nat. Mater.* **2006**, *5*, 567-573.

[5] Cherian C.T.; Sundaramurthy J.; Kalaivani M.; Ragupathy P.; Suresh Kumar P.; Thavasi V.; Reddy M.V.; Sow C.H.; Mhaisalkar S.G.; Ramakrishna S.; Chowdari B.V.R. Electrospun α-Fe_2O_3 Nanorods as a Stable, High Capacity Anode Material for Li-ion Batteries. *J. Mater. Chem.* **2012,** *22*, 12198-12204.

[6] Banerjee A.; Aravindan V.; Bhatnagar S.; Mhamane D.; Madhavi S.; Ogale S. Superior Lithium Storage Properties of α-Fe_2O_3 Nano-assembled Spindles. *Nano Energy* **2013**, *2*, 890-896.

[7] Qu J.; Yin Y.-X.; Wang Y.-Q.; Yan Y.; Guo Y.-G.; Song W.-G. Layer Structured α-Fe_2O_3 Nanodisk/Reduced Graphene Oxide Composites as High-Performance Anode Materials for Lithium-Ion Batteries. *ACS Appl. Mater. Interfaces* **2013**, *5*, 3932-3936.

[8] Aurbach D. Review of Selected Electrode-solution Interactions Which Determine the Performance of Li and Li Ion Batteries. *J. Power Sources* **2000**, *89*, 206-218.

[9] Ensling D.; Thissen A.; Jaegermann W. On the Formation of Lithium Oxides and Carbonates on Li Metal Electrodes in Comparison to $LiCoO_2$ Surface Phases Investigated by Photoelectron Spectroscopy. *Appl. Surf. Sci.* **2008**, *255*, 2517-2523.

[10] Aurbach D.; Markovsky B.; Salitra G.; Markevich E.; Talyossef Y.; Koltypin M.; Nazar L.; Ellis B.; Kovacheva D. Review on Electrode-electrolyte Solution Interactions, Related to Cathode Materials for Li-ion Batteries. *J. Power Sources* **2007**, *165*, 491-499.

[11] Nie M.; Chalasani D.; Abraham D.P.; Chen Y.; Bose A.; Lucht B.L. Lithium Ion Battery Graphite Solid Electrolyte Interphase Revealed by Microscopy and Spectroscopy. *J. Phys. Chem. C* **2013**, *117*, 1257-1267.

[12] Shu Z.X.; Mcmillan R.S.; Murray J.J. Electrochemical Intercalation of Lithium into Graphite. *J. Electrochem. Soc.* **1993**, *140*, 922-927.

[13] Levi M.D.; Aurbach D. Diffusion Coefficients of Lithium Ions during Intercalation into Graphite Derived from the Simultaneous Measurements and Modeling of Electrochemical Impedance and Potentiostatic Intermittent Titration Characteristics of Thin Graphite Electrodes. *J. Phys. Chem. B* **1997**, *101*, 4630-4640.

[14] Kanamura K.; Shiraiski S.; Takezawa H.; Takehara Z. XPS Analysis of the Surface of a Carbon Electrode Intercalated by Lithium Ions. *Chem. Mater.* **1997**, *9*, 1797-1804.

[15] Andersson A.M.; Herstedt M.; Bishop A.G.; Edström K. The Influence of Lithium Salt on the Interfacial Reactions Controlling the Thermal Stability of Graphite Anodes. *Electrochim. Acta* **2002**, *47*, 1885-1898.

[16] Herstedt M.; Andersson A.M.; Rensmo H.; Siegbahn H.; Edström K. Characterisation of the SEI Formed on Natural Graphite in PC-based Electrolytes. *Electrochim. Acta* **2004**, *49*, 4939-4947.

[17] Yamada Y.; Iriyama Y.; Abe T.; Ogumi Z. Kinetics of Lithium Ion Transfer at the Interface between Graphite and Liquid Electrolytes: Effects of Solvent and Surface Film. *Langmuir* **2009**, *25*, 12766-12770.

[18] Lai Y.; Cao Z.; Song H.; Zhang Z.; Chen X.; Lu H.; Jia M.; Li J. Influence of Fe (II) Species in Electrolyte on Performance of Graphite Anode for Lithium-Ion Batteries. *J. Electrochem. Soc.* **2012**, *159*, A1961-A1966.

[19] Pinson M.B.; Bazant M.Z. Theory of SEI Formation in Rechargeable Batteries: Capacity Fade, Accelerated Aging and Lifetime Prediction. *J. Electrochem. Soc.* **2013**, *160*, A243-A250.

[20] Tian B.; Światowska J.; Maurice V.; Zanna S.; Seyeux A.; Klein L.H.; Marcus P. Combined Surface and Electrochemical Study of the Lithiation/Delithiation Mechanism of Iron Oxide Thin Film Anode for Lithium-Ion Batteries. *J. Phys. Chem. C* **2013**, *117*, 21651-21661.

[21] Larcher D.; Masquelier C.; Bonnin D.; Chabre Y.; Mason V.; Leriche J.B.; Tarascon J.-M. Effect of Particle Size on Lithium Intercalation into α-Fe_2O_3. *J. Electrochem. Soc.* **2003**, *150*, A133-A139.

[22] Larcher D.; Bonnin D.; Cortes R.; Rivals I.; Personnaz L.; Tarascon J.-M. Combined XRD, EXAFS, and Mössbauer Studies of the Reduction by Lithium of α-Fe_2O_3 with Various Particle Sizes. *J. Electrochem. Soc.* **2003**, *150*, A1643-A1650.

[23] Reddy M.V.; Yu T.; Sow C.H.; Shen Z.X.; Lim C.T.; Subba Rao G.V.; Chowdari B.V.R. α-Fe_2O_3 Nanoflakes as an Anode Material for Li-Ion Batteries. *Adv. Funct. Mater.* **2007**, *17*, 2792-2799.

[24] Bruce P. G.; Scrosati B.; Tarascon J.-M. Nanomaterials for Rechargeable Lithium Batteries. *Angew. Chem. Int. Ed.* **2008**, *47*, 2930-2946.

[25] Carraro G.; Barreca D.; Cruz-Yusta M.; Gasparotto A.; Maccato C.; Morales J.; Sada C.; Sanchez L. Vapor-Phase Fabrication of β-Iron Oxide Nanopyramids for Lithium-Ion Battery Anodes. *ChemPhysChem* **2012**, *13*, 3798-3801.

[26] Hosono E.; Fujihara S.; Honma I.; Ichihara M.; Zhou H. Fabrication of Nano/Micro Hierarchical Fe_2O_3/Ni Micrometer-Wire Structure and Characteristics for High Rate Li Rechargeable Battery. *J. Electrochem. Soc.* **2006**, *153*, A1273-A1278.

[27] Beamson, G.; Briggs, D. High Resolution XPS of Organic Polymers, the Scienta ESCA 300 Database. *John Wiley & Sons*, **1992**.

[28] Światowska-Mrowiecka J.; Maurice V.; Zanna S.; Klein L.; Marcus P. XPS Study of Li Ion Intercalation in V_2O_5 Thin Films Prepared by Thermal Oxidation of Vanadium Metal. *Electrochim. Acta* **2007**, *52*, 5644-5653.

[29] Światowska-Mrowiecka J.; Martin F.; Maurice V.; Zanna S.; Klein L.; Castle J.; Marcus P. The

Distribution of Lithium Intercalated in V_2O_5 Thin Films Studied by XPS and ToF-SIMS. *Electrochim. Acta* **2008**, *53*, 4257-4266.

[30] Światowska-Mrowiecka J.; Diesbach de S.; Maurice V.; Zanna S.; Klein L.; Briand E.; Vickridge I.; Marcus P. Li-Ion Intercalation in Thermal Oxide Thin Films of MoO_3 as Studied by XPS, RBS, and NRA. *J. Phys. Chem. C* **2008**, *112*, 11050-11058.

[31] McIntyre N.S.; Zetaruk D.G. X-ray Photoelectron Spectroscopic Studies of Iron Oxides. *Anal. Chem.* **1977**, *49*, 1521-1529.

[32] Li J.-T.; Maurice V.; Światowska-Mrowiecka J.; Seyeux A.; Zanna S.; Klein L.; Sun S.-G.; Marcus P. XPS, Time-of-Flight-SIMS and Polarization Modulation IRRAS Study of Cr_2O_3 Thin Film Materials as Anode for Lithium Ion Battery. *Electrochim. Acta* **2009**, *54*, 3700-3707.

[33] Martensson N.; Malmquist P. A.; Svensson S.; Basilier E.; Pireaux J. J.; Gelius U.; Siegbahn K. Molecular and Solid Water, a Comparative ESCA Study. *Nouveau J. Chim.* **1977**, *1*, 191-195.

[34] Benayad A.; Martinem H.; Gies A.; Pecquenard B.; Lavasseur A.; Gonbeau D. XPS Investigations Achieved on the First Cycle of V_2O_5 Thin Films Used in Lithium Microbatteries. *J. Electron Spectrosc. Relat. Phenom.* **2006**, *150*, 1-10.

[35] Chagnes A.; Swiatowska J. Lithium Ion Batteries - New Developments, in: I. Belharouak (Ed.), Electrolyte and Solid-Electrolyte Interphase Layer in Lithium-Ion Batteries. *INTECH*, **2012**, 145-172.

[36] Dedryvère R.; Laruelle S.; Grugeon S.; Gireaud L.; Tarascon J.-M.; Gonbeau D. XPS Identification of the Organic and Inorganic Components of the Electrode/Electrolyte Interface Formed on a Metallic Cathode. *J. Electrochem. Soc.* **2005**, *152*, A689-A696.

[37] Li J.-T.; Światowska J.; Maurice V.; Seyeux A.; Huang L.; Sun S.G.; Marcus P. XPS and ToF-SIMS Study of Electrode Processes on Sn-Ni Alloy Anodes for Li-Ion Batteries. *J. Phys. Chem. C* **2011**, *115*, 7012-7018.

[38] Peled E.; Bar Tow D.; Merson A.; Gladkich A.; Burstein L.; Golodnitsky D. Composition, Depth Profiles and Lateral Distribution of Materials in the SEI Built on HOPG-TOF SIMS and XPS Studies. *J. Power Sources* **2001**, *97-98*, 52-57.

[39] Światowska-Mrowiecka J.; Maurice V.; Zanna S.; Klein L.; Briand E.; Vickridge I.; Marcus P. Ageing of V_2O_5 Thin Films Induced by Li Intercalation Multi-cycling. *J. Power Sources* **2007**, *170*, 160-172.

Supporting Information for Chapter 3

Electrochemical impedance spectroscopy (EIS) is one of the most adequate *in situ* electrochemical techniques for analysis of electrode/electrolyte interfacial properties including formation of the SEI layer. [1-3] Herein, the EIS measurements were carried out at room temperature after cumulated CV cycles in order to evaluate the evolution of the SEI layer upon cycling. The EIS spectra are presented in Fig. S1.

The spectrum obtained at open circuit potential (OCP) on the Fe_2O_3 pristine electrode before cycling (Figure S1, OCP) shows a straight line indicating mostly capacitive behavior (i.e. insertion capacitance) resulting from the accumulation of Li^+ ions on the surface of the thin-film electrode, as usually observed on non-cycled electrode at OCP. [3-8] The electrolyte resistance is about 153 (ohm cm^2) as determined from high-frequency intercept of the Z'-axis.

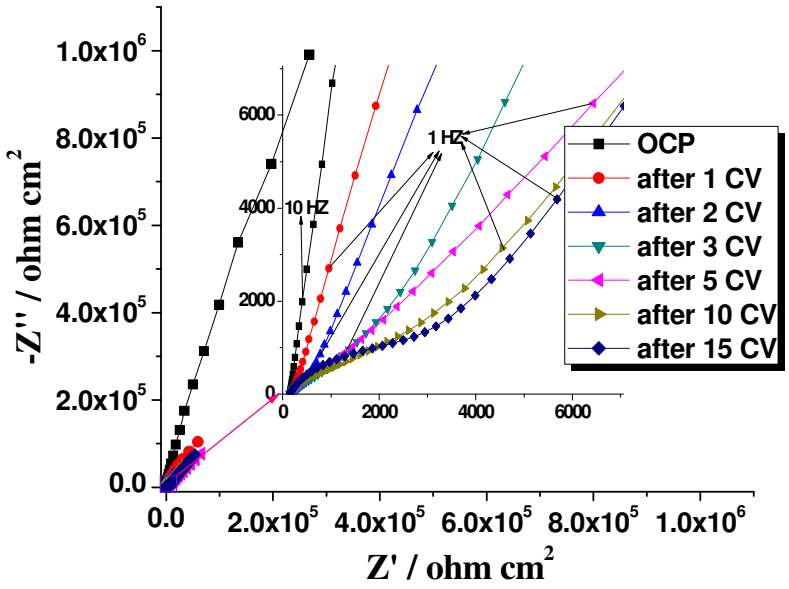

Figure S1. Electrochemical impedance spectra of the iron oxide thin film electrode recorded at OCP prior to and after cycling; Inset: Magnified electrochemical impedance spectra in high frequency region.

After the 1st CV cycle, the slope of the straight line slightly decreases indicating modification of the electrode/electrolyte interface, which can be related to formation of the SEI layer as shown by the XPS and ToF-SIMS results. After 3-5 CV cycles, the EIS data show a nascent deviation from straight line and a depressed semi-circle develops with further cycling, indicating growth of the SEI layer. Moreover, the

inclination of the straight line at lower frequencies decreases with cycling. This indicates a change from an infinite diffusion-like process (Li concentration n(x,t) in the pristine thin film is zero within the layer (n(x,0)=0, x>0) and n_0 outside (n(x, 0)=n_0, x≤0)) to a semi-infinite diffusion-like process (starting at 0 at the surface and spreading infinitely deep in the material), [9] possibly due morphological and chemical modification of the thin-film electrode and growth of the SEI layer. This evolution, initiated already after the first cycle, is confirmed by the ToF-SIMS data presented in the main text. With uptake of the SEI layer thickness and lithium trapping in the bulk electrode, the total thickness of the thin-film electrode covered by SEI layer increases during cycling, influencing the Li^+ transport. Thus these EIS results, in complement with the CV data and the XPS data, show that the SEI layer is mainly formed in the first CV and then increases in thickness together with the deconverted thin-film electrode in the subsequent CV cycles.

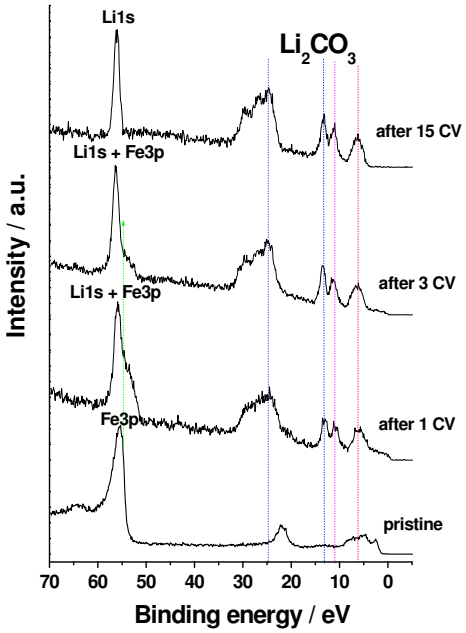

Figure S2. XP Fe3p-Li1s core level and VB region spectra of pristine and cycled samples.

Fig. S2 shows XP Fe3p-Li1s core level and VB region spectra of pristine and cycled samples. The Fe3p-Li1s region, between 50 to 60 eV, presents only the Fe3p peak at E_B = 55.3 eV on the pristine sample. After 1 and 3 CV cycles, an intense Li1s

peak appears at E_B = 56.0 eV in this region with the Fe3p peak becoming a lower binding energy shoulder of decreasing intensity with cycle number. After 15 CV, the Fe3p peak is completely attenuated and only the Li1s peak remains. This is consistent with thickening of the SEI layer with repeated cycling.

The peaks observed at E_B = 5.2, 10.0, 12.0 and 22.9 eV in the VB region (3-30 eV) after electrochemical cycling, are a fingerprint of the presence of Li_2CO_3, [10] the major constituent of the SEI layer.

References

[1] Wang C.; Appleby A.J.; Little F.E. Electrochemical Impedance Study of Initial Lithium Ion Intercalation into Graphite Powders. *Electrochim. Acta* **2001**, *46*, 1793-1813.

[2] Barsoukov E.; Kim J.H.; Kim J.H.; Yoon C.O.; Lee H. Effect of Low-Temperature Conditions on Passive Layer Growth on Li Intercalation Materials: In Situ Impedance Study. *J. Electrochem. Soc.* **1998**, *145*, 2711-2717.

[3] Chang Y.C.; Sohn H.J. Electrochemical Impedance Analysis for Lithium Ion Intercalation into Graphitized Carbons. *J. Electrochem. Soc.* **2000**, *147*, 50-58.

[4] Yang C.R.; Song J.Y.; Wang Y.Y.; Wan C.C. Impedance Spectroscopic Study for the Initiation of Passive Film on Carbon Electrodes in Lithium Ion Batteries. *J. Appl. Electrochem.* **2000**, *30*, 29-34.

[5] Aurbach D.; Moshkovich M.; Cohen Y.; Schechter A. The Study of Surface Film Formation on Noble-Metal Electrodes in Alkyl Carbonates/Li Salt Solutions, Using Simultaneous in Situ AFM, EQCM, FTIR, and EIS, *Langmuir* **1999**, *15*, 2947-2960.

[6] Song J.Y.; Lee H.H.; Wang Y.Y.; Wan C.C. Two- and Three-electrode Impedance Spectroscopy of Lithium-ion Batteries. *J. Power Sources* **2002**, *111*, 255-267.

[7] Etacheri V.; Haik O.; Goffer Y.; Roberts G.A.; Stefan I.C.; Fasching R.; Aurbach D. Effect of Fluoroethylene Carbonate (FEC) on the Performance and Surface Chemistry of Si-Nanowire Li-Ion Battery Anodes. *Langmuir* **2012**, *28*, 965-976.

[8] Yamada Y.; Iriyama Y.; Abe T.; Ogumi Z. Kinetics of Lithium Ion Transfer at the Interface between Graphite and Liquid Electrolytes: Effects of Solvent and Surface Film. *Langmuir* **2009**, *25*, 12766-12770.

[9] Bokshtein B. S.; Bokshtein S. Z.; Zhukhovitskii A. A. Thermodynamics and Kinetics of Diffusion in Solids. *Oxonian Press* **1985**.

[10] Dedryvère R.; Gireaud L.; Grugeon S.; Laruelle S.; Tarascon J.-M.; Gonbeau D. Characterization of Lithium Alkyl Carbonates by X-ray Photoelectron Spectroscopy: Experimental and Theoretical Study. *J. Phys. Chem. B* **2005**, *109*, 15868-15875.

Chapter 4. Kinetics evaluation of thin film α-Fe_2O_3 negative electrode for lithium-ion batteries

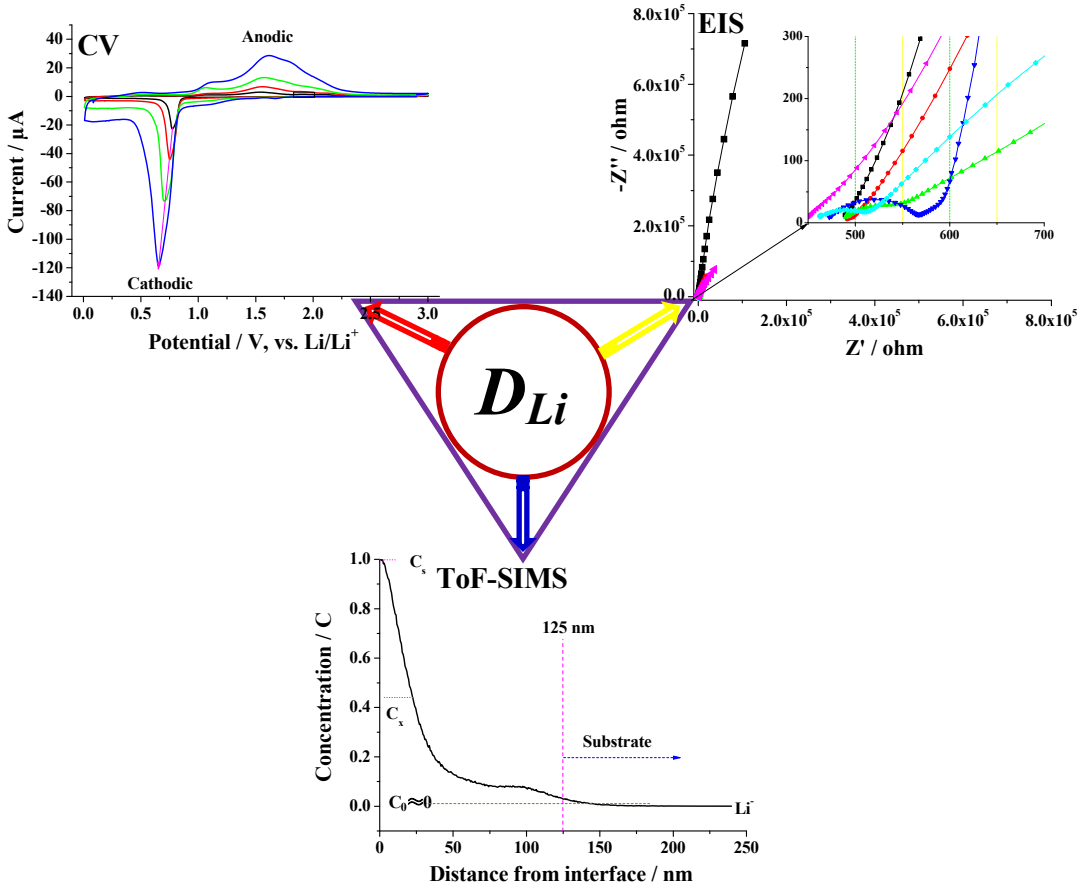

A version of this chapter is to be submitted.

Some results of this chapter also contributed to *IMLB 2014*, June 10-14, 2014, Como, Italy.

Abstract: The solid-state diffusion of lithium into α-Fe_2O_3 thin film electrodes during electrochemical lithiation and delithiation process was investigated using cyclic voltammetry (CV), electrochemical impedance spectroscopy (EIS) and time-of-flight secondary ions mass spectrometry (ToF-SIMS), and the compositional changes of the SEI layer at selected potentials was analysed by X-ray photoelectron spectroscopy (XPS) during discharge/charge. The diffusion coefficient of lithium (D_{Li}) obtained by CV from the cathodic and anodic electrochemical reactions are 1.7×10^{-15} and 2.4×10^{-16} cm^2 s^{-1}, respectively. The D_{Li} values obtained from EIS show a variation from 10^{-15} to 10^{-19} cm^2 s^{-1} as a function of lithiation/delithiation potentials. ToF-SIMS analysis for extracting the diffusion coefficient of lithium (D_{Li}) was based on the in-depth variation of the Li-ion concentration obtained by depth profiling a partially lithiated sample. It allowed excluding the SEI layer and discriminating Li-ion diffusion in the converted electrode ($D_{Li} = 0.6\times10^{-15}$ cm^2 s^{-1}) and in the intercalation regions ahead of the conversion front ($D_{Li} = 2\times10^{-13}$ cm^2 s^{-1}). The D_{Li} value obtained from cyclic voltammetry analysis of the reductive lithiation is 1.7×10^{-15} cm^2 s^{-1}, slightly higher than that measured in the converted electrode by ToF-SIMS, due to the dynamic process of formation of the SEI layer (confirmed by XPS) and dynamic conversion of the electrode in the analysis conditions. The D_{Li} value obtained from EIS is 3.6×10^{-16} cm^2 s^{-1} at a point corresponding to discharge to 0.84 V, in agreement with the value obtained from ToF-SIMS in the converted region and shows an hindering effect of the SEI layer on ionic migration. ToF-SIMS analysis, combined with a thin film approach, as a direct measurement method of the Li diffusion in electrodes, was decisive for making distinction between different regimes of diffusion as a function of the lithiation penetration depth and for excluding the influence of SEI layer on the data analysis.

Keywords: thin film α-Fe_2O_3 negative electrode; lithium diffusion; electrochemical impedance spectroscopy (EIS); cyclic voltammetry (CV); ToF-SIMS; XPS

1. Introduction

Nano-sized transition metal oxides particles (CoO, Co_3O_4, NiO, CuO, Cu_2O, and FeO) were first reported as anode materials for lithium-ion batteries by Poizot et al.[1-4] These types of materials exhibit reversible capacities up to three times higher than graphite electrodes. Among the transition metal oxides, hematite (α-Fe_2O_3) is one of the most interesting and important metal oxide, for its high theoretical capacity (1007 mAh g^{-1}), abundance and low cost, low toxicity and environmental friendliness. Since reported as one of the conversion-type material by D. Larcher et al.,[5,6] it has been studied as candidate anode material for lithium-ions batteries. However, α-Fe_2O_3 suffers from poor electronic/ionic conductivity, the main obstacle for improving rate capability which is a primary demand for high power equipment such as EVs. The future application of such a conversion-type material lies in mastering its electrochemical performances that depend on electrode reactions, interphase chemistry and ion mobility (i.e. lithium diffusion into iron oxide).[7,8] Relatively little attention has been devoted to understanding the diffusion mechanisms by which Li^+ ions migrate through the SEI into the bulk electrode material during the discharge/charge process, and to determine apparent diffusion coefficient of lithium (D_{Li}).

Li^+ ions migration into graphite (intercalation-type) and silicon (alloying-type) anodes has been studied by various techniques including electrochemical impedance spectroscopy (EIS),[9-14] cyclic voltammetry (CV),[12,15,16] potentiostatic intermittent titration technique (PITT),[10,12,17] galvanostatic intermittent titration technique (GITT)[12,18] and potential relax technique (PRT).[19] However, for conversion-type material (e.g. iron oxide), ionic migration has been rarely studied due to lack of theoretical model. It is generally believed that the kinetic regime is a conversion-controlled rather than a diffusion-controlled process. However, in our previous work, conversion proceeding mostly in the outer part of the iron oxide thin film electrode during the lithiation process has been confirmed.[20] This was also observed previously for conversion-type Cr_2O_3.[21] In this case, Li^+ ions migration primarily through the SEI and the converted matrix (Li_2O/Fe^0) then through the non-converted bulk oxide material (Fe_2O_3)) can be assumed as a one-dimensional diffusion process.

In this study, in order to investigate thoroughly the lithiation kinetics of conversion-type iron oxide, three methods were combined to evaluate the diffusion coefficient of Li ions (D_{Li}):

(1) cyclic voltammetry (CV) performed at different scan rates;[22] (2) electrochemical impedance spectroscopy (EIS);[23,24] (3) time-of-flight secondary ions mass spectrometry (ToF-SIMS). The α-Fe_2O_3 thin film electrodes were prepared by thermal oxidation of pure iron substrate. These thin film electrodes possessing large surface-to-volume ratio, without carbon and polymeric binder additives, can provide clearer insight into electrode/electrolyte interfacial reactions and apparent diffusion coefficients of lithium (D_{Li}) into Fe_2O_3 and/or $Li_2O/Fe^0/Fe_2O_3$ matrices can be obtained. Moreover, in order to characterize the kinetics of formation, decomposition and stability of the SEI layer formed on iron oxide electrode during lithiation and delithiation processes, X-ray photoelectron spectroscopy (XPS) was applied to analyse the compositional changes of the iron oxide thin film and SEI layer at selected potentials of discharge/charge.

2. Experimental methods

An iron foil (Goodfellow, purity: 99.5 wt%; thickness: 0.05 mm) was polished with diamond spray down to 1/4 μm, then successively rinsed in acetone, ethanol and Millipore© water (resistivity > 18 MΩ cm) with ultrasonic cleaning for 2 min and dried in a compressed air flow. This as prepared iron foil sheet was annealed at 300°C for 5 min under air atmosphere and then quenched with 0°C water.[20] Then the oxidized sheet was cut into 8 × 8 mm^2 squares for later use. The average thickness of the oxide thin films was 125 nm as evaluated by profilometry after ToF-SIMS depth profiling on the pristine sample. Raman spectroscopy (Horiba Xplora system, Ar^+ laser, λ = 532 nm) was employed for phase identification of the thermal oxide.

The electrochemical measurements (CV, galvanostatic discharge-charge, EIS) were performed in a glovebox (Jacomex) under Ar atmosphere with H_2O and O_2 contents lower than 1 ppm. A three-electrode glass half-cell was used with the iron oxide film as working electrode and Li foil (Sigma-Aldrich) as reference and counter electrodes. All potentials hereafter are given versus Li/Li^+ reference electrode. The electrochemical measurements were performed at room temperature using an Autolab (AUT30) electrochemical workstation. The working electrode area was delimited to 0.28 cm^2 by an O-ring. The electrolyte was 1 M $LiClO_4$ in propylene carbonate (1 mol L^{-1} $LiClO_4$/PC, Sigma-Aldrich). CV was performed over the

potential range of 3.0 - 0.01 V at different scanning rates. Galvanostatic discharge-charge was performed at a current density of 10 μA cm^{-1} in the potential range of 3.0 - 0.01 V. The frequency range of the EIS measurements was 100 KHz to 10 mHz with a low ac voltage amplitude of 5 mV. The cell was kept at selected potential values and the EIS was performed at equilibrium state when a voltage change was less than 0.01 V in 10 min.

For XPS and ToF-SIMS analyses, the thin films were electrochemically treated at various stages of the first discharge-charge cycle. After discharge-charge to the potential of interest, the cell was disassembled and the sample was rinsed with acetonitrile (99.8%, Sigma-Aldrich) and dried with Ar flow. It is then transferred directly from the glovebox to the ultra-high vacuum XPS [25] or ToF-SIMS analysis chamber.

Li^- ion depth profiles were acquired using a ToF-SIMS 5 (Ion Tof - Munster, Germany). The operating pressure of the spectrometer was about 10^{-9} mbar. A pulsed 25 keV Bi^+ primary ion source was employed for analysis, delivering 1.2 pA current over a 100 × 100 μm^2 area. Depth profiling was carried out using a 1 keV Cs^+ sputter beam giving a 70 nA target current over a 300 × 300 μm^2 area. The Ion-Spec software was used for data acquisition and processing.

Surface chemical analysis was performed using a XPS (VG ESCA-LAB 250 spectrometer) operating at 2 × 10^{-9} mbar with an Al Kα monochromatized radiation (hv = 1486.6 eV). Survey spectra and high resolution core level spectra were recorded with a pass energy of 100 eV and 20 eV, respectively. Peak fitting was performed with the Avantage software v. 3.13, using a Shirley type background and Lorentzian/Gaussian (30/70) peak shapes. The binding energies were calibrated by setting the C1s hydrocarbon (-CH_2-CH_2-) peak at 285.0 eV.

3. Results and discussion

3.1. Structure and composition

The structure and surface composition of the iron foil samples before and after oxidation are shown in Figure 1. Figure 1(a) shows the Raman spectra in the range of 100 - 2000 cm^{-1}. There is no detectable crystallized oxide phase on the metal iron surface before oxidation. After oxidation, the surface oxide was crystallized to α-Fe_2O_3 (hematite) with a small amount of Fe_3O_4 (magnetite) and FeOOH as discussed in chapter 2.[20,26-28] The XPS survey spectra

(Figure 1(b)) before and after oxidation both demonstrate that only Fe, O, and C elements are present. However, the higher O intensity and disappearance of sharp low binding energy Fe2p peak corresponding to metallic iron (Fe^0) observed for the oxidized sample (Figure 1(c)) indicate modification of the surface by formation of a thick oxide layer. ToF-SIMS negative ion depth profiles of the pristine sample after oxidation are shown in Figure 1(d). Fe-containing ions (FeO^-, FeO_2^-, Fe_2^-, $Fe_2O_3^-$, $Fe_3O_4^-$) show three distinct regions on the electrode, that correspond to the bulk region of the iron oxide film (mainly Fe_2O_3), the metallic iron substrate region and the interface region between oxide film and metal substrate.

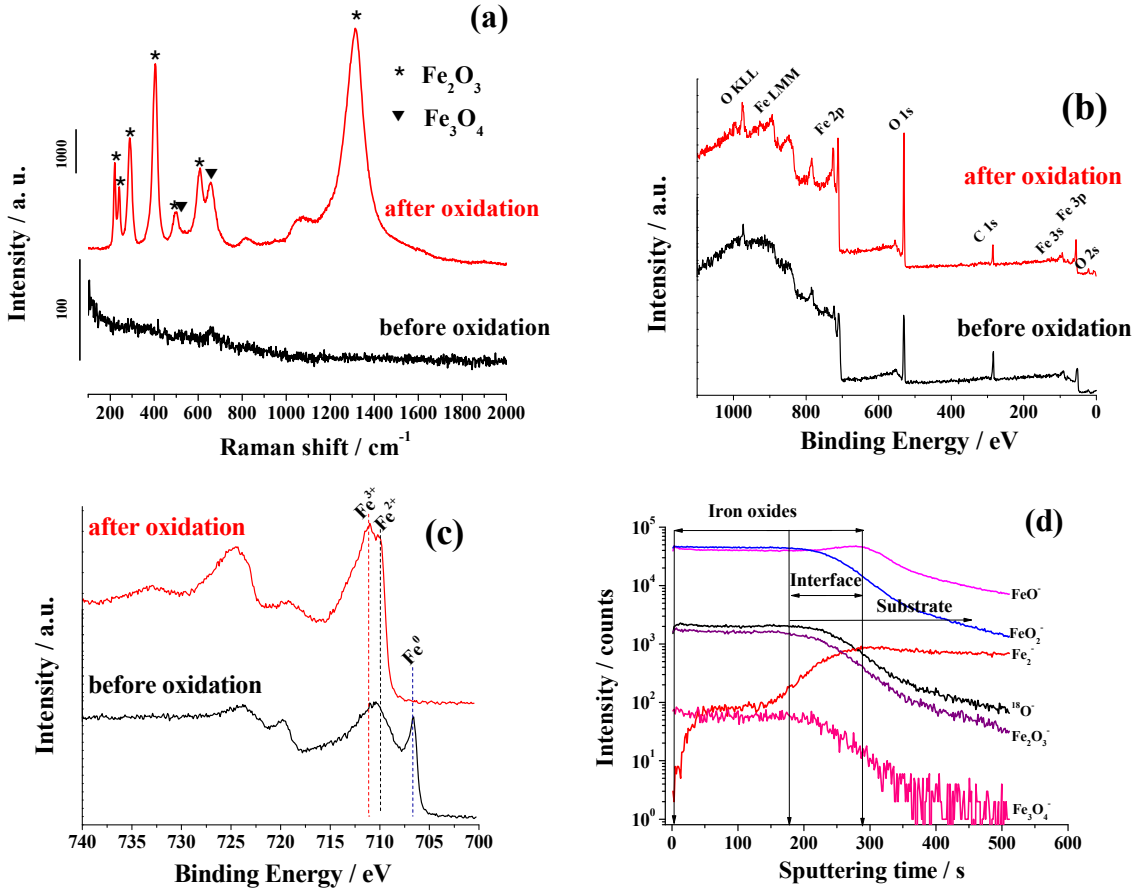

Figure 1 (a) Raman spectra, (b) XP survey spectra, (c) XP Fe2p spectra before and after oxidation of pure iron foil and (d) ToF-SIMS negative ion depth profiles of the pristine sample after oxidation.

3.2. Diffusion evaluation from cyclic voltammetry

Figure 2 shows the first cyclic voltammograms of the thin (~125 nm) film electrodes at different scan rates (v = 0.1 - 1.0 mV s^{-1}) in the voltage range of 3.0 - 0.01 V and the corresponding plot of anodic and cathodic peak current (I_p) vs. $v^{1/2}$.

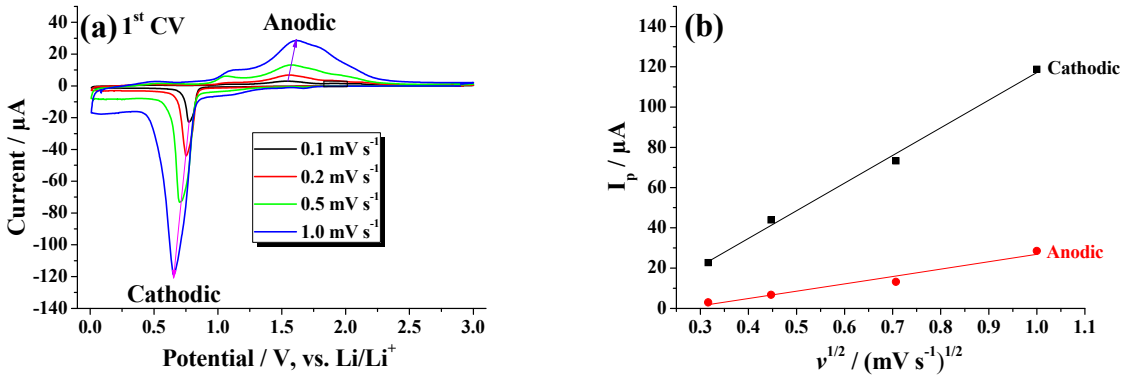

Figure 2 (a) First cyclic voltammograms of the electrodes at different scan rates (v = 0.1 - 1.0 mV s^{-1}) in the voltage range of 3.0 - 0.01 V; (b) corresponding plots of anodic and cathodic peak current (I_p) vs. $v^{1/2}$.

In the reduction half-cycle, the CV curve shows a current increase from about 1.7 V, which corresponds to the intercalation of Li into Fe_2O_3 film to form intermediate $Li_xFe_2O_3$ (0<x<2) and the initial formation of the solid electrolyte interface (SEI) on the surface of the thin film electrode as discussed in chapter 2.[5,6,20] An apparently non-fully reversible reduction peak appears at 0.75 V, which is related to the reduction of Fe_2O_3 to metallic Fe and Li_2O.[5,6,29,30] This reduction process also overlaps partially with the broad cathodic peak corresponding to formation of the SEI film, leading to the irreversible capacity loss in the first cycle as discussed in chapter 3.[20,30] In the anodic scan, a broad peak centered at ~1.56 V indicates an oxidization process of Li_2O with metallic iron. The heterogeneous solid-state uptake/extraction reaction during the lithiation/delithiation process could be written according to the following equation:[5,6,20,30]

$$Fe_2O_3 + 6Li \leftrightarrow 3Li_2O + 2Fe \quad (1)$$

For this reaction, if the cell is simply considered as conventionally described:

$$Li\left|Li^+\right\|Fe_2O_3\left|Fe^0, Li_2O\right. \quad (2)$$

the thermodynamic equilibrium voltage or so-called electromotive force (EMF) value E can be calculated using the Nernst equation from the Gibbs free energy change:

$$\Delta_r G = -nEF \quad (3)$$

where n refers to the number of electrons transferred during the reaction and F is the Faraday

constant. In our experimental conditions, the pressure is approximately equal to standard pressure (p_0 = 0.1 MPa) and T = 298.15 K (experimental temperature is 25°C). In this case, the Gibbs free energy change ($\Delta_r G$) is equal to the standard Gibbs free energy change ($\Delta_r G^o$).[4,31,32,33] The theoretical EMF value (E) for reaction (1) is 1.631 V, which is consistent with re-oxidation potential (1.56 to 1.91 V) in the anodic process but much higher than the electrode reduction potential (0.75 V) in the cathodic process due to the slow mass transport limited kinetics of this conversion-type material.

If this conversion/deconversion reaction of the lithiation/delithiation process is deemed as an approximate reversible process according to equation (1), the apparent diffusion coefficient of lithium (D_{Li}) can be calculated from the CVs performed at different scan rates using the following equation:[16,34-36]

$$I_p = 0.4463 zFA(zF/RT)^{1/2} \Delta C_0 D_{Li}^{1/2} \nu^{1/2} \quad (4)$$

which can be simplified for experiments run at room temperature to:

$$I_p = 2.69 \times 10^5 n^{3/2} A D_{Li}^{1/2} \nu^{1/2} \Delta C_0 \quad (5)$$

where n is the number of electrons per reaction species, A the geometric area of the working electrode, 0.28 cm^2, D_{Li} the apparent diffusion coefficient of Li in the electrode, ΔC_O the change in Li concentration corresponding to the specific electrochemical reaction and v is the scan rate. At very slow scan rate, Li^+ accumulates in the bulk of the thin film and in this case the peak current (I_p) varies linearly with the square root of the scan rate ($v^{1/2}$) according to equation (5). In the present case, as shown in Figure 2 (b), I_p is indeed approximately proportional to the square root of the scan rate (v) confirming a diffusion-controlled behavior. From the slope of the linear fit, the calculated diffusion coefficients corresponding to the cathodic and anodic electrochemical reactions are D_{LiC}=1.7×10^{-15} cm^2 s^{-1} and D_{LiA}=2.4×10^{-16} cm^2 s^{-1}, respectively. These diffusion coefficients are 7 orders of magnitude lower than that obtained for TiO_2/C nanocomposite (1.07×10^{-8} cm^2/s)[37] or nanosized tin (4.15×10^{-8} cm^2 s^{-1}),[36] 5 orders of magnitude lower than that obtained for graphite film electrode (10^{-9}–10^{-11} cm^2 s^{-1})[16,38,39] and even 2 orders of magnitude lower than that obtained for amorphous silicon thin-film electrodes (~10^{-13} cm^2 s^{-1}) as calculated from cyclic voltammetry data.[40,41,42] These quite low values of the diffusion coefficient suggest that the iron oxide has poor kinetic properties, which will lead

to inferior charging and discharging behavior. It is well known that the diffusion coefficient should be smaller than D_{LiC} and larger than D_{LiA} due to the SEI layer contributing to the kinetics of the first cathodic process and non-fully reversible reaction in the anodic process.

3.3. Galvanostatic discharge-charge

Figure 3 displays the first galvanostatic discharge and charge cycle of the iron oxide thin film electrode obtained at a current density of 10 μA cm^{-2} in a potential window of 3.0 - 0.01 V.

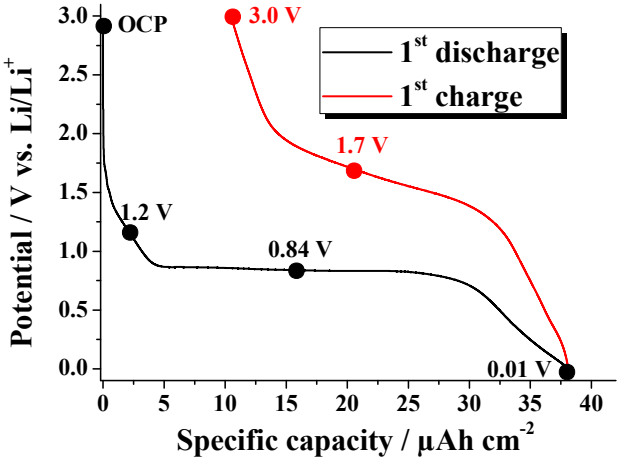

Figure 3 First galvanostatic discharge and charge cycle of the iron oxide thin film electrode obtained at a current density of 10 μA cm^{-2} in a potential window of 3.0 - 0.01 V.

The profiles exhibit an inclined plot between 1.9 and 1.0 V and an extended potential plateau at ~0.84 V in the first discharge curve. The slope corresponds to the early stage of lithiation leading to formation of the $Li_xFe_2O_3$ ($0<x\leq2$) intermediate. The plateau at ~0.84 V is assigned to lithiation of iron oxide with formation of Li_2O/Fe^0 and also to the formation of SEI layer due to reductive decomposition of electrolyte. In the charge curve (delithiation process), the region from ~1.0 to ~2.0 V corresponds to the reversible oxidation of Fe^0 to Fe^{3+}, which is consistent with CV measurements. More details of the electrochemical properties for iron oxide thin film electrodes have been reported in chapters 2 and 3.[20,43] The points marked at different stages of lithiation/delithiation on the discharge/charge curves were selected for the EIS and XPS measurements. They correspond to the open circuit potential (OCP), the potential at the slope of first discharge (1.2 V), the potential at the plateau of first discharge (0.84 V, also selected for ToF-SIMS analysis), the end point of first galvanostatic discharge (0.01 V), the

potential at the plateau of first charge (1.7 V) and the end point of first galvanostatic charge (3.0 V).

3.4. Diffusion evaluation from EIS

Figure 4(a) shows the EIS spectra obtained at different lithiation/delithiation stages after the potential relaxation necessary for obtaining stationary conditions. As already discussed in the literature,[24, 44, 45] different regions can be generally distinguished in electrochemical impedance spectra as a function of frequency: the high frequency semicircle that relates to the resistance corresponding to Li^+ migration through SEI layer, the medium frequency semicircle that corresponds to charge transfer resistance between SEI layer and electrode interface, and the low frequency that is attributed to Warburg impedance (diffusion of Li^+ in the bulk electrode) and insertion capacitance (accumulation of Li^+ in the electrode). Figure 4(b) shows the relationship between real impedance (Z') and radial frequency ($\omega^{-1/2}$) at different lithiation stages of the first discharge-charge cycle. The ohmic resistance ($R_\Omega = R_{el} + R_{ct}$) increases during discharge, which is clearly observed by the appearance of a semicircle (Figure 4(a) inset). This is caused by the thickness variation of the thin film electrode (electrode expansion) and the formation of the SEI layer. During the process of charge, the semicircle decreases (charge to 1.7 V) and almost completely disappears (charge to 3.0 V). These changes correspond to reversible decrease of electrode volume and thickness of the SEI layer.

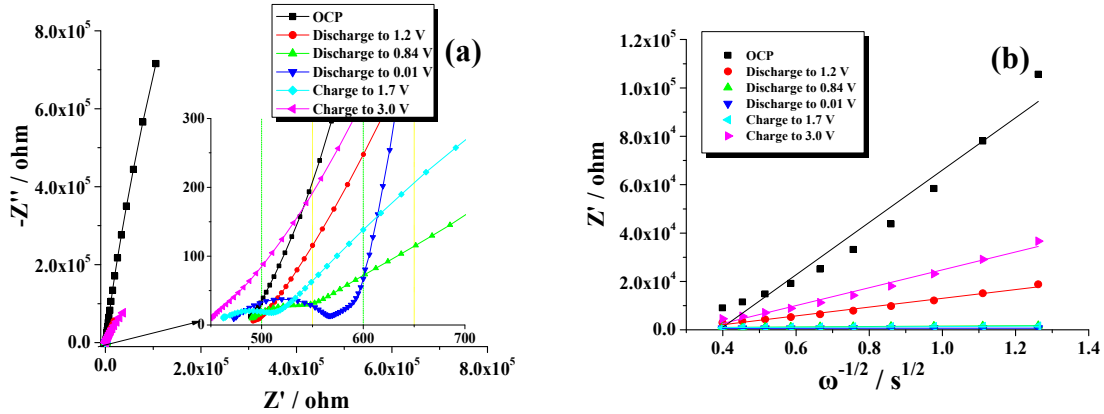

Figure 4 (a) EIS spectra at different lithiation stages after potential relaxation; (b) relationship between real impedance (Z') and radial frequency ($\omega^{-1/2}$) at different lithiation stages of the first discharge-charge cycle.

In order to obtain the diffusion coefficient of Li ions (D_{Li}) into the iron oxide electrode, only the low frequency region attributed to Warburg impedance was considered for calculation. The lithium diffusion coefficient can be deduced from the Warburg impedance, Z_W, as follows:

$$Z_W = \sigma_w(1 - j)\omega^{-1/2} \quad (6)$$

where ω is the radial frequency, and σ_w is the Warburg impedance coefficient. The diffusion coefficient of the lithium ions (D_{Li}) into the electrode materials is then given by the following equation: [46-48]

$$D = 0.5\left(\frac{RT}{AF^2\sigma_w C}\right)^2 = 4.52 \times 10^{-13}\left(\frac{1}{\sigma_w C}\right)^2 \quad (7)$$

where R is the gas constant, T the absolute temperature, C the molar concentration of Li^+ ions (C (mol cm^{-3}) = n_{Li} (mol)/V (cm^3) = [(I×t) C/1.6×10^{-19} C/6.02×10^{23} mol^{-1}]/V (cm^3), with V=3.5 ×10^{-6} cm^3), A the apparent surface area (here the geometric electrode area, 0.28 cm^2, is used for simplicity), and F the Faraday constant. Relation (7) is valid only if the semi-infinite diffusion conditions are fulfilled (ω=2πf>>2D_{Li}/L^2 where L is the finite length). The values of σ_w, C and D_{Li} at various electrode potentials are listed in Table 1.

Table 1 Values of σ_w, C and D_{Li} at various electrode potentials as determined from EIS data in the first discharge-charge cycle.

Potentials (V)	σ_W (Ω $s^{-1/2}$)	C (mol cm^{-3})	D_{Li} (cm^2 s^{-1})
OCP	108281.0	0	+∞
Discharge to 1.2 V	18127.4	0.004923	5.7×10^{-17}
Discharge to 0.84 V	865.4	0.04112	3.6×10^{-16}
Discharge to 0.01 V	117.4	0.09893	3.4×10^{-15}
Charge to 1.7 V	678.9	0.05328	3.5×10^{-16}
Charge to 3.0 V	36951.1	0.02723	4.5×10^{-19}

At OCP, the molar concentration of Li^+ ions in the electrode is close to zero and D_{Li} is theoretically infinite. With the increase of the Li concentration, an increase of D_{Li} can be observed. This should be related to the conversion mechanism and mass transport limitation of this electrode. With the process of lithiation proceeding, more and more reaction product

(Li_2O/Fe^0 matrix) is accumulated in the outer part of the thin film electrode. It is suggested that the lithium migration in the electrode is changed from a conversion-controlled process (conversion of Fe_2O_3 to Li_2O/Fe^0 matrix) to a diffusion-controlled process (diffusion in converted Li_2O/Fe^0 matrix) with diffusion proceeding faster than conversion. However, this is not supported by ToF-SIMS results presented below. On the other hand, pulverization of the thin film electrode material during lithiation may promote the diffusion coefficient increase and account for the observed variation. During the charge process, the D_{Li} decreased with Li extraction (delithiation), showing a deconversion process of Li_2O and metallic Fe into iron oxide with volume shrinkage of the electrode.

The EIS can be considered as an *in situ* electrochemical technique for analysis of kinetics processes occurring in the bulk of electrode material including formation of the SEI layer. The D_{Li} values obtained from EIS show variations as a function of lithiation/delithiation potentials. These variations are similar to previous results calculated from EIS data observed on carbonaceous materials,[10,44,45,49-51] silicon oxycarbide,[52] silicon films,[53,54] Cu_6Sn_5[55] and metal oxides (i.e., nano-sized rutile TiO_2[56] and β-MnO_2[57]).

3.5. Diffusion evaluation from ToF-SIMS

ToF-SIMS has already been applied to study Li transport in the SEI layer formed on the graphite negative electrode[58,59] and in positive $LiFePO_4$ electrode.[60] In the present work, the diffusion coefficient of Li ions in host Fe_2O_3 was estimated from the in-depth variation of Li-ion concentration in the thin film iron oxide electrode discharged to 0.84 V (after 5591 s of lithiation). Figure 5(a) shows the depth profile of Li^- ion where four regions can be distinguished. At the beginning of sputtering, the Li^- ions intensity increases for about 62 s to reach a maximum at the SEI layer/iron oxide thin film interface. From 62 to ~316 s, the intensity of Li^- ions decreases, due to migration of Li in the partially converted Fe_2O_3 electrode. From 316 to 396 s, the very weak Li^- ions intensity indicates only minor Li penetration in the region corresponding to the interface between iron oxide thin film and metallic iron substrate. After 396 s sputtering, the Li^- ions signal becomes negligible, confirming the absence of Li penetration in the bulk region. To get the in-depth variations of concentration as a function of sputtering depth (as shown in Figure 5(b)), sputtering time is converted into depth using a

calibrated value of the sputtering rate (0.374 nm s^{-1}). The first 62 s of sputtering corresponding to the Li ions profile in the SEI layer are neglected and the point 0 nm (in Figure 5(b)) is set to the maximum Li^- ion intensity measured at the SEI/electrode interface (at 62 s of sputtering in Figure 5(a)). The Li concentration is normalized to the maximum Li^- ion intensity at the SEI/electrode interface.

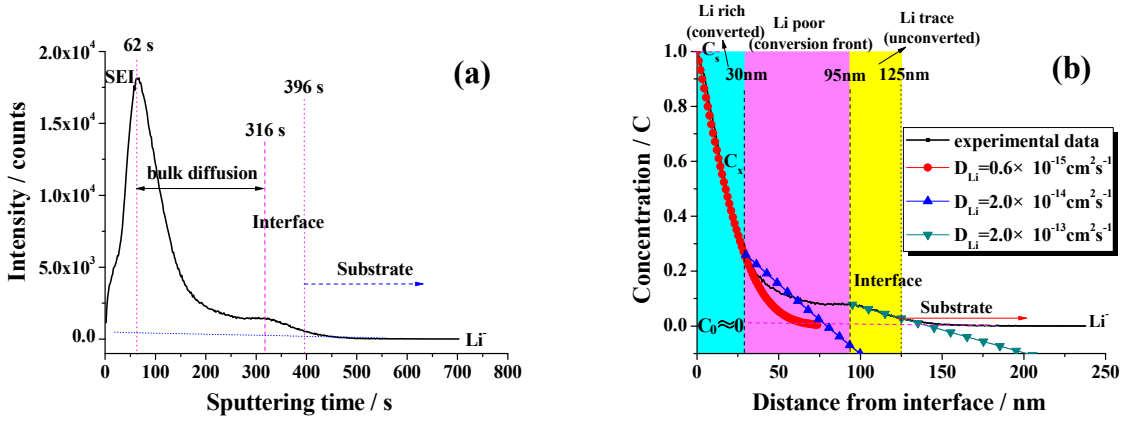

Figure 5 (a) ToF-SIMS depth profile of Li^- ion of the sample discharged to 0.84 V after 5591 s of lithiation, (b) Normalized in-depth variations of the Li-ion concentration.

The apparent Li diffusion coefficient (D_{Li}) in the thin film electrode could be derived from the infinite integration of Fick's second law for one-dimensional diffusion,[61]

$$\frac{C_S - C_{(x,t)}}{C_S - C_0} = erf\left(\frac{x}{2\sqrt{D_{Li}t}}\right), \text{ with } z = \frac{x}{2\sqrt{D_{Li}t}} \quad (8)$$

and error function,

$$erf(z) = \frac{2}{\sqrt{\pi}}\int_0^z e^{-t^2}dt = \frac{2}{\sqrt{\pi}}\sum_{n=0}^{\infty}\frac{(-1)^n z^{2n+1}}{(2n+1)n!} \quad (9)$$

considering the following boundary conditions: C (x=0) = C_s = 1, constant, fixed; C (x=+∞) = C_0, corresponding to the original concentration of Li existing in the bulk phase. C_0 remains constant in the far bulk phase at x=+∞, herein $C_0 \approx 0$.

Using Eqs. (8) and (9), three curves (red, blue and green) were traced using theoretical values of the diffusion coefficient (D_{Li}) and superimposed with the experimental concentration profile obtained by ToF-SIMS (Figure 5(b)). A best fit with the experimental profile is obtained in the first outermost region, called "Li rich", where the diffusion coefficient of lithium (D_{Li}) is around 0.6×10^{-15} cm^2 s^{-1}, indicating a nearly ideal diffusion process. Assuming

that this outer region corresponds to the converted Li_2O/Fe^0 matrix according to reaction (1), it can be concluded that the diffusion coefficient measured in this region is that of lithium in the converted electrode material.

In the third innermost region of the thin film electrode, called "Li trace" and assigned to the interfacial region between the iron oxide thin film and the iron substrate, the best fit (green curve) is obtained with a much higher diffusion coefficient (D_{Li}=2.0×10^{-13} cm^2 s^{-1}). Assuming that the iron oxide matrix is unconverted in this region, the much faster diffusion process would be related to the intercalation reaction of lithium into the α-Fe_2O_3 matrix ahead of the conversion front.

In the second region, called "Li poor" and intermediate between the "Li rich" and "Li trace" regions, no good fit of the experimental profile can be obtained with a diffusion profile. This is assigned to the formation of a transition region between the "Li rich" (converted iron oxide) and "Li trace" (intercalated iron oxide) regions. Most likely, the kinetics of Li migration in this transition "Li poor" region is not only controlled by processes of diffusion (in the converted and unconverted iron oxide matrices) but also by the advancement of the conversion reaction front.

In a homogeneous matrix, the concentration profile should yield one chemical diffusion coefficient independently of the position along the profile. However, in the present case, the experimental data clearly require different values of the diffusion coefficient (D_{Li}) to be considered for fitting the different regions of the concentration profile. In the outermost converted part of the electrode, the extracted D_{Li} value (0.6×10^{-15} cm^2 s^{-1}) is much lower than that in the innermost intercalated and non-converted inner part of the electrode, indicating a slower diffusion process in the converted electrode. The distinction between the two diffusion processes was possible most likely because the kinetics of the conversion reaction is faster than that of migration of the Li ions in the converted electrode. The methodology of partial lithiation of the electrode material adopted for the ToF-SIMS analysis, as a direct, physical measurement method of the reaction kinetics (in this case Li diffusion) in electrodes, was decisive for making distinction between the different types of diffusion as a function of the lithiation penetration depth.

The D_{Li} measured in the converted electrode from ToF-SIMS is in agreement with the

D_{LiC} obtained from cyclic voltammetry data. However, careful comparison of the two values (0.6×10^{-15} cm^2 s^{-1} to 1.7×10^{-15} cm^2 s^{-1}, respectively) suggest that the slightly higher value corresponding to the cathodic reactions (D_{LiC}) must be affected by the dynamic process of formation of the SEI layer and conversion of the electrode in the cathodic scan. ToF-SIMS measurement of the Li concentration profile in a thin film electrode enables to clearly discriminate different regions of varying Li concentrations in the lithiated electrode, and thus to exclude the surface passivation layer (SEI layer) from the data analysis.

Furthermore, the D_{Li} obtained from ToF-SIMS is consistent with EIS results. The D_{Li} value obtained from EIS was 3.6×10^{-16} cm^2 s^{-1} at a point corresponding to discharged to 0.84 V. This slightly lower values than that obtained from ToF-SIMS data may be explained by the presence of the SEI layer, which must have an influence on the electrode kinetics. The evaluation of electrode kinetics by means of EIS is burden by the surface SEI layer which can hinder the ionic transport. It seems that the lithium ion diffusion in SEI layer should not be neglected due to its poor transport properties although the SEI is much thinner than the electrode film. [62]

3.6. Influence of surface modifications of the iron oxide on kinetics

It is believed that the SEI layer plays an important role in the kinetics of electrode materials. In this study, the comparison of diffusion coefficient obtained by *in situ* electrochemical methods (CV and EIS) and a direct measurement of the Li concentration profile by ToF-SIMS points to the importance of this surface layer in the ionic transport. The exact mechanism of the SEI layer formation and its physico-chemical properties still remain a subject of debate. The SEI layer formation strongly depends on temperature, electrolyte as well as electrode morphology and composition.[36,63,64] In our previous work on iron oxide thin film electrode, the formation and variation of SEI layers have been studied thoroughly during CV lithiation/delithiation and cycling.[20,43] In the present work, the iron oxide thin film electrodes were analyzed by XPS at selected potentials of galvanostatic discharge/charge in order to investigate the dynamic compositional change of the SEI on iron oxide thin film electrode during the first discharge-charge cycle.

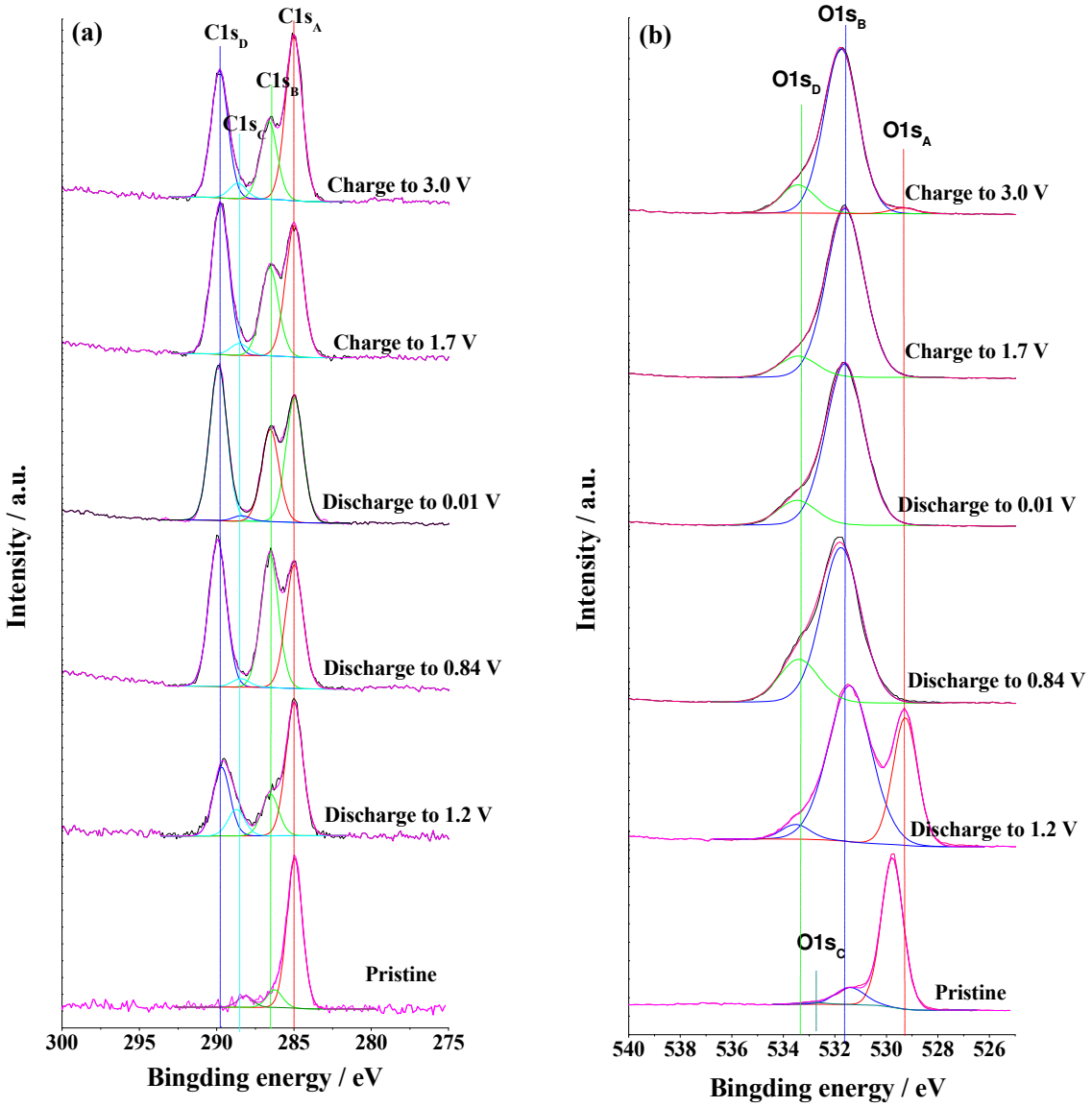

Figure 6 XPS C1s and O1s spectra for the pristine iron oxide thin film and after discharge-charge to different potentials.

Figure 6 shows the XP C1s and O1s spectra for the pristine thin film iron oxide and after discharge-charge to different selected potentials. Binding energies (E_B), full widths at half maximum (FWHM), and relative intensities of the component peaks obtained by peak fitting are given in Table 2.

Table 2 Binding energies (E_B), full widths at half-maximum (FWHM) and relative intensities of the XPS component peaks obtained by peak fitting for the pristine electrode and after discharge/charge to different potentials.

	pristine			1.2 V discharged			0.84 V discharged			0.01 V discharged			1.7 V charged			3.0 V charged		
	E_B (eV)	FWHM (eV)	Area Ratio	E_B (eV)	FWHM (eV)	Area Ratio	E_B (eV)	FWHM (eV)	Area Ratio	E_B (eV)	FWHM (eV)	Area Ratio	E_B (eV)	FWHM (eV)	Area Ratio	E_B (eV)	FWHM (eV)	Area Ratio
$C1s_A$	285.0	1.22	1.00	285.0	1.33	1.00	285.0	1.37	0.84	285.0	1.36	0.80	285.0	1.39	0.87	285.0	1.33	1.00
$C1s_B$	286.3	1.22	0.12	286.5	1.33	0.31	286.6	1.37	0.91	286.5	1.36	0.59	286.6	1.39	0.58	286.6	1.33	0.47
$C1s_C$	288.2	1.22	0.07	288.7	1.33	0.17	288.4	1.37	0.06	288.4	1.36	0.04	288.5	1.39	0.08	288.6	1.33	0.09
$C1s_D$				289.7	1.33	0.52	289.9	1.37	1.00	289.9	1.36	1.00	289.8	1.39	1.00	289.8	1.33	0.77
$O1s_A$	529.8	1.04	1.00	529.3	1.17	0.47										529.3	1.27	0.03
$O1s_B$	531.4	1.39	0.12	531.4	2.05	1.00	531.8	1.84	1.00	531.6	1.82	1.00	531.6	1.80	1.00	531.8	1.62	1.00
$O1s_C$	532.9	1.39	0.01															
$O1s_D$				533.5	1.36	0.06	533.4	1.84	0.28	533.5	1.82	0.15	533.4	1.80	0.12	533.4	1.62	0.17

The C1s signal of the pristine sample is indicative of the carbonaceous contamination routinely observed on oxide surfaces. The C1s spectra are decomposed into three peaks of hydrocarbons at 285.0 eV, lithium alkyl carbonate at 286.3 eV and carbonyl and/or carboxyl bonds at 288.2 eV. The C1s spectrum after electrochemistry shows one more peak corresponding to Li_2CO_3 and/or $ROCO_2Li$ near 289.8 eV.[65,66] The relative intensity of this $C1s_D$ component peak, which is indicative of the main composition of SEI, increases with discharging to 0.01 V and then decreases with charging to 3.0 V, corresponding to a dynamic process of the SEI layer in the first discharge-charge cycle.

The oxygen component at E_B ($O1s_A$) = 529.8 eV on the pristine sample, corresponding to metal (iron and/or lithium)-oxygen bonds, slightly shifts to a lower value of 529.3 eV after lithiation to 1.2 V, indicating a conversion process (Fe^{3+} to Fe^{2+} and/or formation of Li_2O) of iron oxide with Li^+ insertion. The O1s spectrum shows a major oxygen component peak at E_B ($O1s_B$) = 531.8 eV and no metal-oxygen bonds after discharge to 0.84 V, owing to a growth of SEI layer on the electrode surface. The Fe2p intensity (not shown) is also completely attenuated by the growth of SEI layer at this potential stage. After charge to 3.0 V, a minor oxygen component peak at E_B ($O1s_A$) = 529.3 eV, assigned to metal-oxygen bonds, reappears due to partial decomposition of the SEI layer. Except for some minor modifications of C1s and O1s spectra, the SEI layer composition remains stable during discharge/charge. The slight partial decomposition in the anodic process revealed by the changes in the relative intensities of O1s and C1s peak (Table 1) can be indicative of the modification of the SEI layer which affects the transport of Li ions (as particularly observed in D_{Li} data obtained by EIS measurements).

4. Conclusions

CV, EIS and ToF-SIMS were applied to study the kinetics of Li-ion migration into α-Fe_2O_3 thin film electrodes. The diffusion coefficient of lithium (D_{Li}) obtained by CV from the cathodic and anodic electrochemical reactions are 1.7×10^{-15} and 2.4×10^{-16} cm^2 s^{-1}, respectively. The D_{Li} values obtained from EIS show a variation from 10^{-15} to 10^{-19} cm^2 s^{-1} as a function of lithiation/delithiation potentials. From the analysis of the Li-ion concentration profile in the thin film partially converted at 0.84 V measured by ToF-SIMS, the SEI layer

region could be excluded and 3 regions of diffusion could be evidenced. In the outermost region of the electrode, the diffusion coefficient (D_{Li}) was found to be the lowest (around 0.6×10^{-15} cm^2 s^{-1}), which was assigned to slow Li-ion diffusion in the converted Li_2O/Fe^0 matrix. In the innermost region, near the interface with substrate, D_{Li} was found to be more than two orders of magnitude higher (around 2.0×10^{-13} cm^2 s^{-1}), indicating a much faster diffusion process of Li-ion intercalated in the Fe_2O_3 matrix ahead of the conversion front. In the intermediate (transition) region between the outermost converted and innermost intercalated regions, the Li-ion concentration profile could not be fitted by a solid-state diffusion profile, which was assigned to the mixing of the converted and unconverted iron oxide matrices owing to the advancement of conversion reaction front. The fact that the 3 regions could be differentiated suggests that the kinetics of advancement of the conversion front is faster than that of Li-ion diffusion in the converted composite matrix but slower than that of intercalation in the unconverted Fe_2O_3 matrix.

The D_{LiC} obtained by CV was 2-3 times higher than the D_{Li} measured in the converted electrode by from ToF-SIMS, which is assigned to the dynamic process of conversion and formation of the SEI layer during the cathodic scan. The D_{Li} obtained by EIS in the electrode discharged to 0.84 V is ~2 times lower than that measured in the converted electrode by ToF-SIMS, which was assigned to hindering of the ionic transport by the SEI layer. Comparison of the ToF-SIMS, CV and EIS analysis data thus shows that Li-ion diffusion in SEI layer should not be neglected, as also supported by XPS analysis at selected potentials that confirms the dynamic process of formation of the SEI layer that accompanies discharge/charge of the electrode.

ToF-SIMS, applied here for the first time to the study of the kinetics of Li-ion migration into such a conversion-type electrode material and combined with a thin film approach, is proven as a direct methodology for extracting diffusion coefficients of lithium that excludes the influence of the surface passivation layer (SEI layer) on the data analysis and discriminates diffusion into converted and intercalated electrode matrices.

References

[1] Poizot P., Laruelle S., Grugeon S., Dupont L., Tarascon J.-M., Nano-sized Transition-Metal Oxides as Negative-Electrode Materials for Lithium-Ion Batteries, *Nature*, **2000**, *407*, 496-499.

[2] Poizot P., Laruelle S., Grugeon S., Dupont L., Tarascon J.-M., From the vanadates to 3d-metal oxides negative electrodes, *Ionics*, **2000**, *6*, 321-330.

[3] Poizot P., Laruelle S., Grugeon S., Dupont L., Tarascon J.-M., Searching for new anode materials for the Li-ion technology: time to deviate from the usual path, *J. Power Sources*, **2001**, *97-98*, 235-239.

[4] Poizot P., Laruelle S., Grugeon S., Tarascon J.-M., Rationalization of the low-potential reactivity of 3d-metal-based inorganic compounds toward Li, *J. Electrochem. Soc.*, **2002**, *149*, A1212 -A1217.

[5] Larcher D., Masquelier C., Bonnin D., Chabre Y., Mason V., Leriche J.B., Tarascon J.-M., Effect of Particle Size on Lithium Intercalation into α-Fe_2O_3, *J. Electrochem. Soc.*, **2003**, *150*, A133-A139.

[6] Larcher D., Bonnin D., Cortes R., Rivals I., Personnaz L., Tarascon J.-M., Combined XRD, EXAFS, and Mössbauer Studies of the Reduction by Lithium of α-Fe_2O_3 with Various Particle Sizes, *J. Electrochem. Soc.*, **2003**, *150*, A1643-A1650.

[7] Xu X., Cao R., Jeong S., Cho J., Spindle-like Mesoporous α-Fe_2O_3 Anode Material Prepared from MOF Template for High-Rate Lithium Batteries, *Nano Lett.*, **2012**, *12*, 4988-4991.

[8] Aricò A.S., Bruce P., Scrosati B., Tarascon J.-M., Schalkwijk W.V., Nanostructured Materials for Advanced Energy Conversion and Storage Devices, *Nat. Mater.*, **2005**, *4*, 366-377.

[9] Thevenin J., Passivating Films on Lithium Electrodes. An Approach by Means of Electrode Impedance Spectroscopy, *J. Power Sources*, **1985**, *14*, 45-52.

[10] Levi M.D., Aurbach D., Diffusion Coefficients of Lithium Ions during Intercalation into Graphite Derived from the Simultaneous Measurements and Modeling of Electrochemical Impedance and Potentiostatic Intermittent Titration Characteristics of Thin Graphite Electrodes, *J. Phys. Chem. B*, **1997**, *101*, 4641-4647.

[11] Shin H.C., Cho W.II., Jang H., Electrochemical Properties of the Carbon-Coated $LiFePO_4$ as a Cathode Material for Lithium-ion Secondary Batteries, *J. Power Sources*, **2006**, *159*, 1383-1388.

[12] Levi M.D., Aurbach D., Frumkin intercalation isotherm - a tool for the description of lithium insertion into host materials: a review, *Electrochim. Acta*, **1999**, *45*, 167-185.

[13] Guo J., Sun A., Chen X., Wang C., Manivannan A., Cyclability study of silicon-carbon composite anodes for lithium-ion batteries using electrochemical impedance spectroscopy, *Electrochim. Acta*, **2011**, *56*, 3981-3987.

[14] Chen L., Wang K., Xie X., Xie J., Effect of vinylene carbonate (VC) as electrolyte additive on electrochemical performance of Si film anode for lithium ion batteries, *J. Power Sources*, **2007**, *174*, 538-543.

[15] Levi M.D., Levi E., Gofer Y., Aurbach D., Vieil E., Serose J., Dilute Graphite-Sulfates Intercalation Stages Studied by Simultaneous Application of Cyclic Voltammetry, Probe-Beam Deflection, In situ Resistometry,

and X-ray Diffraction Techniques, *J. Phys. Chem. B*, **1999**, *103*, 1499-1508.

[16] Levi M.D., Aurbach D., The mechanism of lithium intercalation in graphite film electrodes in aprotic media. Part 1. High resolution slow scan rate cyclic voltammetric studies and modeling, J. Electroanal. Chem., **1997**, *421*, 79-88.

[17] Levi M.D., Levi E.A., Aurbach D., The mechanism of lithium intercalation in graphite film electrodes in aprotic media. Part 2. Potentiostatic intermittent titration and in situ XRD studies of the solid-state ionic diffusion, J. Electroanal. Chem., **1997**, *421*, 89-97.

[18] Huang H., Kelder E.M., Chen L., Schoonman J., Electrochemical characteristics of $Sn_{1-x}Si_xO_2$ as anode for lithium-ion batteries, *J. Power Sources*, **1999**, *81-82*, 362-367.

[19] Wang Q., Li H., Huang X.. Chen L., Determination of Chemical Diffusion Coefficient of Lithium Ion in Graphitized Mesocarbon Microbeads with Potential Relaxation Technique, *J. Electrochem. Soc.*, **2001**, *148*, A737-A741.

[20] Tian B., Światowska J., Maurice V., Zanna S., Seyeux A., Klein L.H., Marcus P., Combined Surface and Electrochemical Study of the Lithiation/Delithiation Mechanism of Iron Oxide Thin Film Anode for Lithium-Ion Batteries, *J. Phys. Chem. C*, **2013**, *117*, 21651-21661.

[21] Li J.T., Maurice V., Światowska-Mrowiecka J., Seyeux A., Zanna S., Klein L., Sun S.G., Marcus P., XPS, Time-of-Flight-SIMS and Polarization Modulation IRRAS Study of Cr_2O_3 Thin Film Materials as Anode for Lithium Ion Battery, *Electrochim. Acta*, **2009**, *54*, 3700-3707.

[22] Rougier A., Striebel K.A., Wen S.J., Cairns E.J., Cyclic Voltammetry of Pulsed Laser Deposited $Li_xM_2O_4$ Thin Films, *J. Electrochem. Soc.*, **2003**, *145*, 2975 -2980.

[23] Needham S.A., Wang G.X., Konstantinov K., Tournayre Y., Lao Z., Liu H.K., Electrochemical Performance of Co_3O_4-C Composite Anode Materials *Electrochem. Solid-State Lett.*, **2006**, *9*, A315-A319.

[24] Etacheri V., Haik O., Goffer Y., Roberts G.A., Stefan I.C., Fasching R., Aurbach D., Effect of Fluoroethylene Carbonate (FEC) on the Performance and Surface Chemistry of Si-Nanowire Li-Ion Battery Anodes, *Langmuir*, **2012,** *28*, 965-976.

[25] Światowska-Mrowiecka J., Maurice V., Zanna S., Klein L., Marcus P., XPS Study of Li Ion Intercalation in V_2O_5 Thin Films Prepared by Thermal Oxidation of Vanadium Metal, *Electrochim. Acta*, **2007**, *52*, 5644-5653.

[26] Reddy M.V., Yu T., Sow C.H., Shen Z.X., Lim C.T., Subba Rao G.V., Chowdari B.V.R., α-Fe_2O_3 Nanoflakes as an Anode Material for Li-Ion Batteries, *Adv. Funct. Mater.*, **2007**, *17*, 2792-2799.

[27] Zheng Z., Chen Y., Shen Z.X., Ma J., Sow C.H., Huang W., Yu T., Ultra-Sharp Alpha-Fe_2O_3 Nanoflakes: Growth Mechanism and Field-Emission, *Appl. Phys. A*, **2007**, *89*, 115-119.

[28] Faria D.L.A., Venâncio Silva S., Oliveira M.T., Raman Microspectroscopy of Some Iron Oxides and Oxyhydroxides, *J. Raman Spectrosc.*, **1997**, *28*, 873-878.

[29] Thackeray M.M., David W.I.F., Goodenough J.B., High-Temperature Lithiation of α-Fe_2O_3: A

Mechanistic Study, *J. Solid State Chem.*, **1984**, *55*, 280-286.

[30] Hosono E., Fujihara S., Honma I., Ichihara M., Zhou H., Fabrication of Nano/Micro Hierarchical Fe_2O_3/Ni Micrometer-Wire Structure and Characteristics for High Rate Li Rechargeable Battery, *J. Electrochem. Soc.*, **2006**, *153*, A1273-A1278.

[31] Li H., Balaya P., Maier J., Li-Storage via Heterogeneous Reaction in Selected Binary Metal Fluorides and Oxides, *J. Electrochem. Soc.*, **2004**, *151*, A1878-A1885.

[32] Zu C.X., Li H., Thermodynamic analysis on energy densities of batteries, *Energy Environ. Sci.*, **2011**, *4*, 2614-2624.

[33] Barin I., Thermochemical Data of Pure Substances, Third Edition, *VCH Verlagsgesellschaft GmbH*, *Weinheim*, **1995**.

[34] Bard A.J., Faulkner L.R., Electrochemical Methods, *Wiley*, New York, **1980**, p. 218.

[35] Das S.R., Majumder S.B., Katiyar R.S., Kinetic analysis of the Li^+ ion intercalation behavior of solution derived nano-crystalline lithium manganate thin films, *J. Power Sources*, **2005**, *139*, 261-268.

[36] Zhang T., Fu L.J., Gao J., Wu Y.P., Holze R., Wu H.Q., Nanosized tin anode prepared by laser-induced vapor deposition for lithium ion battery, *J. Power Sources*, **2007**, *174*, 770-773.

[37] Fu L.J., Liu H., Zhang H.P., Li C., Zhang T., Wu Y.P., Holze R., Wu H.Q., Synthesis and electrochemical performance of novel core/shell structured nanocomposites, *Electrochem. Commun.*, **2006**, *8*, 1-4.

[38] Guyomard D., Tarascon J.-M., Li Metal-Free Rechargeable $LiMn_2O_4$/Carbon Cells: Their Understanding and Optimization, *J. Electrochem. Soc.*, **1992**, *139*, 937-948.

[39] Uchida T., Morikawa Y., Ikuta H., Wakihara M., Chemical diffusion coefficient of lithium in carbon fiber, *J. Electrochem. Soc.*, **1996**, *143*, 2606-2610.

[40] Kulova T.L., Skundin A.M., Pleskov Y.V., Terukov E.I., Kon'kov O.I., Lithium Intercalation in Thin Amorphous-Silicon Films, *Russ. J. Electrochem.*, **2006**, *42*, 363-369.

[41] Kulova T.L., Skundin A.M., Pleskov Y.V., Terukov E.I., Kon'kov O.I., Lithium insertion into amorphous silicon thin-film electrodes, *J. Electroanal. Chem.*, **2007**, *600*, 217-225.

[42] Xia H., Tang S., Lu L., Properties of amorphous Si thin film anodes prepared by pulsed laser deposition, *Mater. Res. Bull.*, **2007**, *42*, 1301-1309.

[43] Tian B., Świątowska J., Maurice V., Zanna S., Seyeux A., Klein L.H., Marcus P., Aging-induced chemical and morphological modifications of thin film iron oxide electrodes for lithium-ion batteries, *Langmuir*, **2014**, *30*, 3538-3547.

[44] Umeda M., Dokko K., FujitaY., Mohamedi M., Uchida I., Selman J.R., Electrochemical impedance study of Li-ion insertion into mesocarbon microbead single particle electrode Part I. Graphitized carbon, *Electrochim. Acta*, **2001**, *47*, 885-890.

[45] Dokko K., Fujita Y., Mohamedi M., Umeda M., Uchida I., Selman J.R., Electrochemical impedance study of Li-ion insertion into mesocarbon microbead single particle electrode Part II. Disordered carbon,

Electrochim. Acta, **2001**, *47*, 933-938.

[46] Shenouda A.Y., Liu H.K., Electrochemical behaviour of tin borophosphate negative electrodes for energy storage systems, *J. Power Sources*, **2008**, *185*, 1386-1391.

[47] Li X., Qu M.Z., Yu Z.L., Structural and electrochemical performances of $Li_4Ti_{5-x}Zr_xO_{12}$ as anode material for lithium-ion batteries, *J. Alloys Compd.*, **2009**, *487*, L12-L17.

[48] Tian B., Xiang H., Zhang L., Li Z., Wang H., Niobium doped lithium titanate as a high rate anode material for Li-ion batteries, *Electrochim. Acta*, **2010**, *55*, 5453-5458.

[49] Jean M., Desnoyer C., Tranchant A., Messina R., Electrochemical and Structural Studies of Petroleum Coke in Carbonate-Based Electrolytes, *J. Electrochem. Soc.*, **1995**, *142*, 2122-2125.

[50] Takami N., Satoh A., Hara M., Ohsaki T., Structural and Kinetic Characterization of Lithium Intercalation into Carbon Anodes for Secondary Lithium Batteries, *J. Electrochem. Soc.*, **1995**, *142*, 371-379.

[51] Lin K., Xu Y., He G., Wang X., The kinetic and thermodynamic analysis of Li ion in multi-walled carbon nanotubes, *Mater. Chem. Phys.*, **2006**, *99*, 190-196.

[52] Kaspar J., Graczyk-Zajac M., Riedel R., Determination of the chemical diffusion coefficient of Li-ions incarbon-rich silicon oxycarbide anodes by electro-analytical methods, *Electrochim. Acta*, **2014**, *115*, 665-670.

[53] Xie J., Imanishi N., Zhang T., Hirano A., Takeda Y., Yamamoto O., Li-ion diffusion in amorphous Si films prepared by RF magnetron sputtering: A comparison of using liquid and polymer electrolytes, *Mater. Chem. Phys.*, **2010**, *120*, 421-425.

[54] Ding N., Xu J., Yao Y.X., Wegner G., Fang X., Chen C.H., Lieberwirth I., Determination of the diffusion coefficient of lithium ions in nano-Si, *Solid State Ionics*, **2009**, *180*, 222-225.

[55] Zhang J.J, He P., Xia Y.Y, Electrochemical kinetics study of Li-ion in Cu_6Sn_5 electrode of lithium batteries by PITT and EIS, *J. Electroanal. Chem.*, **2008**, *624*, 161-166.

[56] Bach S., Pereira-Ramos J.P., Willmann P., Investigation of lithium diffusion in nano-sized rutile TiO_2 by impedance spectroscopy, *Electrochim. Acta*, **2010**, *55*, 4952-4959.

[57] Bach S., Pereira-Ramos J.P., Willmann P., A kinetic study of electrochemical lithium insertion in nanosized rutile β-MnO_2 by impedance spectroscopy, *Electrochim. Acta*, **2011**, *56*, 10016-10022.

[58] Lu P., Harris S.J., Lithium transport within the solid electrolyte interphase, *Electrochem. Commun.*, **2011**, *13*, 1035-1037.

[59] Shi S., Lu P., Liu Z., Qi Y., Hector L.G., Li H., Harris S.J., Direct Calculation of Li-Ion Transport in the Solid Electrolyte Interphase, *J. Am. Chem. Soc.*, **2012**, *134*, 15476-15487.

[60] Weichert K., Sigle W., Aken van P.A., Jamnik J., Zhu C., Amin R., Acartürk T., Starke U., Maier J., Phase Boundary Propagation in Large $LiFePO_4$ Single Crystals on Delithiation, *J. Am. Chem. Soc.*, **2012**, *134*, 2988-2992.

[61] Schwarzburger N.I., Knobel R., Behrens H., Binnewies M., Horn, I. Pelster A., Arlinghaus H.F., Dörrer L.,

Schmidt H., Kinetics of Lithium Intercalation in Titanium Disulfide Single Crystals, *Z. Phys. Chem.*, **2012**, *226*, 461-489.

[62] Garreau M., Cyclability of the lithium electrode, *J. Power Sources*, **1987**, *20*, 9-17.

[63] Zhang S.S., Xu K., Jow T.R., Understanding formation of solid electrolyte interface film on $LiMn_2O_4$ electrode, *J. Electrochem. Soc.*, **2002**, *149*, A1521-A1526.

[64] Matsuo Y., Kostecki R., McLarnon F., Surface Layer Formation on Thin-Film $LiMn_2O_4$ Electrodes at Elevated Temperatures, *J. Electrochem. Soc.*, **2001**, *148*, A687-A692.

[65] Światowska-Mrowiecka J., Maurice V., Zanna S., Klein L., Marcus P., XPS Study of Li Ion Intercalation in V_2O_5 Thin Films Prepared by Thermal Oxidation of Vanadium Metal, *Electrochim. Acta*, **2007**, *52*, 5644-5653.

[66] Światowska-Mrowiecka J., Diesbach S., Maurice V., Zanna S., Klein L., Briand E., Vickridge I., Marcus P., Li-Ion Intercalation in Thermal Oxide Thin Films of MoO_3 as Studied by XPS, RBS, and NRA, *J. Phys. Chem. C*, **2008**, *112*, 11050-11058.

Chapter 5. Binary (Fe, Cr)-oxide thermally grown on stainless steel current collector as anode material for lithium-ion batteries

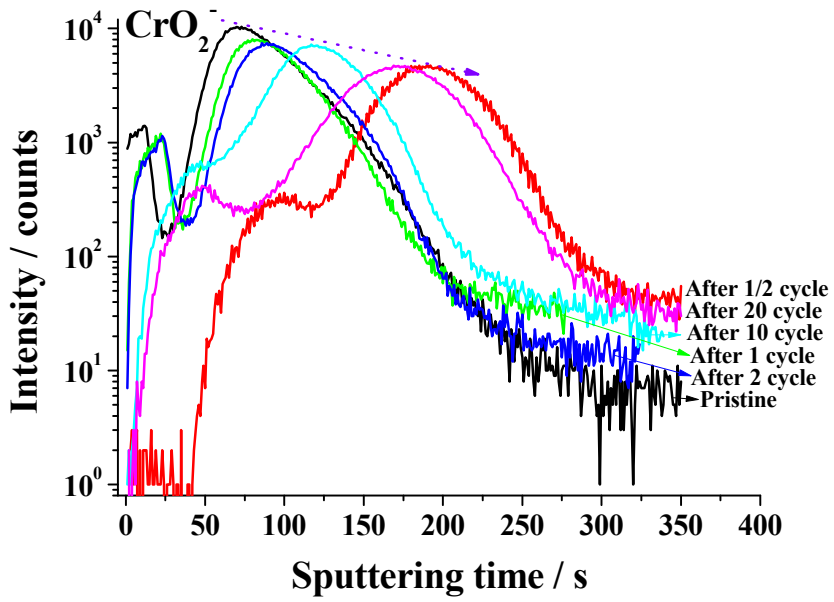

A version of this chapter is to be submitted.

Abstract: Binary (Fe, Cr)-oxide thin film electrodes were prepared as anode material for lithium-ion batteries by thermal growth on a stainless steel (AISI410, $FeCr_{12.5}$) current collector. The mechanisms of lithiation/delithiation of the binary oxide were investigated with electrochemical (CV, galvanostatic cycling), spectroscopic (XPS, ToF-SIMS) and microscopic (SEM, AFM) analytical techniques. The as-prepared binary (Fe, Cr)-oxide electrodes exhibit a good cycling performance except in the first discharge/charge cycle where a high irreversible capacity is observed. The influence of substituting iron oxide by chromium oxide was evaluated. ToF-SIMS depth profiling shows that the inferior electrochemical activity of chromium oxide compared to iron oxide results in hindering lithium diffusion in the bulk electrode. It was observed that the morphology modifications together with SEI evolution are closely associated with electrode conversion and capacity degradation.

Keywords: lithium-ion batteries; binary (Fe, Cr)-oxide; XPS; ToF-SIMS; SEM; AFM

1. Introduction

Conversion-type transition metal oxides (e.g., CoO, Co_3O_4, NiO, CuO, Cu_2O, FeO, Fe_2O_3, Fe_3O_4, MnO and Cr_2O_3) present high technological interest for lithium-ion batteries (LIBs) due to high theoretical capacities, low cost and safety. [1-9] However, these metal oxides suffer from the problem of electrode pulverization induced by huge volume changes, thus leading to poor cycling performance due to severe aggregation of metal oxide particles during the discharge/charge process. [10-12] In order to overcome these obstacles, many methods have been explored. Recently, binary metal oxides, such as $Co_{3-x}Fe_xO_4$ (x=0, 1, 2), [13] $NiFe_2O_4$, [14] $Ca_2Fe_2O_5$ and $Ca_2Co_2O_5$, [15] $CoMoO_4$ [16] and Mn_2CoO_4 [17,18] have shown possibilities of tuning energy density and working voltage by varying the metal content. [19] However, the mechanisms between the two metallic ions are not totally clear yet.

Iron oxide (mainly Fe_2O_3) and chromium oxide (mainly Cr_2O_3) are important candidates of transition metal oxides and have attracted much interest. [20-23] Chromium oxide has a higher theoretical Li storage capacity and lower working voltage in comparison to iron oxide (capacity 1058 mAh g^{-1} *vs.* 1007 mAh g^{-1}, *emf* (electromotive force) 1.085 V *vs.* 1.631 V for chromium and iron oxides, respectively, for electrode materials in a battery). [23,24] It seems that the substitution of iron oxide by chromium could theoretically increase Li storage capacity and lower working voltage. In this study, (Fe,Cr)-binary mixed oxide thin film electrodes were prepared by direct thermal growth on stainless steel current collector without conductive carbon additives and binder (PVDF). The mechanisms of reduction-reoxidation of the binary oxide in lithium ion batteries were investigated by electrochemical (CV, galvanostatic cycling), spectroscopic (XPS, ToF-SIMS) and microscopic (SEM, AFM) analyses. The influence of Cr substitution in iron oxide and the interaction mechanism between Fe and Cr atoms were discussed by comparing the data with our previous work on Fe_2O_3 and Cr_2O_3 thin film electrodes. [25,26]

2. Experimental methods

2.1 Preparation of (Fe, Cr)-binary oxide thin films

Stainless steel plates (AISI410, $FeCr_{12.5}$) were purchased from Goodfellow and then cut into square substrate samples (about 8×8 mm^2). The surfaces were prepared by mechanical

polishing with diamond spray down to 1/4 μm and then rinsed in successive ultrasonic baths of acetone, ethanol, and Millipore water (resistivity > 18 MΩ cm) for 2 min each and dried in a flow of compressed air.

(Fe, Cr)-binary oxide thin films were prepared by thermal oxidation at 300 ^{o}C in air as described in details for iron oxide in chapter 2 and 3. [25,27,28] The average thickness of the oxide thin films was ~46.5 nm as estimated by depth profile analysis on the pristine sample. Raman spectroscopy (Horiba Xplora system, Ar^{+} laser, λ = 532 nm) was employed for phase identification of the thermal oxides.

2.2 Electrochemical measurements

Electrochemical measurements (cyclic voltammetry and galvanostatic cycling) were performed in a glovebox (Jacomex) under Ar atmosphere with H_2O and O_2 contents lower than 1 ppm. A three-electrode glass cell was used with the binary oxide supported thin film as working electrode and Li foil (Sigma-Aldrich) as reference and counter electrodes. The cell was operated at room temperature using an Autolab (AUT30) electrochemical workstation. The working electrode area was delimited to 0.28 cm^2 by an O-ring. The electrolyte was 1 M $LiClO_4$ in propylene carbonate (1 mol L^{-1} $LiClO_4$/PC, Sigma-Aldrich). All potentials hereafter are given versus Li/Li^{+}. Cyclic voltammograms were recorded over the potential range of 0.01 - 3.0 V at a scanning rate of 0.2 mV s^{-1}, starting form OCP into the cathodic scan (discharge) direction. Galvanostatic discharge-charge was performed at a current density of 10 μA cm^{-2} in the potential range of 0.01 - 3.0 V.

For chemical and morphological analyses the binary oxide thin-film electrodes were submitted to varying cycle numbers of galvanostatic discharge-charge. The cell was disassembled and the samples were rinsed with acetonitrile (99.8%, Sigma-Aldrich) and dried with Ar flow for XPS, ToF-SIMS, SEM and AFM analyses.

2.3 Spectroscopic analysis

XPS analysis was carried out on a VG ESCA-LAB 250 spectrometer with an ultra-high vacuum preparation chamber directly connected to the glovebox. [29] An Al Kα monochromatized radiation (*hv* = 1486.6 eV) was employed as X-ray source. Base pressure

during analysis was 10^{-9} mbar. Survey spectra were recorded with a pass energy of 100 eV at a step size of 1 eV and high resolution spectra of the C1s, O1s, Fe2p and Cr2p core level regions were recorded with a pass energy of 20 eV at a step size of 0.1 eV. Peak fitting was performed with the Avantage software v. 3.13 provided by Thermo Electron Corporation, using a Shirley type background and Lorentzian/Gaussian (30%) peak shapes. The binding energies were calibrated by setting the C1s hydrocarbon ($-CH_2-CH_2-$) peak at 285.0 eV.

A ToF-SIMS 5 spectrometer (IonTof - Munster, Germany) operating at 10^{-9} mbar was used for depth profile chemical analysis. Samples were transferred in an air-tight vessel under argon atmosphere from the glovebox to the ToF-SIMS system. A pulsed 25 keV Bi^+ primary ion source was employed for analysis, delivering 1.2 pA current over a 100 μm × 100 μm^2 area. Depth profiling was carried out using a 1 keV Cs^+ sputter beam giving a 70 nA target current over a 300 μm × 300 μm^2 area. Ion-Spec software from ION-TOF GmbH was used for acquiring and processing the data. Negative ion depth profiles were recorded for better sensitivity to fragments originating from oxides matrices.

2.4 Microscopic characterization

SEM imaging of the thin-film binary oxide electrodes before and after electrochemical treatment was performed with a ZEISS Ultra-55 Field Emission Scanning Electron Microscope (FE-SEM, Germany). The electrochemical cells were disassembled in the glovebox and the samples rinsed as described above and then transferred in an air-tight vessel under argon atmosphere to the SEM introduction chamber in order to minimize the reaction with ambient atmosphere.

AFM imaging was performed with an Agilent 5500 Atomic Force Microscope operated in a tapping mode. A silicon tip mounted on a cantilever with a force constant of 25 - 75 N m^{-1} at a resonance frequency of about 282.6 kHz was employed. AFM data visualization and analysis (average value, RMS) were performed with the Gwyddion 2.31 software.

3. Results and discussion

3.1 Composition and phases

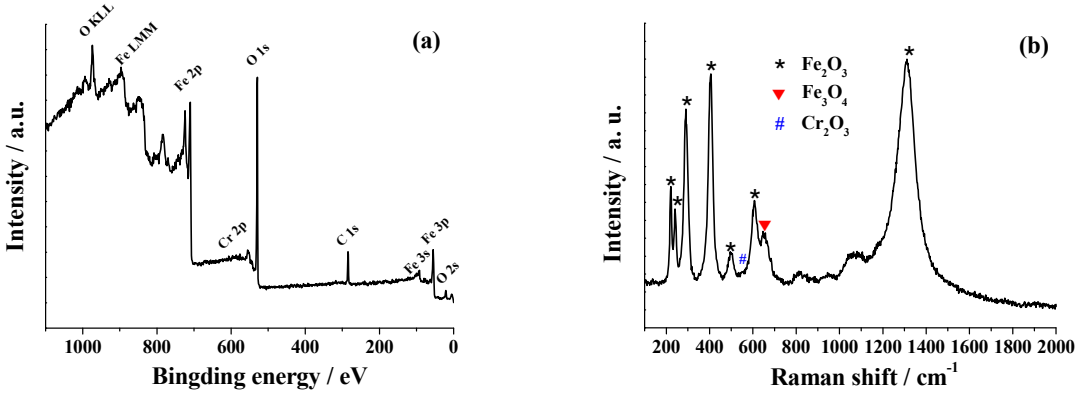

Figure 1 (a) XPS survey spectra in the binding energy region of 0 - 1100 eV and (b) Raman spectra in the range of 100 - 2000 cm^{-1} of the binary (Fe, Cr)-oxide thin film prepared by thermal oxidation of stainless steel substrate at 300 ^{o}C in air.

Figure 1 shows the XPS survey and Raman spectra of the binary (Fe, Cr)-oxide thin film prepared by thermal oxidation of the stainless steel substrate. The XPS survey spectrum shows the presence of only Fe, Cr, O, and organic contamination (C1s signal), indicating a well oxidized metal surface. This is confirmed by the high resolution spectra of Fe2p and Cr2p core levels shown below (no metallic Fe or Cr component observed). The atomic percentage ratio of Fe:Cr calculated from XPS data is 94:6, which is higher than that of the stainless steel substrate (87.5:12.5), showing a Cr concentration decrease in the outer part of the oxide thin film proved by XPS. This is also consistent with ToF-SIMS data on the pristine sample presented below.

The Raman spectrum after oxidation presents a crystallized surface containing thermodynamically stable α-Fe_2O_3 (hematite) together with a small amount of Fe_3O_4 (magnetite). [30-34] The characteristic peak of Cr_2O_3 centered at 549 cm^{-1} (A_{1g} mode of Cr_2O_3) [35] was not detected, indicating a small amount of Cr_2O_3 on the surface, in agreement with the XPS data and the ToF-SIMS data presented below. However, Cr in the Fe_2O_3 lattice to form a $Cr_xFe_{2-x}O_3$ cannot be ruled out here due to the similar ionic radius of Fe^{3+} (0.64 Å) and Cr^{3+} (0.63 Å).

3.2 Conversion mechanism of binary oxide showed by cyclic voltammetry

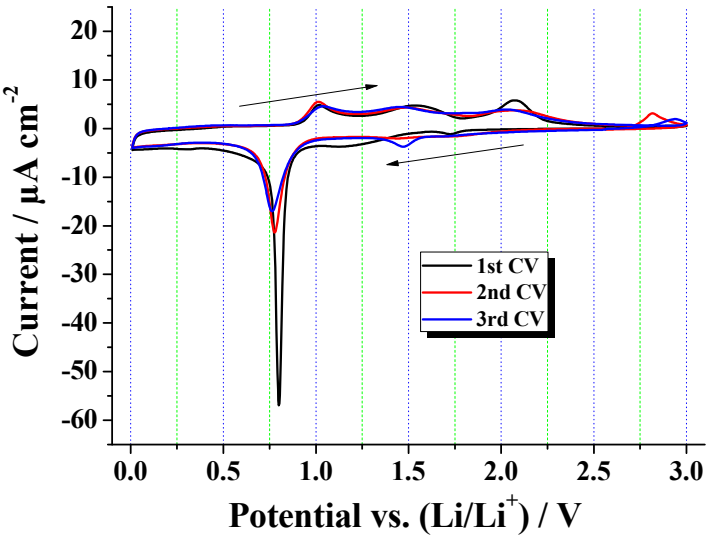

Figure 2 First three consecutive cyclic voltammograms of the binary oxide thin film electrode in 0.01-3.0 V potential range (scan rate of 0.2 mV s^{-1}).

Figure 2 presents the first three consecutive CVs of the binary oxide thin-film electrode. Polarization started from OCP (~3.0 V) into the cathodic direction. In the first CV cycle, a sharp cathodic peak located at about 0.8 V is observed upon electrochemical reduction. This cathodic peak corresponds to the conversion reaction of oxide with lithium and also to the formation of the SEI layer. [25-27,36] The cathodic peak potential (0.8 V) of this binary oxide is slightly higher than that for iron oxide (0.75 V), showing an undiminished lithiation (working) potential after substituting iron by chromium. This is related to the lower electrochemical activity of chromium oxide. A cathodic peak expected at lower potential (i. e. ~0.59 V [26]) for Cr_2O_3 was not observed in the CV curves, in agreement with the small amount of Cr_2O_3 in the binary oxide or lower electrochemical activity of Cr_2O_3 in the reaction. In the anodic process of the first CV cycle, a broad peak (containing three peaks at 1.02, 1.5 and 2.06 V) centered at 1.54 V is related to the deconversion process of Li_2O with metallic iron and/or chromium. The corresponding reactions could be described by equations 1-3: [20,21,25,26,36,37-40]

$$Fe_2O_3 + 6Li^+ + 6e^- \Leftrightarrow 2Fe + 3Li_2O \quad (1)$$

$$Cr_2O_3 + 6Li^+ + 6e^- \Leftrightarrow 2Cr + 3Li_2O \quad (2)$$

or $Fe_xCr_{2-x}O_3 + 6Li^+ + 6e^- \Leftrightarrow xFe + (2-x)Cr + 3Li_2O \quad (0 \le x \le 2)$ (3)

The coulombic efficiency calculated from the ratio of the anodic charge to cathodic discharge is only 57.2%, which is much lower than that for iron oxide (~70%) [25] due to the poorer electrochemical activity of chromium oxide, as demonstrated by ToF-SIMS data below.

In the second CV cycle, a significant decrease of the cathodic peak intensity at ~0.8 V indicates the high irreversible capacity corresponding to formation of the SEI layer. This also confirms the low coulombic efficiency in the first lithiation/delithiation process proved by galvanostatic cycling results presented below. Similarly to the first oxidation process, three main anodic peaks around 1.55, 1.02 and 2.0 V are observed in the second CV cycle but with slightly lower current density, which is assigned to the delithiation process of different valence state of metal oxides as discussed in chapter 2. [25] Another anodic peak was observed at 2.8-3.0 V from the second cycle on, which may originate from the oxidation of Cr(III) to Cr(VI) and/or of Fe directly to Fe(III). [41] However the corresponding reduction process was not observed in the same potential range. This means that an irreversible oxide film was formed on the stainless steel current collector at this potential. Thus, from thermodynamic point of view, it is better to limit the cycling potential (to a value ＜3 V) for this type of electrode material. [41]

In the third CV cycle, a well-defined cathodic peak at about 1.5 V emerges in the reduction process. This peak could correspond to the intercalation of Li^+ into Fe_2O_3 nanoparticles to form the intermediate product $Li_xFe_2O_3$ ($0<x\leq2$), which would confirm a pulverization process of the iron oxide thin-film electrode [25] also revealed by galvanostatic discharge-charge data and the SEM, AFM results discussed below.

3.3 Cycling performance by galvanostatic discharge/charge

Figure 3 (a) shows the first, second, third, fifth, tenth and twentieth discharge-charge voltage profiles of the thin-film (Fe, Cr)-oxide electrode at a current of 10 μA cm^{-2} in the potential range of 3.0 - 0.01 V. It exhibits a ramp-down plot between 2.0 V and 0.85 V and an extended voltage plateau at ~0.85 V in the discharge curves, which are ascribed to the formation of cubic $Li_xFe_2O_3$ ($0<x\leq2$) and the conversion from Fe^{2+} to Fe^0, respectively. [20,21]

However, the small amount of chromium oxide in the electrode can also contribute to the process. In the charge curves, the ramp-up region from 1.0 to 2.2 V corresponds to the reversible oxidation of Fe^0 to Fe^{3+} and/or Cr^0 to Cr^{3+}, which is consistent with CV measurements.

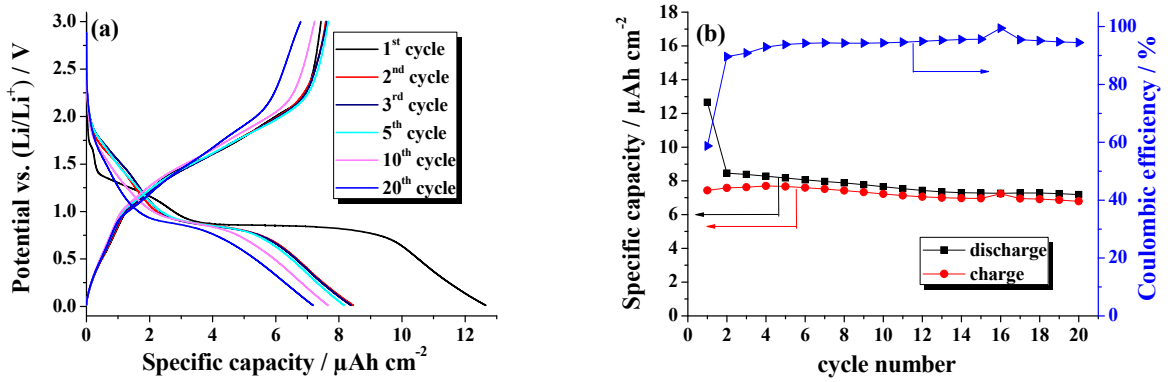

Figure 3 (a) First, second, third, fifth, tenth and twentieth discharge-charge curves; (b) cycling performance and coulombic efficiency of the binary (Fe, Cr)-oxide electrode (current density of 10 µA cm^{-2} in a potential range of 3.0 - 0.01 V).

Figure 3 (b) presents the cycling performance and coulombic efficiency of the (Fe, Cr)-oxide thin-film electrode during the first 20 cycles. The first discharge delivers a capacity of 12.65 µAh cm^{-2}, which is much higher than the first charge capacity (7.43 µAh cm^{-2}). The coulumbic efficiency is 58.7%, in agreement with the CV data. This high irreversible capacity originates from formation of SEI layer (irreversible decomposition of electrolyte) and non-fully reversible conversion/deconversion process in the first discharge-charge cycle. This coulombic efficiency is lower than that for iron oxide (70.1%) [27] but higher than that for chromium oxide (<30%), [26] showing an inferior electrochemical activity of chromium oxide in comparison to iron oxide. Nevertheless, the discharge and charge capacities were well retained during the following cycles suggesting excellent capacity retention of the thin film (Fe, Cr)-oxide electrode. After 20 cycles, this anode material retains 7.19 µAh cm^{-2} (discharge) and 6.79 µAh cm^{-2} (charge), demonstrating a good capacity retention ratio (85.0% and 89.6%, respectively) with respect to the second cycle.

3.4 XPS analysis upon cycling

The XP C1s, O1s, Fe2p and Cr2p spectra for the pristine binary oxide and electrodes

after different cycles are shown in Figure 4. Binding energies (E_B) and full widths at half-maximum (FWHM) of the component peaks obtained by peak fitting are listed in Table 1.

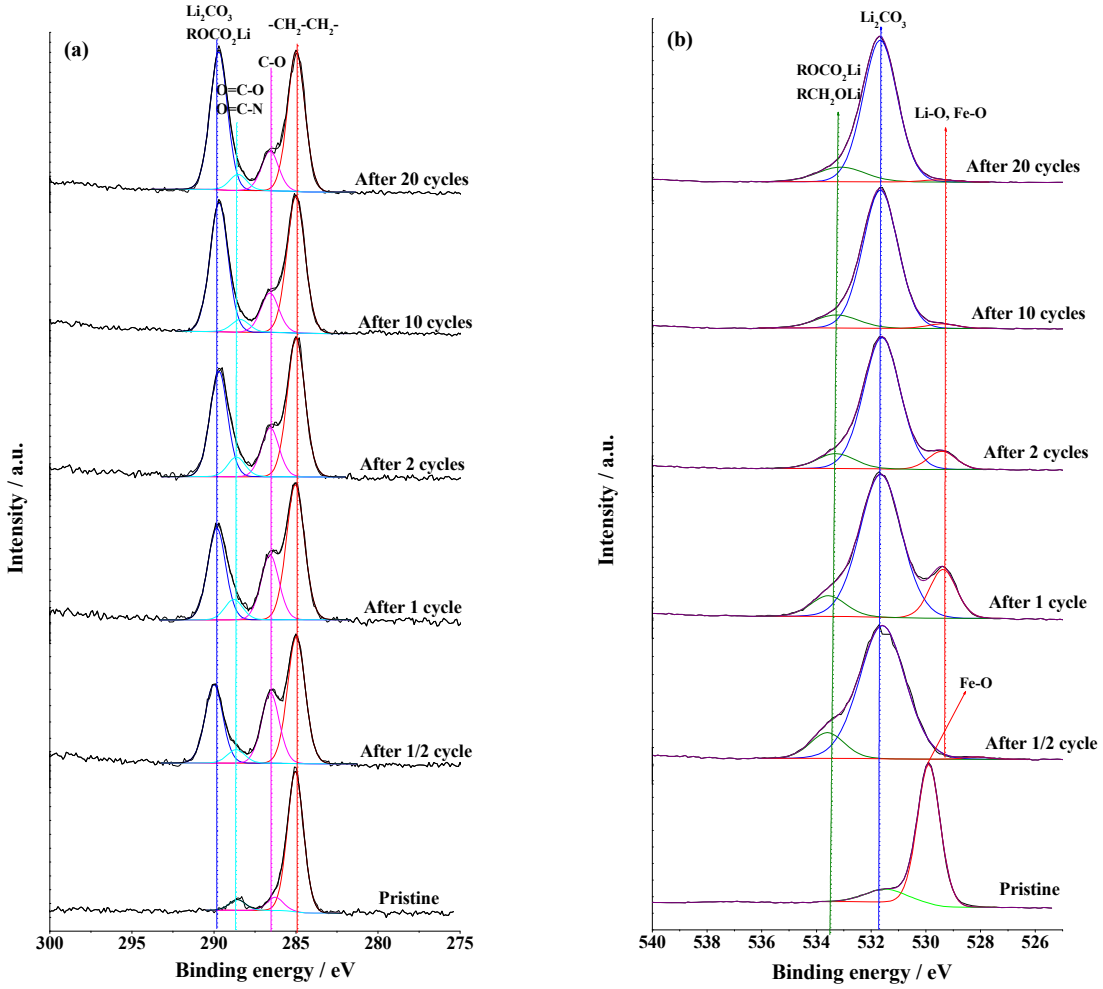

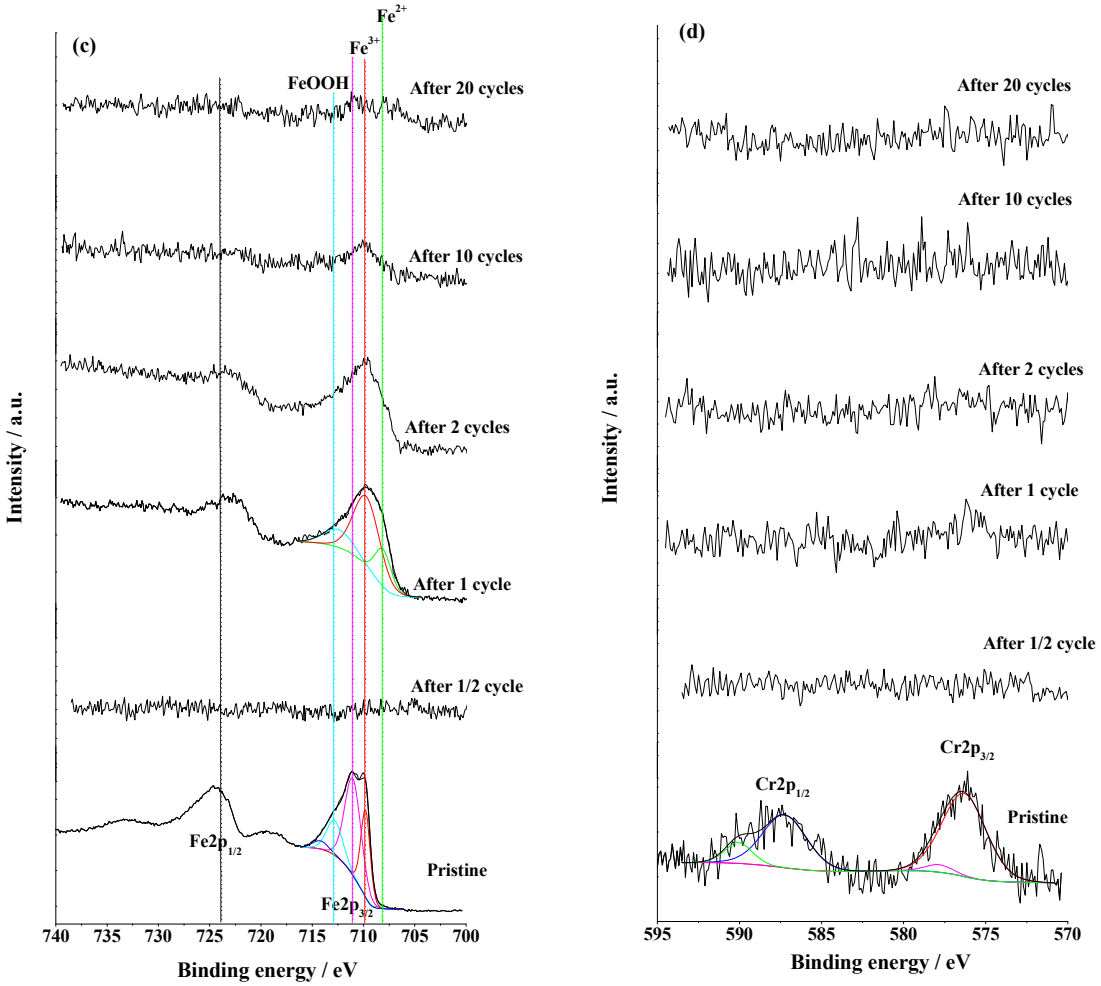

Figure 4 XP (a) C1s, (b) O1s, (c) Fe2p and (d) Cr2p spectra for the pristine binary oxide electrode and after 1/2, 1, 2, 10 and 20 cycles.

Table 1 Binding energies (E_B) and full widths at half-maximum (FWHM) of the C1s, O1s, Fe2p$_{3/2}$ and Cr2p core levels obtained by peak fitting for the pristine electrode and after 1/2, 1, 2, 10 and 20 cycles.

	pristine		after 1/2 cycle		after 1 cycle		after 2 cycles		after 10 cycles		after 20 cycles	
	E_B (eV)	FWHM (eV)	E_B (eV)	FWHM (eV)	E_B (eV)	FWHM (eV)	E_B (eV)	FWHM (eV)	E_B (eV)	FWHM (eV)	E_B (eV)	FWHM (eV)
$C1s_A$	285.0	1.2	285.0	1.3	285.0	1.3	285.0	1.3	285.0	1.3	285.0	1.3
$C1s_B$	286.3	1.2	286.6	1.3	286.6	1.3	286.6	1.3	286.6	1.3	286.6	1.3
$C1s_C$	288.6	1.2	288.7	1.3	288.8	1.3	288.6	1.3	288.4	1.3	288.5	1.3
$C1s_D$			290.0	1.3	289.8	1.3	289.7	1.3	289.7	1.3	289.7	1.3
$O1s_A$	529.9	10	528.2	1.1	529.4	1.2	529.4	1.3	529.4	1.4	529.5	1.5
$O1s_B$	531.5	1.8	531.6	2.0	531.7	1.9	531.6	1.6	531.7	1.6	531.7	1.5
$O1s_C$												
$O1s_D$			533.6	1.5	533.6	1.5	533.3	1.7	533.3	1.9	533.1	2.1
$Fe2p_{3/2A}$	708.2	1.3	708.1	2.0								
$Fe2p_{3/2B}$	709.8	1.1	709.7	3.1								
$Fe2p_{3/2C}$	711.0	1.9										
$Fe2p_{3/2D}$	712.8	1.9	712.4	3.5								
$Fe2p_{3/2E}$	714.2	1.8										
$Cr2p_{1/2A}$	576.3	3.3										
$Cr2p_{3/2B}$	577.8	2.0										
$Cr2p_{3/2C}$	587.3	3.3										
$Cr2p_{3/2D}$	590.1	2.0										

The C1s signal of the pristine sample originates from the organic contaminants present on the surface. After cycling, one new component peak is observed at ~289.9 eV and assigned to Li_2CO_3 and/or $ROCO_2Li$, which is the main component of the SEI layer. [42,43] Moreover, this peak increases with cycling, indicating a dynamic behavior of the SEI layer, which was already observed on other types of electrodes. [44-48] For the O1s spectrum, a major oxygen component assigned to Fe-O bonds in the iron oxide matrix has vanished after 1/2 cycle due to the growth of SEI on the electrode as shown by peaks at ~531.8 and ~533.3 eV. A metal-oxygen (Fe-O and/or Li-O) bond reappeared after 1 cycle, showing some decomposition of the SEI layer at this first delithiation stage. However, the metal-oxygen component peak decreases with further cycling due to SEI thickening as already observed from C1s core level spectra.

The $Fe2p_{3/2}$ spectrum peak fitting for the pristine sample shows five components,

corresponding to Fe^{2+} in Fe_3O_4 (at 708.2 eV), Fe^{3+} in Fe_2O_3 and/or Fe_3O_4 (at 709.8 and 711.0 eV), Fe^{3+} in FeOOH (at 712.8 eV) and satellite of Fe^{2+} (at 714.2 eV), as discussed in detail previously (in chapter 2). [25] The Cr2p spectrum for pristine sample show the presence of a small quantity of Cr_2O_3 (at 576.3 and 587.3 eV) and traces of CrOOH and/or $Cr(OH)_3$ (at 577.8 and 590.1 eV).

The peaks in Fe2p and Cr2p spectra have vanished after 1/2 cycle and reappear attenuated after 1 cycle, which is consistent with the dynamic evolution of the SEI layer already indicated by the XP C1s and O1s core levels. After 1 cycle, the intensity of Fe^{2+} component at E_B ($Fe2p_{3/2A}$)= 708.1 eV obviously increases, showing modification of the iron oxide matrix (Fe^{3+} to Fe^{2+}) due to the not completely reversible lithiation/delithiation process. Due to the significant attenuation of the Fe2p peak after the 2nd cycle, the peak decomposition is very difficult. However, it can be concluded that no important chemical modification is observed on the binary oxide thin film electrode with cycling. After 20 cycles, both Fe2p and Cr2p spectra intensities are completely attenuated by the growth of the SEI layer, confirming continuous thickening of the SEI layer with further electrochemical cycling.

3.5 *ToF-SIMS depth profiling*

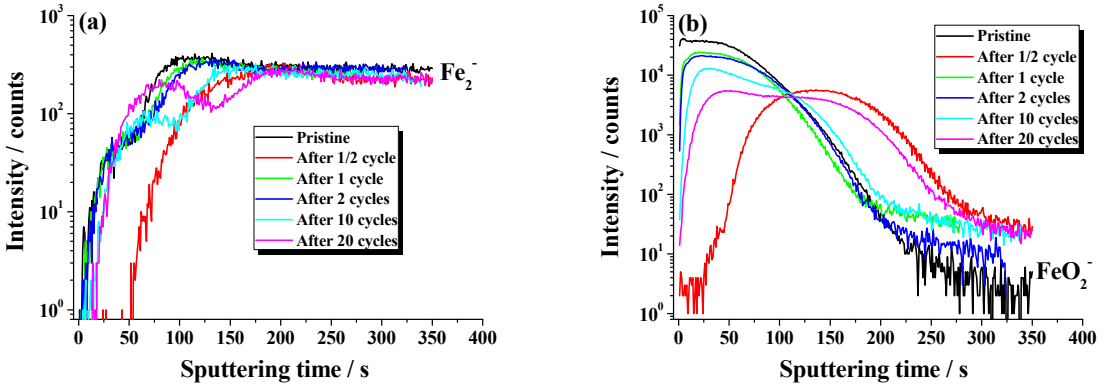

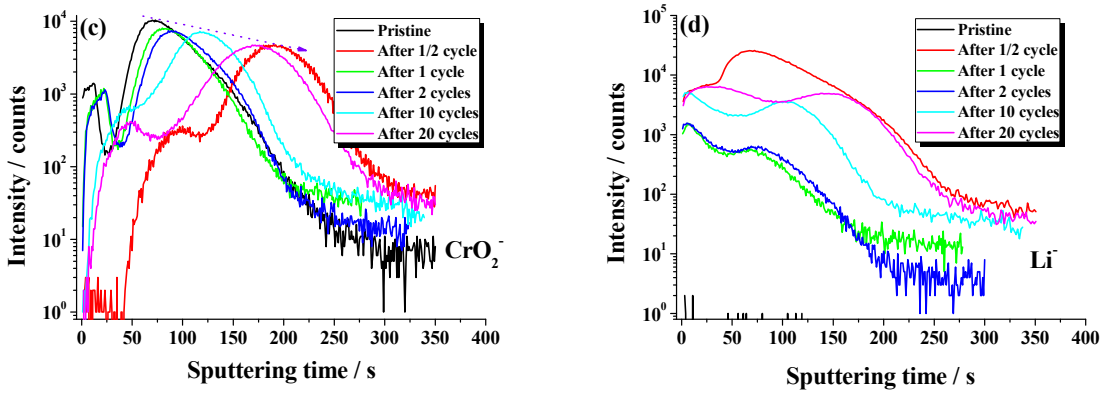

Figure 5 ToF-SIMS negative ion depth profiles of the (a) Fe_2^-, (b) FeO_2^-, (c) CrO_2^- and (d) Li^- ions for the pristine binary oxide electrode and electrodes after 1/2, 1, 2, 10 and 20 cycles.

Figure 5 shows the negative ion depth profiles of the Fe_2^-, FeO_2^-, CrO_2^- and Li^- ions of the pristine and treated samples. The intensity is presented using a logarithmic scale to magnify the low intensity signals. The variation of the ion intensity with sputtering time reflects the variation of the in-depth concentration but it is also dependent on the matrix from which the ions are emitted. [49] The Fe_2^- ions depth profiles (Figure 5 (a)) were selected to characterize the metal substrate. On the pristine sample, the intensity of Fe_2^- ions increases gradually to a stable intensity at about 100 s of sputtering, indicating that the substrate is reached. After 1/2 cycle, the sputtering time increases to 210 s, clearly indicating the swelling of the thin film during the lithiation process. However, matrix effects of the lithiated oxides can also affect the sputtering yield. After 1 cycle, the sputtering time to reach the substrate is decreased to 110 s, reflecting volume shrinking upon delithiation. This value is only slightly higher than that for the pristine sample, which indicates a good reversibility of the binary oxide thin film upon discharge/charge with only small amounts of Li trapped in the electrode (see also Figure 5 (d)). With further cycling (after 2, 10 and 20 cycles), the Fe_2^- ions profiles markedly change after 10 cycles. The sputtering time to reach the substrate increases to 147 s, which indicates volume expansion corresponding to 47 s of sputtering. A plateau region between 49 s and 108 s shows an intensity decrease of the Fe_2^- ions indicating a modification of iron oxide matrix after cycling caused by volume variation.

The FeO_2^- ions intensity (Figure 5 (b)) displays the highest value for the pristine binary oxide film. In the discharge state (after 1/2 cycle), the intensity of FeO_2^- ions decreases due to

conversion of iron oxide to lithium oxide and metallic iron. After 1 cycle (charged to 3.0 V), the FeO_2^- ions intensity increases compared to the discharged sample, but it remains lower than that for the pristine, confirming a non-fully reversible lithiation process. The intensities of the FeO_2^- ions further decreased with cycling (after 2, 10 and 20 cycles), showing an aging process of this binary oxide electrodes.

Figure 5 (c) compares the CrO_2^- ions depth profiles for the pristine, 1/2, 1, 2, 10 and 20 cycled samples. On the pristine sample, the intensity peak ("surface peak") obtained during the first seconds of sputtering indicates an increased concentration of chromium oxide at the electrode surface (over a thickness of around 4 nm estimated from ToF-SIMS sputtering rate). The second peak ("interfacial peak") observed in the CrO_2^- ion profile at around 75 s of sputtering indicates the presence of chromium oxide at the interface of the binary oxide thin film electrode with the substrate. The intensity of CrO_2^- ions (interfacial peak) decreases less (from ~10^4 to ~5000 counts) than that of FeO_2^- ions (from ~4×10^4 to ~5000 counts) after 1/2 cycle. This indicates that the chromium oxide remains much more stable, showing a poor electrochemical activity of the chromium oxide during the lithiation/delithiation process. The less converted chromium oxide in the discharge/charge process must be responsible for the low coulombic efficiency of this thin film binary oxide electrode. It is well known that Cr favors the passivation of stainless steel when the Cr content exceeds ~12%. In the lithium transport process, the chromium oxide forming a compact passive layer on the electrode surface may block or reduce the Li diffusion in the bulk electrode. More significant modifications of the CrO_2^- ion profiles, like progressive decrease of the first ("surface peak") and the second ("interfacial peak") peaks intensities can be observed after 10 and 20 cycles. The increase of sputtering time as a function of cycle number is in agreement with the volume expansion of the thin film electrode material during cycling.

The Li^- ions (Figure 5 (d)) were selected to analyse changes of in-depth composition of lithium in the thin film electrode and SEI layer. As expected, no lithium is found in the pristine electrode. After cycling, the intensities of the Li^- ions profiles increase due to accumulation (discharged state) and trapping (charged states) in the bulk thin film electrode and SEI layer. However, the increase of the Li^- ions intensities can also be related to the matrixes from which the ions are emitted, i.e., different matrixes of the electrode caused by

thickening and in-depth penetration of SEI layer, and/or morphological modifications of the thin film electrodes (volume expansion and pulverization). [27,50] The maximum intensity of Li^- ion profile for the cycled electrodes (1-20 cycles) can be observed in the first seconds of sputtering corresponding to Li accumulation in the SEI layer, in agreement with the XPS data. However, this maximum Li^- ion intensity is observed slightly before the maximum in the CrO_2^- ion profile intensity, which can be explained by hindering of Li diffusion by the superficial chromium oxide layer. The exception is a discharged state, where a maximum Li^- ions intensity is observed in the bulk, converted binary Fe-Cr oxide electrode. At the same time, the extension of sputtering time up to 36 s (marking the beginning of the increase of the FeO_2^-, CrO_2^- and Li^- signals to attain a maximum) for the discharged sample indicates a growth of the SEI during discharge.

3.6 SEM characterization

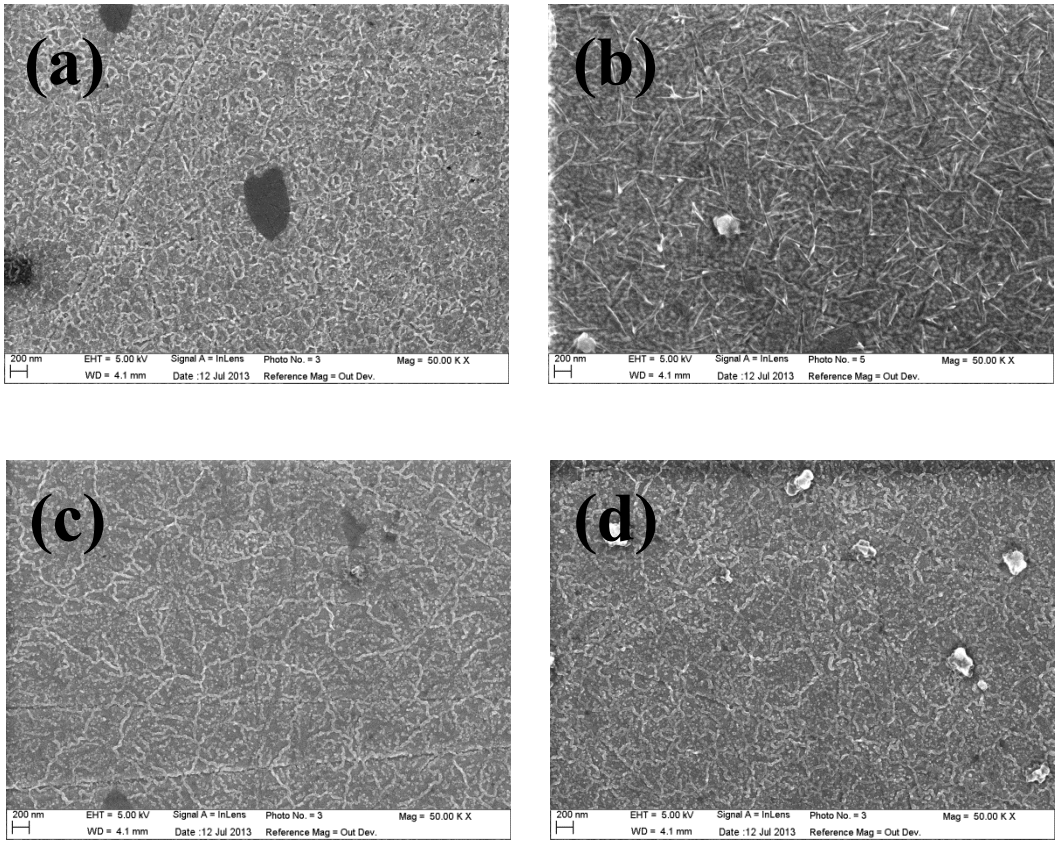

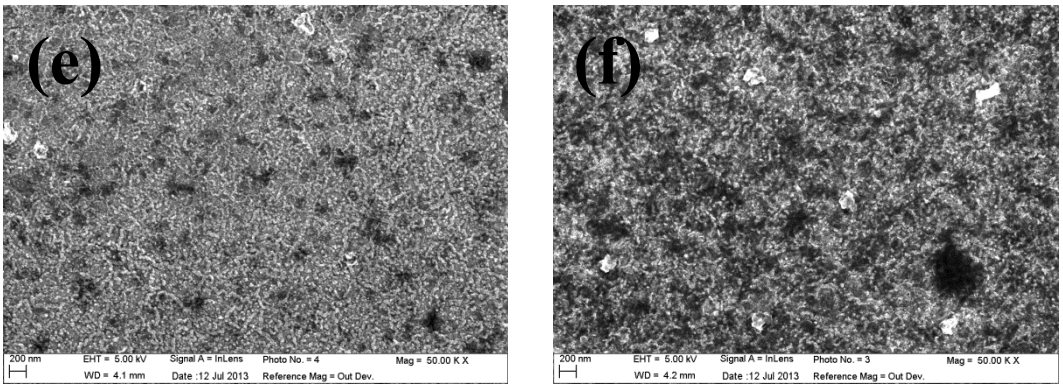

Figure 6 FE-SEM images of the pristine (a) and cycled electrodes after 1/2 (b), 1 (c), 2 (d), 10 (e) and 20 (f) cycles.

Figure 6 displays the FE-SEM images of the pristine and cycled samples (after 1/2, 1, 2, 10 and 20 cycles). The morphology of the pristine thin film electrode appears approximately flat and homogeneous except some scratches left by the substrate polishing and naked defects (pinholes) due to the nanometric thickness of the oxides film. The morphology shows a textured structure with presence of nano-grains (100-200 nm) which are well delimited by grain boundaries. After 1/2 cycle in the lithiated state (Figure 6 (b)), the grain boundaries evolve into spicules. The growth of the dielectric SEI on the electrode surface should blur the morphology which is not observed. Also it is well known that transition metal oxides electrodes undergo volume expansion (i.e. swelling) during the conversion process, which will cause pulverization and/or crash of the materials. [6,10] This is also not observed for our thin-film electrode. That maintains a good integrity after the lithiation process, indicating the nanometric thin film has a good adhesion to the substrate. The spicules grown at the surface suggest that the lithiation induced volume expansion would occur perfectly at the boundary.

After 1 complete cycle in the delithiated state (Figure 6 (c)), a flatter and more homogeneous morphology is recovered, which is consistent with volume shrinkage of the material and partial decomposition of the SEI layer in agreement with XPS and ToF-SIMS results. This shows a reversible morphological modification of the thin-film electrode at this stage. After 2 cycles, the morphology of the thin oxide layer is still well preserved (Figure 6 (d)). However, the disappearance of partial grain boundaries indicates recombination (pulverization and aggregation) of the electrode material. After 10 cycles, the morphology of the thin-film electrode is markedly modified (Figure 6 (e)), especially in the grain boundaries.

Some darker areas indicate SEI uneven thickening and these modifications are more significant on the sample after 20 cycles (Figure 6 (f)). At the same time, grain aggregation may occur along with SEI thickening and in-depth penetration, as shown by XPS and ToF-SIMS above.

3.7 AFM characterization

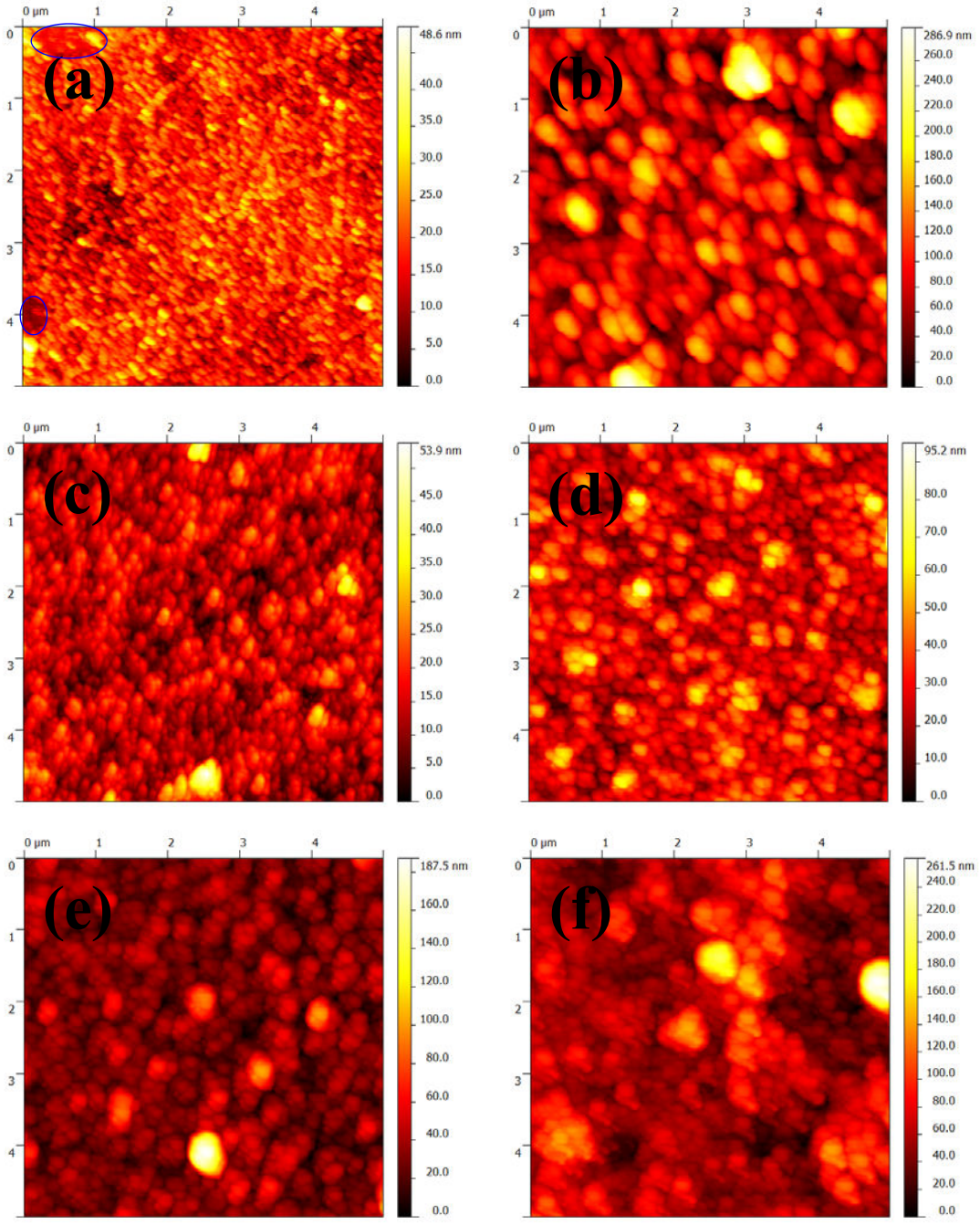

Figure 7 Topographic AFM images of the pristine (a) and cycled electrodes after 1/2 (b), 1 (c), 2 (d), 10 (e) and 20 (f) cycles.

Figure 7 presents the topographic AFM images of pristine binary oxide and cycled samples (after 1/2, 1, 2, 10 and 20 cycles). The topographic morphology of the pristine sample (Figure 7 (a)) shows a rough surface covered by nanometric nodules. The average lateral dimension of the nodules is ~14 nm and the RMS roughness is 4.6 nm. Moreover, some defects (delimited by ovals) are present on the surface due to the nanometric thickness, in good agreement with the pinholes observed by SEM data.

After 1/2 cycle in the converted state (Figure 7 (b)), the surface morphology shows an obvious growth of the nodule size. The lateral dimensions increase to ~89 nm and the RMS roughness to 40 nm, which is consistent with a volume expansion of the thin-film electrode during the lithiation process, in agreement with the ToF-SIMS results.

After 1 cycle in the delithiated state (Figure 7 (c)), the mean lateral dimension of the nodules is ~16 nm and the RMS roughness is 6.8 nm, showing volume shrinkage on the electrode surface compared to the lithiated state. The values are only slightly higher than that of the pristine surface, indicating good reversibility of the electrode material, as also shown by the ToF-SIMS and SEM data in the delithiated state. However, pulverization of the electrode material may also cause the formation of smaller nodule, as also clearly shown on grain boundaries of the SEM data.

After 2 cycles (Figure 7 (d)), the mean lateral dimension of the nodules further increase to ~30 nm and the RMS roughness to 10.4 nm, showing irreversible surface morphological modifications of the electrode material. The repeated volume expansion/shrinkage of the conversion-type electrode material during cycling causes more lithium trapping in the electrode. After 10 cycles, the surface is covered by much bigger aggregated nodules with an average lateral dimension of ~34 nm and a RMS roughness of 16.5 nm. Despite all this, the grains on the surface present a quite homogenous distribution. After 20 cycles, the surface is covered by even larger nodules (mean lateral dimension: 64 nm) and becomes much rougher (RMS roughness: 30.4 nm). An inhomogeneous surface modification accompanied by SEI layer penetration in the bulk thin film electrode is observed, as also confirmed by the SEM and ToF-SIMS data.

4. Conclusions

(Fe, Cr)-binary oxide thin films were grown as anode for lithium ion batteries by direct thermal oxidation of the stainless steel current collector. Electrochemical properties (coulombic efficiency and cathodic peak position) show that substituting a minor part of iron oxide by chromium oxide (~12.5%) improved neither the specific capacity nor the working voltage. Chemical surface analysis by XPS shows a dynamic process of formation and decomposition of the SEI layer on this binary oxide electrode during lithiation and delithiation, respectively. Thickening of the SEI layer is observed as a function of cycling. ToF-SIMS depth profiling reveals a lower electrochemical activity of chromium oxide, which may be responsible for the absence of enhanced electrochemical performance for this binary oxide electrode. The cycling-induced morphological changes of the electrode, as observed by SEM and AFM images, show reversible modifications of the thin film electrode surface in the first two cycles. However, a modified electrode surface is observed due to grain aggregation and SEI thickening and penetration in the electrode during further cycling after 10 and 20 cycles. The morphological modifications of the electrodes, mainly caused by lithium trapping upon non-completely reversible lithiation/delithiation and the formation of SEI layer, is accompanied by capacity fading upon cycling. Moreover, the kinetically controlled conversion process of this binary oxide shows that lithium transport in the bulk electrode also depends on oxide species. Chromium oxide present at the surface in the present case hinders the lithiation process of the oxide.

References

[1] Poizot P., Laruelle S., Grugeon S., Dupont L., Tarascon J.-M., Nano-sized transition-metal oxides as negative-electrode materials for lithium-ion batteries, *Nature*, **2000**, *407*, 496-499.

[2] Wang G.X., Chen Y., Konstantinov K., Lindsay M., Liu H.K., Dou S.X., Investigation of cobalt oxides as anode materials for Li-ion batteries, *J. Power Sources*, **2002**, *109*, 142-147.

[3] Aricò A.S., Bruce P., Scrosati B., Tarascon J.-M., Schalkwijk W.V., Nanostructured materials for advanced energy conversion and storage devices, *Nat. Mater.*, **2005**, *4*, 366-377.

[4] Taberna P.L., Mitra S., Poizot P., Simon P., Tarascon J.-M., High rate capabilities Fe_3O_4-based Cu nano-architectured electrodes for lithium-ion battery applications, *Nat. Mater.*, **2006**, *5*, 567-573.

[5] Nam K.T., Kim D.W., Yoo P.J., Chiang C.Y., Meethong N., Hammond P.T., Chang Y.M., Belcher A.M., Virus-enabled synthesis and assembly of nanowires for lithium ion battery electrodes, *Science*, **2006**, *312*, 885-888.

[6] M.V. Reddy, G.V. Subba Rao, B.V.R. Chowdari, Metal Oxides and Oxysalts as Anode Materials for Li Ion Batteries, *Chem. Rev.*, **2013**, *113*, 5364-5457.

[7] Hu J., Li H., Huang X.J., Cr_2O_3-based anode materials for Li-ion batteries, *Electrochem. Solid-State Lett.*, **2005**, *8*, A66-A69.

[8] Li H., Wang Z.X., Chen L.Q., Huang X.J., Research on advanced materials for Li-ion batteries, *Adv. Mater.*, **2009**, *21*, 4593-4607.

[9] Wang P.C., Ding H.P., Bark T., Chen C.H., Nanosized alpha-Fe_2O_3 and Li-Fe composite oxide electrodes for lithium-ion batteries, *Electrochim. Acta*, **2007**, *52*, 6650-6655.

[10] He Y., Huang L., Cai J.S., Zheng X.M., Sun S.G., Structure and electrochemical performance of nanostructured Fe_3O_4/carbon nanotube composites as anodes for lithium ion batteries, *Electrochim. Acta*, **2010**, *55*, 1140-1144.

[11] Fan Q., Whittingham M.S., Electrospun manganese oxide nanofibers as anodes for lithium-ion batteries, *Electrochem. Solid-State Lett.*, **2007**, *10*, A48-A51.

[12] Lian P.C., Cai D., Luo K.B., Jia Y., Sun Y.L., Wang H.H., Preparation and electrochemical properties of $(Fe_{2.5}Ti_{0.5})_{1.04}O_4$-graphene nanocomposite, *Electrochim. Acta*, **2013**, *104*, 267-273.

[13] Lavela P., Ortiz G., Tirado J.L., Zhecheva E., Stoyanova R., Ivanova Sv., High-performance transition metal mixed oxides in conversion electrodes: A combined spectroscopic and electrochemical study, *J. Phys. Chem. C*, **2007**, *111*, 14238-14246.

[14] Vidal-Abarca C., Tirado J.L., Lavela P., The origin of capacity fading in $NiFe_2O_4$ conversion electrodes for lithium ion batteries unfolded by ^{57}Fe Mössbauer spectroscopy, *J. Phys. Chem. C*, **2010**, *114*, 12828-12832.

[15] Sharma N., Shaju K.M., Subba Rao G.V., Chowdari B.V.R., Mixed oxides $Ca_2Fe_2O_5$ and $Ca_2Co_2O_5$ as anode materials for Li-ion batteries, *Electrochim. Acta*, **2004**, *49*, 1035-1043.

[16] Christie T.C., Reddy M.V., Sow C.H., Chowdari B.V.R., Interconnected network of $CoMoO_4$ sub-micron particles as high capacity anode material for Lithium ion battery, *ACS Appl. Mater. Interfaces*, **2013**, *5*, 918-923.

[17] Lavela P., Tirado J.L., Vidal-Abarca C., Sol-gel preparation of cobalt manganese mixed oxides for their use as electrode materials in lithium cells, *Electrochim. Acta*, **2007**, *52*, 7986-7995.

[18] Kim M.H., Hong Y.J., Kang Y.C., Electrochemical properties of yolk-shell and hollow $CoMn_2O_4$ powders directly prepared by continuous spray pyrolysis as negative electrode materials for lithium ion batteries, *RSC Adv.*, **2013**, *3*, 13110-13114.

[19] Cherian C.T., Reddy M.V., Subba Rao G.V., Sow C.H., Chowdari B.V.R., Li-cycling properties of nano-crystalline $(Ni_{1-x}Zn_x)Fe_2O_4$ ($0 \leq x \leq 1$), *J. Solid State Electr.*, **2012**, *16*, 1823-1832.

[20] Larcher D., Masquelier C., Bonnin D., Chabre Y., Mason V., Leriche J.B., Tarascon J.-M., Effect of particle size onlithium intercalation into α-Fe_2O_3, *J. Electrochem. Soc.*, **2003**, *150*, A133-A139.

[21] Larcher D., Bonnin D., Cortes R., Rivals I., Personnaz L., Tarascon J.-M., Combined XRD, EXAFS, and Mössbauer studies of the reduction by lithium of α-Fe_2O_3 with various particle sizes, *J. Electrochem. Soc.*, **2003**, *150*, A1643-A1650.

[22] Liu H., Du X., Xing X., Wang G., Qiao S.Z., Highly ordered mesoporous Cr_2O_3 materials with enhanced performance for gas sensors and lithium ion batteries, *Chem. Commun.*, **2012**, *48*, 865-867.

[23] Grugeon S., Laruelle S., Dupont L., Chevallier F., Taberna P.L., Simon P., Gireaud L., Lascaud S., Vidal E., Yrieix B., Tarascon J.-M., Combining Electrochemistry and Metallurgy for New Electrode Designs in Li-Ion Batteries, *Chem. Mater.*, **2005**, *17*, 5041-5047.

[24] H. Li, P. Balaya, J. Maier, Li-Storage via Heterogeneous Reaction in Selected Binary Metal Fluorides and Oxides, *J. Electrochem. Soc.*, **2004**, *151*, A1878-A1885.

[25] Tian B., Świątowska J., Maurice V., Zanna S., Seyeux A., Klein L.H., Marcus P., Combined surface and electrochemical study of the lithiation/delithiation mechanism of iron oxide thin film anode for lithium-Ion batteries, *J. Phys. Chem. C*, **2013**, *117*, 21651-21661.

[26] Li J.-T., Maurice V., Swiatowska-Mrowiecka J., Seyeux A., Zanna S., Klein L., Sun S.-G., Marcus P., XPS, time-of-flight-SIMS and polarization modulation IRRAS study of Cr_2O_3 thin film materials as anode for lithium ion battery, *Electrochim. Acta*, **2009**, *54*, 3700-3707.

[27] Tian B., Świątowska J., Maurice V., Zanna S., Seyeux A., Klein L.H., Marcus P., Aging-induced chemical and morphological modifications of thin film iron oxide electrodes for lithium-ion batteries, *Langmuir*, **2014**, *30*, 3538-3547.

[28] Tian B., Świątowska J., Maurice V., Pereira-Nabais C., Seyeux A., Marcus P., Kinetics evaluation of thin film α-Fe_2O_3 negative electrode for lithium-ion batteries, to be submitted.

[29] Swiatowska-Mrowiecka J., Maurice V., Zanna S., Klein L., Marcus P., XPS study of Li ion intercalation in V_2O_5 thin films prepared by thermal oxidation of vanadium metal, *Electrochim. Acta*, **2007**, *52*,

5644-5653.

[30] Reddy M.V., Yu T., Sow C.H., Shen Z.X., Lim C.T., Subba Rao G.V., Chowdari B.V.R., α-Fe_2O_3 nanoflakes as an anode material for Li-Ion batteries, *Adv. Funct. Mater.*, **2007**, *17*, 2792-2799.

[31] Beattie I.R., Gilson T.R., The single-crystal Raman spectra of nearly opaque materials. Iron(III) oxide and chromium(III) oxide, *J. Chem. Soc. A*, 1970, 5, 980-986.

[32] Zheng Z., Chen Y., Shen Z.X., Ma J., Sow C.H., Huang W., Yu T., Ultra-sharp α-Fe_2O_3 nanoflakes: growth mechanism and field-emission, *Appl. Phys. A*, **2007**, *89*, 115-119.

[33] Faria D.L.A., Venancio Silva S., Oliveira M.T., Raman microspectroscopy of some iron oxides and oxyhydroxides, *J. Raman Spectrosc.*, **1997**, *28*, 873-878.

[34] Bellot-Gurlet L., Neff D., Réguer S., Monnier J., Saheb M., Dillmann P., Raman studies of corrosion layers formed on archaeological irons in various media, *JNanoR*, **2009**, *8*, 147-156.

[35] Yu T., Shen Z.X., He J., Sun W.X., Tang S.H., Lin J.Y., Phase control of chromium oxide in selective microregions by laser annealing, *J. Appl. Phys.*, **2003**, *93*, 3951-3953.

[36] Hosono E., Fujihara S., Honma I., Ichihara M., Zhou H., Fabrication of nano/micro hierarchical Fe_2O_3/Ni micrometer-wire structure and characteristics for high rate Li rechargeable battery, *J. Electrochem. Soc.*, **2006**, *153*, A1273-A1278.

[37] Thackeray M.M., David W.I.F., Goodenough J.B., Temperature lithiation of α-Fe_2O_3: A mechanistic study, *J. Solid State Chem.*, **1984**, *55*, 280-286.

[38] Laruelle S., Grugeon S., Poizot P., Dolle M., Dupont L., Tarascon J.-M., On the origin of the extra electrochemical capacity displayed by MO/Li cells at low potential, *J. Electrochem. Soc.*, **2002**, *149*, A627-A634.

[39] Nuli Y.-N., Zeng R., Zhang P., Guo Z.P., Liu H.K., Controlled synthesis of α-Fe_2O_3 nanostructures and their size-dependent electrochemical properties for lithium-ion batteries, *J. Power Sources*, **2008**, *184*, 456-461.

[40] Chaudhari S., Srinivasan M., 1D hollow α-Fe_2O_3 electrospun nanofibers as high performance anode material for lithium ion batteries, *J. Mater. Chem.*, **2012**, *22*, 23049-23056.

[41] Myung S.-T., Sasaki Y., Saito T., Sun Y.-K., Yashiro H., Passivation behavior of Type 304 stainless steel in a non-aqueous alkyl carbonate solution containing $LiPF_6$ salt, *Electrochim. Acta*, **2009**, *54*, 5804-5812.

[42] Światowska-Mrowiecka J., Martin F., Maurice V., Zanna S., Klein L., Castle J., Marcus P., The distribution of lithium intercalated in V_2O_5 thin films studied by XPS and ToF-SIMS, *Electrochim. Acta*, **2008**, *53*, 4257-4266.

[43] Swiatowska-Mrowiecka J., Diesbach S., Maurice V., Zanna S., Klein L., Briand E., Vickridge I., Marcus P., *J. Phys. Chem. C*, **2008**, *112*, 11050-11058.

[44] Bryngelsson H., Stjerndahl M., Gustafsson T., Edström K., How Dynamic Is the SEI? *J. Power Sources* **2007**, *174*, 970-975.

[45] Bar-Tow D., Peled E., Burstein L., A Study of Highly Oriented Pyrolytic Graphite as a Model for the Graphite Anode in Li-Ion Batteries, *J. Electrochem. Soc.*, **1999**, *146*, 824-832.

[46] Liao F., Światowska J., Maurice V., Seyeux A., Klein L.H., Zanna S., Marcus P., Ageing mechanisms of conversion-type electrode material studied oniron sulfide thin films, *Electrochim. Acta*, **2014**, *120*, 359-368.

[47] Pereira-Nabais C., Światowska J., Chagnes A., Gohier A., Zanna S., Seyeux A., Tran-Van P., Cojocaru C.-S., Cassir M., Marcus P., Insight into the Solid Electrolyte Interphase on Si Nanowires in Lithium-Ion Battery: Chemical and Morphological Modifications upon Cycling, *J. Phys. Chem. C*, **2014**, *118*, 2919-2928.

[48] Pfanzelt M., Kubiak P., Jacke S., Dimesso L., Jaegermann W., Wohlfahrt-Mehrens M., SEI Formation on TiO_2 Rutile, *J. Electrochem. Soc.*, **2012**, *159*, A809-A814.

[49] Li J.-T., Światowska J., Maurice V., Seyeux A., Huang L., Sun S.-G., Marcus P., XPS and ToF-SIMS Study of Electrode Processes on Sn-Ni Alloy Anodes for Li-Ion Batteries, *J. Phys. Chem. C*, **2011**, *115*, 7012-7018.

[50] Besenhard J.O., Winter M., Yang J., Biberacher W., Filming mechanism of lithium-carbon anodes in organic and inorganic electrolytes, *J. Power Sources*, **1993**, 54, 228-231.

Chapter 6. Conclusions and perspectives

1. Conclusions

In this thesis, an iron oxide (mostly α-Fe_2O_3) thin film model electrode was prepared by direct thermal oxidation of pure metallic iron substrate at 300 ^oC in air, used also as a current collector. A systematic study on this electrode was performed by electrochemical (CV, EIS and galvanostatic cycling), spectroscopic (XPS, ToF-SIMS and Raman spectroscopy) and microscopic (SEM and AFM) characterization techniques. Conversion, capacity degradation, and surface passivation mechanisms (formation of SEI layer) were investigated. Thermodynamic and kinetic properties of the thin-film iron oxide electrodes were revealed to evaluate the electrochemical properties of iron oxide as an anode for LIBs.

In Chapter 2, surface and depth profile analysis (XPS and ToF-SIMS) were combined with electrochemical techniques (CV and EIS) to study thoroughly the lithiation/delithiation mechanisms of iron oxide as anode material in LiBs. Raman spectroscopy, XPS and ToF-SIMS showed that the crystalline thin film contains mainly α-Fe_2O_3 (hematite) and small amount of FeOOH phase on the surface, and a Fe_3O_4 phase in the inner part of the film at the interface with the current collector. The SEI layer formed by reductive decomposition of the $LiClO_4$-PC electrolyte on the iron oxide thin film electrode is mainly composed of Li_2CO_3 with $ROCO_2Li$ as a minor constituent, independently of the lithiation/delithiation of the electrode. The main conclusion of this part of the work is related to the evolution of the SEI layer thickness upon lithiation/delithiation process. Upon lithiation, the conversion reaction mostly proceeding in the outer part of the electrode causes material swelling accompanied by SEI layer thickening. Upon delithiation, lithium is trapped in the deconverted electrode subjected to shrinking and the SEI layer decomposes and reduces in thickness, showing the non-reversibility of the conversion and surface passivation reactions.

In Chapter 3, the aging mechanisms of iron oxide thin film anode during multi-cycling were investigated thoroughly by combining spectroscopic (XPS, ToF-SIMS) and microscopic (SEM and AFM) analytical techniques. Multi-cycling induces no marked changes of the SEI composition but increases the thickness in the delithiated state. Penetration of the SEI layer and cumulative trapping of Li^+ ions due to irreversible conversion/deconversion occur in the

bulk electrode material upon cycling. Both effects contribute to irreversible swelling and compositional changes of the electrode material. Pulverization of the thin film electrode material and agglomeration of oxide nano-grains cause morphological changes upon cycling, which promote capacity in the first few cycles but results in rapid capacity fading during further cycling.

In Chapter 4, measurements of apparent diffusion coefficient of lithium (D_{Li}) into the thin film electrodes were performed using CV, EIS and ToF-SIMS. ToF-SIMS, as a direct method of evaluation of lithium diffusion, has been applied for the first time for the measurement of the D_{Li} into a conversion-type electrode material. The D_{Li} value was extracted from the in-depth variation of the Li-ion concentration by fitting theoretical values of the diffusion coefficient derived from the infinite integration of Fick's second law for 1-dimensional diffusion. The measured value of 0.6×10^{-15} cm^2 s^{-1} in the converted electrode, is lower than that obtained by CV from the cathodic electrochemical reactions (1.66×10^{-15} cm^2 s^{-1}) due to the dynamic process of conversion and formation of the SEI layer during the cathodic scan. The D_{Li} obtained by EIS in the electrode discharged to 0.84 V is ~2 times lower than that measured in the converted electrode by ToF-SIMS, which was assigned to hindering of the ionic transport by the SEI layer. Comparison of the ToF-SIMS, CV and EIS analysis data thus shows that Li-ion diffusion in SEI layer should not be neglected, as also supported by XPS analysis at selected potentials that confirms the dynamic process of formation of the SEI layer that accompanies discharge/charge of the electrode. The measured value of $\sim10^{-15}$ cm^2 s^{-1} in a converted electrode evidences that iron oxide has slow lithiation kinetics owing to its conversion mechanism and thus inferior C-rate charge/discharge behavior. ToF-SIMS, applied to the study of the kinetics of Li-ion migration into such a conversion-type electrode material and combined with a thin film approach, is proved as a direct methodology for extracting diffusion coefficients of lithium that excludes the influence of the surface passivation layer (SEI layer) on the data analysis and discriminates diffusion into converted and intercalated electrode matrices. The ToF-SIMS methodology presented here enlarged the horizon of studying Li diffusion kinetics into electrode for LiBs.

In Chapter 5, a (Fe, Cr)-binary oxide thin film was prepared on stainless steel (AISI410, $FeCr_{12.5}$) current collector. Electrochemical properties (coulombic efficiency and cathodic

peak position) show that the substitution of iron oxide by chromium does not improve the specific capacity or the working voltage. The coulombic efficiency of the thin film binary oxide electrode in the first discharge/charge cycle is slightly lower than that for iron oxide, but higher than that for chromium oxide due to the substitution of iron oxide by chromium. The cycling performance during 20 cycles shows a good capacity retention ratio, higher than 85%. ToF-SIMS results show that the lithium transport in the binary oxide also depends on the types of oxides. SEM and AFM data show that the morphological modifications of the electrode are minor in the first two cycles but significantly increase during the further cycling (i.e. after 10 and 20 cycles).

The systematic studies of iron oxide thin film electrodes have demonstrated the potential application of this anode material for lithium ion batteries. This iron oxide electrode, directly grown on the pure metallic iron or stainless steel substrate without conductive additives and binder, is also an ideal electrode for lithium ion microbatteries which can provide power sources for microelectronic systems.

2. Perspectives

Two perspectives are proposed for future work. One is atomic layer deposition (ALD) of iron oxide nanomaterial using AAO membrane template to improve performance of the iron oxide anode for LIBs. The other is the preparation and electrochemical study of metal-air batteries electrode materials for the next generation batteries, especially Fe-air batteries based on metallic iron substrate. The role of sulfide (i.e., Na_2S) on the inhibition of hydrogen evolution should be explored by electrochemical and surface analysis techniques. Some preliminary results are reported in Appendix 2.

Appendix 1

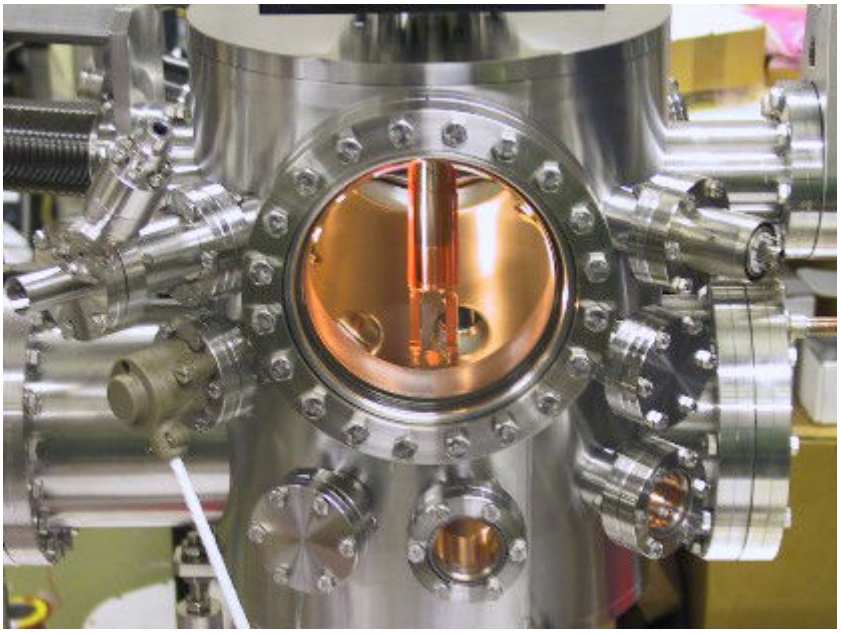

Abstract: In this part, the techniques, equipment and their principles are introduced in details. Thin film electrodes (iron oxides and/or iron/chromium binary oxides) were prepared by thermal oxidation of pure metal iron and/or stainless steel substrates in air. The electrochemical performances of electrode materials were studied by cyclic voltammetry (CV), electrochemical impedance spectroscopy (EIS) and galvanostatic discharge-charge. The chemical modifications were analyzed by surface science analytical techniques (X-ray Photoelectron Spectroscopy (XPS) and Time-of-Flight Secondary Ion Mass Spectrometry (ToF-SIMS). The morphology changes were studied by Scanning Electron Microscopy (SEM) and Atomic Force Microscopy (AFM). The corresponding analysis conditions are presented in the corresponding sections.

Keywords: Electrochemical measurements; XPS; ToF-SIMS; SEM; AFM

1. Sample preparation

Pure metal iron (a: iron plates, 99.99 wt%, 8×8×1 mm^3; b: iron foil, 99.5 wt%, 32×17×0.05 mm^3, Goodfellow) and stainless steel (AISI410, Fe/Cr12.5, 8×8×0.5 mm^3, Goodfellow) were used as substrates. Mechanical polishing and thermal oxidation were performed on these substrates to prepare the thin-film electrodes.

1.1 Mechanical polishing

The substrate surfaces were first polished with 1200 grit SiC paper, and then with diamond spray of 6 μm, 3 μm, 1 μm and 1/4 μm up to uniform flat surface as verified by an optical microscope (Achat France, NS 50). After polishing, the surfaces were rinsed in successive ultrasonic baths of acetone, ethanol, and Millipore water (resistivity >18 MΩ cm) for 2 min and dried in a flow of compressed air before thermal oxidation.

1.2 Thermal oxidation

The as prepared samples were placed in a quartz tube that could be inserted in a cylindrical oven (as shown in Figure A-1). The samples were oxidized in pre-thermalized oven at 300 ^oC for 5 min under air atmosphere and then quenched by 0 ^oC water. Then the oxidized samples were transferred into the glovebox for later use.

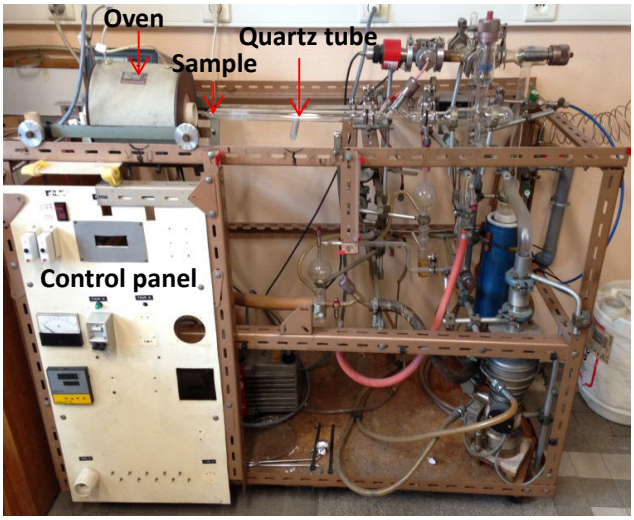

Figure A-1 Thermal oxidation system for preparation of thermal oxides on metallic substrates.

2. Electrochemical measurements

The electrochemical techniques used in this work are cyclic voltammetry (CV), electrochemical impedance spectroscopy (EIS) and galvanostatic discharge-charge cycling.

2.1 Cyclic voltammetry (CV)

Cyclic voltammetry (CV) is a type of potentiodynamic electrochemical measurement. In a cyclic voltammetry experiment the working electrode potential is ramped linearly versus time like in linear sweep voltammetry. Cyclic voltammetry takes the experiment a step further than linear sweep voltammetry which ends when it reaches a set potential. When cyclic voltammetry reaches a set potential, the working electrode's potential ramp is inverted. This inversion can happen multiple times during a single experiment. The current at the working electrode is plotted versus the applied voltage to give the cyclic voltammogram trace. Cyclic voltammetry is generally used to study the electrochemical properties of an analyte in solution and is the most widely used technique for acquiring qualitative information about electrochemical reactions. [1-3]

In cyclic voltammetry, the electrode potential ramps linearly versus time. This ramping is known as the experiment's scan rate (V/s). The potential is applied between the reference electrode and the working electrode and the current is measured between the working electrode and the counter electrode. These data are then plotted as current density (i) vs. potential (E). As the waveform shows in Figure A-2, the forward scan produces a current peak for any analytes that can be reduced (or oxidized depending on the initial scan direction) through the range of the potential scanned. The current will increase as the potential reaches the reduction potential of the analyte, but then falls off as the concentration of the analyte is depleted close to the electrode surface. If the redox couple is reversible then when the applied potential is reversed, it will reach the potential that will reoxidize the product formed in the first reduction reaction, and produce a current of reverse polarity from the forward scan. This oxidation peak will usually have a similar shape to the reduction peak. As a result, information about the redox potential and electrochemical reaction rates of the compounds is obtained. [3,4]

For instance if the electronic transfer at the surface is fast and the current is limited by

the diffusion of species to the electrode surface, then the current peak will be proportional to the square root of the scan rate. This relationship is described by the following equation: [5]

$$I_p = 0.4463 zFA(zF / RT)^{1/2} \Delta C_0 D_{Li}^{1/2} v^{1/2} \quad \text{(A-1)}$$

which can be simplified for experiments run at room temperature to:

$$I_p = 2.69 \times 10^5 n^{3/2} A D_{Li}^{1/2} v^{1/2} \Delta C_0 \quad \text{(A-2)}$$

where n is the number of electrons per reaction species, A the geometric area of the working electrode, 0.28 cm^2, D_{Li} the apparent diffusion coefficient of Li in the electrode, ΔC_O the change in Li concentration corresponding to the specific electrochemical reaction and v is the scan rate.

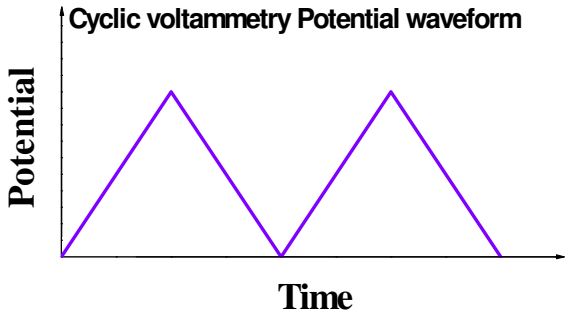

Figure A-2 Cyclic voltammetry waveform.

In this thesis, the CV was performed at room temperature using an Autolab (AUT30) electrochemical workstation. A three-electrode glass cell was used with the oxide thin film (prepared as described above) as a working electrode and two Li foils used as reference and counter electrodes. And the CV measurements were carried out from the open circuit potential (OCP) first in the cathodic direction and then in the anodic direction. More details of the tests (i.e. scan rates, cycle number) are given in each chapter.

2.2 Electrochemical impedance spectroscopy (EIS)

Electrochemical impedance spectroscopy (EIS) is a non-destructive technique often used to understand the interfacial behavior in electrochemical systems. The ability of this technique to differentiate various processes, i.e., ohmic conduction, charge transfer interfacial charging, mass transfer etc., makes it an elegant technique for electrochemical systems. [6] Its

applicability to lithium ion cells is further enhanced by the fact that surface films cover both the electrodes and especially the anode. Briefly, this technique involves a determination of cell impedance, in response to a small (~5 mV amplitude) AC signal at any constant DC potential, over a span of frequencies ranging. From the measured cell impedance in the form of real and imaginary components and phase angle, it is possible to examine and qualitatively determine several processes such as the electronic/ionic conduction in the electrode and electrolytes, interfacial charging either at the surface films or the double-layer, charge transfer processes and the mass transfer effects, if any. The time constants for these different processes being different, their features will show up at different frequencies in the EIS spectra. The advantages of this technique include: 1) its non-destructive nature, since the polarization applied is low enough that linear polarization conditions (i.e. where the polarization increases linearly with current) are maintained and the rate equations are simplified accordingly; 2) rapid and easy measurement methods as presently possible with the advent of computer-controlled equipment such as potentiostats and frequency response analyzers and appropriate software, which enormously simplify the data collection as well as subsequent analyses. The deficiency of this technique, on the other hand, is mainly related to the difficulty in interpreting the data, i.e. in envisaging a suitable electrical equivalent circuit to represent the electrochemical system and in quantitatively determining the relevant electrical parameters that would help understand the response of system. [7,8]

In this thesis, EIS has been successfully applied to the study of lithium ion batteries anode materials and been proven to be a powerful and accurate method for measuring lithium diffusion rates. In this work, EIS was also performed at room temperature using an Autolab (AUT30) electrochemical workstation, over a frequency range of 10 mHz to 1 MHz under a potential perturbation of 5 mV.

2.3 Galvanostatic charge-discharge

Galvanostatic techniques generally apply a constant current source across the cell between working and counter electrodes and measure the potential response. Some electrochemical performances of a cell could be expressed on the galvanostatic charge-discharge curves, such as specific capacity, reaction plateau and coulombic efficiency.

A charge-discharge cycle is the process of charging a rechargeable battery and discharging it as required into a load. The term is typically used to specify a battery's expected life, as the number of charge-discharge cycles affects life time more than the mere passage of time. In general, the number of cycles (cycling) for a rechargeable battery indicates how many times it can undergo the process of complete charging and discharging until failure or it starting to lose capacity. Coulombic efficiency describes the efficiency with which charge (electrons) are transferred in a system facilitating an electrochemical reaction. [9]

In this study, galvanostatic discharge-charge was performed in two kinds of cells (a: three-electrode glass cell (see below); b: two-electrode Swagelok-type Teflon cell) at a constant current density in the potential range of 3.0 - 0.01 V using Autolab (AUT30) potentiostat/galvanostat and EC-Lab electrochemical workstation (Bio-Logic Science Instruments), respectively, with oxide thin film as working electrode and Li foil for counter and reference electrodes.

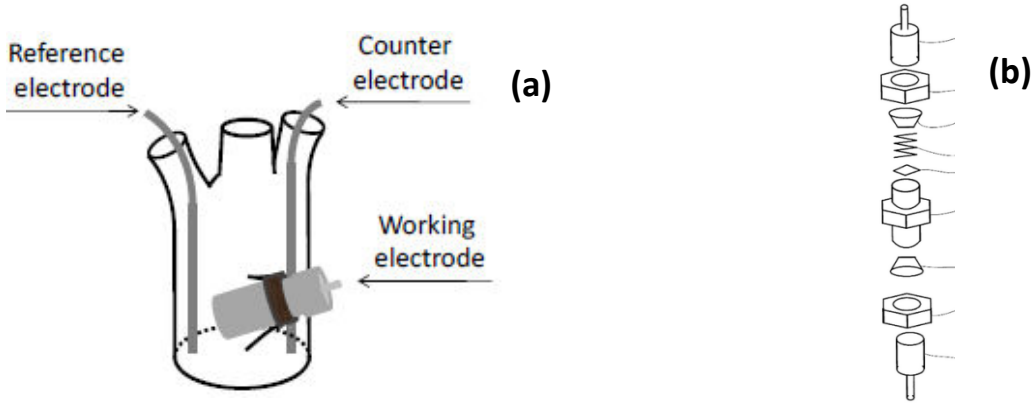

Figure A-3 Schematic illustration of (a) three-electrode glass cell (b) two-electrode Swagelok-type Teflon cell.

3. X-ray photoelectron spectroscopy (XPS)

XPS, also known as ESCA (Electron Spectroscopy for Chemical Analysis), is the most widely used surface analysis technique because of its relative simplicity in use and data interpretation. XPS - ESCA was developed in the middle 1960s by the K. Siegbahn group (University of Uppsalla, Sweden). In cooperation with Siegbahn, a small group of engineers (M. Kelly, C. Bryson, L. Faye, R. Chaney) at Hewlett-Packard in the USA, produced the first commercial monochromatic XPS instrument in 1969. In 1981, Siegbahn received the Nobel Prize in Physics to acknowledge his extensive efforts for developing XPS into a useful

analytical tool.

In principle XPS detects all elements. In practice, using typical laboratory-scale X-ray sources, XPS detects all elements with an atomic number (Z) of 3 (lithium) and above. It cannot easily detect hydrogen (Z = 1) or helium (Z = 2). The information XPS provides about surface layers or thin film structures is of value in many applications including: polymer surface modification, catalysis, corrosion, adhesion, semiconductor and dielectric materials, electronics packaging, magnetic media and thin film coatings used in a number of industries.[10]

3.1 Principles

A sample, introduced in an ultrahigh vacuum chamber, is irradiated with an X-ray beam. The kinetic energy (in electron volts, eV) of emitted photoelectrons of all elements (except H and He) present at the surface (analysed depth between 1 and 10 nm) is measured with a precision of about 0.2 eV. An electron energy analyzer determines the kinetic energy of the photoelectrons. From the binding energy determined from kinetic energy and intensity of a photoelectron peak, the identity, chemical state and quantity of an element are determined. Shape and position of peaks depend on the chemical state of the element (the so-called "chemical shift" effect). Area of peaks used in combination with sensitivity factors allow to calculate mole fractions with a detection limit of a few tenths of percent. A detailed analysis of certain well-resolved peaks allows quantifying functionalities present at the surface. On most recent systems the minimum spatial resolution is of about 15 μm and 5 μm for XPS analysis and XPS imaging respectively. In most cases XPS can be considered as a non-destructive technique. [11]

A scheme showing the principles of XPS is presented in Figure A-3.

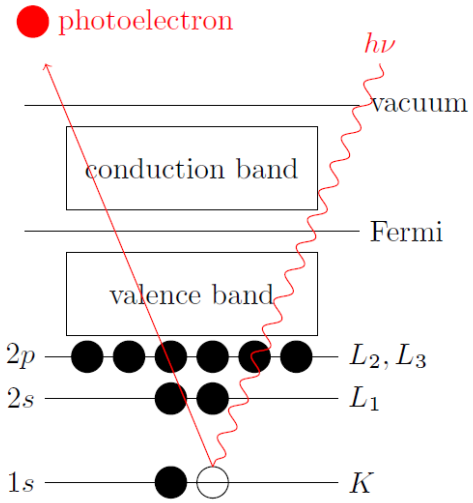

Figure A-3. Photoelectron effect for XPS analyses. [12]

3.2 Instrument

The main components of a commercially XPS system include: [13]

- A source of X-rays,
- An ultra-high vacuum (UHV) stainless steel chamber with UHV pumps,
- An electron collection lens,
- An electron energy analyzer,
- Mu-metal magnetic field shielding,
- An electron detector system,
- A moderate vacuum sample introduction chamber,
- Sample mounts,
- A sample stage,
- A set of stage manipulators.

Monochromatic aluminium K-alpha X-rays are normally produced by diffracting and focusing a beam of non-monochromatic X-rays off of a thin disc of natural, crystalline quartz with a <1010> orientation. The resulting wavelength is 8.3386 angstroms (0.83386 nm) which corresponds to a photon energy of 1486.7 eV. The energy width of the monochromated X-rays is 0.16 eV, but the common electron energy analyzer (spectrometer) produces an ultimate energy resolution in the order of 0.25 eV which, is the ultimate energy resolution of most commercial systems. Non-monochromatic magnesium X-rays have a wavelength of

9.89 angstroms (0.989 nm) which corresponds to a photon energy of 1253.6 eV. The energy width of the non-monochromated X-ray is roughly 0.70 eV, which, in effect is the ultimate energy resolution of a system using non-monochromatic X-rays. Non-monochromatic X-ray source do not use any crystals to diffract the X-rays which allows all primary X-rays lines and the full range of high-energy bremsstrahlung X-rays (1-12 keV) to reach the surface. [11,13]

In this work, a VG ESCA-LAB 250 spectrometer from Thermo Electron Corporation (as shown in Figure A-5) was used for XPS analysis. The UHV preparation chamber is directly connected to the glovebox (Figure A-6) for sample transfer in anhydrous and anaerobic conditions. An Al Kα monochromatized radiation ($h\nu$ = 1486.6 eV) was employed as X-ray source. Base pressure during analysis was about 2×10^{-9} mbar. Take-off angle of the photoelectrons was 90^{o}. Survey spectra were recorded with a pass energy of 100 eV at a step size of 1 eV and high resolution spectra and valence band (VB) regions were recorded with a pass energy of 20 eV at a step size of 0.1 eV. The data processing (curve fitting) was performed using the Avantage software provided by Thermo Electron Corporation. An iterative Shirley-type background and Lorentzian/Gaussian peak shape at a fixed ratio of 30/70 were used. Binding energies were calibrated by setting the C1s hydrocarbon ($-CH_2-CH_2-$) component peak at 285.0 eV.

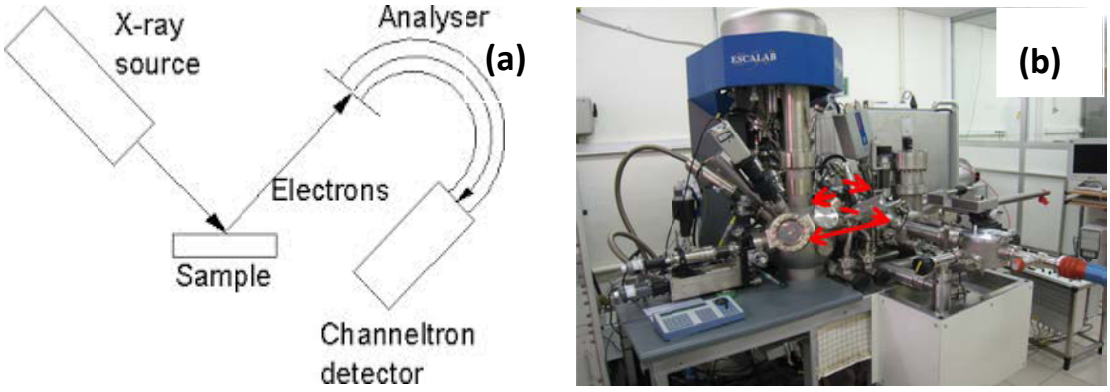

Figure A-5 (a) Schematic diagram of the XPS instrument; (b) XPS instrument (VG ESCA-LAB 250 spectrometer).

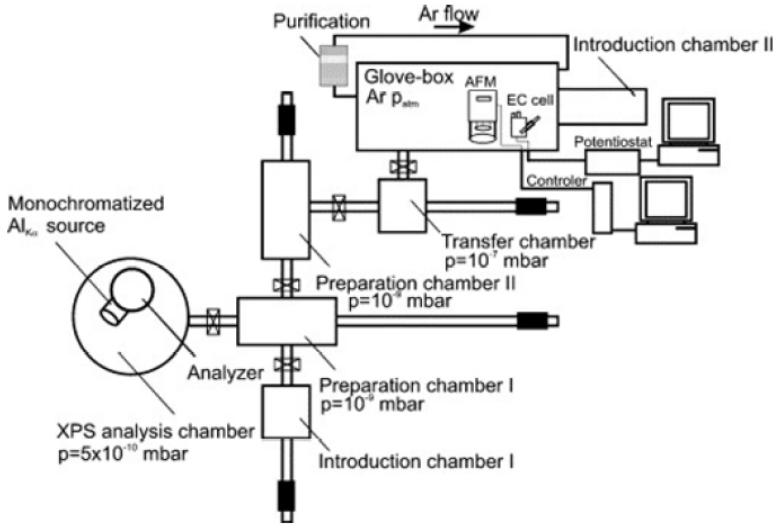

Figure A-6 Schematic diagram of the XPS with a UHV preparation chamber directly connected to the glovebox used in this study. [14]

4. Time-of-flight secondary ion mass spectrometry (ToF-SIMS)

ToF-SIMS is an acronym for the combination of the analytical technique SIMS (Secondary Ion Mass Spectrometry) with Time of Flight mass analysis (ToF). ToF-SIMS and many of its applications have been pioneered by Prof. Benninghoven and his group in the early 80's. Two instrument generations for surface spectroscopy were developed at the University of Muenster. In 1989 ION-TOF started to commercialise the technique and has continued the development of ToF-SIMS instrumentation. [15,16]

In principle, ToF-SIMS is applicable to any surface-mediated reaction such as: catalysis, sorption, redox, and dissolution/precipation reactions. Recently, ToF-SIMS is widely used in material science disciplines in studies of materials such as polymers, pharmaceuticals, semi-conductors and metals. [15,16]

4.1 Principles

ToF-SIMS is a surface sensitive analytical method that uses a pulsed ion beam (such as Cs^+, Ar^+, O_2^+, C_{60}^+, … or microfocused Ga^+, In^+, Au_n^+, Bin_x^+, …) to remove atomic or molecules fragments from the very outermost surface of the sample. The particles removed from atomic monolayers on the surface (include neutrals and secondary ions, as shown in Figure A-7). These secondary ions are then accelerated into a "flight tube" and their mass is

determined by measuring the exact time at which they reach the detector (i.e. time-of-flight). Under typical operating conditions, analytical capabilities of ToF-SIMS include: the results of ToF-SIMS analysis include:[15-18]

- Mass resolution of 0.00X amu. Particles with the same nominal mass are easily distinguished from one to another because there is a slight mass shift as atoms enter a bound state,
- Mass range of 0-10,000 amu. Ions (positive or negative), isotopes and molecular compounds (including polymers, organic compounds, and up to ~amino acids) can be detected,
- Trace element detection limits in the ppm range,
- Sub-micron resolution imaging to map any mass number of interest,
- Depth profiling capabilities. Sequential sputtering of surfaces allows analysis of the chemical stratigraphy on material surfaces (typical sputtering rates are ~100 Å/min),
- Retrospective analysis. Every pixel of a ToF-SIMS map represents a full mass spectrum. This allows an analyst to retrospectively produce maps for any mass of interest, and to interrogate regions of interest for their chemical composition via computer processing after the dataset has been instrumentally acquired.

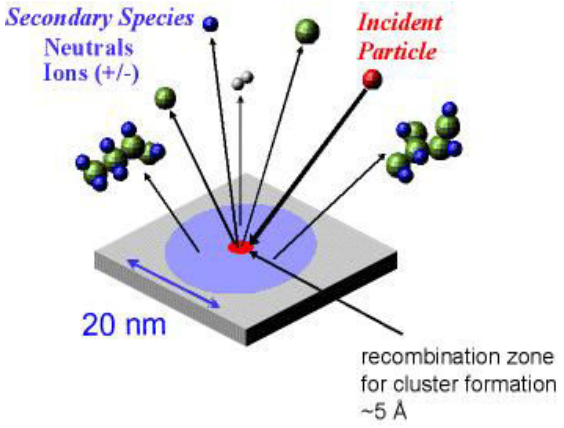

Figure A-7 Schematic representation of secondary ion generation. [16]

ToF-SIMS is also referred to as "static" SIMS because a low primary ion current is used to "tickle" the sample surface to liberate ions, molecules and molecular clusters for analysis. In contrast, "dynamic" SIMS is the method of choice for quantitative analysis because a higher primary ion current result in a faster sputtering rate and produces a much higher ion

yield (Figure A-7). Thus, dynamic SIMS creates better counting statistics for trace elements. Organic compounds are effectively destroyed by "dynamic" SIMS, and no diagnostic information is obtained. [16]

There are three different modes of analysis in ToF-SIMS; 1) spectroscopy: mass spectra are acquired to determine the elemental and molecular species on a surface; 2) imaging: images are acquired to visualize the distribution of individual species on the surface; and 3) depth profiling: depth profiles are used to determine the distribution of different chemical species as a function of depth from the surface. [19] Furthermore, by combination of the high lateral resolution images and the depth profiles, 3-dimensional chemical reconstructions of microstructures are possible.

4.2 Instrument

ToF-SIMS instruments typically include the following components: [16]

- An ultrahigh vacuum system, which is needed to increase the mean free path of ions liberated in the flight path,
- A particle gun, that typically uses a Ga or Cs source,
- The flight path, which is either circular in design, using electrostatic analyzers to direct the particle beam, or linear using a reflecting mirror, and
- The mass detector system.

One of the key features of the ToF-SIMS software is the ability to perform "retrospective" analysis, that is, every molecule from the sample detected by the system can be stored by the computer as a function of the mass and its point of origin. This allows the user to obtain chemical maps or spectra of specific regions not previously defined after the original data has been collected.

In this work, a ToF-SIMS 5 spectrometer (Ion Tof - Munster, Germany) operating at 10^{-9} mbar (Figure A-8) was used for depth profile chemical analysis. Samples were transferred in an air-tight vessel under argon atmosphere from the glovebox to the ToF-SIMS system. A pulsed 25 keV Bi^+ primary ion source was employed for analysis, delivering 1.2 pA current over a 100 × 100 μm^2 area. Depth profiling was carried out using a 1 keV Cs^+ sputter beam giving a 70 nA target current over a 300 × 300 μm^2 area. Ion-Spec software was

used for acquiring and processing the data. Negative ion depth profiles were recorded for better sensitivity to fragments originating from oxide matrices.

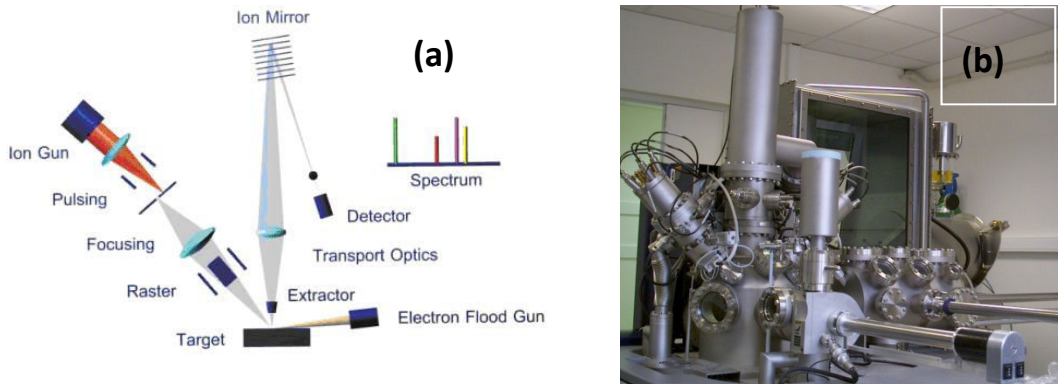

Figure A-8 (a) Schematic diagram of the IonTof ToF-SIMS instrument; [20] **(b) ToF-SIMS 5 spectrometer (IonTof) used in this study.**

5. Scanning electron microscopy (SEM)

A scanning electron microscope is a type of electron microscope that produces images of a sample by scanning it with a focused beam of electrons. The electrons interact with atoms in the sample, producing various signals that can be detected and that contain information about the sample's surface topography and composition. The electron beam is generally scanned in a raster scan pattern, and the beam's position is combined with the detected signal to produce an image. SEM can achieve resolution better than 1 nanometer. Specimens can be observed in high vacuum, in low vacuum, and (in environmental SEM) in wet conditions. The most common mode of detection is by secondary electrons emitted by atoms excited by the electron beam. The number of secondary electrons is a function of the angle between the surface and the beam. On a flat surface, the plume of secondary electrons is mostly contained by the sample, but on a tilted surface, the plume is partially exposed and more electrons are emitted. By scanning the sample and detecting the secondary electrons, an image displaying the tilt of the surface is created. [21,22]

5.1 Principles

Accelerated electrons in a SEM carry significant amounts of kinetic energy, and this energy is dissipated as a variety of signals produced by electron-sample interactions when the incident electrons are decelerated in the solid sample. These signals include secondary

electrons (that produce SEM images), backscattered electrons (BSE that are reflected from the sample by elastic scattering), diffracted backscattered electrons (EBSD that are used to determine crystal structures and orientations of minerals), photons (characteristic X-rays that are used for elemental analysis and continuum X-rays), visible light (cathodoluminescence-CL) and etc., as shown in Figure A-9. Secondary electrons and backscattered electrons are commonly used for imaging samples: secondary electrons are most valuable for showing morphology and topography on samples and backscattered electrons are most valuable for illustrating contrasts in composition in multiphase samples (i.e. for rapid phase discrimination). X-ray generation is produced by inelastic collisions of the incident electrons with electrons in discrete orbitals (shells) of atoms in the sample. As the excited electrons return to lower energy states, they yield X-rays that are of a fixed wavelength (that is related to the difference in energy levels of electrons in different shells for a given element). Thus, characteristic X-rays are produced for each element in a mineral that is "excited" by the electron beam. SEM analysis is considered to be "non-destructive", that is, X-rays generated by electron interactions do not lead to volume loss of the sample, so it is possible to analyze the same materials repeatedly. [23,24]

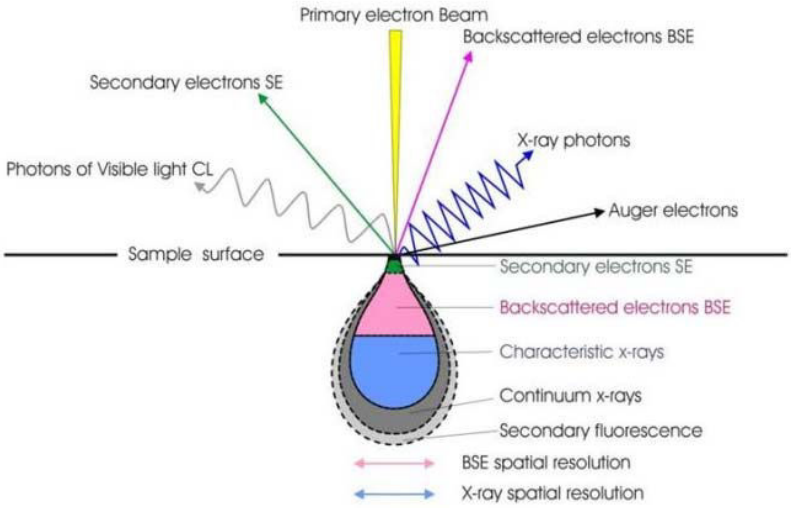

Figure A-9 The interaction zone of electrons and specimen atoms below a specimen surface.[25]

5.2 Instrument

Essential components of all SEMs include the following:

- Electron Source ("Gun" including Thermionic guns and Field emission guns,)

- Electron Lenses
- Sample Stage
- Detectors for all signals of interest
- Display/Data output devices
- Infrastructure Requirements: power supply, vacuum system, cooling system, vibration-free floor, and room free of ambient magnetic and electric fields.

SEMs always have at least one detector (usually a secondary electron detector), and most have additional detectors. The specific capabilities of a particular instrument are critically dependent on which detectors it accommodates. [23]

In this work, SEM imaging of the thin film electrodes was performed with a ZEISS Ultra-55 Field Emission Scanning Electron Microscope (FE-SEM, Germany) in Laboratoire Interfaces et Systemes Electrochimiques, Université Pierre et Marie Curie, as shown in Figure A-10.

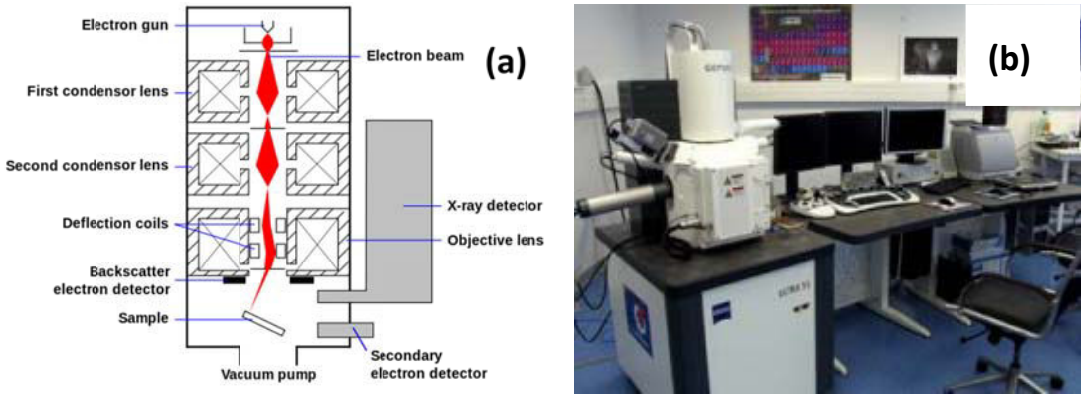

Figure A-10 (a) Schematic diagram of the SEM instrument; [26] (b) SEM instrument used in this study.

6. Atomic force microscopy (AFM)

Atomic force microscopy (AFM) or scanning force microscopy (SFM) is a very high-resolution type of scanning probe microscopy, with demonstrated resolution on the order of fractions of a nanometer. The precursor to the AFM, the scanning tunneling microscope, was developed by G. Binnig and H. Rohrer in the early 1980s at IBM Research - Zurich, a development that earned them the Nobel Prize for Physics in 1986. Binnig, Quate and Gerber

invented the first atomic force microscope (also abbreviated as AFM) in 1986. The first commercially available atomic force microscope was introduced in 1989. The AFM is one of the foremost tools for imaging, measuring and manipulating matter at the nanoscale. The information is gathered by "feeling" the surface with a mechanical probe. Piezoelectric elements that facilitate tiny but accurate and precise movements on (electronic) command enable the very precise scanning. In some variations, electric potentials can also be scanned using conducting cantilevers. In more advanced versions, currents can be passed through the tip to probe the electrical conductivity or transport of the underlying surface, but this is much more challenging with few research groups reporting consistent data. [27,28]

6.1 Principles

The AFM consists of a cantilever with a sharp tip (probe) at its end that is used to scan the specimen surface. The cantilever is typically silicon or silicon nitride and the tip radius of curvature is on the order of nanometers. When the tip is brought into proximity of a sample surface, forces between the tip and the sample lead to a deflection of the cantilever according to Hooke's law. [29] Depending on the situation, forces that are measured in AFM include mechanical contact force, van der Waals forces, capillary forces, chemical bonding, electrostatic forces, magnetic forces, Casimir forces, solvation forces, etc. Along with force, additional quantities may simultaneously be measured through the use of specialized types of probes. Typically, the deflection is measured using a laser spot reflected from the top surface of the cantilever into an array of photodiodes. Other methods that are used include optical interferometry, capacitive sensing or piezoresistive AFM cantilevers. These cantilevers are fabricated with piezoresistive elements that act as a strain gauge. Using a Wheatstone bridge, strain in the AFM cantilever due to deflection can be measured, but this method is not as sensitive as laser deflection or interferometry. [30]

If the tip was scanned at a constant height, a risk would exist that the tip collides with the surface, causing damage. Hence, in most cases a feedback mechanism is employed to adjust the tip-to-sample distance to maintain a constant force between the tip and the sample. Traditionally the tip or sample mounted on a 'tripod' of three piezo crystals, with each responsible for scanning in the x, y and z directions. [31] In 1986, the same year as the AFM

was invented, a new piezoelectric scanner, the tube scanner, was developed for use in STM. Later tube scanners were implemented into AFMs. The tube scanner can move the sample in the x, y, and z directions using a single tube piezo with a single interior contact and four external contacts. An advantage of the tube scanner is that being composed of a single crystal it has a higher resonant frequency, which, in combination with a low resonant frequency isolation stage, provides better vibrational isolation. A disadvantage is that the x-y motion can cause unwanted z motion resulting in distortion. [32]

The AFM can be operated in a number of modes, depending on the application. In general, the primary imaging modes of operation for an AFM are divided into static (also called contact) modes and a variety of dynamic (non-contact or "tapping") modes where the cantilever is vibrated. [33] In static mode, the cantilever is "dragged" across the surface of the sample and the contours of the surface are measured directly using the deflection of the cantilever. In the dynamic mode, the cantilever is externally oscillated at or close to its fundamental resonance frequency or a harmonic. The oscillation amplitude, phase and resonance frequency are modified by tip-sample interaction forces. These changes in oscillation with respect to the external reference oscillation provide information about the sample's characteristics. In brief, AFM operation modes can be classified in three traditional modes according to interaction force of probe-sample separation (Figure A-11) and some special cases (i.e. Current Sensing AFM (CS-AFM) for studying electrical characteristics.[34-37]

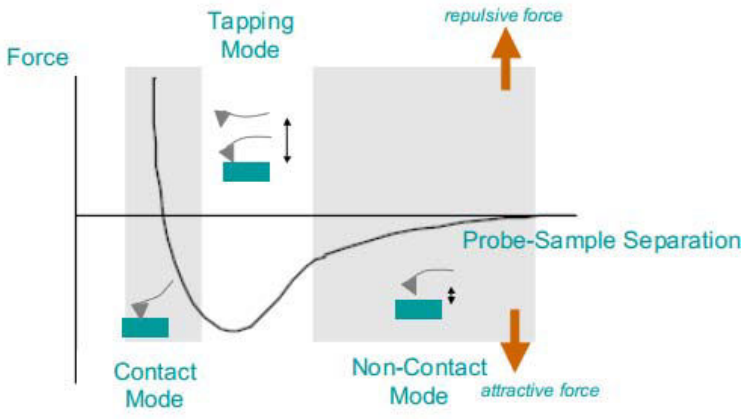

Figure A-11 Plot of force as a function of probe-sample separation. [38]

6.2 Instrument

The basic atomic force microscope is composed of a stylus-cantilever probe attached to the probe stage, a laser focused on the cantilever, a photodiode sensor (recording light reflected from the cantilever), a digital translator-recorder, and a data processor and monitor (Figure A-12 (a)).

In this thesis, AFM imaging was performed with an Agilent 5500 Atomic Force Microscope (Figure A-12 (b)) using a silicon tip operated in intermittent contact (tapping) mode in air. The AFM images were acquired in topographic and differential modes using a silicon tip with a force constant of 25 - 75 N m^{-1} and a resonance frequency of 282.6 kHz. AFM data visualization and analyses (average value, RMS) were performed with the Gwyddion 2.31 software.

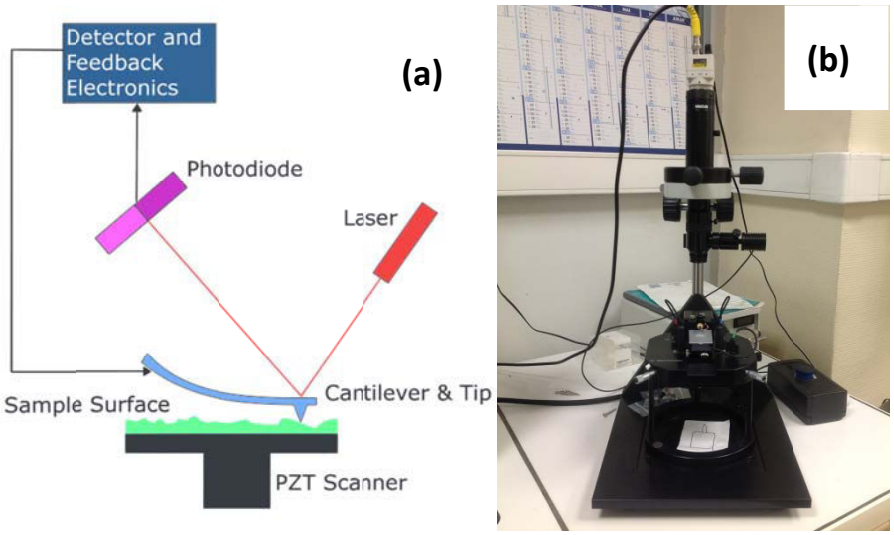

Figure A-12 (a) Schematic diagram of the AFM instrument;[39] (b) AFM instrument used in this study.

7. Raman spectroscopy

Raman spectroscopy (named after C.V. Raman) is a spectroscopic technique used to observe vibrational, rotational and other low-frequency modes in a system. [40] It relies on inelastic scattering, or Raman scattering, of monochromatic light, usually from a laser in the visible, near infrared or near ultraviolet range. The laser light interacts with molecular vibrations, phonons or other excitations in the system, resulting in the energy of the laser photons being shifted up or down. The shift in energy gives information about the vibrational modes in the system. Infrared spectroscopy yields similar, but complementary information. Raman spectroscopy is commonly used in chemistry, since vibrational information is specific

to the chemical bonds and symmetry of molecules. [41]

7.1 Principles

The Raman effect occurs when light impinges upon a molecule and interacts with the electron cloud and the bonds of that molecule. For the spontaneous Raman effect, which is a form of light scattering, a photon excites the molecule from the ground state to a virtual energy state. When the molecule relaxes, it emits a photon and it returns to a different rotational or vibrational state. The difference in energy between the original state and this new state leads to a shift in the emitted photon's frequency away from the excitation wavelength. If the final vibrational state of the molecule is more energetic than the initial state, the emitted photon will be shifted to a lower frequency for the total energy of the system to remain balanced. This shift in frequency is designated as a Stokes shift. If the final vibrational state is less energetic than the initial state, then the emitted photon will be shifted to a higher frequency, and this is designated as an anti-Stokes shift (Figure A-13). Raman scattering is an example of inelastic scattering because of the energy transfer between the photons and the molecules during their interaction. A change in the molecular polarization potential or amount of deformation of the electron cloud - with respect to the vibrational coordinate is required for a molecule to exhibit a Raman effect. The amount of the polarizability change will determine the Raman scattering intensity. The pattern of shifted frequencies is determined by the rotational and vibrational states of the sample. [42,43]

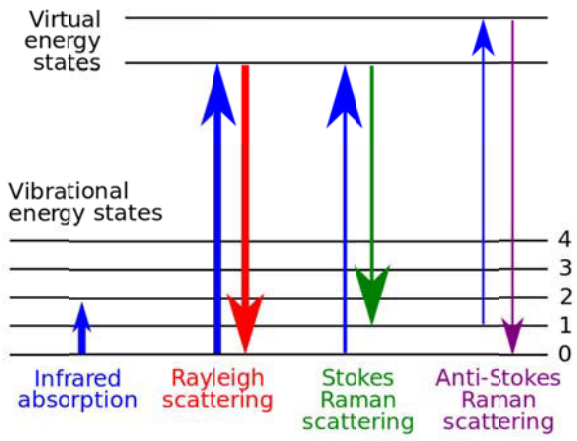

Figure A-13 Energy-level diagram showing the states involved in Raman signal. The line thickness is roughly proportional to the signal strength from the different transitions. [44]

7.2 Instrument

A typical Raman spectrometer is made up of five basic parts: [45]

- Excitation source (generally a laser),
- Sample illumination and scattered light collection system (probe),
- Sample holder,
- Spectrograph,
- Detection system (optical multichannel analyser, photomultiplier tube - PMT, intensified photo array, or a charged coupled device - CCD),

In this work, Raman spectroscopy was performed using a Horiba Labram Aramis Raman spectrograph (T64000) in a back scattering geometry (Institut de minéralogie, de physique des matériaux et de cosmochimie, Université Pierre et Marie Curie) under ambient conditions. A green laser operating at a wavelength of 532 nm was used as the excitation source. The laser power was ~0.1 mW, focused onto a spot of 1 μm diameter through a 100× objective lens.

References

[1] Bard A.J., Faulkner L.R., Electrochemical Methods: Fundamentals and Applications (2nd Edition), *Wiley*, **2001**, ISBN: 978-0-471-04372-0.

[2] Nicholson, R.S., Theory and Application of Cyclic Voltammetry for Measurement of Electrode Reaction Kinetics, *Analytical Chemistry*, **1965**, 37, 1351-1355.

[3] Jurgen H., Cyclic Voltammetry - "Electrochemical Spectroscopy". New Analytical Methods (25). *Angewandte Chemie International Edition in English*, **1984**, 23, 831-847.

[4] Kissinger P.T., Heineman W.R., Cyclic voltammetry, *J. Chem. Educ.*, **1983**, 60, 702-706.

[5] Bard A.J., Faulkner L.R., Electrochemical Methods, *Wiley, New York,* **1980**, p. 218.

[6] Orazem M.E., Tribollet B., Electrochemical Impedance Spectroscopy, *John Wiley & Sons*, **2008**, ISBN: 978-0-470-04140-6.

[7] Ratnakumar B.V., Smart M.C., Surampudi S., Electrochemical impedance spectroscopy and its applications to lithium ion cells, *Conference: Annual Battery Conference on Applications and Advances - BCAA*, **2002**, 273-277.

[8] Barsoukov E., Macdonald J. R., Impedance Spectroscopy Theory, Experiment, and Applications (Second Edition), *John Wiley & Sons, Inc.*, **2005**.

[9] Li J.-T., Investigation of Electrode/Electrolyte Interfacial Reactions Involving in Li Ion Batteries, *PhD Dissertation – Xiamen university*, **2009**, 55.

[10] Ray S., Shard A.G., Quantitative Analysis of Adsorbed Proteins by X-ray Photoelectron Spectroscopy, *Analytical Chemistry*, **2011**, 83, 8659-8666.

[11] Watts J.F., Wolstenholme J., An Introduction to Surface Analysis by XPS and AES, *Wiley Interscience*, **2003**.

[12] Laurin M., Example: Principle of X-ray photoelectron spectroscopy (XPS), **2009**, http://www.texample.net/tikz/examples/principle-of-x-ray-photoelectron-spectroscopy-xps/

[13] Nunney T., White R., Characterizing Materials for Energy Generation Using X-ray Photoelectron Spectroscopy (XPS), *Microscopy Today*, **2011**, 19, 22-28.

[14] Światwoska-Mrowiecka J., Maurice V., Zanna S., Klein L., Marcus P., XPS study of Li ion intercalation in V_2O_5 thin films prepared by thermal oxidation of vanadium metal, *Electrochimica Acta*, **2007**, 52, 5644-5653.

[15] Benninghoven, A., Chemical Analysis of INorganic and Organic Surfaces and Thin Films by Static Time-of-Flight Secondary Ion Mass Spectrometry (ToF-SIMS), *Angewandte Chemie International in English*, **1994**, 33, 1023-1043.

[16] Mogk D.W., Time-of-Flight Secondary Ion Mass Spectrometry (ToF-SIMS), *Montana State University*, http://serc.carleton.edu/research_education/geochemsheets/techniques/ToFSIMS.html

[17] VanVaeck, L., Adriaens, A., Gijbels, R., Static Secondary Ion Mass Spectrometry: (S-SIMS)

Part 1. Methodology and Structural Interpretation, *Mass Spectrometry Reviews*, **1999**, 18, 1-47.

[18] Adriaens, A., VanVaeck, L., Adams, F., Static Secondary Ion Mass Spectrometry (S-SIMS) Part 2: Material Science Applications, *Mass Spectrometry Reviews*, **1999**, 18, 48-81.

[19] TOF-SIMS, http://www.phi.com/surface-analysis-techniques/tof-sims.html

[20] Time-of-Flight Mass Spectrometer - Technique, *IONTOF GmbH*, http://www.iontof.com/technique-timeofflight-IONTOF-TOF-SIMS-TIME-OF-FLIGHT-SURFACE-ANALYSIS.htm

[21] Goldstein J., Newbury D.E., Joy D.C., Lyman C.E., Echlin P., Lifshin E., Sawyer L., Michael J.R., Scanning Electron Microscopy and X-ray Microanalysis: 3rd Edition, *Joseph Michael Kluwer Academic Publishers*, New York, **2003**, 1-20. ISBN 0306472929.

[22] Reimer L., Scanning electron microscopy: physics of image formation and microanalysis, *Springer*, **1998**, 13-56. ISBN: 3-540-13530-8.

[23] Swapp S., Scanning Electron Microscopy (SEM), *University of Wyoming*, http://serc.carleton.edu/research_education/geochemsheets/techniques/SEM.html

[24] Egerton, R.F., Physical principles of electron microscopy: an introduction to TEM, SEM, and AEM, *Springer*, **2005**, 202.

[25] ISAAC: Imaging Spectroscopy and Analysis Centre - Scanning Electron Microscopy (SEM), http://www.gla.ac.uk/schools/ges/research/researchfacilities/isaac/services/scanningelectronmicroscopy/

[26] Grayer J., *Schematic of a Scanning Electron Microscope (SEM)*, Posted June 20, **2011**.

[27] Lang K.M., Hite D.A., Simmonds R.W., McDermott R., Pappas D.P., Martinis J.M., Conducting atomic force microscopy for nanoscale tunnel barrier characterization, *Review of Scientific Instruments*, **2004**, 75, 2726-2731.

[28] Leite F.L., Mattoso L.H.C., Oliveira Jr O.N., Herrmann Jr P.S.P., The Atomic Force Spectroscopy as a Tool to Investigate Surface Forces: Basic Principles and Applications, *Modern Research and Educational Topics in Microscopy*, **©FORMATEX 2007**, 747-757.

[29] Cappella, B., Dietler, G., Force-distance curves by atomic force microscopy, *Surface Science Reports*, **1999**, 34, 1-104.

[30] Tong C.X., Advanced Materials for Thermal Management of Electronic Packaging, *Springer*, **2011**, 30, 114. ISBN: 978-1-4419-7759-5.

[31] Binnig G., Quate, C. F., Atomic Force Microscope, *Physical Review Letters*, **1986**, 56, 930-933.

[32] Atomic force microscopy, http://en.wikipedia.org/wiki/Atomic_force_microscopy

[33] Binnig G., Smith D.P.E., Single-tube three-dimensional scanner for scanning tunneling microscopy, *Review of Scientific Instruments*, **1986**, 57, 1688.

[34] Gross, L., Mohn, F., Moll, N., Liljeroth, P., Meyer, G., The Chemical Structure of a Molecule

Resolved by Atomic Force Microscopy, *Science*, **2009**, 325, 1110-1114.

[35] Giessibl F.J., Advances in atomic force microscopy, *Reviews of Modern Physics*, **2003**, 75, 949-983.

[36] Zhong Q., Inniss D., Kjoller K., Elings V., Fractured polymer/silica fiber surface studied by tapping mode atomic force microscopy, *Surface Science Letters*, **1993**, 290, L688-L692.

[37] Roiter Y., Minko S., AFM single molecule experiments at the solid-liquid interface: in situ conformation of adsorbed flexible polyelectrolyte chains, *Journal of the American Chemical Society*, **2005**, 127, 15688-15689.

[38] Wilson R.A., Bullen H.A., Introduction to Scanning Probe Microscopy (SPM): Basic Theory - Atomic Force Microscopy (AFM), Department of Chemistry, *Northern Kentucky University*, http://asdlib.org/onlineArticles/ecourseware/Bullen/SPMModule_BasicTheoryAFM.pdf

[39] Bhardwaj R., Gupta V., Characterization Techniques for Nano-Materials in Nanoelectronics: A Review, *2nd International Conference on Role of Technology in Nation Building*, **ICRTNB-2013**, 43-47. ISBN: 97881925922-1-3.

[40] Gardiner D.J., Practical Raman spectroscopy, 1st ed., *Springer-Verlag Berlin And Heidelberg Gmbh & Co. K*, **1989**, ISBN-13: 978-3-540-50254-8.

[41] Colthup N.B, Dal L.H., Wiberley S.E., Introduction to Infrared and Raman Spectroscopy (Third Edition), *Academic Press, Inc.*, **1990**.

[42] Turrell G., Corset J., Raman Microscopy: Developments and Applications, *Academic Press*, London, **1996**, ISBN: 978-0-12-189690-4.

[43] Das R.S., Agrawal Y.K., Raman spectroscopy: Recent advancements,techniques and applications, *Vibrational Spectroscopy*, **2011**, 57, 163-176.

[44] Čorluka V., Hederić Ž., Hadžiselimović M., Moisture measurement in solid samples using Raman spectroscopy, *Przegląd Elektrotechniczny*, **2011**, 87, 25-28.

[45] Murcia-Mascarós S., García-Ramos J.V., Modern Raman Spectroscopy: A Practical Approach - Chapter 4.1: Raman Spectroscopy - Principles and Some Case Studies, *John Wiley & Sons, Ltd*, **2005**, ISBNs: 0-471-49668-5 (HB).

Appendix 2

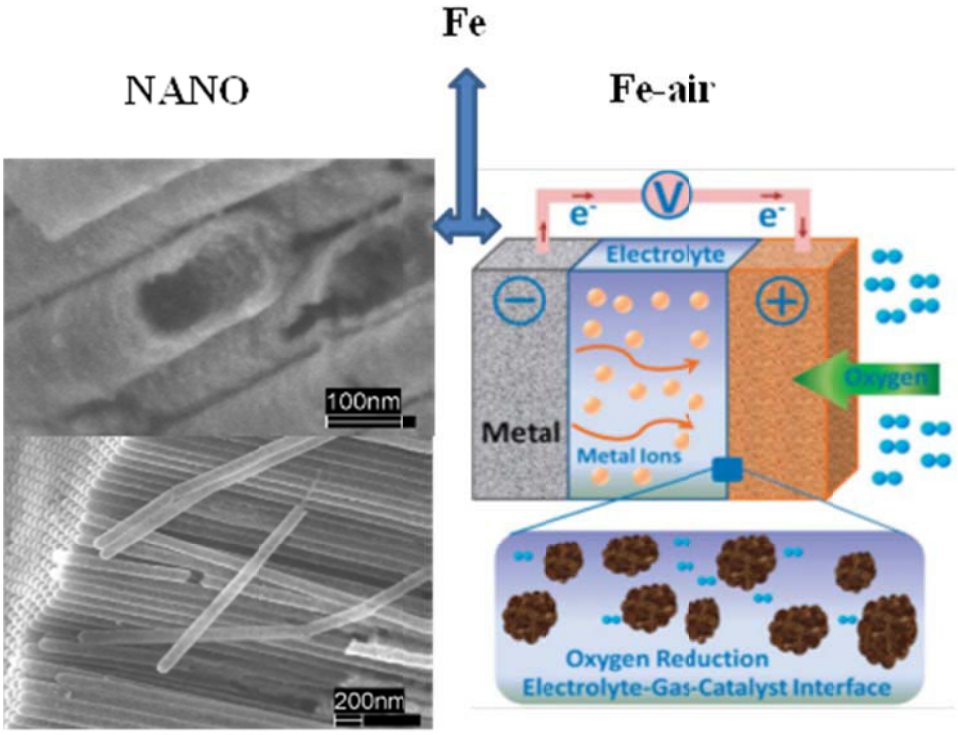
Fe
NANO
Fe-air
100nm
200nm
e-
V
e-
Electrolyte
Metal
Metal Ions
Oxygen
Oxygen Reduction
Electrolyte-Gas-Catalyst Interface

Abstract: Investigations on iron oxide anode materials for lithium ion batteries have been presented in the previous chapters. In this part, two suggestions for further works and some initial attempts concerning the application of iron oxide as electrode material in battery are proposed:

- Synthesis of nanostructured iron oxide by means of atomic layer deposition (ALD) using anodic aluminum oxide (AAO) membrane template for application in lithium ion microbatteries;
- Electrochemical behaviour of iron & iron oxide in Fe-air batteries with emphasis on the role of electrolyte additives (i.e. Na_2S) on the inhibition of hydrogen evolution in Fe-air batteries.

Keywords: Anode; Iron oxide; Nanomaterial; ALD; Fe-air battery

1. ALD iron oxide nanomaterial for LIBs

There are numerous reports discussing nanostructured iron oxide for LIBs, [1-5] due to the advantages of nanostructured materials, i.e., (i) better accommodation of the strain of lithium insertion/removal, improving cycle life; (ii) new reactions not possible with bulk materials; (iii) higher electrode/electrolyte contact area leading to higher charge/discharge rates; (iv) short path lengths for electronic transport (permitting operation with low electronic conductivity or at higher power); and (v) short path lengths for Li^+ transport (permitting operation with low Li^+ conductivity or higher power).[6,7] Despite all reported data of nanostructured iron oxide materials, it appears to be inherently difficult to fabricate arrays in a well-ordered pattern. One route to obtain well-ordered arrays is to use a template and transfer the pattern to a desired material. [8-10] This can be made in several ways. One method is to deposit a thin film of the desired material on the template as a surface modification. [11,12] Another method is to etch away the template after the deposition of the desired material. This results in a negative projection of the structure. [13,14] A suitable template for this method is anodic aluminum oxide (AAO) (for example ANOPORE™ inorganic membrane from Whatman, as shown in Figure 6-1). The most interesting feature of AAO membranes is their highly aligned pores of uniform cylindrical shape and size. The pore size, pore density, and AAO thickness can be controlled by the anodization conditions. [15] However, this approach excludes many of the thin film techniques used for deposition of iron oxide, since most techniques are not able to conformally cover the pore walls of the AAO. One technique that is very well-suited for the template deposition method is ALD. In ALD, reactant gas pulses saturate the surface of the substrate during each pulse, and growth is achieved through self-limiting surface reactions.[16,17]

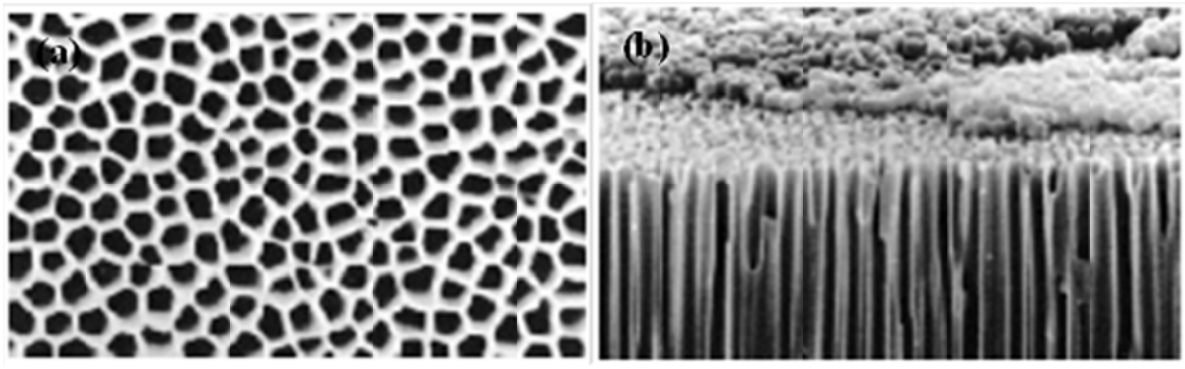

Figure 6-1 (a) Top view of a 0.2 μm ANOPORE™ from Whatman and (b) a cross-sectional view.

Therefore, ALD of iron oxide using AAO membrane template appears a promising direction of developing well-ordered iron oxide nanomaterials as anode materials for lithium ion batteries.

2. Fe-air batteries

Rechargeable metal-air batteries represent one class of promising power sources for applications in next-generation electronics, electrified transportation and energy storage of smart grids, due to the remarkably high theoretical energy output (11586, 8135, 1085, 2867 and 764 Wh kg^{-1} for Li-air battery, Al-air battery, Zn-air battery, Mg-air battery and Fe-air battery, respectively, in aqueous electrolytes based on metal alone). [18,19] Metal-air batteries using several different metals have been investigated. [19-23] Among them, Fe-air batteries have received considerable attention due to their high theoretical capacity, long cycle life, high electrochemical stability, low cost, and environmental safety. [24,25] However, the use of iron anodes still suffers from a number of problems including hydrogen evolution and passivation. Hydrogen evolution is the most significant obstacle to the practical application of iron electrodes in alkaline aqueous solutions. The potentials of the reduction reaction of $Fe/Fe(OH)_2$ and hydrogen evolution are very close, [26,27] and the hydrogen overpotential on iron surfaces is low which limits its application in commercial batteries. [28] Sulfide salts are used as additives to improve its performance. Studies have shown that the addition of both FeS to the electrode's active material [29] and Na_2S to the KOH electrolytic solution [30,31] increases significantly the iron electrode capacity. However, these studies did not clarify the exact mechanism through which the additives increase the electrode capacity. The role of sulfide on the iron electrode performance may be revealed by electrochemical (i.e., CV and galvanostatic charge/discharge) and surface analysis techniques (i.e., XPS and ToF-SIMS) using a thin film iron electrode approach. Some preliminary studies of the iron electrode have been performed in an aqueous electrolyte of 6 M KOH without and with 0.01 M Na_2S additive (as shown in Figure 6-2). The cyclic voltammograms of the pure iron foil electrode show that hydrogen evolution was significantly suppressed and the capacity of the iron electrode were obviously improved when Na_2S additive was added to the electrolyte.

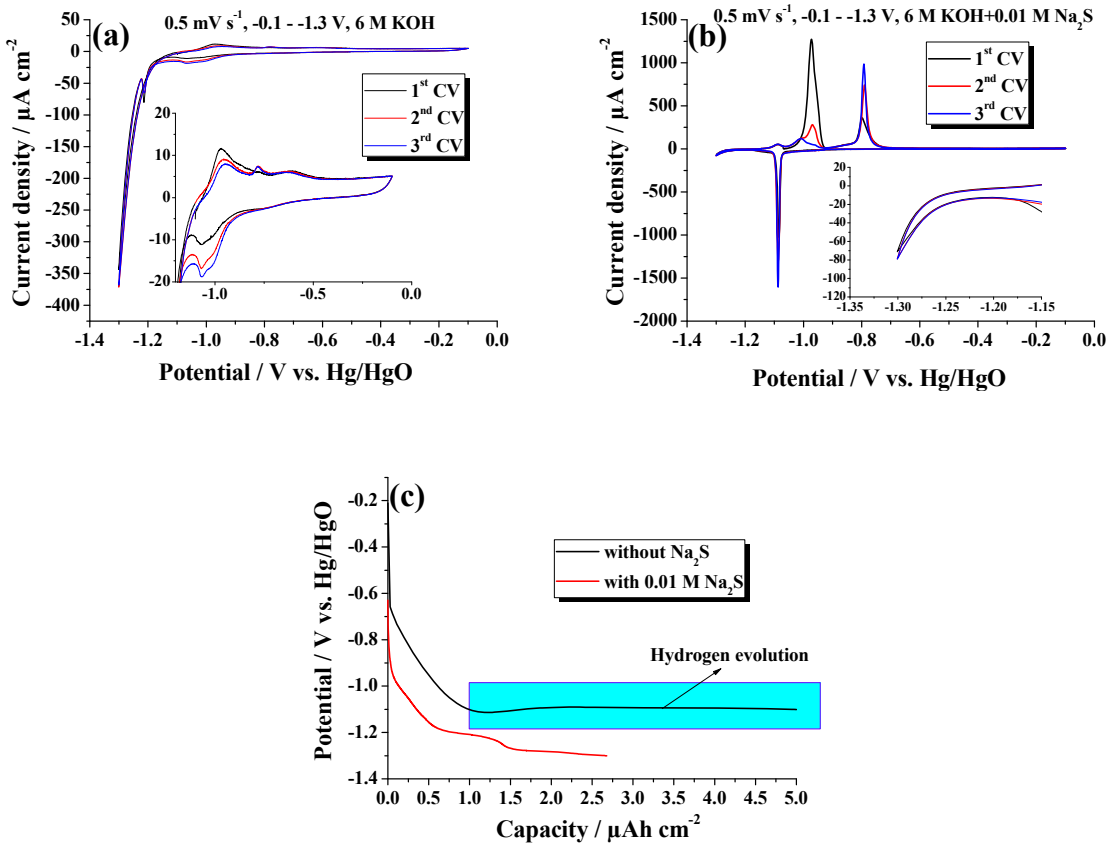

Figure 6-2 The first three consecutive cyclic voltammograms of the pure iron foil electrode in 6 M KOH electrolyte (a) without and (b) with 0.01 M Na_2S in the potential range of -0.1 - -1.3 V vs. Hg/HgO (scan rate of 0.5 mV s^{-1}); (c) the first galvanostatic discharge curves of pure iron foil electrodes in electrolytes without and with 0.01 M Na_2S (at a current density of 20 µA cm^{-2}).

References

[1] Poizot, P., Laruelle, S., Grugeon, S., Dupont, L., Tarascon, J.-M., Nano-sized Transition-Metal Oxides as Negative-Electrode Materials for Lithium-Ion Batteries, *Nature*, **2000**, *407*, 496-499.

[2] Larcher D., Masquelier C., Bonnin D., Chabre Y., Mason V., Leriche J.B., Tarascon J.-M., Effect of Particle Size on Lithium Intercalation into α-Fe_2O_3, *J. Electrochem. Soc.*, **2003**, *150*, A133-A139.

[3] Larcher D., Bonnin D., Cortes R., Rivals I., Personnaz L., Tarascon J.-M., Combined XRD, EXAFS, and Mössbauer Studies of the Reduction by Lithium of α-Fe_2O_3 with Various Particle Sizes, *J. Electrochem. Soc.*, **2003**, *150*, A1643-A1650.

[4] Reddy M.V., Yu T., Sow C.H., Shen Z.X., Lim C.T., Subba Rao G.V., Chowdari B.V.R., α-Fe_2O_3 Nanoflakes as an Anode Material for Li-Ion Batteries, *Adv. Funct. Mater.*, **2007**, *17*, 2792-2799.

[5] Carraro G., Barreca D., Cruz-Yusta M., Gasparotto A., Maccato C., Morales J., Sada C., Sanchez L., Vapor-Phase Fabrication of β-Iron Oxide Nanopyramids for Lithium-Ion Battery Anodes, *ChemPhysChem*, **2012**, *13*, 3798-3801.

[6] Aricò A.S., Bruce P., Scrosati B., Tarascon J.-M., Schalkwijk W.V., Nanostructured Materials for Advanced Energy Conversion and Storage Devices, *Nat. Mater.*, **2005**, *4*, 366-377.

[7] P.G. Bruce, B. Scrosati, J.-M. Tarascon, Nanomaterials for Rechargeable Lithium Batteries, *Angew. Chem. Int. Ed.*, **2008**, *47*, 2930-2946.

[8] Charles R. Martin, Membrane-Based Synthesis of Nanomaterials, *Chem. Mater.*, **1996**, *8*, 1739-1746.

[9] Bachmann J., Jing J., Knez M., Barth S., Shen H., Mathur S., Gosele U., Nielsch K., Ordered Iron Oxide Nanotube Arrays of Controlled Geometry and Tunable Magnetism by Atomic Layer Deposition, *J. Am. Chem. Soc.*, **2007**, *129*, 9554-9555.

[10] Taberna, P. L., Mitra, S., Poizot, P., Simon, P., Tarascon, J.-M., High Rate Capabilities Fe_3O_4-based Cu Nano-architectured Electrodes for Lithium-ion Battery Applications, *Nat. Mater.* **2006**, *5*, 567-573.

[11] Xiong G., Elam J.W., Feng H., Han C.Y., Wang H.-H., Iton L.E., Curtiss L.A., Pellin M.J., Kung M., Kung H., Stair P.C., Effect of Atomic Layer Deposition Coatings on the Surface Structure of Anodic Aluminum Oxide Membranes, *J. Phys. Chem. B*, **2005**, *109*, 14059-14063.

[12] Johansson A., Torndahl T., Ottosson L.M., Boman M., Carlsson J.-O., Copper nanoparticles deposited inside the pores of anodized aluminium oxide using atomic layer deposition, *Mater. Sci. Eng. C*, **2003**, *23*, 823-826.

[13] Rooth M., Johansson A., Boman M., Harsta A., Ordered and Parallel Niobium Oxide Nano-Tubes Fabricated using Atomic Layer Deposition in Anodic Alumina Templates, *Mater. Res. Soc. Symp.*, **2006**, *901E*, 0901-Ra24-05.1.

[14] Shin H., Jeong D.-K., Lee J., Sung M.M., Kim J., Formation of TiO_2 and ZrO_2 Nanotubes Using Atomic Layer Deposition with Ultraprecise Control of the Wall Thickness, *Adv. Mater.*, **2004**, *16*, 1197-1200.

[15] O'Sullivan J. P., Wood G. C., The Morphology and Mechanism of Formation of Porous Anodic Films

on Aluminium, Proc. *R. Soc. London, Ser. A*, **1970**, *317*, 511-543.

[16] Puurunen R.L., Surface chemistry of atomic layer deposition: A case study for the trimethylaluminum/water process, *J. Appl. Phys.*, **2005**, *97*, 121301-121352.

[17] Rooth M., Johansson A., Kukli K., Aarik J., Boman M., Hårsta A., Atomic Layer Deposition of Iron Oxide Thin Films and Nanotubes using Ferrocene and Oxygen as Precursors, *Chem. Vap. Deposition*, **2008**, *14*, 67-70.

[18] Cheng F., Chen J., Metal–air batteries: from oxygen reduction electrochemistry to cathode catalysts, *Chem. Soc. Rev.*, **2012**, *41*, 2172-2192.

[19] Zhang J.-G., Bruce P.G., Zhang X.G., Metal-Air Batteries, Handbook of Battery Materials, Second Edition. Edited by Claus Daniel and Jürgen O. Besenhard, *Wiley-VCH Verlag GmbH & Co. KGaA*, **2011**, *22*, 759-795.

[20] Blurton K.F., Sammells A.F., Metal/air batteries: Their status and potential - a review, *J. Power Sources*, **1979**, *4*, 263–279.

[21] Zeng X.X., Wang J.M., Wang Q.L., Kong D.S., Shao H.B., Zhang J.Q., Cao C.N., The effects of surface treatment and stannate as an electrolyte additive on the corrosion and electrochemical performances of pure aluminum in an alkaline methanol-water solution, *Mater. Chem. Phys.*, **2010**, *121*, 459-464.

[22] Wang T., Kaempgen M., Nopphawan P., Wee G., Mhaisalkar S., Srinivasan M., Silver nanoparticle-decorated carbon nanotubes as bifunctional gas-diffusion electrodes for zinc–air batteries, *J. Power Sources*, **2010**, *195*, 4350-4355.

[23] Casellato U., Comisso N., Mengoli G., Effect of Li ions on reduction of Fe oxides in aqueous alkaline medium, *Electrochim. Acta*, **2006**, *51*, 5669–5681.

[24] Ito A., Zhao L., Okada S., Yamaki J., Synthesis of nano-Fe_3O_4-loaded tubular carbon nanofibers and their application as negative electrodes for Fe/air batteries, *J. Power Sources*, **2011**, *196*, 8154-8159.

[25] Narayanan S.R., Surya Prakash G.K., Manohar A., Yang B., Malkhandi S., Kindler A., Materials challenges and technical approaches for realizing inexpensive and robust iron–air batteries for large-scale energy storage, *Solid State Ionics*, **2012**, *216*, 105-109.

[26] Shukla A.K., Ravikumar M.K., Balasubramanian T.S., Nickel/iron batteries, *J. Power Sources*, **1994**, *51*, 29-36.

[27] Periasamy P., Ramesh Babu B., Venkatakrishna Iyer S., Performance characterization of sintered iron electrodes in nickel/iron alkaline batteries, *J. Power Sources*, **1996**, *62*, 9-14.

[28] Vijayamohanan K., Balasubramanian T.S., Shukla A.K., Rechargeable alkaline iron electrodes, *J. Power Sources*, **1991**, *34*, 269-285.

[29] Vijayamohanan K., Shukla A.K., Sathyanarayana S., Kinetics of ektrode reactions occurring on porous iron electrodes in alkaline media, *J. Electroanal. Chem.*, **1990**, *295*, 59-70.

[30] Periasamy P., Ramesh Babu B., Venkatakrishna Iyer S., Electrochemical behaviour of Teflon-bonded

iron oxide electrodes in alkaline solutions, *J. Power Sources*, **1996**, *63*, 79-85.

[31] M. Jayalakshmi, B. Nathira, V.R. Chidmbaram, R. Sabapathi, V.S. Muralidharan, Role of activation on the performance of the iron negative electrode in nickel/iron cells, *J. Power Sources*, **1992**, *39*, 113-119.

Notation

Symbol	Description
A	area
D_j	diffusion coefficient
D_{Li}	diffusion coefficient of lithium ions
E	potential
eV	electron volt
F	Faraday constant
i	current
P	pressure
t	time
T	temperature
wt%	weight percentage
V	volt
s	second
Å	angstroms
Ω	ohm
^oC	centigrade temperature
μm	micrometer

Abbreviation	Description
AFM	Atomic force microscopy
amu	atomic mass unit
BSE	backscattered electrons
E_B	Binding energy
CCD	charged coupled device
CV	Cyclic Voltammetry
DEC	Diethyl carbonate
DMC	Dimethyl carbonate

EBSD	diffracted backscattered electrons
EC	Ethylene carbonate
FE-SEM	Field Emission Scanning Electron Microscope
FWHM	full width at half maximum
LIB	Lithium-ion battery
LIBs	Lithium-ion batteries
min	minute
nm	nanometer
NMR	nuclear magnetic resonance
OCV	Open circuit voltage
OCP	Open circuit potential
PC	Propylene carbonate
PE	Polyethylene
PMT	photomultiplier tube
PP	Polypropylene
RMS	root mean square
SEI	solid electrolyte interphase
SEM	scanning electron microscopy
SFM	scanning force microscopy
ToF-SIMS	time-of-flight secondary ion mass spectrometry
THF	Tetrahydrofuran
UHV	ultra-high vacuum
VB	Valence band
W	Watt
XPS	X-ray photoelectron spectroscopy
XRD	X-ray diffraction

List of publications

This Ph.D. work has resulted in the following publications and contributed to the following international and national conferences.

Papers presented to journals

1. **B. Tian**, J. Światowska, V. Maurice, S. Zanna, A. Seyeux, L.H. Klein, P. Marcus. Combined Surface and Electrochemical Study of the Lithiation/Delithiation Mechanism of Iron Oxide Thin Film Anode for Lithium-Ion Batteries. **The Journal of Physical Chemistry C**, 2013, 117, 21651-21661.
2. **B. Tian**, J. Światowska, V. Maurice, S. Zanna, A. Seyeux, L.H. Klein, P. Marcus. Aging-induced chemical and morphological modifications of thin film iron oxide electrodes for lithium-ion batteries. **Langmuir**, 2014, 30, 3538-3547.
3. **B. Tian**, J. Światowska, V. Maurice, C. Pereira-Nabais, A. Seyeux, S. Zanna, P. Marcus. Kinetics evaluation of thin film α-Fe_2O_3 negative electrode for lithium-ion batteries. **Electrochimica Acta**. To be submitted.
4. **B. Tian**, J. Światowska, V. Maurice, S. Zanna, A. Seyeux, L.H. Klein, P. Marcus. Binary (Fe, Cr)-oxide thermally grown on stainless steel current collector as anode material for lithium-ion batteries. To be submitted.

Papers presented to conferences

5. **B. Tian**, J. Światowska, V. Maurice, C, Pereira-Nabais, A. Seyeux, P. Marcus. Direct Evaluation of Lithium Diffusion Kinetics in Electrodes for Lithium-ion Batteries by ToF-SIMS. **IMLB 2014**, Poster, June 10-14, 2014, Como, Italy.
6. **B. Tian**, J. Światowska, V. Maurice, S. Zanna, A. Seyeux, L.H. Klein, P. Marcus. Spectroscopy (XPS, ToF-SIMS) and Microscopy (SEM, AFM) study capacity degradation of cycled iron oxide thin films in lithium-ion batteries. **4ème journée «Batterie Lithium Ile de France»**, Oral presentation, September 10, 2013, Thiais, France.
7. **B. Tian**, J. Światowska, V. Maurice, S. Zanna, A. Seyeux, L.H. Klein, P. Marcus. XPS and ToF-SIMS study of iron oxide thin films as negative electrodes for lithium-ion batteries. **LiBD 2013**, Oral presentation and poster, June 16-21, 2013, Arcachon, France.

Acknowledgements

I would like to express my sincere gratitude to:

First and foremost, my supervisors, Prof. Dr. Philippe Marcus, Dr. Vincent Maurice, and Dr. Jolanta Światowska for accepting me as a PhD student in your group, and for your guidance, encouragement, support and excellent inspiration;

My co-authors, Dr. Lorena H. Klein, Dr. Sandrine Zanna, Dr. Antoine Seyeux, for your guidance, sharing your knowledge, inspiring discussions and fruitful collaborations;

The secretaries, Sylvie Gandziarski, Marie-Jose Michel for your helps with the administrative matters;

All the present and former members in Laboratoire de Physico-Chimie des Surfaces at Institut de Recherche de Chimie Paris, CNRS - Chimie ParisTech, Feng, Catarina, Mathieu, Thomas, Carole, Sophie, Hao, Jun, Toni, Maud, Lily, Ning, Zuzana, Emna, Shadi, Jae Dong, Clément, Arnaud, Antoine, Maria, Elise, Blanca, Oumaïma, Marion, Remi, Viacheslav, Hu, … for sharing the good times and happy hours in Paris;

The Chinese Scholarship Council (CSC) for the financial support;

Finally, my family, especially my wife Xiyan Fan, for your selflessness and understanding; without your love and support, I may not be able to earn this degree.

Bingbing TIAN

Campus Pierre et Marie Curie

06/2014

Preparation and characterization of iron oxide electrode materials for lithium-ion batteries by electrochemical and spectroscopic (XPS, ToF-SIMS) methods

Lithium-ion batteries (LIBs) are widely used as power sources for portable electronic devices. Iron oxide (mainly α-Fe_2O_3), as one of the most important transition metal oxide, has attracted attention due to its high theoretical capacity (1007 mAh g^{-1}), environmental friendliness, abundance and low cost since reported as anode material for LIBs. In this thesis, an iron oxide thin film model electrode was prepared by simple thermal oxidation of pure metallic iron substrate at 300 ^{o}C in air, also used as a current collector. Electrochemical methods (CV, EIS and galvanostatic cycling) were combined with surface (XPS, ToF-SIMS) and microscopic (SEM, AFM) analytical techniques to investigate the reaction mechanisms and the surface chemistry of the iron oxide thin film at different stages of lithiation/delithiation and upon cycling.

Keywords: Lithium-ion batteries; iron oxide; conversion; SEI; CV; EIS; XPS; ToF-SIMS; SEM; AFM

Préparation et caractérisation des matériaux d'électrode en oxyde de fer pour les batteries lithium-ion par méthodes électrochimiques et spectroscopiques (XPS, ToF-SIMS)

Les batteries lithium-ion sont largement utilisées comme source d'énergie pour les appareils électroniques portables. L'oxyde de fer (principalement α-Fe_2O_3), l'un des oxydes de métal de transition les plus important, a suscité l'intérêt scientifique depuis qu'il a été reporté comme matériau d'anode pour les batteries lithium-ion en raison de sa capacité théorique élevée (1007 mAh g^{-1}), de son respect de l'environnement, de son abondance et de son faible coût. Dans cette thèse, une électrode modèle en couche mince d'oxyde de fer a été préparée par simple oxydation thermique à 300 °C dans l'air d'un substrat de fer métallique pur, utilisé aussi comme collecteur de courant. Une variété de techniques d'analyse, électrochimiques (CV, EIS et cyclage galvanostatique), spectroscopiques (XPS, ToF-SIMS) et microscopiques (MEB et AFM), ont été mises en oeuvre pour étudier les mécanismes réactionnels et la chimie de surface de l'oxyde de fer à différents stades de lithiation/délithiation et cyclage.

Mots-clés : Batteries lithium-ion; oxyde de fer; conversion; SEI; CV; EIS; XPS; ToF-SIMS; MEB; AFM

Bingbing TIAN

Institut de Recherche de Chimie Paris, CNRS – Chimie ParisTech (UMR 8247),

11 rue Pierre et Marie Curie, 75005 Paris, France